Constraining the CO_2 and non-CO_2 contributions to the rate of warming and implications for the Paris Agreement

Stuart Jenkins

Wadham College
University of Oxford

A thesis submitted for the degree of
Doctor of Philosophy

Hilary 2023

Abstract

Anthropogenic climate change is well established, with historical emissions of greenhouse gases and aerosols causing 1.1 °C warming today, and rising at +0.2 °C/decade. At this rate the Paris Agreement's 1.5 °C warming threshold is reached within two decades. For policymakers this proximity means that the anthropogenic warming rate is one of the most important variables to constrain today. Several methodologies exist to determine warming contributions utilizing Earth observations and climate models of varying complexity. However, many of these approaches do not establish the impact of recent emissions trends in short-lived aerosol pollutants, and consequently may underestimate the present-day rate of warming. This thesis begins by investigating the CO_2, non-CO_2 greenhouse gas, and aerosol contributions to anthropogenic global warming today, focusing on evidence presented by trends in satellite and in-situ observations. These trends are attributed to anthropogenic and natural sources using simplified climate models, informed by full-complexity general circulation models, to assess the observational evidence for an aerosol-induced warming acceleration. The simplified modelling approach is then pursued to evaluate physical constraints on future policy. For CO_2, the use of a 'remaining carbon budget' — the emissions compatible with a warming threshold — simplifies policy objectives until net zero. However, the combined physical requirements of CO_2 and non-CO_2 mitigation 'budgets' is complicated by the varied lifetimes and efficacies displayed by non-CO_2 pollutants, resulting in a non-trivial relationship between emissions and warming. In this thesis, I show how the forcing-equivalent metric can produce physically-coherent estimates of individual pollutants' contribution to the remaining budget. Finally, I explore the physical conditions required for warming stabilisation, based on a mathematical framework describing the long-term properties of the carbon and thermal cycles. As a whole, my work demonstrates how models and observational constraints can be combined to provide the physical guide rails over which climate policy can be optimised.

Constraining the CO_2 and non-CO_2 contributions to the rate of warming and implications for the Paris Agreement

Stuart Jenkins
Wadham College
University of Oxford

Supervised by

Myles R. Allen
Roy G. Grainger

A thesis submitted for the degree of
Doctor of Philosophy
Hilary 2023

Acknowledgements

The acknowledgements feels too short a section to communicate the gratitude I feel towards those who have shepherded me through my time at AOPP. When I started four years ago I could not have imagined the position I would be in today: the work completed, knowledge shared, and coffee consumed is substantial; all of it only possible because of the people who have supported me.

I would like to thank my supervisors, Myles Allen for his unerring enthusiasm for the solutions to climate change and constant supply of encouragement and ideas, and Don Grainger for his sharp eye to detail and focus on building a story.

I would also like to thank the various co-authors who helped shape my work: Michelle Cain, Glen Peters, Ben Sanderson, Philip Stier, Trude Storelvmo, Nick Leach, Nathan Gillett, Pierre Friedlingstein, Thomas Frölicher, Andrew Gettelmann, Adam Povey, Cecile Girardin and Tristram Walsh. And the editors and anonymous reviewers who (albeit frustratingly!) improved my research and writing, helping me practise the art of science communication.

There are several others whose interest and enthusiasm kept me going when times were hard: Graeme Stephens and Johannes Quaas for their insight on the spatiotemporal fingerprints in observations, along with their push to get work published when it was 'quite good enough'. And Eli Mitchell-Larson, Margriet Kuijper, Ingrid Sundvor and Mirte Boot: for your support on the CTBO and building real-world policy to tackle climate change.

I am very grateful to the Natural Environmental Research Council for my stipend and research grant, Wadham College for my fees, and the European Space Agency's Climate Change Initiative who topped up my stipend and research grant to make it slightly more livable! To Victoria Forth, Lucy Li and Andrea Simpson: thank you for administering the DTP and AOPP. And Heather Waller: thank you for keeping me in Myles' diary, and therefore on his mind.

To Nick, Beth and Fraser: I did not know what we were getting ourselves into when we started the DPhil, but I could not have asked for better friends to accompany me through it. Andy, Pete and Braddy, as well as Misha, Arthur and Joe, your friendships mean the world to me. I don't know why you put up with me, but I'm very glad you do.

Matthew, Rachel, Mom and Dad: thank you for always being there with advice, with support and with love. By listening to you I knew that anything was possible.

And finally Jane, to whom I owe everything these last four years. You are my inspiration.

Abstract

Anthropogenic climate change is well established, with historical emissions of greenhouse gases and aerosols causing 1.1 °C warming today, and rising at +0.2 °C/decade. At this rate the Paris Agreement's 1.5 °C warming threshold is reached within two decades. For policymakers this proximity means that the anthropogenic warming rate is one of the most important variables to constrain today. Several methodologies exist to determine warming contributions utilizing Earth observations and climate models of varying complexity. However, many of these approaches do not establish the impact of recent emissions trends in short-lived aerosol pollutants, and consequently may underestimate the present-day rate of warming. This thesis begins by investigating the CO_2, non-CO_2 greenhouse gas, and aerosol contributions to anthropogenic global warming today, focusing on evidence presented by trends in satellite and in-situ observations. These trends are attributed to anthropogenic and natural sources using simplified climate models, informed by full-complexity general circulation models, to assess the observational evidence for an aerosol-induced warming acceleration. The simplified modelling approach is then pursued to evaluate physical constraints on future policy. For CO_2, the use of a 'remaining carbon budget' — the emissions compatible with a warming threshold — simplifies policy objectives until net zero. However, the combined physical requirements of CO_2 and non-CO_2 mitigation 'budgets' is complicated by the varied lifetimes and efficacies displayed by non-CO_2 pollutants, resulting in a non-trivial relationship between emissions and warming. In this thesis, I show how the forcing-equivalent metric can produce physically-coherent estimates of individual pollutants' contribution to the remaining budget. Finally, I explore the physical conditions required for warming stabilisation, based on a mathematical framework describing the long-term properties of the carbon and thermal cycles. As a whole, my work demonstrates how models and observational constraints can be combined to provide the physical guide rails over which climate policy can be optimised.

Contents

List of Figures

List of Tables

List of Abbreviations

ACI . . . . . Aerosol Cloud Interactions, referring to the component of aerosol ERF caused by aerosol cloud interactions.

AGW . . . . . Anthropogenic Global Warming, referring to the anthropogenic contribution to global temperature change.

AMV . . . . . Atlantic Multi-decadal Variability.

ARI . . . . . Aerosol Radiation Interactions, referring to the component of aerosol ERF caused by aerosol radiation interactions.

AOD . . . . . Aerosol Optical Depth, referring to the aerosol content of an atmospheric column.

AR5 or AR6 . Fifth or Sixth Assessment Report, referring to IPCC reports commissioned for the UNFCCC.

BC . . . . . Black Carbon.

CCN . . . . . Cloud Condensation Nuclei.

CDNC . . . . . Cloud droplet number concentration, referring to the concentration of cloud water droplets observed in a cloudy-sky pixel.

CH_4 . . . . . Methane.

CMIP . . . . . Coupled Model Intercomparison Project.

CO_2 . . . . . Carbon Dioxide.

CO_2-fe . . . . . CO_2-forcing-equivalent emissions.

COP . . . . . Conference of Parties.

ECMWF . . . . Europeaan Centre for Mid-range Weather Forecasting.

ECS . . . . . Equilibrium Climate Sensitivity.

EMIC . . . . . Earth-system Model of Intermediate Complexity.

ENSO . . . . . El Niño and the Southern Oscillation.

EOF . . . . . Empirical Orthogonal Function.

ERF . . . . . Effective Radiative Forcing, like RF but where rapid adjustments to the perturbation are included.

ESM . . . . . Earth System Model, like a GCM but including an fully-interactive model of the Earth surface (including land and biosphere).

FaIR . . . . . Finite amplitude Impulse Response, referring to the simple climate model.

GCM . . . . . (Coupled) General Circulation Model, geophysical model of the atmosphere (and ocean).

GHG . . . . . Greenhouse Gas.

GLS . . . . . Generalised Least Squares, often used having assumed auto-correlated residuals (GLSAR).

GMST . . . . . Global mean surface temperature, referring to the globally-averaged surface temperature observations (typically spatially incomplete, or infilled with a statistical infilling approach).

GSAT . . . . . Global surface air temperature, referring to the globally-averaged near-surface air temperature (typically a model-derived, spatially complete quantity).

GTP . . . . . Global Temperature Potential, referring to the metric for comparing greenhouse gas emissions.

GWP . . . . . Global Warming Potential, referring to the metric for comparing greenhouse gas emissions.

GWP* . . . . . Referring to a GHG metric for comparing short-lived climate pollutants making use of GWP values (see Cain *et al.* (2019)).

HTHH . . . . . Hunga Tonga-Hunga Ha'apai, refering to the volcanic eruption on 15th January 2022.

IPCC . . . . . Intergovernmental Panel on Climate Change, referring to the body who provide reports to the UNFCCC on the scientific consensus on climate change.

LLCP . . . . . Long-Lived Climate Pollutant.

LOESS . . . . . LOcally Estimated Scatterplot Smoothing.

LW . . . . . Longwave, referring to integrated broadband radiative flux over infrared wavelengths.

LWP . . . . . Liquid Water Path, referring to the integrated liquid water path for a cloudy-sky pixel.

NASA . . . . . National Aeronautics and Space Administration.

NH . . . . . Northern Hemisphere.

N_2O . . . . . Nitrous Oxide.

OC . . . . . Organic Carbon.

OLS . . . . . Ordinary Least Squares.

PDO . . . . . Pacific Decadal Oscillation.

RACF . . . . . Rate of Adjustment to Constant Forcing.

RAZE . . . . . Rate of Adjustment to Zero Emissions.

RF . . . . . Radiative Forcing, referring to the top of atmosphere energy imbalance caused by a perturbation to the Earth System (atmospheric pollutant concentrations or surface boundary conditions).

SCM . . . . . Simple Climate Model.

SH . . . . . Southern Hemisphere.

SLCP . . . . . Short-Lived Climate Pollutant.

SO_2 . . . . . Sulphur Dioxide.

SOCRATES . . Suite Of Community RAdiative Transfer codes based on Edwards and Slingo.

SR1.5 . . . . . Special Report on the Global Warming of 1.5 °C, referring to the IPCC report commissioned by the UNFCCC.

SSP . . . . . Shared Socioeconomic Pathways.

SST . . . . . Sea Surface Temperature, referring to the surface air temperature averaged over oceans.

SW . . . . . Shortwave, referring to integrated broadband radiative flux over visible wavelengths.

TCR . . . . . Transient Climate Response.

TCRE . . . . . Transient Climate Response to cumulative CO_2 Emissions.

TCRF . . . . . Transient Climate Response to Forcing, referring to the transient warming in response to a unit forcing change.

TLS . . . . . Total Least Squares.

TOA . . . . . Top of Atmosphere, for example referring to satellite observation of outgoing radiative fluxes, or the output of radiation from the top level of a model.

UNFCCC . . . United Nations Framework Convention on Climate Change.

WMO . . . . . World Meteorological Organisation.

ZEC . . . . . Zero Emissions Commitment.

The combustion of coal by civilized man is gradually warming the atmosphere so that in the course of a few cycles of 10,000 years the Earth will be baked in a temperature close to the boiling point.

— The Selma Morning Times (1902)

1 Introduction

This chapter begins by describing the history of anthropogenic global warming, from the first mention of how humans influence global temperatures, through to the modern day approaches to constrain anthropogenic global warming. I briefly discuss motivations for this thesis, centering on the need in policy for a constraint on the rate of warming today, and how this shapes the direction for mitigation policy in this century. I introduce prominent research estimating contributions to warming, including work modelling individual pollutants' influence on the climate system, and studies analysing satellite and in-situ observations of the recent historical period. I conclude with a thesis overview.

Contents

1.1 Human influence on the climate system

The idea that anthropogenic emissions of carbon dioxide (CO_2) contribute to global climate change was first discussed in the late-19th century (*1*, *2*). The link between anthropogenic pollutants and global warming has now been established more concretely (*3*), including for greenhouse gases such as CO_2, methane (CH_4) and nitrous oxide (N_2O); and aerosols and their precursors such as sulphur dioxide (SO_2), black carbon and organic carbon. Although the mechanism of interaction with the climate system is different for each pollutant (*4*), taken together anthropogenic emissions of greenhouse gases and aerosols cause a net warming of the climate system at present day, relative to an unperturbed climate (*5*). This global warming has huge implications for the natural world, changing the frequency of extreme weather events (*6*); and for human society more widely, exacerbating drought and flood risk in already drought- and flood-prone regions through the intensification of the global hydrological cycle, further stressing vulnerable populations (*7*).

Many of the recent advances in assessing the anthropogenic contribution to climate change rely on the attribution approaches developed in the literature in the late-20th century. Although research had inferred the human influence on the climate system earlier than this, confirming it remained challenging given decade-to-decade surface temperature variability averaged $\pm 0.2\,^{\circ}C$ (*8*) and the forced contribution to warming was relatively small. By the 1990s a larger anthropogenic forcing signal had emerged which, along with improved detection methodologies, allowed the anthropogenic trend to be detected above internal variability for the first time. Hasselmann (1993) described the first 'optimal fingerprinting' methodology, whereby various spatiotemporal patterns are combined to best reproduce an observational record (*9*). Hegerl *et al.* (1996) were the first to apply this technique to the attribution problem specifically (*10*). In the following decade Hasselmann and others refined the approach further (*11*–*13*), expanding it over a wider range of climatological variables, and across alternative spatial and temporal scales (e.g. regional attribution studies). These studies provided the statistical basis for

assessing the anthropogenic influence on an observed climatological record, separating the internal variability from the long-term human-induced trends.

The most recent reports by the Intergovernmental Panel on Climate Change (IPCC) (the 6th Assessment Report, herein AR6 (*3*); and the Special Report on the Global Warming of 1.5 °C, herein SR1.5 (*14*)) use refined versions of these methodologies to assess the anthropogenic influence on the climate system over history. This includes the assessment of the anthropogenic contribution to global mean surface temperature change since preindustrial — the anchor point for framing much of the debate around anthropogenic climate change. Haustein *et al.* (2017) outlines the approach taken in SR1.5 (*15*, *16*), which uses an ordinary least squares (OLS) regression of temperature response profiles generated with a simple climate model. Complementary approaches to Haustein are discussed in Gillett *et al.* (2021) and Ribes *et al.* (2021). Gillett replaces the simple model-derived temperature response shapes with those generated by more complex general circulation models (GCMs) (*17*), and Ribes additionally fits them to observations using alternative statistical methodologies (*18*). These three approaches were formally combined to estimate the level and rate of anthropogenic global warming (AGW) in AR6 (*8*), which determined AGW reached 1.1°C over the decade 2010-2019, relative to the 1850-1900 baseline. In addition, SR1.5 and AR6 gave the IPCC's first estimate of the current rate of warming, at +0.2 °C/decade.

Research assessing the level of anthropogenic global warming since preindustrial has received significantly more attention than assessments of the rate of warming over shorter intervals. This is likely because of the difficulty of assessing short-term forced trends in variables which themselves exhibit large interannual variability, without detailed knowledge of the shapes of individual pollutants' energy perturbations over time. This information has been lacking for many pollutants, particularly very short-lived pollutants (e.g. aerosols) for whom a precise assessment of the preindustrial climate state is required (*19*). In AR6, Forster *et al.* (2021) reassessed the energy imbalance contributions from individual pollutants over history, and produced timeseries of radiative forcing between 1750 and 2100, allowing updated assessments of the level and rate of warming at present day (*5*).

1.2 The level and rate of warming

The World Meteorological Organisation (WMO) (*20*) and UN Framework Convention on Climate Change (UNFCCC) (*21*) have sought a definition of global warming which is robust enough to form the basis for policymaking, while remaining flexible enough to adapt to updates in input datasets' trends. This flexibility is particularly important in the context of policy which targets stabilisation of global temperatures in the mid-21st century, where we need to be able to accurately attribute the warming level and rate to remaining anthropogenic emissions in near-real time.

The observed global mean surface temperature (GMST) compared to its average over some pre-defined historical baseline (typically 1850-1900 in the IPCC (*22*)) is the crudest possible measure of global warming over time. This is because, although the GMST anomaly is expected to rise as humans continue to release greenhouse gas (GHG) emissions, it is also impacted by natural variability. Natural influences on the climate system include volcanic eruptions, variations in net insolation, and trends in ocean heat uptake causing temporary sea surface temperature (SST) anomalies.

A good example of how these natural influences complicate the assessment of anthropogenic global warming comes from the eruption of Hunga Tonga-Hunga Ha'apai (HTHH) on 15th January 2022. Ranked with a Volcanic Explosivity Index of 5 (*23*), this was the most explosive eruption since Pinatubo in 1991, producing perturbations in surface pressure which reverberated around the globe for days after the eruption event itself (*24*). The eruption was also notable because of the composition of its stratospheric perturbation — an estimated 0.42 MtSO_2 sulphur dioxide injection (*23*, *25*) and 146 MtH_2O water vapour injection (*26*). The HTHH eruption resulted in the largest stratospheric water vapour perturbation observed in the satellite era (a 10-15% increase in the water vapour content of the stratosphere), with a modest accompanying SO_2 injection (approximately 1/50th the size of the Pinatubo eruption (*27*)). Water vapour is a potent greenhouse gas (*5*), meaning the HTHH eruption causes a temporary spike in global temperature.

In Jenkins *et al.* (2022) I calculated the contribution of HTHH eruption to the GMST anomaly using an offline radiative transfer calculation in SOCRATES (*28*) (assuming the

146 MtH_2O emission is distributed between 40 and 7.5 hPa, and 60°S and 60°N) and the FaIRv2.0 simple climate model (*29*). The peak warming contribution from HTHH is +0.035 °C and decays over a ~5-10 year interval as the water vapour perturbation is removed from the stratosphere (*26*). Small deviations in GMST like this affect policy-relevant warming metrics, such as the WMO's near-term climate assessment (*30*), which assesses the likely global temperature anomaly trend in the next five years. Their 2022 assessment suggested a 50% chance of the GMST anomaly exceeding 1.5 °C in at least one of the next five years (2022-2026) (*30*), but did not include the additional perturbation from HTHH. Doing so adds an additional 7% to this risk of GMST temporarily exceeding 1.5 °C before 2026 (*31*).

Clearly, the definition of global warming must account for the stochastic nature of the global surface temperature anomaly year-on-year. Noting this, in the late-20th century it was proposed to measure global warming using changes in the 30-year average of the GMST anomaly timeseries (*32*). This definition was used because, while the internal variability contribution to GMST was poorly constrained, a 30-year average was deemed sufficiently long to negate its effect. By the turn of the 21st century, the 30-year average GMST anomaly had emerged above the level of internal variability in GMST over the wider historical period, meaning a clear global warming trend was visible in observations for the first time. However, while this 30-year average approach did smooth over the noise in GMST observations, it did not constrain the rate of warming over shorter intervals (i.e. less than 30 years), and so could not be easily extended to estimate global warming in near real-time. It also had the problem that estimates of the current level of warming were always 15 years out of date. Recognising this, alternative methodologies for defining global warming, such as Locally Estimated Scatterplot Smoothing (LOESS) regression of the GMST timeseries (*33*), were proposed to isolate multi-decadal trends. This methodology was an improvement over the 30-year average approach, although the former approach's simplicity mean both remain used in many derivations of decadal trends in the GMST record (*34*). While a LOESS regression partially addresses the concern of projecting the global warming trend closer to present-day, it still fails to

produce a truly current warming level and rate assessment, and cannot robustly isolate the anthropogenic contribution to that warming anomaly.

The fingerprinting methodologies discussed by Hasselman (1993) were devised to resolve precisely this problem (*9*). Using them, Haustein *et al.* (2017) proposed an attribution methodology where the forced contributions from natural and anthropogenic sources are regressed onto the GMST anomaly, producing best-estimate contributions from each to the time-history of GMSTs. This setup is described by

$$\vec{y} = \vec{\beta}\mathbf{x} + \vec{\epsilon}, \tag{1.1}$$

where $\vec{y}$ is a vector containing the observed GMST anomaly, $\vec{\beta}$ is a vector of linear regression parameters to be estimated, $\mathbf{x}$ is a matrix containing the regressors (columns are the perceived forced contributions to the GMST vector), and $\vec{\epsilon}$ is an uncorrelated error term. An OLS regression determines the best-fit combination of the columns in the regressor matrix which minimises the sum-squared distance from $\vec{y}$

$$\hat{\beta} = \arg_{\beta}\min \|\vec{y} - \vec{\beta}\mathbf{x}\|^2. \tag{1.2}$$

Columns of the regressor matrix rescaled with the $\hat{\beta}$ vector describe the individual best-estimate contributions to the GMST anomaly. As discussed above, Haustein's approach is combined with two others to produce the overall warming assessment in AR6. All three approaches follow similar fundamental methodologies:

The second approach by Gillett *et al.* (2021) completes a TLS regression in a near-identical setup to Haustein *et al.* (2017), but replaces simple climate model-derived forced contributions in the regressor matrix with CMIP6-model equivalents (globally-averaged surface air temperature (GSAT) timeseries produced using subsets of anthropogenic and natural forcings (*17*)). This finds a higher anthropogenic warming rate at present day (see table 1.1), due to the higher recent historical warming trends exhibited by some CMIP6 models (*35*). Gillett's approach provides additional context to Haustein's AGW estimate by sampling the warming behaviour of more complex GCMs, but is not readily updatable since it requires rerunning the CMIP6 DECK historical experiments (*36*) with updated inputs. This exercise is not yet routinely completed,

but could be streamlined if modelling centres are encouraged to save their historical experiment's restart state in the future.

The third approach by Ribes *et al.* (2021) uses an 'errors in variables' statistical framework similar to a total least squares (TLS) regression (*18*). In this case, the CMIP6 ensemble of all-forcing GSAT responses are sampled as a Gaussian distribution, while the observed GMST vector is assumed to be composed of this forced response plus a Gaussian error

$$\vec{y} = \mathbf{H}\vec{x} + \vec{\epsilon}, \text{ where } \vec{x} \sim \mathcal{N}(\vec{\mu}, \Sigma_{\text{mod}}) \text{ and } \vec{\epsilon} \sim \mathcal{N}(\vec{0}, \Sigma_{\text{obs}}). \tag{1.3}$$

Here, $\vec{y}$ is again a vector of observed monthly GMST anomalies, $\vec{x}$ is a multivariate Gaussian distribution (with normal vector $\vec{\mu}$ and covariance matrix Σ_{mod}) describing the distribution of CMIP6 model-derived GSAT responses to historical all-forcing experiments, smoothed with a sixth-order smoothing spline (*37*) to remove internal variability (*18*). $\vec{\epsilon}$ is a multivariate Gaussian distribution describing internal variability in the GMST observations. $\mathbf{H}$ is the *observation operator*, which selects the portion of the forced response vector ($\vec{x}$) which is expressed within the observations vector ($\vec{y}$).

Since the vectors $\vec{x}$ and $\vec{\epsilon}$ defined in equation 1.3 are multivariate normal distributions, equation 1.3 can be recast as

$$\begin{pmatrix} \vec{x} \\ \vec{y} \end{pmatrix} \sim \mathcal{N}\left(\begin{pmatrix} \vec{\mu} \\ \mathbf{H}\vec{\mu} \end{pmatrix}, \begin{pmatrix} \Sigma_{\text{mod}}, & \Sigma_{\text{mod}}\mathbf{H}' \\ \mathbf{H}\Sigma_{\text{mod}}, & \mathbf{H}\Sigma_{\text{mod}}\mathbf{H}' + \Sigma_{\text{obs}} \end{pmatrix} \right). \tag{1.4}$$

Here, the $\begin{pmatrix} \vec{x} \\ \vec{y} \end{pmatrix}$ vector has been written as another Gaussian distribution, partitioned into its respective mean vectors and covariance matrices (*38*). Ribes *et al.* (2021) considers the conditional distribution of $\vec{x}$ given the observed GMST vector $\vec{y} = \vec{y}_0$, i.e. $(\vec{x} \,|\, \vec{y} = \vec{y}_0)$. Using the Gaussian conditioning theorem (*38*), this means the forced GSAT response distribution $\vec{x}$ is conditioned according to the observed GMST timeseries $\vec{y}_0$ and the characteristics of the covariance in observed GMST ($\mathbf{H}\Sigma_{\text{mod}}\mathbf{H}' + \Sigma_{\text{obs}}$), contributed to by both the internal variability of the climate system (Σ_{obs}), and uncertainty in the forced GSAT response ($\mathbf{H}\Sigma_{\text{mod}}\mathbf{H}'$).

Ribes' approach is more sophisticated in explicitly considering how the distribution of forced GSAT response shapes will impact on the attribution, compared to considering

the individual model response shapes to be perfect representations of the time-history of anthropogenic influences on the climate system in Gillett *et al.* (2021) and Haustein *et al.* (2017). However, it is also limited by failing to capture more rapid changes in the forced GSAT response shapes, as is possible in the two former approaches (so long as it is captured in the matrix of regressors). This is because, in order to derive internal-variability-free forced GSAT response shapes, Ribes *et al.* (2021) uses a sixth-order smoothing spline. This also removes forced responses which occur over sub-decadal timescales, as can be seen in the forced response shapes used in Ribes' study (*18*). Ribes also assumes that the CMIP6 all-forcing GSAT responses contain the correct relative contribution from aerosols and GHGs (i.e. that the CMIP6 distribution contains no significant bias), and that they can be appropriately sampled as a Gaussian distribution. These assumptions are questionable given Gillett *et al.* (2021) finds altering the aerosol/GHG ratio in CMIP6 models produces a better fit to the GMST anomaly, and the second assumption may also not be valid if GCMs tune against GMST when completing performance benchmarks. For these reasons, and because CMIP6 models' historical experiments are not routinely updated, in this thesis I use Haustein *et al.* (2017)'s methodology to define AGW.

By combining the results of all three methodologies, AR6 reports the level and rate of anthropogenic global warming (AGW) over history: 1.07 °C in 2010-2019 relative to 1850-1900, and rising at +0.2 °C/decade. The level of warming is estimated from a formal combination of the three approaches (averaging), while the rate is a lot more subjective — essentially based on noting that 0.2 °C/decade is not inconsistent with any approach. Note that while the assessments generally agree on the AGW level, they do not produce identical estimates of the rate of warming (compare the three individual attribution studies in table 1.1). There is both substantial uncertainty around the anthropogenic warming rate (±50%), and disagreement on the best-estimate value. These discrepancies provide the key motivation for this thesis, with my defining question *what is the anthropogenic contribution to the current rate of warming?*

Study	Warming level 2010-2019 (°C)	Warming rate 2010-2019 (°C/decade)
Haustein *et al.* (2017)	1.06 (0.94 to 1.22)	0.23 (0.19 to 0.35)
Gillett *et al.* (2021)	1.11 (0.92 to 1.30)	0.35 (0.30 to 0.41)
Ribes *et al.* (2021)	1.03 (0.89 to 1.17)	0.23 (0.18 to 0.29)
AR6 Assessment	1.07 (0.8 to 1.3)	0.2 (0.1 to 0.3)
Fig. SPM.1 (SR1.5)	1.04 (0.84 to 1.24)	0.20 (0.16 to 0.24)
Fig. SPM.1 (AR6)	1.10 (0.90 to 1.30)	0.32 (0.26 to 0.38)

Table 1.1: Assessments of the present-day level and rate of warming used in IPCC's AR6 (Haustein, Gillett and Ribes). Present-day anthropogenic warming assessment from figure 1.1 also shown for comparison.

1.3 Why the rate of warming matters today

In 2015 the UNFCCC's COP21 meeting produced the Paris Agreement (*39*), a landmark accord which commits governments to "hold[ing] the increase in the global average temperature to well below 2 °C above preindustrial levels and to pursue efforts to limit the temperature increase to 1.5 °C above preindustrial levels". In order to achieve this long-term temperature goal, parties should "aim to reach global peaking of greenhouse gas emissions as soon as possible [...] and to undertake rapid reductions thereafter in accordance with best available science, so as to achieve a balance between anthropogenic emissions by sources and removals by sinks of greenhouse gases in the second half of this century".

To produce a mitigation effort which follows the 'best available science', the UNFCCC periodically commissions reports from the IPCC which summarise the current state of knowledge in climate change research, including the Assessment Reports (e.g. AR4 (*40*), AR5 (*41*), AR6 (*3*)), and special reports on particular subjects of interest (e.g. SR1.5 (*14*)). These IPCC reports play a prominent role in setting the direction for physical climate change research by highlighting important remaining knowledge gaps for policymakers. Above I introduced the key attribution methodologies used to determine the level and rate of AGW in AR6 (*8*). I argued these methodologies are typically more confident in the level of AGW today and less assured on the trend in AGW over the most recent decade. The lack of consensus on the rate of warming today presents a major knowledge gap for policymakers, with uncertainty on this variable projecting

into assessments of the time remaining to future warming thresholds and the design of mitigation policy. To demonstrate this, below I consider how the present-day warming rate, assessed using either SR1.5-era or AR6-era inputs, impacts on the outcome of a stylised 1.5 °C-compatible mitigation scenario.

1.3.1 SR1.5's and AR6's projected warming rates

The simplest assessment of the near-term warming linearly projects the present decade's warming trend forward over the following decade. This approach was used in the warming rate projection in figure SPM.1, SR1.5's headline figure defining the criteria by which a scenario is considered 1.5 °C-compatible. The figure contains a historical warming attribution, a projected date of 1.5 °C-exceedance if the warming trend continues unabated, and a scenario which includes mitigation in order to remain 1.5 °C-compatible over the 21st century. Clearly, changing the anthropogenic warming rate today will impact on the requirements of 1.5 °C mitigation policy shown on this figure.

The headline scenario from figure SPM.1 is reproduced twice in figure 1.1, once with SR1.5-consistent inputs (dotted warming plume on panel a), and again with AR6-consistent inputs (solid plume on panel a). The AGW attribution follows Haustein *et al.* (2017)'s approach, as discussed above, with updates to the GMST anomaly and forced anthropogenic contributions to the regressor matrix in the case of the AR6 update. The future scenario is estimated using the FaIR Simple Climate Model (*42*), additionally sampling physical climate response parameter uncertainty (methodology described in SR1.5 (*16*)). Note that, other than updating the GMST anomaly and the relevant GHG and aerosol forcings (which show a stronger historical forcing trend in AR6, compared to SR1.5; see historical period on panel d), the production methodology for these two scenarios is identical.

The impact of these revisions on the attributed level and rate of warming is reported in table 1.1 for comparison with the attribution studies discussed above. When using SR1.5-era inputs, the 2010-2019 warming level is approximately 1.04 °C, the warming rate +0.2 °C/decade, and hence 1.5 °C warming is exceeded by 2040 (marked with an open black scatterpoint on panel a). With the AR6-era updates, the 2010-2019

warming level is 1.1 °C, and the present-day warming rate exceeds +0.3 °C/decade. These revisions cause 1.5 °C-exceedance to occur a full decade earlier (approximately in 2030, marked with a filled black scatterpoint on panel a), assuming the present-day warming rate continues unabated. Equal contributions arise from each major dataset revision in the AR6-era scenario, with a five-year reduction from the upward revision to the GMST anomaly (*43*), and the other five-year reduction due to a larger non-CO_2 forcing trend in AR6 (*44*).

This rate of warming assessment dramatically alters the outcome of a mitigation scenario previously considered 1.5 °C-consistent in SR1.5. The grey scenario in figure 1.1b, c and d considers a linear decline in CO_2 emissions from 2020 to reach net zero in 2055 (panel b) along with a peak and decline of net non-CO_2 radiative forcing (a measure of the energy imbalance caused by non-CO_2 pollutants) after 2030 (panel d) (*45*). The resulting warming trajectory is shown with a grey plume on panel a for the AR6-consistent attribution, and with dotted lines for the SR1.5-consistent attribution. Remember that the future portion of the two scenarios are identical in both stylised mitigation pathways in figure 1.1, with the only differences arising due to updates in the GMST anomaly and the historical non-CO_2 forcing trend. The peak and end-of-century warming distributions for the two plumes are marked with uncertainty bars on panel a. While the grey scenario achieves a 50% chance of remaining below 1.5 °C at peak warming and a 66% chance of remaining below 1.5 °C by 2100 using the SR1.5-consistent attribution, when including the AR6 updates it peaks at 1.7 °C and remains above 1.5 °C with greater than 50% confidence.

Hence, figure 1.1 highlights a key issue for AR6: although table 1.1 suggests the Haustein warming rate is +0.2 °C/decade, the Haustein methodology in fact attributes a warming rate of +0.3 °C/decade using AR6 inputs in figure 1.1, and this has a material impact on the outcomes of 1.5 °C policy. The difference between the Haustein *et al.* (2017) warming rate in table 1.1 and the warming rate in figure 1.1 reflects an inconsistency in the use of AR6-era inputs when estimating AGW in Eyring *et al.* (2021): namely that the Haustein *et al.* (2017) result used HadCRUT5's updated GMST (*43*), but did not use the updated non-CO_2 radiative forcing timeseries from

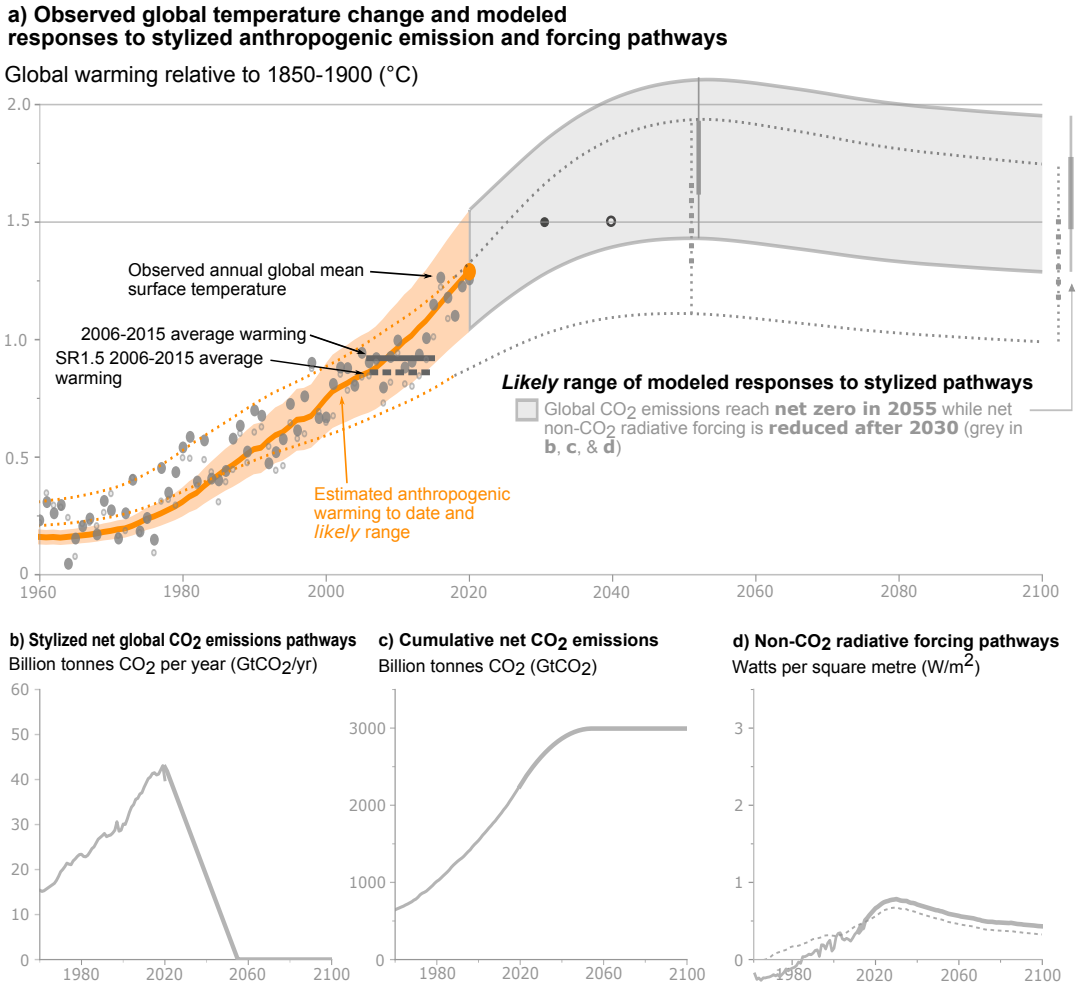

Figure 1.1: Updates to figure SPM.1 from the Summary for Policymakers document of IPCC's Special Report on the Global Warming of 1.5 °C. The figure shows stylised mitigation pathways which are consistent with the 1.5 °C warming threshold. Panel a shows the attributed anthropogenic temperature anomaly in orange over GMST observations (grey-filled points) along with a future mitigation scenario plume outlined with grey solid lines. The grey scenario achieves net zero CO_2 emissions in 2055 (panel b, cumulative emissions in c), along with declining net non-CO_2 RF after 2030 (panel d; original non-CO_2 ERF dashed line, updated non-CO_2 ERF solid line). The original SPM.1 figure's grey plume is shown with dotted orange/grey lines on panel a along with the original GMST anomaly points (small unfilled black circles). The peak warming distribution are shown on panel a with vertical error bars positioned at the year of peak warming (solid = updated, dotted = original). The 2100 warming distribution is also shown to the right of panel a for the updated scenario. Horizontal dark grey bars over the orange plume show the 2006-2015 average anthropogenic warming level in the original SPM.1 figure (dotted) and in the updated SPM.1 figure scenarios (solid). The black (open) dot shows the median 1.5 °C crossing time for the updated (original) SPM.1 figure. The original figure can be found at https://www.ipcc.ch/report/sr15/summary-for-policymakers/spm1-4/.

Forster *et al.* (2021). This makes the original Haustein assessment incompatible with Gillett's and Ribes' CMIP6-derived warming trends in table 1.1, which do include the updated forcings (*17*, *18*). Correcting for this, Haustein's warming rate is 50% higher, and closer to Gillett *et al.* (2021) than Ribes *et al.* (2021) — enough to alter the overall warming rate assessment of AR6.

Separately, AR6 also assessed CMIP6 scenario warming projections, determining that GCMs estimate similar time remaining to 1.5 °C regardless of scenario ambition, since all scenarios were estimated to reach 1.5 °C in the window between 2021 and 2040 (see tables 4.2 and 4.5 in Lee *et al.* (2021) (*46*)). This 2021-2040 1.5 °C-exceedance window is consistent with the stylised scenarios presented in figure 1.1 and the warming trends in table 1.1, although the use of a 20-year window makes it extremely likely this would be the case given our proximity to the 1.5 °C threshold.

In summary, most of the uncertainty in the 1.5 °C crossing time arises from uncertainty in the current rate, not level, of warming. The various projected warming trends in table 1.1 do not present consistent estimates of the present-day AGW rate. AR6's headline AGW assessment suggests 1.5 °C-exceedance in 2036 if the current warming trend of +0.2 °C/decade continues. This is five years after 1.5 °C is exceeded according to the central year in tables 4.2 and 4.5 of Lee *et al.* (2021). It is also inconsistent with two of the three warming attribution studies used in AR6's own warming rate assessment, if those assessments are first fully updated to include AR6 inputs (Haustein and Gillett assessements then both suggest 1.5 °C-exceedance around 2030). Alongside updates to the GMST anomaly, figure 1.1's warming rate increase is due to a substantial increase in the non-CO_2 historical forcing trend in AR6. Forster *et al.* (2021) acknowledges the potential for the recent forcing trend updates to impact on the warming attribution in this way, but does not assess how uncertainty in the recent forcing trend impacts on the warming trend assessment. They also fail to communicate these forcing updates for Eyring *et al.* (2021)'s warming assessment, leading to inconsistent warming rate and forcing trend assessments between the different chapters of AR6's Working Group 1 report.

1.3.1.1 Key questions relating to the rate of warming

This thesis focuses on constraining the CO_2 and non-CO_2 contributions to the rate of warming. Figure 1.1 demonstrates how this measurement provides the guide rails for climate policy design, and how uncertainty in the warming rate today impacts on the outcome of an ambitious mitigation scenario. Based on these discussions, below I summarise three topics for further study:

i) Present day

Our proximity to the 1.5 °C threshold today means that changes to the next decade's warming rate substantially alters the time remaining to 1.5 °C. With AGW reaching 1.1 °C between 2010-2019 and rising at +0.2 °C/decade, the 1.5 °C threshold is surpassed in the decade 2030-2039. If the warming rate increases to +0.3 °C/decade, then the crossing time lies in the decade 2025-2034. Our lack of knowledge of the precise anthropogenic contribution to the warming rate today presents a major problem for climate policy planning for a rapid mitigation effort consistent with the most ambitious goals of the Paris Agreement. Accurate measurement of the trend in GMST, and the means to estimate the anthropogenic contribution to it, are cornerstones of effective policy design.

ii) The remaining budget

With an assessment of the current warming level and rate, one can estimate the total additional warming allowable under a pre-defined policy ambition. Accurately determining and comparing the contributions to this total from the full range of anthropogenic pollutants is vital for designing complex multi-gas mitigation policy. The remaining carbon budget framework (*47*), where a quantity of CO_2 emissions consistent with a set warming threshold is estimated, is a powerful methodology for simplifying this analysis. However, the inclusion of non-CO_2 pollutants into this budget framework is not trivial. Non-CO_2 GHGs and aerosols causes AGW through various mechanisms: direct interaction with insolation, interactions with outgoing infrared radiation, and manipulation of other properties of the climate system which indirectly impact the Earth's

energy balance. They have various efficacies and atmospheric residence times, making their contribution to the remaining carbon budget framework more challenging to assess.

iii) AGW stabilisation

Finally, an understanding of the long-term drivers of the warming trend is also necessary to determine the conditions required for AGW to stabilise. This has received very little research attention to date, beyond the accepted notion that "reaching and sustaining net zero global anthropogenic CO_2 emissions and declining net non-CO_2 radiative forcing would halt AGW on multi-decadal time scale" (*14*). In order to stabilise AGW at any level, any ongoing emissions at that time must be balanced against Earth system feedbacks and responses of the climate system to the time-history of forcing. For some pollutants, such as CO_2, these multi-decadal responses may be substantial if the carbon and thermal cycles have sufficiently different multi-century responses, making the emissions consistent with warming stabilisation non-zero.

Together, these three topics present the key areas I will explore in this thesis. The key motivation for this work is to produce a self-consistent and updated assessment of the warming rate at present day, including an attribution of the anthropogenic and natural contributions. This will inform the physical requirements for mitigation policy aiming for a long-term global temperature goal, which I will explore in later chapters.

1.4 Constraining anthropogenic global warming

Having defined the research questions motivating this thesis above, this section now goes into greater detail introducing relevant background material for constraining the level and rate of warming.

The anthropogenic influence on the climate system can be studied using a mixture of in-situ observations, satellite observations and physical models. Of course these approaches can be applied in isolation. They are also complementary: research will often condition an ensemble of model responses using real-world measurements, producing an *observationally-constrained* assessment of a variable or parameter. This thesis leverages

such approaches a number of times to produce estimates of physical climate parameters which are consistent with both climate models and historical Earth observations.

Below I discuss recent research which estimates AGW using a mixture of model-based and observation-based approaches, split into discussions on the CO_2, non-CO_2 GHG and aerosol contributions to warming. This is split into two key sections. Section 1.4.1 first briefly introduces the key modelling ensembles and experiments used in this thesis, before discussing the prominent literature constraining individual pollutants' contributions to global warming today. Section 1.4.2 then introduces the satellite and in-situ observation datasets used in this thesis, before discussing studies which have applied these datasets to constrain present-day global energy imbalance.

1.4.1 The physical response to anthropogenic pollutants

1.4.1.1 The hierarchy of model complexity

The most complex models of the climate system today are coupled GCMs and their associated Earth System Models (ESMs) variants. Coupled GCMs are a gridded physical model of the ocean and atmosphere, which include a dynamical core based on the Navier Stokes equations and a radiative transfer code to compute energy perturbations based on the composition of the atmosphere and properties of the land surface. ESMs additionally include a dynamic model of the land and biosphere, meaning they can also capture carbon, nitrogen and other biogeochemical cycles. A GCM is driven by gridded atmospheric concentration datasets and boundary conditions for the surface, while an ESM can also be driven by gridded emissions datasets for some pollutants (e.g. CO_2). Examples of GCMs include HadGEM3-GC31-LL (*48*), UKESM (*49*), CanESM5 (*50*), IPSL-CM6A-LR (*51*), and MIROC6 (*52*).

In order for modelling groups to benchmark their performance against one another and for researchers make best use of the full range of GCMs, the Coupled Model Intercomparison Project (or CMIP) coordinates a series of standardised experiments (*53*). A number of these experiments are utilised in the research presented in this thesis, the most important of which are outlined in table 1.2.

Experiment name or modelling tool name	Short name	Description
Diagnostic, Evaluation and Characterisation of Klima	DECK	Common experiments for all participating GCMs that maintains continuity and helps document basic characteristics of models. Includes 4xCO_2 and 1%/yr CO_2 concentration increase experiments, and CMIP historical simulations (1850 – near-present). See ref. (*36*).
Radiative Forcing Model Intercomparison Project	RFMIP	Assesses the radiative forcing calculated by GCMs for historical and future climate studies. Includes present-day time-slice experiments (to diagnose IRF and ERF) and transient experiments (to diagnose transient ERF). See ref. (*54*).
Aerosol and Chemistry Model Inter-comparison Project	AerChemMIP	Quantifies the climate and air quality impacts of aerosols and chemically-reactive gases in GCMs. Includes historical and future scenario simulations with preindustrial Short-Lived Climate Pollutants and/or aerosols, along with counterparts with prescribed SSTs. See ref. (*55*).
Detection and Attribution Model Inter-comparison Project	DAMIP	Fully-coupled historical and future scenario simulations run individually for natural, GHG and aerosol forcings, for use in attribution studies. See ref. (*56*).
Zero Emissions Commitment Model Inter-comparison Project	ZECMIP	Quantifies and investigates the unrealised temperature change that occurs after CO_2 emissions reach net zero. Includes zero-emissions experiments which are branched from 1%/yr CO_2 concentration increase or bell-curve CO_2 emissions-driven experiments, once a predefined cumulative emissions budget is exhausted. See ref. (*57*).
Finite amplitude Impulse Response model	FaIRv2.0	Impulse response model framework for all anthropogenic pollutants: 4 gas cycle pools coupled to 3 thermal cycle pools. See ref. (*29*).
Model for the Assessment of Greenhouse gas induced Climate Change	MAGICC7.0	Multi-layer energy balance model of the thermal cycle, coupled to multi-pool carbon cycle model. See ref. (*58*).

Table 1.2: CMIP6 experiments and simple modelling tools used in this thesis.

Since these models are run with such high spatiotemporal resolution they produce only a very sparse sampling of the full parameter space available. Hence, to supplement these GCM experiments researchers have produced Earth system Models of Intermediate Complexity (EMICs) and simple climate models or emulators (SCMs). These are more lightweight, low-dimensionality models, which can be run over large ensembles (up to millions of members) to sample the parameter spaces more thoroughly. Prominent examples include the FaIR model (*29*, *42*, *59*), MAGICC (*58*), and CICERO-SCM (*60*).

FaIR is used in several places in the Working Group 1 contribution to AR6, including to produce estimates of the level and rate of human-induced warming as discussed above. It is also the model used to produce the warming outcomes in SR1.5's SPM.1 figure, reproduced in figure 1.1 above. In this thesis FaIRv2.0 (*29*) is used extensively, and a full discussion of its structure is provided in chapter 2.

1.4.1.2 Scenarios for evaluating global climate policy

Over the historical period scenarios for input into climate models use emissions/concentration timeseries from direct observations, or from collated inventories. Examples of these emissions inventories include the Global Carbon Budget (*61*), Community Emissions Data System (CEDS) (*62*, *63*) and Emissions Database for Global Atmospheric Research (EDGAR) (*64*).

Experiments are also needed which explore modelled responses to forcings beyond that which has been observed historically. This includes both realistic multi-gas emissions experiments, as well as idealised experimental setups to explore fundamental properties of the model Earth system (e.g. $2\times CO_2/4\times CO_2$ concentration increase experiments, as well as 1%/yr CO_2 concentration increase experiments, and preindustrial control experiments).

The CMIP6 experiments, summarised in table 1.2, run realistic multi-gas mitigation scenarios to model climate change beyond the end of the historical period (i.e. after Dec. 2014 in CMIP6 experiments). Simple climate models (e.g. FaIRv2.0 (*29*)) and the simplified modelling framework used in this thesis also rely on such scenarios to provide realisations of global climate policy beyond the present day. The standard set of scenarios used in physical climate modelling for this purpose are named the Shared Socioeconomic Pathways (SSPs) (*65*). These multi-gas emissions or concentrations scenarios use five narratives which provide a backdrop for climate policy design (SSP1-SSP5), and additionally include mitigation ambition in the form of a target for end of century radiative forcing (1.9, 2.6, 3.4, 4.5, 6.0, or 8.5 W/m^2). Together these scenarios provide a range of futures for climate policy, spanning both varying levels of population growth, regional cooperation and trade, technological development, GDP growth etc., and varying levels of climate policy ambition. SSP scenarios feature heavily in research into the climate system response to anthropogenic emissions over the 21st century (*14*, *36*, *54*, *55*).

The SSP scenario's emissions timeseries span a wide range of climate policy, and can broadly be categorised as follows (where below 'X' refers to storylines of the future evolution of the global economy and society independent of climate mitigation policy): SSPX-19 – 1.5 °C-compatible, reaching net zero CO_2 emissions around 2050;

SSPX-26 – below-2.0 °C, reaching net zero CO_2 emissions around 2075; SSPX-34 – 2.0 °C-compatible; SSPX-45 – above-2.0 °C (current policies trajectory); SSPX-60 – above-3.0 °C; and SSPX-85 – high emissions scenario (~4.0 °C) (*8*). The SSPX-45 scenario is now commonly viewed as a current policies baseline scenario, with approximately stable CO_2 emissions through the 21st century (*66*). More information on the design and production of the SSP emissions and concentrations timeseries can be found in Meinshausen *et al.* (2020) (*67*).

1.4.1.3 Defining radiative forcing

In model studies there is a need for a variable which provides a common scale to compare contributions to AGW. Although emissions and concentration timeseries are typically used as inputs for climate models, they are poorly suited for this task. The various pollutants themselves have various efficacies and lifetimes which makes the warming response difficult to assess (*4*). Further, there are other non-emissions-based drivers, such as insolation variability and albedo changes, which also impact on surface temperature but do not release emissions.

An better variable for this comparison is the *Radiative Forcing* (RF) (*68*), which is defined as

$$\mathrm{F_{i,T}(t) = N_{i,T}(t) - N_{o,T}(t)} \tag{1.5}$$

where the subscript T refers to the use of an externally provided tropospheric temperature profile (plus surface conditions). $\mathrm{N_{i,T}(t)}$ is the net outgoing radiative flux (in Watts per square metre) evaluated at the tropopause using an offline radiative transfer calculation, for an experiment where a perturbation i has been applied and the stratospheric temperature allowed to adjust. $\mathrm{N_{o,T}(t)}$ is the net outgoing radiative flux for a second experiment, identical in setup but without the perturbation applied. The perturbation itself can be anything producing a radiative response in the model, such as changes to atmospheric composition, surface albedo, cloud radiative properties, or insolation. The difference between the two radiative fluxes approximates the radiative imbalance at the top of atmosphere (TOA) caused solely by the perturbation i.

If the calculation is repeated but allows the tropospheric temperature profile to adjust (still using prescribed SST and sea ice boundary conditions), the difference between the two TOA fluxes then defines the *Effective Radiative Forcing* (ERF) (*68*). This captures both the direct radiative perturbation and the rapid adjustments resulting from the direct radiative perturbation. Hence, ERF better reflects the immediate impact of a perturbation on the energy imbalance of the Earth system (*45*), providing a uniform scale for comparing relative contributions from a wide range of pollutants.

Recent studies have reassessed the line-by-line calculations for estimating the radiative perturbations of several GHGs (*69*), as well as the ERFs from aerosol-radiation and aerosol-cloud interactions (*54*, *70*, *71*). Using these, AR6 updated a set of simplified emissions-to-ERF relationships for the major pollutants (*72*), based on a harmonization between CMIP6 emissions-to-ERF relationships (*54*, *55*) and observational constraints (*73*). These are used by Forster *et al.* (2021) to estimate individual pollutant's contribution to anthropogenic ERF (*44*) from historical emissions estimates (*61*, *62*, *64*) and from the SSP emissions and concentration timeseries (*67*). A full description of the production methodology can be found in the Supplementary Material to Chapter 7 of IPCC's AR6 (*72*). CO_2 contributes 2.16 (1.92-2.41) W/m^2 in 2019 relative to 1750 — the majority of the anthropogenic ERF perturbation (2.72 [1.96-3.48] W/m^2); non-CO_2 GHG ERF contributes 1.68 (1.40 to 1.96) W/m^2; and aerosol ERF contributes -1.06 (-1.71 to -0.41) W/m^2. For reference, these present-day forcing estimates are presented in figure 7.6 of Forster *et al.* (2021) (*5*), and the full timeseries are shown in figure 3.2 in chapter 3.

Dessler and Forster (2018) presents the methodology used to combine these individual pollutant's best-estimate ERF timeseries into a large ensemble (*74*). They first sample distributions for each pollutant's ERF timeseries using a sample drawn from the CMIP6 models' present-day ERF distribution. These individual ERF component ensembles are combined to produce a large ensemble of anthropogenic ERFs using a linear combination of the individual components, assuming no correlation between individual ERF distributions. This is the approach used to produce the ERF ensemble used in Forster *et al.* (2021) to constrain TCR, ECS and attribute warming using

the FaIRv1.6 simple climate model. An ERF ensemble produced in this way is also used extensively in this thesis.

1.4.1.4 The linear forcing-feedback framework

The ERF timeseries defined above describes the energy imbalance of an emissions perturbation, but it does not directly reflect the temperature response to this perturbation. The temperature response can include additional feedbacks from the climate system in response to the perturbation. Examples of such feedbacks include changes to global cloud properties (i.e. cloud radiative feedbacks (*75*)), changes in atmospheric composition or temperature structure over time (e.g. the water vapour and lapse rate feedbacks (*76*)), and the influence of a heterogeneous or time-varying surface temperature distribution due to ocean heat uptake, or changing surface albedo (e.g. the ice-albedo feedback (*77*)).

Diagnosing the full transient surface temperature response in a GCM requires relaxing the boundary conditions on SSTs and sea ice used to derive the ERF, to allow the climate system to dynamically respond to the energy imbalance. The DECK historical simulations and DAMIP experiments described in table 1.2 allow this dynamic response, with the resulting GSAT anomalies used in Gillett *et al.* (2021) and Ribes *et al.* (2021) to attribute contributions to historical warming (*17*, *18*). In simple climate models the relationship between the forcing and surface temperature response is often captured empirically based on one-dimensional multi-layer energy balance frameworks described by Gregory, Winton, Held and Geoffroy in the early 2010s (*78*, *79*). Held's and Geoffroy's models allow for energy exchange between the surface and deep ocean layers, resulting in a transient response to an energy perturbation at the surface. This has been shown to capture the multi-decade temperature response in the more complex GCMs (*29*). The FaIRv2.0 model uses an impulse response structure to capture similar dynamics to these energy balance frameworks, using three boxes with relaxation timescales representing heat exchange between the surface and the upper/deep ocean (*29*, *42*) (see chapter 2).

By considering a layered energy balance framework in this way (*78*), an even simpler representation of the ERF-temperature relationship can be written as

$$\Delta F = \Delta N + \lambda \Delta T, \tag{1.6}$$

where ΔN refers to the TOA radiative flux perturbation in the transient warming scenario, ΔF to the ERF perturbation, and ΔT the surface temperature anomaly in response to the forcing scenario. λ is the net radiative feedback parameter, which linearises the radiative response to a unit surface temperature perturbation, and ΔN relates to the rate of heat uptake by the ocean and cryosphere (assuming a small heat capacity of the atmosphere). CMIP6 models suggest a positive net feedback parameter in response to 4xCO_2 experiments (1.0 $\pm$ 0.34 W/m^2/°C, one standard deviation; using the sign convention defined in equation 1.6) (*80*, *81*). Equation 1.6 can be additionally split into longwave (LW; referring to integrated broadband infrared radiation) and shortwave (SW; referring to integrated broadband visible radiation) components, with the feedback components then correspondingly split into λ_{LW} (~+2.2 W/m^2/°C) and λ_{SW} (~-1.2 W/m^2/°C) (*81*). This split helps portray the relative contributions of LW and SW feedbacks to the overall TOA energy imbalance (*82*). Feedbacks can be additionally split by process, e.g. water vapour, lapse rate, SW cloud, LW cloud (*81*).

The ultimate temperature response to an ERF perturbation is estimated from equation 1.6 by setting ΔN to zero. If the ERF used is the forcing resulting from doubling CO_2 concentrations, $F_{2\times}$, then the ultimate temperature response here defines the *Equilibrium Climate Sensitivity* parameter, or ECS:

$$\text{ECS} = \frac{F_{2\times}}{\lambda}. \tag{1.7}$$

Sherwood *et al.* (2020) collected a wide range of evidence, from satellite and in-situ observations, CMIP5 and CMIP6 models, and process-based constraints, to determine the best-estimate ECS is 3.0 °C (likely range between 2.5 and 4 °C). This represented a major step forward in constraining ECS, which had proved elusive despite 40 years of physical climate research (*83*). Further constraints on the ECS remain limited by co-varying uncertainties on other key aspects of the climate change problem, such as the contribution from anthropogenic aerosol emissions to historical warming trends, and the strength of cloud feedbacks as the Earth system warms (*80*). Targeting tighter constraints on the ECS is an ongoing challenge for the community.

Since the ECS describes a climate system's equilibrium warming in response to an ERF perturbation, the lack of a tight constraint on its value limits our understanding of the climate response to anthropogenic perturbations. However, as ECS reflects the equilibrium warming, it is also a relatively poor predictor of the near-term warming trend (*84*), which is the more policy-relevant quantity. A better descriptor of this short-term, transient, warming is given by the *Transient Climate Response* (TCR) parameter (*5*). The TCR is defined as the warming response in year 70 to an experiment where CO_2 concentrations increase by 1%/year (in year 70 the CO_2 concentrations have doubled). Hence, the TCR represents the transient warming response while ERF is changing, while the ECS describes the equilibrium warming that results once that CO_2 perturbation equilibrates.

AR6 determines the TCR is 1.8 (1.4-2.2) °C and the ECS is 3.0 (2.5-4.0) °C. CMIP6 models' diagnosed TCR and ECS parameters (*80*, *81*) broadly support this assessment, although several do exceed these ranges, particularly for the ECS where some models display ECS > 5.0 °C (*80*).

Explaining the behaviour of model-derived warming over the historical period is important to provide context for analysing future emissions scenarios (*85*, *86*). The link between the historical warming trends in models and the TCR and ECS parameters has been exploited to constrain these key physical response characteristics. Otto *et al.* (2013) demonstrated how observed decadal warming trends and forcing estimates could be combined to assess the TCR and ECS and evaluate model performance (*87*). Tokarska *et al.* (2020) similarly used observations of the historical warming trend to constrain future warming in CMIP6 models (*86*), producing emergent constraints on the TCR and ECS parameters. The size of late-20th century warming trends in CMIP6 models has also received research attention (*88*), with groups noting that high warming rates in some models are caused by both increased aerosol forcing trends (*89*) and increased cloud-radiative feedbacks (causing higher TCR and ECS) (*35*, *90*).

Simple climate models provide a key tool to assess emergent constraints on the TCR and ECS parameters. Leach *et al.* (2021) and Smith *et al.* (2021) produce large ensembles of warming responses sampling both anthropogenic forcing inputs

and physical climate response parameters (*29*, *73*). They then apply observational constraints (observed ocean heat uptake and GMST) to estimate the anthropogenic ERF and physical climate response parameter distributions in parallel. Similar approaches have also been used to sample the joint aerosol forcing and ECS distributions (*91*), and to constrain the CO_2 warming response (*92*). In this thesis I use TCR and ECS distributions to define the range of thermal responses in the FaIRv2.0 SCM.

1.4.1.5 The warming contribution from CO_2

The CO_2 warming response depends on the joint behaviour of the carbon cycle and thermal cycle. In a simple model, the carbon cycle can be broadly split into five pools, representing: the atmosphere, upper ocean, lower ocean, biosphere and geosphere (*42*). These pools are associated with lifetimes reflecting the average residence time of carbon in that pool, with connections between pools weighted to reflect the relative carbon flux between them. Joos *et al.* (2013) demonstrated that an impulse response framework with this structure can be tuned to capture the globally-averaged behaviour of fully-coupled GCMs, and hence capture the broad dynamics of the carbon cycle following an anthropogenic CO_2 perturbation (*93*, *94*).

Following a pulse emission of CO_2 a fraction of it remains in the atmosphere over multi-millennial intervals, despite the system acting to equilibrate the non-atmospheric carbon pools over time (*93*). This fraction is labelled the *airborne fraction*. For the contemporary carbon cycle the airborne fraction is around 45% over a 100 year interval (*93*). It is expected that the 100-year airborne fraction will increase as the carbon cycle perturbation increases, since the non-atmospheric pools saturate and become weaker sinks over time. Evidence is mixed on whether the airborne fraction exhibits a trend over the recent historical period, with claims of a negative trend (*95*) being contested as statistically insignificant by others (*96*). The CO_2 which remains in the atmosphere causes a radiative perturbation which can be measured and used to estimate the CO_2 ERF (*97*). For CO_2, the relationship between the CO_2 concentration change and resulting ERF is approximately logarithmic (*69*), meaning successive CO_2 concentration doublings

result in a linear ERF increase in models. The ERF perturbation induces a surface temperature response, which can be estimated with the approaches outlined above.

The estimation of CO_2-induced warming has been revolutionised in the past decade, following the realisation that models display a near-linear relationship between cumulative CO_2 emissions and surface temperature anomaly (*98*). In the late 2000s several papers noted this (*99*–*101*) and labelled the constant of proportionality between them the *Transient Climate Response to cumulative CO_2 Emissions*, or TCRE. The TCRE relates to the aforementioned TCR parameter, describing the transient warming in response to an ERF change, but additionally captures the transient carbon cycle response to emissions (i.e. the airborne fraction). This combination produces an approximate linearity overall (*102*) with offsetting non-linearities in the carbon and thermal cycle responses (*103*).

Recent research estimates the TCRE is +0.45 (0.27-0.63) °C/TtCO_2 (*3*), suggesting CO_2 emissions in this decade (approximately 40 GtCO_2/yr in Friedlingstein *et al.* (2021) (*61*)) has caused warming of +0.18 (0.11-0.25) °C. This range is supported by both modelling studies (*92*, *104*–*106*) and by observations comparing human-induced warming and historical CO_2 emissions (*92*, *105*, *107*), although observational constraints often produce a log-normal TCRE distribution, while model-based constraints are typically more normally-distributed (*47*). Macdougall (2016) presents a helpful review of the foundations of the TCRE concept (*102*).

The TCRE relationship has been confirmed in models to well beyond the level of Paris-compatible mitigation scenarios (up to 2000 GtC, or 7340 GtCO_2, cumulative emissions (*47*)). It has proven extremely useful for simplifying climate policy, since for a given warming threshold the CO_2 contribution is limited solely by a cumulative emissions budget prescribed by the TCRE (*47*). Less research has probed the non-linearities which exist alongside the linear TCRE behaviour, with examples including *Earth System Feedbacks*, the contributions from non-CO_2 pollutants, and the *Zero Emissions Commitment*.

Earth System Feedbacks, which act as an additional source of CO_2 emissions in response the initial perturbation (e.g. permafrost thawing (*108*)), are often neglected in estimates of the TCRE over the historical period (*47*). They are estimated to contribute 0-100 GtCO_2 additional CO_2 emissions between 2020 and 2100 in 1.5 °C

scenarios in SR1.5 (*14*). More recent studies of permafrost CO_2 feedbacks (*109*) support this, with the IPCC's Special Report on the Oceans and Cryosphere in a Changing Climate (*110*) suggesting permafrost thawing could contribute 70-210 $GtCO_2$ in a 2 °C-compatible scenario (*111*). AR6 has updated evidence on several other Earth Systems feedbacks in figure 5.29 (*111*).

The *Zero Emissions Commitment* (ZEC) was originally defined as the difference in the temperature anomaly at the time of reaching net zero and over multi-millennial timescales (i.e. the equilibrium warming) (*112*). This definition is cumbersome in practise. In contemporary literature, ZEC more commonly refers to the multi-decade or multi-century warming response following the cessation of CO_2 emissions (*57*), with this period capturing the policy-relevant behaviour. ZEC arises as a result of differences in the rate of heat and carbon uptake by the thermal and carbon cycles following net zero. To study ESM and EMIC responses following net zero, Jones *et al.* (2019) proposed the ZEC Model Inter-comparison Project (ZECMIP) (*57*). ZECMIP ran emissions-driven experiments producing a 1%/year increase in atmospheric CO_2 concentrations until a predefined cumulative emissions budget was reached (e.g. 1000 GtC). Thereafter, the models are left to re-equilibrate over a 100-year period. Based on these experiments, Macdougall *et al.* (2020) determines ZEC is close to zero over 20- 50- and 100-year timescales, with uncertainty spanning approximately ± 0.2 °C in models over a 100-year interval (*113*), and explore how individual model ZEC's arise from the thermal and carbon cycle responses following a CO_2 emissions perturbation.

Simple models provide a well-established mathematical framework which can be used to probe the warming response to CO_2 emissions. FaIRv2.0 reproduces the range of TCREs demonstrated in GCMs (*29*), and can be tuned to emulate individual model responses or the time-history of AGW (*94*). Chapters 5 and 6 make use of FaIR to produce large ensembles of historical warming to constrain the TCRE, and to emulate CMIP6 GCM responses to various emissions scenarios.

1.4.1.6 TCRE and the remaining carbon budget

The TCRE relationship helps set the requirements of policymaking (*3*), since, for a given quantity of remaining warming one can define a finite quantity of CO_2 emissions compatible with that warming threshold (*41*). Rogelj *et al.* (2019) outlines the standard framework used to derive this remaining carbon budget (*47*), which is followed in SR1.5 (*14*) and AR6 (*3*).

A schematic of Rogelj's approach to derive the remaining carbon budget is presented in figure 1.2. The methodology converts a remaining warming quantity into a remaining carbon budget using an estimate of the TCRE, along with assumptions of the quantity of warming required for remaining non-CO_2 emissions until the time of net zero, the ZEC (the residual warming over multi-decade intervals following net zero (*113*)), and emergent Earth System Feedbacks. In this thesis, I discuss the physics relating to two key assumptions in this framework:

The first is how non-CO_2 pollutants contribution to warming are compared to CO_2, where currently the non-CO_2 contribution is removed as a quantity of warming before the TCRE is used to estimate the budget. This is problematic unless care is taken to correlate the warming responses from CO_2 and non-CO_2 pollutants. This discussion is the focus of chapter 5.

The second assumption is that the ZEC is small, centred on zero, and uncorrelated with TCRE, meaning it can be ignored in remaining budget calculations. This is refuted by recent ZECMIP experiments, which show a diverse GCM response to net zero (*113*), and by Allen *et al.* (2022) who demonstrate a connection between the multi-decadal ZEC and TCRE in the FaIR simple climate model (*103*). To address this assumption, I introduce a novel mathematical framework relating the ZEC and the TCRE, and uses it to show the conditions under which CO_2-induced warming stabilises. This is the focus of chapter 6.

1.4.1.7 Non-CO_2 greenhouse gases

Non-CO_2 GHGs contribute a sizeable positive ERF at present day (~1.68 W/m^2 relative to 1750 (*5*)), the bulk of which comes from N_2O, CH_4, and their associated ozone

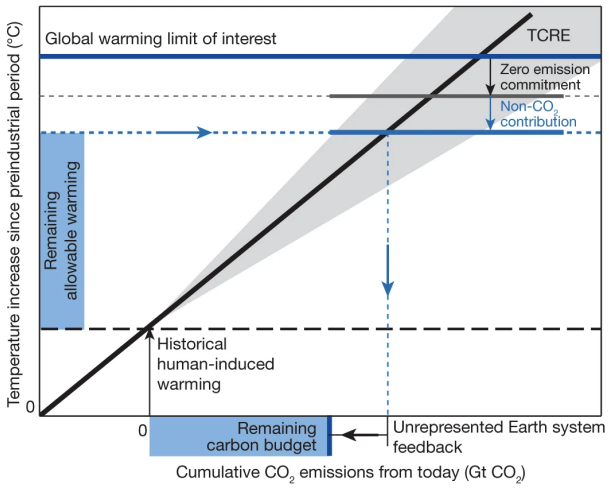

Figure 1.2: Schematic visualising the methodology to estimate the remaining carbon budget using the historical human-induced warming, the zero-emissions commitment (ZEC), the contribution of future non-CO_2 warming, the TCRE, and unrepresented Earth system feedbacks. The grey shading illustrates uncertainty in the TCRE parameter. Figure reproduced from Rogelj *et al.* (2019) (*47*).

perturbation (*69*). While CO_2 is a cumulative pollutant with a remarkably simple warming response, the non-CO_2 GHGs are a group of many pollutants with various atmospheric residence times and efficacies. This makes their bulk climate assessment more challenging. For example, CH_4 is a short-lived climate pollutant (SLCP) with a short atmospheric residence time (~12 years (*114*)) but large radiative efficiency compared to CO_2 (*115*), while N_2O is a long-lived climate pollutant (LLCP; lifetime ~120 years) and a similar radiative efficiency to CH_4 (*68*). A brief summary of the major GHGs is given below.

Methane

CH_4 is the second-largest contributor to GHG ERF following CO_2, adding 1.19 (0.81 to 1.58) W/m^2 between 2019 and 1750 (*116*), when including methane's abundance lifetime feedback, tropospheric ozone production and stratospheric water vapour feedback. Ozone chemistry in the troposphere and stratosphere is complex and includes the production and destruction of a large number of volatile organic compounds (*117*). Most relevant for CH_4: stratospheric ozone is the dominant source of hydroxyl ions which oxidise CH_4 and cause the majority of CH_4 removal from the atmosphere; while tropospheric ozone is in part formed via alternative CH_4 reaction pathways (*118*). The prevalence of

hydroxyl ions determines the lifetime of CH_4, with ongoing anthropogenic perturbations contributing to extending the CH_4 lifetime. When including these effects CH_4 ERF estimates are 1.6 times higher than they would be based on CH_4 abundance alone (*117*) (see figure 6.12 in Szopa *et al.* (2021)).

The fact that CH_4's lifetime is only 12 years means its atmospheric abundance is maintained by the continual emission of CH_4 replacing that which was broken down. CH_4 emissions are split between natural (40%) and anthropogenic (60%) sources, with human emissions arising predominantly in the oil and gas sector, landfills, and livestock, and natural emissions predominantly from tropical wetlands and tundra thawing (*114*). The 40% natural emissions provide a source large enough to balance natural CH_4 sinks in the preindustrial climate state, with additional anthropogenic emissions causing CH_4 concentrations to rise over the historical period to find a new balance with enhanced sinks (*119*). Since 2000, CH_4 concentrations have exhibited a variable growth rate, slowing in the late-2000s before accelerating in the 2010s (*114*). This behaviour has been attributed to several causes, with the most recent evidence suggesting 85% of this acceleration is due to natural wetland emissions (*120*) based on the analysis of C^{12}/C^{13} isotope ratios in ice cores. The fact that CH_4 concentration trends track GMST trends further suggests warming-related feedbacks and natural variability may have contributed to these trends (*121*).

Nitrous Oxide

N_2O is the third-largest contributor to GHG ERF after CH_4, adding 0.24 (0.13 to 0.34) W/m^2 based on emissions-based modelling estimates (*116*). N_2O acts as an ozone sink, but the effect is small and offset by its influence increasing CH_4 lifetime (since it competes with the CH_4 for hydroxyl to be broken down in the atmosphere). Tian *et al.* (2020) completes a comprehensive review of sources and sinks since 1980, determining total N_2O emissions were 17 (12-23) TgN/yr over the decade 2007-2016 (*122*), with anthropogenic emissions contributing approximately 40% of this total, predominately from the use of fertilizers on cropland.

CFCs, HCFCs and HFCs

Finally, various chloro-fluro-carbon (CFC), hydro-chloro-fluro-carbon (HCFC) and hydro-fluro-carbon (HFC) compounds contribute a small amount to GHG ERF at present day. These pollutants have very wide-ranging lifetimes and efficacies, but together produce a perturbation of approximately 0.2 W/m^2 (*116*), having accounted for their direct radiative perturbation (+0.4 W/m^2) and ozone/methane lifetime interactions (-0.2 W/m^2).

Metrics for comparing GHGs

Comparing GHGs based on their ERF perturbation, as I did above, is the most physically-coherent way to compare pollutants contributions to historical warming. However, it is impractical for policymakers, who do not run physical models, to diagnose ERFs when designing emissions scenarios. Instead, policy routinely uses *GHG metrics* to convert non-CO_2 pollutants emissions timeseries into a timeseries of CO_2 emissions, thus allowing them to compare contributions from different pollutants. Examples of these metrics include the Global Warming Potential (GWP) (*68*), Global Temperature Potential (GTP) (*123*), CO_2-forcing-equivalence (CO_2-fe) (*94*, *124*), and GWP* (*125*, *126*).

Much has been written on the appropriateness of these metrics for the conversion between GHGs (*4*, *115*, *127*, *128*). One important concern surrounds the use of the GWP metric for comparing CH_4 and CO_2 emissions. The GWP metric is a numerical multiplier applied to an emissions timeseries to convert it to a CO_2 timeseries, calculated as the ratio of the absolute global warming potential of the two pollutants. Here, the absolute global warming potential refers to the integral (with time horizon H) of the radiative forcing in response to a unit-sized pulse emission of the pollutant. Hence, the GWP is the ratio of the cumulative energy perturbation caused by a unit-sized emission of each pollutant (*68*). For example, the $GWP_{CH4,\ 100yrs}$ is 29.8 (*5*), meaning a one-tonne emission of CH_4 is equivalent to a 29.8-tonne emission of CO_2.

The issue with the GWP metric is its failure to account for the different lifetimes of the two pollutants. While CH_4 is a much more potent GHG in the short-term (over 100 times more so immediately following emission) (*129*), over a multi-decade interval CO_2 warming dominates because the CH_4 ERF perturbation decays towards zero (the

warming perturbation lags the ERF perturbation, but is still many times weaker than the CO_2 perturbation after the first several decades). Hence, each pollutant's global energy budget perturbation behaves in a different way: CO_2 scaling with the cumulative stock of emissions over time, and CH_4 with its recent emissions rate (multiplied by its lifetime). GWP fails to account for this correctly because it integrates over the radiative forcing perturbation, losing the temporal information. Aggregate CO_2-equivalent emissions calculated using GWP are a poor gauge of the peak warming (*126*), and reaching net-zero annual CO_2-equivalent emissions is a poor gauge of achieving temperature stabilisation.

As a solution, in chapter 5 I use the CO_2-forcing-equivalent (CO_2-fe) metric, demonstrating how this can be used to compare anthropogenic pollutants according to their time-varying energy perturbation in the climate system. With the CO_2-fe metric, a pollutant's emissions pathway is converted into a timeseries of CO_2 emissions, where those CO_2 emissions exactly reproduce the ERF, and hence the warming response, to the pollutant's original emissions pathway over all timescales. This makes the CO_2-fe metric a more physically-coherent metric for comparing complex multi-gas emissions scenarios, since the metric unambiguously simplifies the scenario down to a single pollutant without losing the temporal information key to differentiating the behaviour of short- and long-lived pollutants. Further, CO_2 emissions timeseries produced with the CO_2-fe metric inherit all the properties of CO_2, meaning non-CO_2 CO_2-fe emissions timeseries reproduce the TCRE relationship. Other metrics have been designed to improve on GWP which do account for the lifetime of pollutants (*4*, *130*), based on emulating the behaviour of the CO_2-fe metric, but their discussion is beyond the scope of this thesis.

1.4.1.8 Aerosols

Aerosols are a range of small particulate pollution in the atmosphere, with common examples include sulphates (e.g. SO_4^{2-}), organic carbon (OC), black carbon (BC), nitrates (NO_x), mineral dust, and sea salt (*116*). This wide range of compounds include particulates from both anthropogenic and natural sources; all the aforementioned species are produced in both the unperturbed and contemporary climate system. Natural aerosols account for the majority observed in the atmosphere today, with combined satellite and

GCM studies suggesting 70-85% of the atmospheric aerosol burden has natural origins (based on aerosol optical depth retrievals) (*71*). The remainder has anthropogenic origins, largely through fossil fuel combustion producing SO_2 (a precursor to sulphate aerosols), and biomass burning producing OC and BC (*63*). The exact aerosol burden of the preindustrial climate system, and hence the size of the anthropogenic perturbation, remain key uncertainties for the estimate of the overall aerosol radiative impact (*5*).

Aerosols are another example of SLCPs, but compared to the major GHGs have extremely short lifetimes (around one week) before they are removed from the atmosphere via dry deposition or precipitation (*68*). This means that aerosol density in an atmospheric column is concentrated around large emissions sources, and the distribution of aerosols is highly heterogeneous. For natural aerosols, prominent emission sources include the major deserts producing dust (most notably the Sahara, whose dust is transported across the Atlantic), the global oceans producing sea salt, and large forests producing OC and BC aerosols (e.g. Amazon rainforest). Anthropogenic aerosol emissions are concentrated around highly industrialised environments (e.g. Po valley, Italy) and locations of high coal use. In the mid- and late-20th century this was largely Western Europe and the north eastern USA, and today is China, India and the wider south east Asian region (*63*).

Averaging globally and summing over the contributions of individual aerosol species, Forster *et al.* (2021) estimated the anthropogenic aerosol perturbation today is -1.06 (-1.71 to -0.41) W/m^2 (*5*). Forster assessed multiple lines of evidence, including: satellite, flight campaign and in-situ observations; CMIP6 model-derived ERF estimates; and process-based modelling estimates.

ARI and ACI contributions

This total perturbation is split between the direct radiative effects (aerosol radiation interactions, or ARI), contributing -0.22 (-0.47 to 0.04) W/m^2, and aerosol cloud interactions (ACI), contributing -0.84 (-1.45 to -0.25) W/m^2. Stephens *et al.* (2022) argues observations of SW radiative balance at the TOA suggest the ARI/ACI split may be more equal than this (*131*), but it is generally accepted ACI contributes the

majority of aerosol forcing overall. The mechanisms of this forcing were discussed in a comprehensive review of aerosol forcing by Bellouin *et al.* (2020) (*71*).

The ARI ERF varies by aerosol species. For example, sulphate particulates scatter incoming solar radiation, reducing net SW radiation at the TOA and producing a negative ARI ERF, while BC absorbs it, heating the atmospheric layer holding the BC but shading the surface beneath. Tang *et al.* (2021) uses experiments from the Precipitation Driver and Response Model Intercomparison Project (PDRMIP) to compare the surface radiative response with identical TOA radiative perturbations from five aerosol species, as well as other drivers of surface warming (*132*). They find that the surface temperature response to scattering aerosols is largely governed by radiative heating or cooling terms, and hence the TOA radiative perturbation acts as a reasonable measure of the warming response. Conversely, BC's net surface radiative response is the combination of a reduced downward SW radiation flux (due to BC's SW absorption in the atmospheric column), and increased LW downward radiation (due to the heating perturbation caused by the BC absorption in the atmospheric column). Tang *et al.* (2021) determines BC causes a reduction in the net downward surface radiation overall, but still results in a surface temperature increase, arguing this results from increased air stability reducing the efficiency with which surface energy fluxes can be dissipated (*132*).

The ACI ERF occurs because aerosols act as the 'seeds', or cloud condensation nuclei (CCN), for cloud water droplets and ice crystals to nucleate (*133*). In pristine environments CCN are composed of natural aerosols. In heavily aerosol polluted environments the quantity of CCN increases dramatically, leading to a larger number of smaller cloud liquid water droplets overall, assuming the amount of water available to condense to form droplets remains fixed. This behaviour, named the Twomey effect (*133*), brightens clouds and induces a net negative radiative perturbation at the TOA. The Twomey effect is the largest contribution to ACI ERF and has received extensive study (*134*). Bellouin *et al.* (2020) estimates warm cloud ACI RF from the Twomey effect alone is between -1.10 and -0.33 W/m^2 (*71*), while Forster *et al.* (2021) suggests $-0.7 \pm 0.5\,W/m^2$ (and a medium confidence interval) (*5*). Narrowing this range remains a significant challenge: although considering energy balance constrains the upper bound

of this range somewhat, Gryspeerdt *et al.* (2022, in review) show that uncertainties in both the size of the anthropogenic aerosol perturbation and the radiative properties of pristine clouds themselves remain key barriers limiting the constraint on the size of the Twomey effect at present day (*135*).

Additional ACI contributions arise from aerosols impact on the cloud liquid water path (the integrated water content in a cloud column, LWP), the location and prevalence of cloud fields (the cloud fraction) (*5*). Gryspeerdt *et al.* (2016, 2019) present helpful summaries of both these contributions (LWP (*136*) and cloud fraction (*137*), respectively).

The former relationship is studied via the cloud droplet number concentration (CDNC) and LWP co-variability. This CDNC-LWP sensitivity is thought to be negative in most regions, causing a positive feedback which offsets some of the negative RF from the Twomey effect (*136*). However, a number of studies also note the CNDC-LWP relationship is non-linear over the range of observed aerosol optical depths (AODs): at low CDNC in precipitating clouds a reduced cloud droplet effective radius suppresses precipitation, increasing cloud depth and LWP (*138*, *139*); while higher CDNC can cause a LWP reduction in clouds where precipitation does not reach the surface (*140*, *141*). LWP variability is also strongly dependent on local meteorology, making observational constraints challenging to de-bias (*136*).

The possible causes of a positive correlation between aerosol loading and cloud fraction were discussed in Quaas *et al.* (2010). These include: meteorological co-variability (large-scale convergence will correlate high aerosol burden with high cloud cover), satellite retrieval errors (aerosol can be misinterpreted as cloud and vice versa, particularly where aerosol swelling increases the perceived AOD, or for broken cloud structures (*142*)), and the cloud-lifetime aerosol effect (aerosol increase the CDNC, suppressing precipitation and increasing cloud lifetime) (*143*). Even having accounted for major biases like the underestimate of CDNC for broken clouds (*142*), the CDNC-cloud fraction relationship remains positive (*144*), meaning anthropogenic aerosols are expected to increase global cloudiness on average.

Bellouin *et al.* (2020) combines evidence from a number of regional estimates of LWP and cloud fraction sensitivity to suggest globally-averaged LWP adjustments span

0 to +0.56 W/m^2 in the contemporary climate system. AR6 estimated the CDNC-LWP adjustment at 0.2 $\pm$ 0.2 W/m^2 based on the Bellouin result and Toll *et al.* (2019) (*145*), but acknowledge that limited studies are available to make this assessment. Similarly, Bellouin assesses cloud fraction adjustments span -1.14 to 0 W/m^2, with AR6 suggesting -0.5 $\pm$ 0.4 W/m^2. Combining these with the Twomey effect RF, ACI ERF is estimated at between -2.2 and -0.6 W/m^2 (likely range) by Bellouin, and -1.1 $\pm$ 0.7 W/m^2 in AR6. Both assessments are made for the interval 2010-2019, spanning the modern satellite era.

As with ARI, the ACI also depends strongly on the aerosol species. SO_4^{2-} aerosols reduce the cloud droplet effective radius and hence brightens clouds (lengthening the cloud lifetime), and have been linked with precipitation suppression (*146*). BC aerosol-cloud interactions are complex, with literature suggesting BC encourages SW absorption and hence droplet evaporation (the semi-direct effect), but also linking BC with larger cloud droplet radius for low liquid water paths over the Indian Ocean (*147*). BC pollution has also been linked to precipitation enhancement over the Indian sub-continent by acting as a heat pump during summer monsoon season (*148*). On shorter timescales large aerosol pollution events can also act to suppress intra-seasonal monsoon rainfall by enhancing atmospheric stability and increased moisture divergence (*149*). For the majority of the northern hemisphere the anthropogenic aerosol perturbation is dominated by the radiative heating/cooling caused by SO_2 emissions trends. A better understanding of the influence of BC and OC pollution on cloud optical properties is important for characterising many southern hemisphere aerosol-cloud-radiation interactions, and is the subject of ongoing research (*150*).

Model-derived aerosol forcing and energy balance constraints

The Radiative Forcing MIP (RFMIP) (*54*) and Aerosol and Chemistry MIP (AerChemMIP) (*55*) were proposed to diagnose ERF contributions over the historical period and over a range of future emissions scenarios (see relevant descriptions in table 1.2). These coordinated experiments allow the present-day ERF level to be diagnosed for the full range of pollutants across a wide range of CMIP6 models, and the spatio-temporally varying ERF patterns for aerosols, GHGs, and natural forcings to be diagnosed for a

subset of models. Complementing this, the Detection and Attribution MIP (DAMIP) (*56*) project used near-identical experiments, but with transient SST and sea ice included, to estimate the transient temperature responses to individual forcing agents for use in attribution studies.

Smith *et al.* (2020, 2021) used these experiments to diagnose the aerosol ERF for 17 CMIP6 models, determining the aerosol forcing in 2014 spanned -0.63 to -1.37 W/m^2 relative to 1850 (*89*) — both a narrowing of the range and a positive shift for the mean forcing compared to CMIP5. Smith *et al.* (2020) also noted that the aerosol forcing appeared uncorrelated with climate sensitivity in the models surveyed, suggesting that the increasing spread in ECS observed in CMIP6-iteration models (*80*), particularly related to high-sensitivity models (*49*, *50*, *90*), is not a consequence of a stronger negative present-day aerosol forcing. Zelinka *et al.* (2020) determines the larger ECS suggested by some models are instead caused by more positive cloud feedbacks (*80*). The extent to which future revisions to these feedbacks alter the aerosol forcing-feedback relationship remains unclear. Together, these studies form the basis for Forster *et al.* (2021)'s assessment that model-derived forcing is -1.1 $\pm$ 0.8 W/m^2 in 2014 relative to 1850. This, combined with observational evidence, produces their overall aerosol ERF assessment of -1.3 (-2.0 to -0.6) W/m^2 in 2014 relative to 1750, with the uncertainty range widened to account for non-negligible processes not currently included in CMIP6-iteration GCMs (predominantly ice cloud processes (*5*)).

A complementary approach to constrain aerosol ERF uses energy balance constraints on top of the aforementioned model-based and satellite-based assessments. Such approaches rely on a downstream observation, such as the GMST anomaly or TOA radiative flux anomaly, to provide a measure of quality of fit for the prior aerosol ERF distribution. Smith *et al.* (2021) uses a constraint on GMST and ocean heat uptake to provide a joint distribution of present-day aerosol ERF and the TCR parameter, arguing aerosol ERF is more-likely -1.1 (-1.8 to -0.5) W/m^2 over the decade 2005-2014, revised down from the AR6 best-estimate above. Bellouin *et al.* (2020) also uses energy balance constraints from GMST to reduce their upper bound on aerosol ERF, which is produced from process-based and satellite-based estimates. Other examples in the

literature include: Sherwood *et al.* (2020)'s ECS review, which used observational and energy balance constraints to tighten the overall ECS distribution (*151*); Stevens (2015)'s use of hemispheric energy balance constraints to limit the lower bound on aerosol ERF (*152*); and Watson-Parris and Smith (2022)'s discussion of the joint distribution between ECS and aerosol forcing (*91*).

In this thesis observations are used to provide constraints on model-derived outputs several times, including in chapters 3 and 4 for the aerosol forcing trend and warming trend estimates, and in chapter 5 to produce an observationally-constrained estimate of the TCRE parameter.

The aerosol trend

The ERF trend is a key input for the recent warming trend assessment, as was seen in figure 1.1 where the AR6 ERF revisions dramatically altered the stylised mitigation scenario. Despite being the key control on the rate of anthropogenic warming, the ERF trend has received relatively little research attention to date. This is likely a result of the ongoing challenges in assessing the ERF level using models and observations, and particularly in finding agreement between model-derived and observationally-constrained estimates of aerosol forcing (*5*, *68*). Since AR5, a sustained research effort has aimed to better reconcile the model- and observationally-derived estimates, resulting in better agreement on the aerosol (and hence total anthropogenic) ERF in the AR6 report.

Confidence in the aerosol assessment is vital for assessing the anthropogenic ERF trend: despite the GHG ERF trend being the dominant contributor to the multi-decadal ERF trend, aerosols are the key contributor to its uncertainty at present day. GHG trends are more tightly constrained by observations (e.g. CO_2 and CH_4 atmospheric concentration change), whereas substantial uncertainty still remains in recent aerosol emissions trends (*63*), the anthropogenic aerosol burden (*153*, *154*), and the global radiative response to aerosols (*71*).

The vast majority of aerosol forcing assessments completed in the literature and discussed above are based on analysis over the 2010-2019 decade, centred on 2014. This is done because the CMIP6 historical period ends in Dec. 2014, and since much of the

satellite-based observational evidence relies on a multi-decadal observational record to determine a 'present-day forcing' estimate. These constraints produce the -1.3 (-2.0 to -0.6) W/m^2 overall AR6 assessment quoted on the previous page. Forster *et al.* (2021) notes that "there is limited evidence available for the assessment of how aerosol ERF has changed from 2014 to 2019" (*5*). Forster does produce an aerosol ERF estimate updated until 2019, based on trends in global mean AOD and emissions of aerosols and aerosol precursors (*63*). They assess that the aerosol ERF has decreased in magnitude by around 0.2 W/m^2 since 2014, and thus the headline aerosol forcing assessment for 2019 is -1.06 (-1.71 to -0.41) W/m^2, relative to 1750 (medium confidence).

Although more detailed studies on the recent aerosol forcing trend are lacking, researchers have identified processes by which rapid aerosol emissions trends impact on the climate system. Wilcox has produced seminal work studying the regional response to aerosol emissions trends over history. Using the HadGEM3.1 GCM driven with and without aerosol emissions from China, Wilcox identifies mechanisms by which these regional aerosol emissions impact on the wider northern hemisphere and global temperature anomaly (*155*). This is explored in work by Samset *et al.* (2019), who discuss recent aerosol emissions trends in Asia and the emergence of local aerosol-induced warming response patterns (*156*). The local response to decadal emissions trends in Asia is also discussed by Dong *et al.* (2019), who suggests a role for aerosol emissions trends since the late-20^{th} century in explaining the observed southward shift in the Intertropical Convergence Zone and a weakening of the East Asian Monsoon (*157*).

The short lifetime of aerosols means they also play a prominent role in the outcome of the next decade's climate policy. Matthews and Zickfeld (2012), and later Smith *et al.* (2019), have modelled the warming commitment if emissions of all pollutants cease immediately (*158*, *159*). Since aerosols have a much shorter lifetime than the prominent GHGs, zeroing all emissions from the present day results in a temporary warming rate spike, followed by a relaxation towards the equilibrium warming level over a multi-decade interval. Samset considers impact of removing anthropogenic aerosol emissions alongside achieving other high ambition climate policy (*160*), further demonstrating the importance of the historical aerosol-masked warming. Although not

realistic, this extreme experiment highlights the importance of co-mitigation of aerosol and short-lived GHG emissions over a multi-decade interval, if the aim is to minimise the overall warming impact of the non-CO_2 mitigation.

Although less extreme, more realistic aerosol emissions reduction pathways do still suggest a sizeable quantity of aerosol-masked warming may be revealed in the coming decade. Persad, Samset and Wilcox highlight this challenge for policy (*161*), noting the importance of greater understanding of the regional impacts of reducing aerosol emissions in the UNFCCC's COP process. To better quantify this effect, Wilcox *et al.* (2022, in review) have proposed a Regional Aerosol MIP to better understand the regional impact of varying aerosol emissions (*162*), focusing on SO_2 mitigation in South East Asia and BC and OC mitigation in Africa and South America. This will contribute significantly to our knowledge of the climate response to varying regional aerosol emissions, although the challenge of constraining the aerosol contribution to AGW today remains.

Finally, and uniquely for this decade, it is likely we are now at a turning point in the aerosol era. Bauer *et al.* (2022) discusses this possibility using the GISS-E2.1-G CMIP6-iteration model to demonstrate that aerosol forcing and induced cooling reaches a maximum before declining in the 2020s, and that this is a robust feature across scenarios regardless of mitigation ambition (*163*). Quass *et al.* (2022) presents an equivalent analysis of observations over the past two decades, considering the 20-year trend in aerosol-relevant satellite observations since 2000 (*164*). The trends in AOD, TOA fluxes and cloud properties reveal that aerosol forcing is stabilizing, if not declining, globally over the satellite era. This realisation is the starting point for a detailed discussion of the aerosol contribution to present-day warming trends in chapters 3 and 4.

1.4.2 Observations of the climate system

Alongside model-based studies of individual pollutants' ERF contributions, direct observational evidence of the anthropogenic global warming trend is available. In-situ GMST timeseries produced through the collection and harmonising of local surface temperature records over the industrialised period (1850-present) are the most accurate measure of global surface temperatures (*8*). Modern GMST datasets include statistical

infilling approaches to handle missing data in the spatiotemporal record (*43*). Examples of GMST datasets used in this thesis are: HadCRUT5 (*43*), GISTEMP (*165*), NOAA (*166*), and Berkeley Earth (*167*) (see table 1.3). The methodologies commonly used to attribute AGW using the GMST anomaly has been briefly introduced above, while in-depth studies attributing recent GMST trends to anthropogenic pollutants are discussed in chapters 3 and 4.

Over the last two decades continuous satellite observations have provided a near-global measurement of several important properties of the climate state in real-time. This has proved of great value to the physical climate research community, providing simultaneous observation of several important atmospheric properties co-observed on platforms with well-calibrated equipment and known drift characteristics (*168*). Examples of observations important for this thesis include AOD, TOA radiative fluxes (shortwave, longwave and net broadband fluxes), cloud optical properties (e.g. cloud fraction, cloud optical depth, cloud top height, pressure and temperature etc.) and global surface temperature. Although earlier satellites have observed subsets of these quantities since the late-20th century (*169*, *170*), these missions were often short and blighted by poorly characterised satellite drift and measurement equipment. This limits the utility of these records for establishing trends in energy balance and surface temperature over multi-decade periods. In contrast, these more recent satellites have now continuously observed for over two decades, providing insights into long-term observed trends in climate system properties for the first time (*164*). A summary of the satellite observations used in this thesis can also be found in table 1.3.

NASA's Clouds and Earth's Radiative Energy System (CERES) equipment (*168*) has been analysed repeatedly to produce energy balance constraints for investigating forcings and feedbacks on the Earth system. Based on equation 1.6 above, identifying the feedback parameter relies on isolating the trend in a scatterplot of TOA flux and GMST observations, having first adjusted TOA fluxes to account for ERF trends over the interval (*171*). This approach is typically referred to as a Gregory regression, and is the standard means to derive the ECS parameter (*80*), defined as the intersection of the

linear regression with the temperature-axis. A summary of research utilising TOA flux observations in this way is provided in AR6 (*5*) and in Sherwood's ECS review (*151*).

In the 2000s the CERES record appeared reasonably successful in estimating the net feedback parameter (*82*, *172*). In later assessments this success diminished (suggesting the precision offered in these earlier assessments was illusory), likely due to stronger internal variability in the second half of the record decoupling the short-term feedback from the long-term ECS response (*74*, *173*). Despite this, TOA radiative fluxes do still remain a useful gauge of the net feedback, its shortwave and longwave components, and hence the multi-decadal climate response. Dessler and Forster (2018) demonstrates how estimating the feedback using tropical near-surface air temperature, instead of GMST, improves correlation with long-term feedbacks (*74*), since the former variable is better correlated with ENSO variability. This result still relies on the short-term TOA flux variability informing long-term feedbacks, a point on which the literature is not agreed (*173*).

Kramer *et al.* (2021) and Raghuraman *et al.* (2021) use the 20-year trends in CERES TOA flux observations to identify evidence of the anthropogenic ERF trend between 2000-2020. Kramer uses radiative kernels to estimate the ERF contributions of GHGs and aerosols to the observed 20-year linear trend in TOA flux, showing that GHG forcing is required to reproduce the observed CERES trend (*97*). This result is supported by Raghuraman, who determines the CERES trend is both statistically significant and anthropogenic in origin (*174*). Neither paper finds a major role for aerosols in the CERES observations, despite clear trends visible in all sky and clear sky SW fluxes. Analysis of the aerosol contribution is potentially hampered by both groups only considering a 20-year linear trend, while aerosol trends have more likely varied decade-to-decade (*63*).

Loeb *et al.* (2019, 2021) and Stephens *et al.* (2022) also discuss trends in the CERES record, focusing on the SW anomaly and evidence for an aerosol contribution (*131*, *173*, *175*). Loeb argues that aerosol emissions trends contribute only a small amount to the all sky SW flux anomaly variability, determining a more important role for cloud variability (*173*). This is somewhat refuted by Stephens *et al.* (2022), who agree with the claim that cloud feedbacks contribute significantly to the all sky flux,

Observation name	Variable	Description
CERES	TOA fluxes	CERES equipment flown on NASA's Terra and Aqua satellites (*168*). Measures TOA flux observations with near-global coverage, split between broadband shortwave, longwave and net radiative flux, and additionally subset into clear-sky and all-sky conditions. Monthly averages gridded onto $1°\times1°$ (lat,lon) grid, and spanning March, 2000 to present.
MODIS	AOD/cloud optical properties	MODIS equipment flown on NASA's Terra and Aqua satellites (*176*). Measures AOD, along with cloud optical properties to infer cloud droplet effective radius, CDNC, cloud fraction, LWP. Monthly averages gridded onto $1°\times1°$ (lat,lon) grid, and spanning March, 2000 to present.
Sogacheva *et al.* (2020)	AOD	Merged AOD record using several overlapping AOD records from a range of satellite products, validated against in-situ measurements (*153*). Monthly averages gridded onto $1°\times1°$ (lat,lon) grid, and spanning Jan, 1995 to Dec, 2017.
HadCRUT5	GMST	In-situ surface temperature record produced by the Met Office. Includes a 200-member ensemble to sample uncertainty, and additional products which use alternative infilling approaches (*43*). Monthly averages gridded onto $5°\times5°$ (lat,lon) grid, and spanning 1850 to present.
GISTEMPv4	GMST	In-situ surface temperature product completed by NASA's Goddard Institute for Space Studies and based on NOAA's surface temperature observation network (*165*). Global, monthly averages spanning 1850 to present.
NOAA	GMST	In-situ surface temperature product from NOAA's surface temperature observation network (*177*). Global, monthly averages spanning 1850 to present.
Berkeley Earth	GMST	In-situ surface temperature product from Berkeley Earth's land surface temperature dataset and HadCRUT3 SST dataset (*167*). Global, monthly averages spanning 1850 to present.
Copernicus Atmosphere Monitoring Service	CAMS	Reanalysis product from ECMWF's Integrated Forecasting System (*178*).

Table 1.3: Summary of key observation datasets used in this thesis.

but determine a larger role for the clear sky SW trend in explaining the overall SW flux anomaly (where aerosols are the major contributor to decadal trends in the clear sky SW flux observations). The contribution of aerosols to the recent SW flux anomaly behaviour requires further research, which is addressed in chapters 3 and 4 of this thesis.

The MODerate resolution Imaging Spectroradiometer (MODIS) equipment allows

simultaneous observations of cloud and aerosol optical properties coinciding with CERES TOA flux observations. Products observed with the MODIS equipment include CDNC, LWP, cloud fraction in cloudy sky conditions, as well as AOD in clear sky conditions. These were employed extensively in studies contributing to Bellouin's aerosol forcing review discussed above (*71*), as well as providing the basis for the observationally-constrained forcing assessment in AR6 (*5*). The 20-year linear trends in MODIS and CERES observations together provided the evidence basis for Quaas *et al.* (2022)'s claim that aerosol forcing has reversed its trend since 2000 (*164*). Quaas' paper is the first to make such a claim based on a direct analysis of observations. I expand on this assessment in chapter 4.

1.4.2.1 Variability in the observed climate system

A key challenge when attributing observed AGW using satellite and in-situ records is determining the contribution of internally-generated variability. The climate system exhibits natural variability which, although chaotic in nature, has several identifiable patterns. Key modes of GMST variability include the El Niño Southern Oscillation (ENSO), Pacific Decadal Oscillation (PDO), Atlantic Multidecadal Variability (AMV), and Quasi-Biennial Oscillation (QBO) (*8*, *179*). Each of these reflect repeating cycles in the atmosphere-ocean system which impact on the variables we use to measure AGW over multi-annual to multi-decadal periods. Other variability signals are also exhibited over seasonal and sub-seasonal timescales, e.g. the Madden-Julien Oscillation (*180*).

For this thesis, a particular focus is on ENSO and PDO variability. ENSO alone represents the largest contribution to multi-annual variability in GMST (*181*) and is a key influence on regional weather patterns worldwide (*8*). ENSO is characterised using eastern tropical pacific SSTs and is split into three phases: El Niño, La Niña, and neutral conditions (*119*). El Niño events are characterised by a warm pool of eastern tropical pacific SSTs (3-5 °C above the historical mean). This shifts the rising branch of the Walker circulation eastwards and pulls the jet stream southwards in the northern hemisphere. Conversely, La Niña events are characterised by a cool pool of eastern tropical pacific SSTs (3-5 °C below the historical mean). This strengthens the rising

branch of the Walker circulation over the maritime continent, and pushes the jet stream northwards in the northern hemisphere (*182*). The PDO spatial pattern resembles that of the primary ENSO mode but is exhibited over longer intervals (typically decadal or multi-decadal periods) (*183*).

How models capture these key modes of atmosphere-ocean variability has been studied extensively. Brown *et al.* (2015) analysed models' ability to capture ENSO, PDO and AMV dynamics in their GSAT timeseries. They determined that models disagree on the most prominent modes of variability in global surface temperature, including several which emphasise Atlantic, over Pacific, internal variability (*183*). CMIP5 and CMIP6 model ensembles have also been used to project changes in the amplitude of ENSO with increasing global warming. Warming-induced ENSO amplitude changes are not detected in the subset of models which exhibit realistic ENSO dynamics, although other model subsets do display trends (*184*). The anthropogenic influence on ENSO teleconnections (particularly with the NH jet stream) are equally poorly constrained by CMIP6 models, with substantial inter-model and inter-regional differences (*185*). Despite these uncertainties, ENSO's influence on the jet stream suggests an important role in explaining recent NH GMST trends. This is discussed in greater detail chapters 3 and 4.

1.5 Thesis overview

This chapter began with a discussion of the approaches taken in the literature to define the level and rate of AGW today. Summarising this, the latest IPCC report suggests consensus on the level of AGW, but substantial uncertainty on the present-day rate of warming, despite refinements of both modelling approaches and observational datasets of the climate system. The rate of warming estimate is arguably the most prominent output of the IPCC in this assessment cycle, given our proximity to the 1.5 °C warming threshold. The defining question of this thesis is *what is the anthropogenic contribution to the current rate of warming?*

To provide context, the introduction also included a brief discussion of the relevant literature on contributions to global warming. For CO_2, this focused on the TCRE parameter and remaining carbon budgets, which are necessary prerequisites to chapters

5 and 6. For non-CO_2 pollutants this focused on the individual contributions to warming based on their radiative forcing, and the differences in their physical properties. These differences necessitate the use of GHG metrics for policy design, but many of these metrics are poorly suited from a physical science perspective. This provides the knowledge base for chapter 5. Finally, there was a discussion of the aerosol ERF level and trend, including the major contributions to uncertainty today, and approaches to constrain forcing trends using observations and models together. I discussed recent work constraining the trend in aerosol ERF, identifying the 'turning point in the aerosol era' (*163*, *164*), and the aerosol-induced warming contribution in ambitious mitigation scenarios. Together, these provide the knowledge base for chapters 3 and 4.

This thesis focuses on different aspects of the core question. These are split across chapters 3–6 and can be summarised as:

- *What determines the present day rate of warming?* In chapter 3 this includes defining a robust definition for the rate of warming, and constraining the contributions to it from individual anthropogenic and natural sources. Answering this also requires an estimate of the aerosol and anthropogenic ERF trend over the past two decades, which is explored in chapter 4.

- *How do CO_2 and non-CO_2 pollutants contribute to near-future rates of warming and, hence, the remaining carbon budget?* This requires deriving a physically-coherent methodology to compare the CO_2 and non-CO_2 contributions to remaining warming until 1.5 °C, and constraining the value of the TCRE parameter. These are explored in chapter 5.

- *What determines the conditions under which anthropogenic warming stabilises?* The Paris Agreement highlights the need for a balance between residual anthropogenic sources and removals by sinks in order to limit warming, implying at least a temperature stabilization. The wording of Article 4 of the Paris Agreement is deliberately ambiguous, so chapter 6 explores the physical requirements for stabilizing temperatures on multi-decadal timescales.

Before this, chapter 2 first introduces the simple climate modelling framework which is used throughout the rest of this thesis. Chapters 3, 4, 5 and 6 then answer the individual research questions raised above, and chapter 7 concludes.

There is a 50:50 chance of the annual average global temperature temporarily reaching 1.5°C above the pre-industrial level for at least one of the next five years.

— *Global Annual to Decadal Climate Update*, WMO.
Geneva, 9 May 2022

2

A model of the physical climate system

This chapter presents a mathematical framework for modelling the physical climate system's response to anthropogenic pollutants and natural forcing. I derive this framework based on the FaIRv2.0 simple climate model, and present how it can be used to model: the physical response of the climate system to CO_2 emissions, the radiative forcing response from the emissions of non-CO_2 pollutants, and the globally-averaged aerosol emissions-to-forcing relationship. These derivations are based on work published in AGU's Geophysical Research Letters: Jenkins *et al.* (2018) Framing Climate Goals in Terms of Cumulative CO_2-Forcing-Equivalent Emissions, and Jenkins *et al.* (2022) The Multi-Decadal Response to Net Zero CO_2 Emissions and Implications for Emissions Policy. See refs. (*186*, *187*).

Contents

2.1 A model of the physical climate response to emissions

A simple model of the climate system is a useful starting point to explore the characteristics of the global climate system's response to a wide range of anthropogenic pollutants. In this thesis I use the mathematical framework described by the FaIRv2.0 simple climate model (*29*). FaIR's design is substantially simpler than full-complexity GCMs, allowing for studies which are not possible in full GCMs (e.g. large ensemble searches of the multi-dimensional parameter space). Despite this reduced complexity, FaIR has been shown to emulate the behaviour of individual full-complexity models across a broad range of scenarios and parameter sets (*29*, *93*, *94*), with these 'emulator' parameter sets being used as estimates of key diagnostic parameters of the GCMs (e.g. TCR, ECS, TCRE). Its performance has also been benchmarked against observations of the climate system, producing observational-constraints on FaIR's parameters for use in future scenario projections (e.g. in Smith *et al.* (2018) (*59*)).

I split the description of the important mathematical frameworks used in this thesis into three subsections. First, I derive the multi-decadal response to CO_2 emissions by introducing the impulse response framework used by FaIRv2.0. From this, I derive the TCRE parameter by expanding the equation set over multi-decade intervals, and demonstrate how the second-order terms in this expansion relate the ZEC to the TCRE in FaIR. Second, I introduce the CO_2-forcing-equivalent metric, which can be used to convert non-CO_2 emissions timeseries into CO_2 timeseries in a physically-coherent way. Finally, I discuss the equations for estimating the forcing response to aerosol emissions in FaIRv2.0, based on the equation set introduced in Smith *et al.* (2021) (*73*).

2.1.1 The climate response to CO_2 emissions

At a globally-averaged scale, the climate system's response to a perturbation in CO_2 emissions can be explored using a series of impulse response functions (*42*, *78*, *79*). The FaIR model is based on this, using four carbon cycle pools (adjustment timescales representing the rate of decay of atmospheric CO_2 perturbations into the biosphere, upper ocean, deep ocean, and geosphere) (*68*, *93*, *188*), and two or three thermal

cycle boxes (where the timescales and efficacies of the boxes parameterise the heat uptake by the upper and deep ocean, respectively) (*78*).

2.1.1.1 ERF to temperature response

FaIRv2.0 assumes that the surface temperature anomaly, $T(t)$, is approximated by an impulse response model

$$\frac{dS_i(t)}{dt} = \frac{c_i F - S_i}{d_i} \text{ and } T(t) = \sum_{i=1}^{n} S_i(t), \tag{2.1}$$

where $F(t)$ is the radiative forcing timeseries, $S_i(t)$ is the portion of the surface temperature anomaly associated with the i^{th} box, and d_i and c_i are the thermal response timescales and thermal response efficacies of the individual boxes (*78*). Solving this differential equation produces an expression for the surface temperature as a function of the radiative forcing

$$T(t) = \sum_{i=1}^{n} \frac{c_i}{d_i} \int_{t'=0}^{t} F(t') e^{-\frac{t-t'}{d_i}} dt'. \tag{2.2}$$

The efficacies, c_i, represent the equilibrium warming contribution per unit forcing from each box (*29*). The timescales, d_i, model the thermal cycle relaxation towards the equilibrium temperature response. Leach *et al.* (2021) finds that for many CMIP5/6 models two of the three thermal response timescales are approximately a decade or less, while the other is several hundred years (*29*, *189*) (d_1=0.903 years, d_2=7.92 years, d_3=355 years). Although this is not the case for every GCM, with some finding a best-fit response containing an explicit multi-decade timescale (*190*), most emulation parameters can be approximated using two sub-decadal and one multi-century timescale. Leach *et al.* (2021) includes the third thermal response timescale as Tsutsui (2020) suggested this better captures the climate response to a rapid radiative forcing change (*189*). Since this third timescale is very short (of order 1 year), the multi-decadal response is still well-captured using just two timescales (*59*).

Given this, an expression for the warming response over multi-decade intervals can be found by expanding the terms on the right-hand side of equation 2.2. For simplicity, I reduce equation 2.2 to a two timescale impulse response model (one sub-decadal

and one multi-century timescale). Seshadri (2017) shows this expansion leads to a remarkably simple expression for the warming response to a forcing timeseries $F(t)$ over a multi-decade time interval (*191*)

$$T(t) = \kappa_F\left(F\left(t - \frac{c_1 d_1}{c_2}\right) + \rho\int_{t'=0}^{t} F(t')dt'\right). \tag{2.3}$$

$T(t)$ is the temperature change over the interval t, and $F(t - c_1\tau_1/c_2)$ is approximately the change in forcing over that period (the offset $c_1\tau_1/c_2$ is small and can be ignored over multi-decade intervals). $\int_{t'=0}^{t} F(t')dt'$ is equal to the average forcing over the period (compared to preindustrial) multiplied by the length of the time period, and ρ is the *Rate of Adjustment to Constant Forcing* (RACF). The RACF relates to the linear trend in the temperature anomaly once radiative forcing is stabilised, i.e. it describes the residual warming resulting from stable ERFs over a multi-decade interval. Equivalently, ρ defines the rate of forcing decline required to stabilise global surface temperatures over a multi-decade period. Mathematically, $\rho \approx c_2/(c_1 d_2)$ in a two-box impulse response model where subscript 1/2 refers to the sub-decadal/multi-century timescales. The κ_F parameter is the sub-decadal thermal response efficacy (i.e. $\kappa_F = c_1$ in the two-box setup), and can be thought of as the net Transient Climate Response to Forcing parameter, or TCRF (*103*).

Equation 2.3 defines a simple relationship for the globally-averaged surface temperature anomaly as a function of ERF. With FaIR's standard parameters (*29*), $\rho \approx$ 0.3 %/year for the contemporary climate system, meaning anthropogenic radiative forcing must decline by around 3 %/decade for global warming to halt over multi-decadal timescales (*125*).

2.1.1.2 CO_2 emissions to ERF

An impulse response structure can also be used to describe the carbon cycle response to a CO_2 emissions timeseries (*42*, *93*). In FaIR, a four-pool impulse response structure determines the atmospheric CO_2 concentration following a CO_2 emissions timeseries. These CO_2 concentrations timeseries are converted to ERF, $F(t)$, using an approximately logarithmic concentration-to-ERF relationship (*29*, *68*, *69*).

Combining these two steps formulates a single relationship between the ERF and emissions timeseries

$$F(t) = \sum_{j=1}^{4} \mu_j \int_{t'=0}^{t} E(t') e^{-\frac{t-t'}{\tau_j}} dt' \tag{2.4}$$

where τ_j are the carbon cycle response timescales and μ_j are forcing efficacies in units $W/m^2/GtCO_2$ for each of the four carbon pools, and $E(t)$ is the CO_2 emissions timeseries. I have assumed that non-linearities in the carbon cycle response to CO_2 emissions (*42*) exactly cancel with non-linearities introduced in the logarithmic relationship between CO_2 concentrations and forcing (*69*). This need not be the case, but in a wide range of climate model simulations and in the observed Earth system this appears to approximately hold true (*29*, *94*).

As was done with the thermal response by Seshadri (2017), this equation can be recast in terms of two timescales and expanded to explore the multi-decadal carbon cycle response: τ_1, which captures the short timescale (< 10 years) response to a CO_2 emissions perturbation; and τ_2 which captures the multi-century response (> 100 years). Considering only two characteristic timescales, and replacing the general CO_2 emissions timeseries with an order α polynomial, $E(t) = \sum_{\alpha=0}^{N} E_\alpha t^\alpha$, I have

$$F(t) = \sum_{k=1}^{2} \mu_k \int_{t'=0}^{t} \sum_{\alpha=0}^{N} E_\alpha t'^\alpha e^{-\frac{t-t'}{\tau_j}} dt'. \tag{2.5}$$

By swapping the order of the integral and sum over each polynomial component, this integral can be solved, finding

$$F(t) = \sum_{k=1}^{2} \mu_k \sum_{\alpha=0}^{N} E_\alpha \tau_k \Big[\Big(\sum_{\beta=0}^{\alpha} \frac{(-1)^\beta \alpha!}{(\alpha-\beta)!} \tau_k^\beta t^{\alpha-\beta} \Big) + (-1)^{\alpha+1} (\alpha!) \tau_k^\beta e^{-\frac{t}{\tau_k}} \Big]. \tag{2.6}$$

Now considering times where $\tau_1 << t << \tau_2$: for the $k = 1$ term (herein referred to as the first term), I can ignore terms which are proportional to e^{-t/τ_1}, meaning it simplifies to

$$\text{First term} \approx \mu_1 \sum_{\alpha=0}^{N} E_\alpha \tau_1 \sum_{\beta=0}^{\alpha} \frac{(-1)^\beta \alpha!}{(\alpha-\beta)!} \tau_1^\beta t^{\alpha-\beta}. \tag{2.7}$$

Going further, and keeping only the leading order term from each component in the outer sum (i.e. keeping only $\beta = 0$ terms, since all other terms are at least an order τ_1/t smaller) gives

$$\text{First term} \approx \mu_1\tau_1 \sum_{\alpha=0}^{N} E_\alpha t^\alpha = \mu_1\tau_1 E(t). \tag{2.8}$$

For the second term in the outer sum in equation 2.6 ($k = 2$; $t << \tau_2$), I expand the terms proportional to e^{-t/τ_2}, finding

$$\text{Second term} = \mu_2 \sum_{\alpha=0}^{N} E_\alpha \tau_2 \left[\left(\sum_{\beta=0}^{\alpha} \frac{(-1)^\beta \alpha!}{(\alpha-\beta)!} \tau_2^\beta t^{\alpha-\beta} \right) + (-1)^{\alpha+1}(\alpha!)\tau_2^\alpha \sum_{\gamma=0}^{\infty} \frac{(-1)^\gamma}{\gamma!} \left(\frac{t}{\tau_2}\right)^\gamma \right]. \tag{2.9}$$

The infinite sum over γ on the right hand side can be separated into two contributions, one sum including the terms $0 \to \alpha$, and the other including the terms $\alpha \to \infty$. Then, noting that the terms $0 \to \alpha$ in the sum over γ cancel the terms in the sum over β, this second term simplifies to

$$\text{Second term} = \mu_2 \sum_{\alpha=0}^{N} E_\alpha \alpha! \tau_2^{\alpha+1} \sum_{\gamma=\alpha+1}^{\infty} \frac{(-1)^\gamma}{\gamma!} \left(\frac{t}{\tau_2}\right)^\gamma. \tag{2.10}$$

All of the terms in this second term are proportional to $(t/\tau_2)^\gamma$. Hence keeping only the two leading order terms which remain in the sum over γ gives

$$\text{Second term} \approx \mu_2 \sum_{\alpha=0}^{N} E_\alpha \left[\frac{\alpha!}{(\alpha+1)!} t^{\alpha+1} - \frac{\alpha!}{(\alpha+2)!\tau_2} t^{\alpha+2} + ... \right] \tag{2.11}$$

which can be identified with the integral of the annual emissions polynomial, $E(t)$, and the double integral of $E(t)$, respectively

$$\text{Second term} \approx \mu_2 \left[\int E(t)dt - \frac{1}{\tau_2} \int\int E(t)dtdt + ... \right]. \tag{2.12}$$

Putting the first and second terms in equation 2.6 back together, I have derived the approximate form for $F(t)$ over inter-decadal timescales, where $\tau_1 << t << \tau_2$

$$F(t) \approx \mu_1\tau_1 E(t) + \mu_2 \int E(t)dt - \frac{\mu_2}{\tau_2} \int\int E(t)dtdt. \tag{2.13}$$

While this result is of interest in itself, to derive the TCRE from the above expressions I need the inverse of this relationship (i.e. an expression for the cumulative CO_2 emissions

as a function of $F(t)$). To find this, note that the middle term in equation 2.13 dominates over inter-decadal timescales (the other two terms are factors τ_1/t and t/τ_2 smaller, respectively). Hence, I can approximate the terms $\frac{dF}{dt}(t) \sim \mu_2 E(t)$, and $\int F(t)dt \sim \mu_2 \int\int E(t)dtdt$. Substituting these into equation 2.13 and rearranging yields

$$\int E(t)dt \approx \frac{1}{\mu_2}\Big(F\Big(t - \frac{\mu_1\tau_1}{\mu_2}\Big) + \frac{1}{\tau_2}\int F(t)dt\Big), \tag{2.14}$$

where I have used the fact that on timescales where $t >> \tau_1$, $F(t - \frac{\mu_1\tau_1}{\mu_2}) \approx F(t) - \frac{\mu_1\tau_1}{\mu_2}\frac{dF}{dt}(t)$ (*103*).

2.1.1.3 Deriving the TCRE

The expression in equation 2.14 appears to mirror the expression in equation 2.3, where the quantity on the lefthand side of each equation is proportional to the sum of the change in ERF and the integral of the ERF over the time period. These two lefthand quantities are the cumulative CO_2 emissions, herein labelled $G(t)$, and the temperature anomaly, $T(t)$. Hence, combining equations 2.3 and 2.14 derives the well-known TCRE relationship — cumulative CO_2 emissions are proportional to CO_2-induced warming. Further, these two equations highlight the requirements for the TCRE to be time and scenario independent: the timescales in equations 2.3 and 2.14 must exactly match ($(\mu_1\tau_1)/\mu_2 \equiv (c_1s_1)/c_2$, $1/\tau_2 \equiv \rho$), they must not vary in time, or depend too heavily on the time history of the radiative forcing. If these conditions are met the temperature response is determined exactly over all timescales by the cumulative CO_2 emissions multiplied by a constant TCRE parameter (where the TCRE $= \mu_2\kappa_F$).

If the various timescales are not identical then the temperature response can lead or lag the cumulative CO_2 emissions. Over short intervals differences between the sub-decadal timescales ($(\mu_1\tau_1)/\mu_2$, $(c_1s_1)/c_2$) can cause some residual warming to occur shortly following net zero. However, over multi-decade intervals warming induced by mismatched short timescales quickly becomes irrelevant as these differences are of order 1-3 years. More important for mitigation policy is the response following a CO_2 perturbation if the multi-century timescales of the carbon and thermal cycles are

mismatched ($1/\tau_2$, ρ). In this case, when equations 2.3 and 2.14 are combined there is an additional term beyond the TCRE linearity

$$\Delta T = \kappa_E(\Delta G + o\bar{G}\Delta t), \tag{2.15}$$

where $o = \rho - 1/\tau_2$ is the RAZE, or *Rate of Adjustment to Zero Emissions* parameter, ΔG is the cumulative CO_2 emissions change over the interval Δt, κ_E is the TCRE parameter ($\kappa_E = \mu_2\kappa_F$, the combination of the transient warming response to a unit forcing change, κ_F, and multi-century forcing resulting from a unit emissions perturbation, μ_2), and $\bar{G}$ is the quantity of cumulative CO_2 emissions released since preindustrial averaged over the interval Δt.

Since ρ can be rewritten in terms of the TCR and ECS parameters (*103*, *187*), the RAZE parameter can also be written

$$o = \frac{1}{d_2}\left(\frac{ECS - TCR}{TCR}\right) - \frac{1}{\tau_2}, \tag{2.16}$$

where d_2 is the multi-century response timescale of the thermal cycle. In this case, the requirements for RAZE to be exactly zero (and hence the TCRE relationship to exactly hold) is

$$\frac{ECS - TCR}{d_2} = \frac{TCR}{\tau_2}, \tag{2.17}$$

i.e. the rate at which energy is added to the system by the thermal cycle releasing the remaining warming after net zero, (TCR-ECS)/d_2, must equal the rate at which the carbon cycle is absorbing CO_2 and reducing the warming which occurred to date, TCR/τ_2. If the thermal cycle is more rapidly adjusting than the carbon cycle, or the fraction of warming yet to be realised is large (TCR/ECS small), then we observe a positive RAZE (the thermal cycle is relaxing towards the long-term equilibrium more rapidly than the carbon cycle can compensate). For a negative RAZE the opposite is true: either the long-timescale response for the carbon cycle adjusts more rapidly than the thermal cycle, or the TCR/ECS ratio is large (in either case the thermal cycle cannot add thermal energy into the atmosphere as quickly as it is dissipated by the relaxing carbon cycle).

In summary, equation 2.15 describes the multi-decadal warming response arising from a CO_2 emissions perturbation in the FaIRv2.0 simple climate model. The first

term describes the well-known linearity between cumulative CO_2 emissions and warming (the TCRE relationship), while the second introduces the RAZE parameter. This RAZE term describes the residual warming trend once CO_2 emissions have reached net zero, where residual warming or cooling occurs because of an imbalance between the multi-century response of the thermal cycle (described by the RACF, ρ) and the carbon cycle (described by $1/\tau_2$). Both of these terms are of order a fraction of one percent, meaning the RAZE parameter (the difference between them) is of that size or smaller, and may be positive or negative (*103*). Further investigation of the properties of the RAZE parameter is left to chapter 6, where I derive the physical requirements to stabilise global surface temperatures over a multi-decade interval.

2.1.2 The contribution from non-CO_2 pollutants

In chapter 1 I discussed the use of GHG metrics to compare the contributions of various pollutants to AGW. This discussion highlighted the failure of the most commonly used metric, GWP, to compare pollutants in a physically accurate manner. This occurs because the GWP metric uses an integral in its definition, losing information on the lifetime of the pollutant in question, relative to that of CO_2 (*127*). Variations on GWP have been proposed to address this issue (*125*, *192*, *193*), but these depend on relatively arbitrary choices, such as the binary distinction between 'long-lived' and 'short-lived' climate pollutants (*4*). This begs the question: *how can we define a physically-coherent conversion between a pollutant's emissions timeseries and a quantity of CO_2?*

One proposal, building on the notion of a forcing equivalent index proposed by Wigley (1998) (*124*) and elaborated on by Manning and Reisinger (2011) (*194*), is to express net total anthropogenic radiative forcing in terms of CO_2-forcing-equivalent (CO_2-fe) emissions, defined simply as the time history of CO_2 emissions that would result in a given radiative forcing pathway (similar to the approach of Zickfeld *et al.* (2009), who go a step further and diagnose anthropogenic radiative forcing from temperatures (*195*)). I outlined such an approach in a 2018 paper, discussing the mathematical approach in the FaIRv1.0 model (*94*). A carbon cycle model is required to compute CO_2-fe emissions, but since the relationship between radiative forcing

and CO_2-equivalent concentrations is relatively unambiguous, and CO_2 emissions are diagnosed from CO_2 concentrations in many climate modeling experiments already (*104*, *196*, *197*), calculating CO_2-fe emissions in this way is no more model dependent than calculating CO_2 emissions themselves.

CO_2-fe emissions are diagnosed by inverting the radiative forcing timeseries to determine the corresponding timeseries of CO_2 emissions. This requires inverting the approximately logarithmic concentration-to-ERF relationship for CO_2

$$C(t) = C_0 \exp\Big(\frac{F(t)\ \ln(2)}{F_{2\times}}\Big), \tag{2.18}$$

where C_0 is the preindustrial CO_2 concentration, and $F_{2\times}$ is the radiative forcing resulting from doubling CO_2 concentrations. This inversion is an approximation since Etminan *et al.* (2016)'s revised forcing relationships additionally include small corrections to the pure logarithmic term (*69*), modelled as $F \propto \left[\ \ln(C), C^2, \sqrt{C}\ \right]$ (*29*, *68*). These corrections are sufficiently small to be neglected to first order.

Given this concentration timeseries, I diagnose the CO_2-fe emissions at each timestep by inverting FaIR's carbon cycle impulse response model

$$\frac{dR_i(t)}{dt} = a_i E(t) - \frac{R_i(t)}{\alpha(t)\tau_i}, \tag{2.19}$$

$$C(t) = C_0 + \sum_{i=1}^{4} R_i(t). \tag{2.20}$$

Here, R_i are the concentrations of four carbon reservoirs with corresponding decay timescales, τ_i, and uptake fractions a_i. α is a state-dependent adjustment factor, introduced in Millar *et al.* (2017) to account for the change in rate of carbon uptake by non-atmospheric carbon pools as their perturbation increases. α is a monotonically increasing function of the atmospheric and non-atmospheric CO_2 perturbation, and the surface temperature anomaly. In the original formulation of FaIR, Millar defined α using the integrated Impulse Response Function over a 100 year interval

$$iIRF_{100} = \sum_i \alpha a_i \tau_i \Big[1 - \exp\Big(\frac{-100}{\alpha\tau_i}\Big)\Big] = r_0 + r_C C_{acc} + r_T T, \tag{2.21}$$

where r_0, r_C and r_T coefficients describe the preindustrial $iIRF_{100}$ value (r_0), the $iIRF_{100}$'s linear relationship with CO_2 accumulated in non-atmospheric pools ($r_C C_{acc}$),

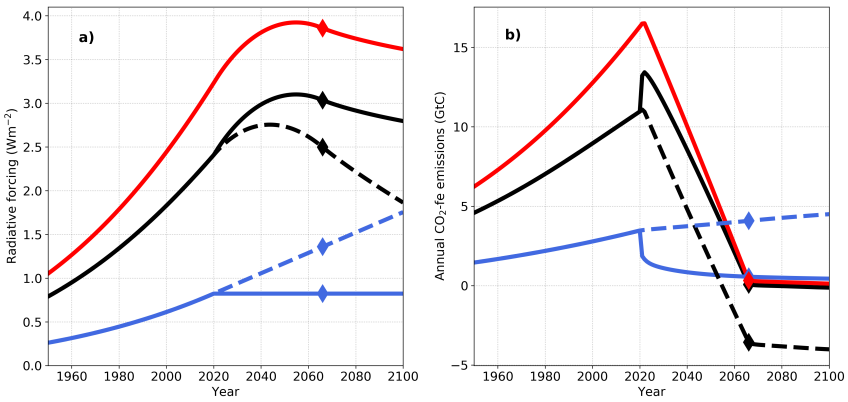

Figure 2.1: Two idealized radiative forcing profiles (panel a; solid and dotted lines) are split so that their total radiative forcing is identical (red), but with different proportions arising from CO_2 (black) and non-CO_2 (blue) sources after 2020. Panel b shows these scenarios expressed in terms of CO_2-fe emissions. Since the total forcing is identical, the diagnosed total CO_2-fe emissions are the same, but with different contributions coming from CO_2 and non-CO_2 sources in each case. The temperature response to these total CO_2-fe emissions pathways would be identical, assuming non-CO_2 forcings have been accurately expressed in terms of ERF. Diamond symbols show the year of temperature stabilization.

and its linear relationship with the surface temperature anomaly ($r_T T$) (*42*). Alternatively, a functional form for α can be found based on an analytic approximation to the numerical solution to equation 2.21 (*29*). Diagnosed emissions found by inverting FaIR's carbon cycle are subject to two-time-step noise which is removed with a Gaussian kernel ($\sigma = 5$ years).

2.1.2.1 Example outputs of the CO_2-fe metric

Figure 2.1 shows a stylised example of the application of CO_2-fe metric to determine CO_2 emissions. Panel a contains two idealized radiative forcing scenarios (dotted and solid lines), with the same total forcing (red) but where different proportions are from CO_2 (black) and non-CO_2 (blue) sources after 2020. The dotted lines show a scenario in which non-CO_2 forcing continues to increase, while solid lines show a scenario in which it is stabilized. Panel b shows the corresponding CO_2-fe emissions for each scenario: note that increasing non-CO_2 forcing equates to approximately steady positive CO_2-fe emissions, mimicking the cumulative impact of CO_2, while stabilizing non-CO_2 forcing equates to an immediate decrease of CO_2-fe emissions toward zero. The total CO_2-fe

emissions (red, panel b) are identical except for smoothing errors and small non-linearities from the calculation method. Temperature responses to these two scenarios would also be identical, since they produce identical radiative forcing timeseries, and diamond symbols show the year in which temperatures stabilize. Unlike CO_2 emissions alone, or CO_2-equivalent emissions calculated with the GWP metric, CO_2-fe emissions reaching net zero is an accurate and scenario-independent indicator of "emissions balance" if interpreted in terms of the conditions required for temperature stabilization (*198*), subject to a small RAZE parameter, as discussed above.

In summary, CO_2-fe emissions recast a complex multi-gas emissions scenario into a single timeseries of CO_2 emissions. The physical response to these are significantly easier to conceptualise than the underlying multi-gas scenario, and can be approximated with the extended TCRE framework derived in equation 2.15. To use the CO_2-fe metric, one first needs an ERF timeseries for the emissions scenario of interest. For the major non-CO_2 GHGs (CH_4 and N_2O) this can be calculated using the simplified concentration-to-forcing relationships defined in Etminan (2016), or with the similar relationships used to produce the headline ERF assessments in Forster *et al.* (2021) (*69*, *72*). Corresponding concentration timeseries for individual GHGs can either be measured over the historical period (*199*), or estimated using single-pool gas cycle models (*29*) or full-complexity GCMs (*55*). Since non-CO_2 GHGs are well-mixed and relatively easily observed in the atmosphere, their resulting ERF estimates are generally well-constrained at present day. For aerosols, global emissions-to-forcing relationships are more uncertain, and must capture both the direct interactions between particulates and radiation, and the radiative response to aerosol-cloud interactions. The aerosol emissions-to-forcing expressions used in FaIRv2.0 are discussed below.

2.1.3 Aerosol emissions-to-forcing framework

A simple model for the ARI and ACI contributions to total aerosol ERF was proposed by Smith et al. (2021) (*73*) (based on earlier work by Stevens (2015) (*152*)). This

made ARI ERF a linear function of individual aerosol species emissions

$$F_{ARI}(t) = \sum_{i=1}^{N} \alpha_i E_i(t) = \alpha_{SO2} E_{SO2}(t) + \alpha_{BC} E_{BC}(t) + \alpha_{OC} E_{OC}(t) \quad (2.22)$$

where $\alpha_{SO2,BC,OC}$ is the radiative efficacy of SO_2, BC and OC emissions (the three dominant anthropogenic aerosol emissions species).

For ACI ERF, Smith proposed a log-linear functional form

$$F_{ACI}(t) = -\beta \log\left(1 + \frac{E_{SO2}(t)}{s_{SO2}} + \frac{(E_{BC}(t) + E_{OC}(t))}{s_{OC+BC}}\right) \quad (2.23)$$

where the strength of the non-linearity is encoded by the relative size of s_{SO2} and s_{BC+OC} compared to $E_{SO2}(t)$ and $E_{BC}(t) + E_{OC}(t)$, and β is the overall ACI radiative efficacy parameter (in units W/m^2). Equation 2.23's log-linear form is inspired by Stevens (*152*), who argued it better reflected the saturating effects of aerosols on cloud properties at very high aerosol loading, compared to a linear relationship (*152*). The total aerosol ERF is the sum of the F_{ARI} and the F_{ACI}.

Smith *et al.* (2021) demonstrated these two expressions emulate the individual aerosol ERF responses of CMIP6 model's RFMIP and AerChemMIP experiments (*73*), fitting them using a least-squares regression. Responses are shown for individual RFMIP and AerChemMIP-contributing GCMs in figure 2.2, with coloured lines showing the simplified emissions-to-forcing equation set emulation of these more complex models. The multi-model mean α coefficients (-2.5, +28.5, and -8.5 $mW/m^2(Tg/yr)^{-1}$ for SO_2, BC, and OC, respectively) are similar to the radiative efficacies found from Aerocom models (*200*). The multi-model mean β, s_{SO2} and s_{BC+OC} values (1.22 W/m^2, 157 $TgSO_2$/yr, and 76.7 TgC/yr) span several orders of magnitude across the CMIP6 models in figure 2.2. Small s_{SO2} and s_{BC+OC} parameters produce a highly logarithmic ERF_{ACI}, while large s_{SO2} and s_{BC+OC} mean ERF_{ACI} is linear to a change in emissions. The degree of logarithmicity for ERF_{ACI} differs substantially between GCMs (*29*, *201*), with some models exhibiting near-linear responses (e.g. GFDL-ESM4, NorESM2-LM), and others exhibiting highly non-linear responses (e.g. HadGEM3-GC31-LL, CanESM5).

CMIP6 models exhibit a range of aerosol forcing magnitudes and shapes in response to identical emissions inputs, but only provide a very sparse sampling of the overall

parameter space. A table of the individual parameter fits is provided in Smith *et al.* (2021). Some parameters in equations 2.22 and 2.23 co-vary substantially, particularly those defining the ACI response, therefore ensemble searches must be careful to account for this when sampling parameter distributions. With the equation set defined above and the CMIP6 model parameter distributions, a wide aerosol ERF ensemble can be produced based on CMIP6 model responses. This technique is used at the end of chapter 4 to assess the aerosol-induced warming trend and trend change over the past two decades.

2.1.3.1 Aerosol ERF trends

These simple aerosol ERF expressions can be differentiated to produce an equation of the aerosol ERF trend contributions

$$\frac{dF(t)}{dt} = \sum_i \alpha_i \frac{dE_i}{dt}(t) - \beta \frac{(E'_{SO_2}(t)/s_{SO_2} + E'_{BC+OC}(t)/s_{BC+OC})}{(1 + E_{SO_2}(t)/s_{SO_2} + E_{BC+OC}(t)/s_{BC+OC})} \tag{2.24}$$

where the index i sums over SO_2, BC and OC emissions and the prime on the right-hand side of equation 2.24 refer to time derivatives. In equation 2.24 the ARI contribution is a linear function of the individual aerosol emissions trends, while the ACI contribution is a function of the fractional rate of change of emissions over the period.

With some additional approximations this aerosol ERF trend can be simplified further: 1) the emissions quantities (E(t)/s) are small enough to use a Taylor expansion in the logarithm; and 2) $E_{SO_2}(t)/s_{SO_2} \gg E_{BC+OC}(t)/s_{BC+OC}$, meaning the ERF trends majority contributor is SO_2 emissions. These two assumptions are valid for the multi-model mean parameter values from Smith *et al.* (2021) above (*73*) and CEDS emissions inventories (*63*). With these approximations, equation 2.24 simplifies to

$$\frac{dF(t)}{dt} \approx \frac{dE_{SO_2}}{dt}(t)\left(\alpha_{SO_2} - \frac{\beta}{s_{SO_2}} + \frac{\beta E_{SO_2}(t)}{(s_{SO_2})^2} + ...\right). \tag{2.25}$$

Hence, the aerosol ERF trend is, to first order, proportional to the trend in SO_2 emissions, plus a correction term proportional to the emissions trend multiplied by the normalised emissions quantity ($E_{SO_2}(t)/s_{SO_2}$). If this correction term is small, then the aerosol ERF trend is approximately linear over the time period of interest; if it is close to one the ERF trend is highly non-linear and this approximation becomes invalid.

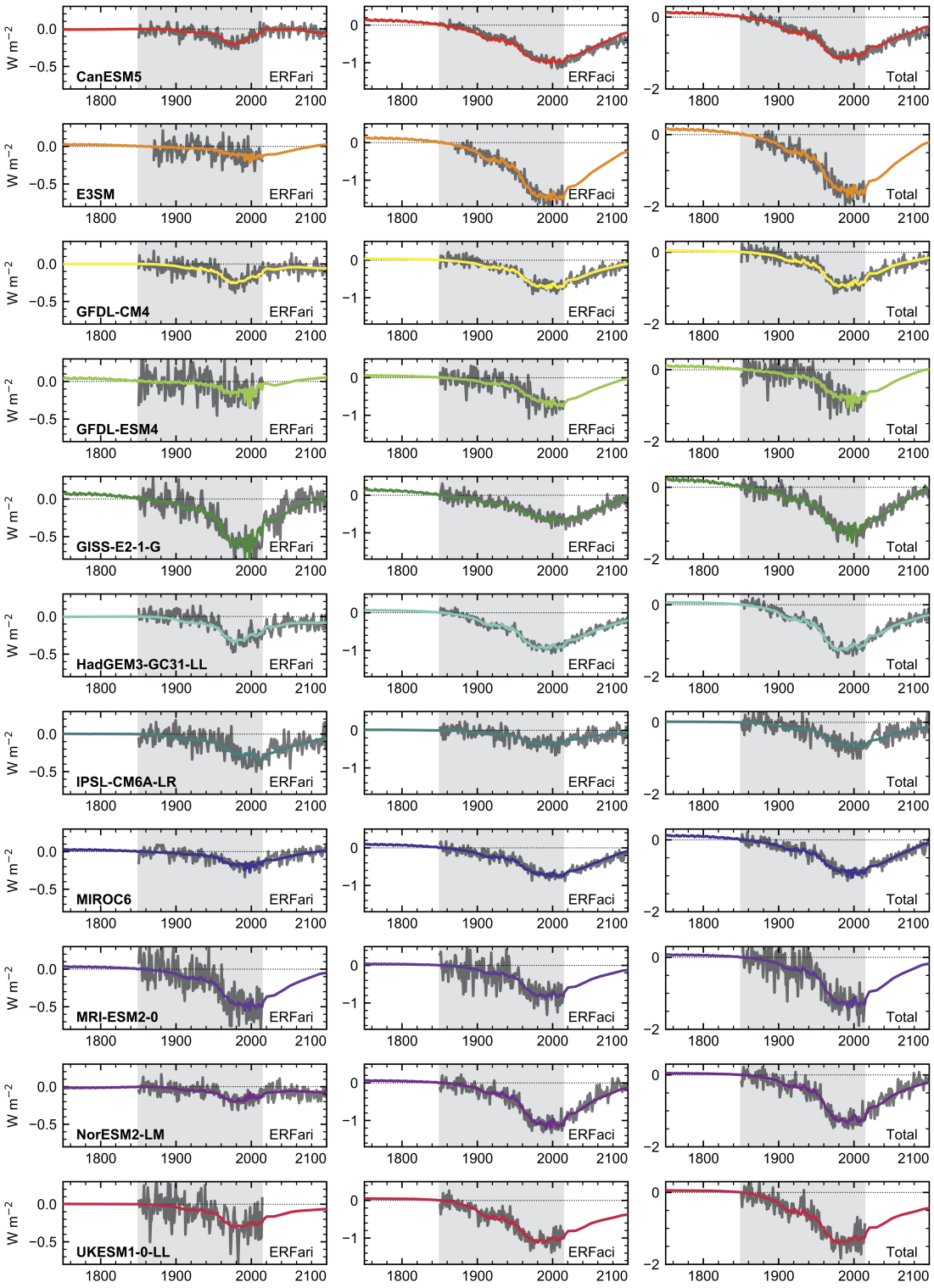

Figure 2.2: CMIP6-model diagnosed aerosol ERF relative to 1850 (grey) with emulated ERF shown with coloured lines. Figure reproduced from Smith *et al.* (2021). A table of the individual parameter fits is also provided in Smith *et al.* (2021).

2.2 Discussion

This chapter demonstrates how a simple modelling framework can be used to capture key properties of the physical climate system's response to anthropogenic emissions.

I began by introducing the impulse response frameworks used by FaIRv2.0 to model the carbon and thermal cycles. On the basis climate policy is interested in the warming response of the climate system over multi-decade intervals, these expressions were expanded assuming the timescales of physical climate responses can be separated broadly into sub-decadal and multi-century responses. The resulting expansions of the carbon cycle (equation 2.14) and thermal cycle (equation 2.3) shared a common structure, which can be exploited to derive the TCRE relationship.

By completing the expansion, I also derived the conditions which were required for this TCRE relationship to be exact. In FaIR, these conditions related to the relative size of timescales in the thermal and carbon cycles, in particular, differences in the multi-century responses which are responsible for maintaining the stability of the TCRE relationship in the long-term. These were discussed in equation 2.17, which shows how multi-decadal warming halts at net zero if the TCR, ECS and multi-century responses timescales in the thermal and carbon cycles exactly offset. This framework forms the basis for the analysis of ZEC in terms of the RAZE framework in chapter 6.

Next, I introduced the concept of CO_2-forcing-equivalent emissions, demonstrating how it can be derived in FaIRv2.0 and used to compare radiative forcing timeseries. CO_2-forcing-equivalent emissions are particularly helpful as a GHG metric: defined as the CO_2 emissions which produce the same radiative forcing pathway as an arbitrary pollutant's emissions timeseries. By construction they produce a physically-identical temperature response to that arbitrary pollutant's emissions timeseries, as the resulting ERF pathways for each emissions timeseries are identical. CO_2-fe emissions are also functionally identical to CO_2 emissions, and therefore inherit all the useful properties derived in the first section governing the multi-decadal warming response to a CO_2 emissions timeseries. These facts together make the CO_2-fe metric a powerful simplifier of multi-gas emissions scenarios. Chapter 5 uses them to diagnose the non-CO_2 contribution to historical warming to derive an observationally-constrained TCRE, and

to allocate a non-CO_2 portion to future warming by incorporating non-CO_2 pollutants into the remaining carbon budget framework.

Finally, I introduced the equations which FaIRv2.0 uses to define the globally-averaged aerosol emissions-to-ERF relationship. These are based on earlier work by Smith *et al.* (2021) and Stevens (2015); basing the ARI relationship on linear rescalings of the SO_2, OC and BC emissions timeseries, and the ACI relationship on a log-linear expression which saturates the ACI ERF for very high anthropogenic aerosol emissions. I demonstrated they successfully model the aerosol emissions-to-forcing relationships presented by aa wide range of CMIP6 models, and discussed the properties of an aerosol ERF trend ensemble derived using them. Equation 2.25 highlighted that it is the underlying SO_2 emissions trends which drive the aerosol ERF trend behaviour in the simplified ERF ensembles. The simplified aerosol ERF equations described in this chapter are used to produce the headline aerosol ERF ensemble in AR6 (*72*), and also to produce the globally-averaged aerosol ERF ensemble used in several places in this thesis (including in the warming attributions of chapters 3 and 4, and the historical TCRE assessment in chapter 5).

Life is divided into three terms - that which was, which is, and which will be. Let us learn from the past to profit by the present, and from the present, to live better in the future.

— William Wordsworth

3

Is Anthropogenic Global Warming Accelerating?

This chapter discusses evidence supporting ERF trend assumptions in prominent datasets using globally-averaged observations of the climate system. This work is based on the publication *Is Anthropogenic Global Warming Accelerating?* Jenkins, S., Povey, A., Gettelman, A., Stier, P., Grainger, R. and Allen, M. (2022). Journal of Climate. See ref. (*186*).

Contents

3.1 Introduction

AR6 reported AGW was around 1.1°C (±0.2°C) above preindustrial levels between 2000-2019 and rising at +0.2°C/decade (see table 1.1). Over the same period the globally-averaged ERF (*45*, *68*) has monotonically increased by around +0.4 W/m^2/decade, with the 2000-2020 mean anthropogenic ERF reaching around 2.1 W/m^2 (1.3-3.0 W/m^2) above preindustrial levels (*5*, *68*).

In chapter 1 I introduced the linearized forcing-feedback framework (equation 1.6), which describes the linearised relationship between global radiative forcing changes and the global surface temperature anomaly response

$$\Delta F = \Delta N + \lambda \Delta T. \tag{3.1}$$

This equation can be used with observations of the climate system's TOA radiative flux anomaly (ΔN) and surface temperature anomaly (ΔT) to estimate the time-history of ERF. Dong *et al.* (2021) uses this approach to diagnose CMIP6 model ERFs from historical experiments (*202*). Equivalently, given an assumed ERF timeseries, equation 3.1 can be used to constrain the net feedback parameter (*74*, *82*, *172*).

Chapter 1 also discussed AR6's updates to ERF timeseries as part of the IPCC's global warming attribution (*5*). Datasets now suggest net anthropogenic ERF has accelerated since 2000, principally because of declining anthropogenic aerosol emissions since the early 2000s (*63*) and rising emissions of major GHGs (CO_2, CH_4 and N_2O) (*166*). Figure 3.1 shows anthropogenic SO_2 emissions from the CEDS database, a major contribution to aerosol ERF, coloured by region according to broad regional denominations in CEDS (*63*). SO_2 emissions have declined by around a third since peaking in 2005, and simultaneously have shifted geographically from the northern hemisphere mid-latitudes to predominantly be emitted in south east Asia. These aerosol emissions estimates have a large and almost immediate impact on aerosol ERF trends. The approximate contribution can be estimated with the simple aerosol ERF trend formula derived in equation 2.25.

Care must be taken in attributing an acceleration in human-induced global warming to these changes in aerosol emissions. Short-term GMST variability is strongly influenced

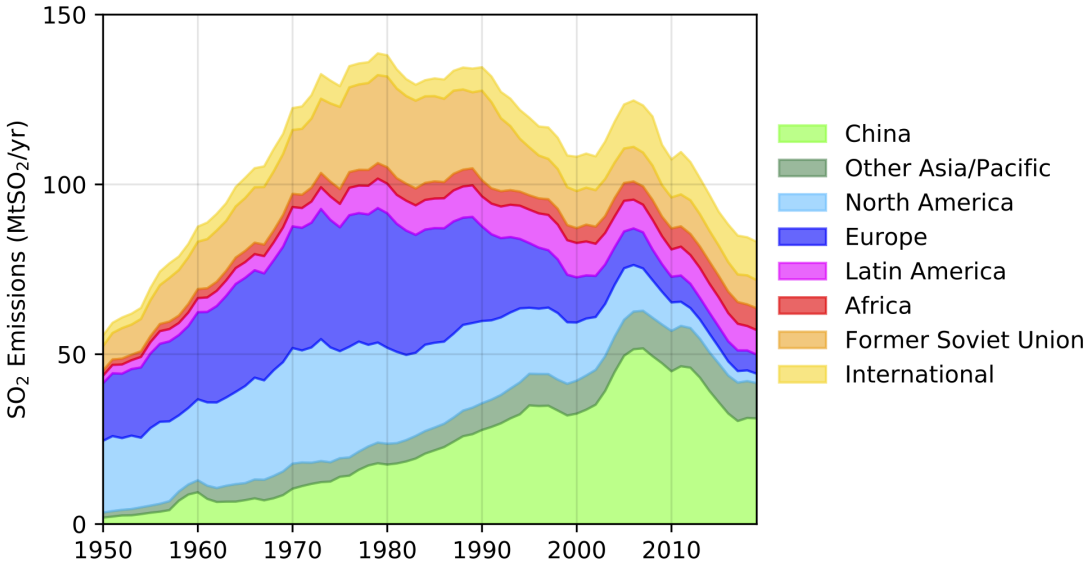

Figure 3.1: CEDS SO_2 emissions inventory showing global SO_2 emissions since 1960 (*63*). SO_2 emissions are coloured by region, such that global emissions are the sum of all stacked regions. International emissions category includes global shipping and aircraft emissions, since these are not aligned with any single territory.

by internal variability processes and other factors unrelated to anthropogenic forcing (e.g. the relative ENSO and PDO state, variability in sea surface temperatures and the rate of ocean heat uptake, and volcanic eruptions), meaning the underlying anthropogenic ERF trend changes can be obscured over short observational records. Even if the impact of internal variability were well understood and could be accounted for over the historical record, there remain uncertainties in the ERF timeseries used for an attribution procedure, due to upstream uncertainties in anthropogenic emissions accounting and because of uncertainties in the climate system's response to individual forcing agents. This problem is particularly prominent for aerosol ERF estimates, where quantifying the magnitude of aerosol-cloud interactions over the historical record remains challenging (*71*).

Earth-observing satellites provide a stream of real-time information which can be used to constrain the ERF trend. Since 2000, NASA's CERES (*168*) and MODIS (*203*) equipment has measured key climate system properties (e.g. AOD, SW and LW TOA fluxes, cloud optical properties; see details in table 1.3). Alongside these, ERF timeseries derived from partial radiative perturbation experiments in GCMs (see details in table 1.2) provide an estimate of the underlying anthropogenic contribution to global energy

imbalance. Together, these provide a novel constraint on global energy imbalance today, and thus the level and trend in components of ERF.

In the literature discussed in the introduction I highlighted two studies which use observations in this way: Raghuraman, Paynter, and Ramaswamy (2021) identifies a statistically-significant linear trend in the net TOA flux which cannot be explained by internal variability alone, but is explained once anthropogenic forcing is included (*174*); Kramer et al. (2021) uses radiative kernels to deconstruct CERES TOA fluxes (*168*) into forced contributions and temperature-mediated feedbacks, identifying the 20-year linear trend in net TOA flux which they attribute to the linear trend in greenhouse gas ERF (*97*). These studies provide direct observational evidence of the linear trend in anthropogenic ERF, attributing the positive trend to greenhouse gas emissions since 2000.

Isolating an aerosol contribution is more challenging. Kramer et al. (2021) finds the SW TOA flux record is largely controlled by temperature-mediated feedbacks and changes in cloud cover (similar to the discussion in Loeb *et al.* (2019)). Loeb et al. (2021) uses a partial radiative perturbation to decompose the observed TOA flux anomaly into contributions from meteorological conditions and external forcings. They determine that aerosol forcing has contributed very little to the overall trend in Earth's energy imbalance in CERES observations, with much greater influence from cloud cover variability and temperature-mediated feedbacks (*175*). However, all these studies only consider the 20-year linear trend in observations. Hence, they ignore the possibility that the *rate of anthropogenic warming* has changed since 2000, despite ERF datasets suggesting that the anthropogenic ERF trend was not constant over this interval.

In this chapter I analyse the direct observational evidence of an acceleration in ERF between 2000 and 2020. Section 3.2 explores contributions to the globally-averaged ERF trend presented in AR6's dataset, demonstrating that aerosols are the principal driver of a perceived acceleration in ERF since 2000. In section 3.3 these ERF trends are tested against three observational datasets which have near-global coverage over the last two decades: 1) the GMST anomaly, 2) the TOA radiative flux anomaly, and 3) AOD observations. Section 3.4 concludes and discusses options to generate an ERF ensemble which reflects recent observations of the global climate system.

3.2 Near-present ERF estimates

Forster *et al.* (2021) derives their best-estimate historical ERF shape based on simplified global relationships describing a pollutant's ERF as a function of its emissions or concentrations timeseries (*72*). These relationships are validated against GCM-derived ERFs, and appear robust over the range of policy-relevant emissions and concentrations inputs; more information on this approach is available in chapter 1, and, as an example, the expressions for aerosol ERF components are discussed in chapter 2. Using these simplified forcing expressions, the historical + Shared Socioeconomic Pathways (SSPs) emissions and/or concentration timeseries (used as inputs for historical + scenario projection experiments in CMIP6) can be re-expressed as ERF timeseries (*44*). These historical emissions timeseries are produced as a collaborative effort pulling on a number of emissions accounting projects (*61*, *63*, *204*). The SSPs sample a wide range of possible emissions trajectories between 2015 and 2100, including both narratives for underlying society over the 21st century (population growth rates, technological development rates, regional cooperation and trade etc.) and for the level of mitigation ambition. A brief overview of the SSPs is given in chapter 1, and further information can be found in Riahi *et al.* (2017) (*65*).

In figure 3.2 the historical+SSP2-45 net anthropogenic ERF timeseries (*44*) is plotted (black), along with contributions from CO2 (red), other well-mixed GHGs and minor contributors (blue) and aerosols (orange). Figure 3.2a plots the individual ERF component timeseries between 1850 and 2100, relative to a preindustrial baseline set in 1750. SSP2-45 is used beyond 2015 to approximate a 'current policies' future trajectory, as this approximately represents current ambition for CO_2 and other GHG emissions (SSP2-45 is also used to extend many historical experiments to 2100 in CMIP6 DECK simulations (*54*)). SSP2-45, SSP1-26 and SSP1-19 variants show similar reductions in aerosol emissions between 2015 and 2020, which approximately match the CEDS emissions timeseries in figure 3.1, while SSP3-70 delays mitigation until later in the 21st century (*205*). Panel c shows corresponding ERF trends for each component of ERF plotted in panel a, where the trend is calculated using a triangularly-weighted mean of rolling 10-year OLS linear regressions on the timeseries in panel a. Alternative

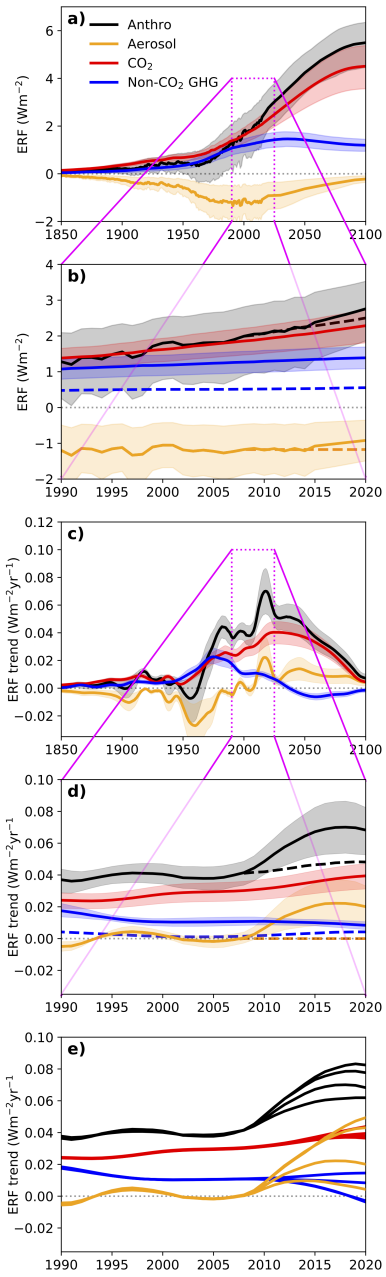

Figure 3.2: Globally averaged Effective Radiative Forcing (ERF) timeseries. Panel a shows the contributions from CO_2 (red), non-CO_2 GHGs and other minor contributors (blue), and aerosols (orange) to the total anthropogenic ERF timeseries (black). Panel c plots the contributions of each component to the total ERF trend, estimated with a triangularly weighted mean over 10-year linear gradients estimated with OLS regression. Best-estimate ERF is plotted with a solid line, and plumes show the 5-95th percentile range. Historical ERF estimates run to Dec. 2014; ERF is extended to 2100 using SSP2-45. Panels b and d show zoomed in versions of panels a and c, highlighting the period 1990-2020. Panel e shows the best-estimate trends of other SSP variants (SSP1-19, SSP1-26, SSP2-45 and SSP3-70). Dashed blue lines in panels b and d show the methane ERF level and trend in isolation. On the same panels, orange dashed lines show an alternative aerosol ERF scenario where the ERF trend remains zero after 2010. Black dashed lines show the corresponding anthropogenic ERF for this aerosol ERF scenario.

trend estimation methodologies yield similar results (see figure A.1 in appendix A). Panels b and d highlight the period 1990-2020 where near-global and near-continuous observational records exist. In the context of decadal global trends, this study ignores data beyond 2020, arguing it is anomalous due to the impact of COVID (the impact of COVID on emissions has been explored elsewhere e.g. Le Quéré *et al.* (2020) (*206*)).

The 5-95th percentile uncertainty range of each ERF component is shown with a shaded plume around the median ERF timeseries. Indiviudal ERF components uncertainties are taken from AR6 (*5*), and the anthropogenic ERF is calculated by summing independently sampled ERF components (assuming no correlation between individual forcing agents) to produce a 1000-member ERF ensemble. This methodology correlates the uncertainty in ERF levels (panel b) and trends (panel d), since the present-day uncertainty is sampled by rescaling a single best-estimate ERF shape over history. Consequently, extremes in a pollutant's present-day ERF level only arise for timeseries which also exhibit extreme trends over the near-present period, potentially under-sampling the range of plausible ERF trends.

Figure 3.2b shows that the majority of the historical ERF comes from CO_2, a well-mixed GHG for which we have a long observational record (*61*, *207*). The contribution from non-CO_2 GHGs in panel b is smaller, and over much of history approximately offsets a negative aerosol ERF. Most of the warming signal at present day is attributed to CO_2, but this could change rapidly in the future if non-CO_2 GHG forcing persists while aerosol forcing declines. This scenario is often overlooked in idealised mitigation scenarios, where mitigation takes place uniformly over many pollutants simultaneously, but may already be happening as nations put particulate emissions controls in place (*208*) with less clear action on CO_2 and other non-CO_2 pollutants.

Anthropogenic ERF has accelerated since 2000 (+0.4 W/m^2/decade in 2000-2009 to +0.6 W/m^2/decade in 2010-2019; black line in panel 3.2d). The acceleration is present in the full 5-95th percentile range plotted, meaning that SSP2-45's ERF ensemble assumes the rate at which humans are contributing to global warming is increasing. The extent of this acceleration is shown in black in figure 3.3 over the two decades 2000-2020. SSP2-45's trend is around +0.25 W/m^2/decade higher in the second

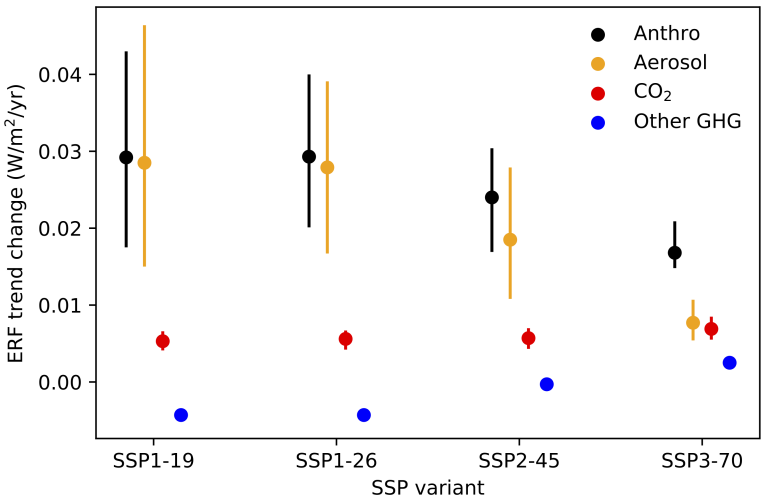

Figure 3.3: The ERF decadal trend change is driven by aerosol trends. Trend change between (2000-2010) and (2010-2020) in each SSP variant plotted in figure 3.2e. The decadal trend changes between 2000 and 2020 are calculated using the average gradient in each decade, as calculated in figure 3.2d, with each component's gradient change shown for each SSP variant (red = CO_2; blue = non-CO_2 GHGs; orange = aerosols; black = total).

decade (2010-2019) compared to the first decade (2000-2009) — a substantial increase compared to historical anthropogenic ERF trends. Further, the driver for this trend increase is unusual compared to the historical drivers of ERF trends. In the 20th century the predominant cause of an increasing anthropogenic ERF trend has been the rise in annual CO_2 emissions. Figure 3.2 suggests that since 2000 the predominant cause of the acceleration is aerosols, driven by a peak and decline in the (negative) aerosol ERF (see the aerosol ERF shape in figure 3.2a). CH_4 ERF contributes little to the anthropogenic ERF trend change: the dashed blue line in panels b and d shows that the CH_4 ERF trend rose from +0.49 to +0.54 W/m^2 between 2000 and 2020 (*44*). Recent revisions to the Global Carbon Budget (*61*) also suggest that CO_2 emissions have been stable, not increasing, since 2010, meaning that the CO_2-induced ERF trend is approximately constant since 2010 as well. SSP2-45's +0.19 W/m^2/decade increase in aerosol ERF trend between 2000-2009 and 2010-2019 accounts for the majority of the anthropogenic ERF trend change in figure 3.2.

The accelerating anthropogenic ERF is not a unique feature of the SSP2-45 scenario either. SSP1-26 and SSP1-19 suggest aerosols are the cause of anthropogenic ERF acceleration since 2000, while SSP3-70 (with delayed aerosol mitigation) has a smaller

trend change. Figure 3.2e and 3.3 show how the choice of SSP variant beyond 2014 changes the relative size of the anthropogenic ERF trend change, and the contribution from aerosols to this trend change. The aerosol ERF trend covers a range from +0.05 to +0.45 W/m^2/decade in 2020 depending on the chosen scenario's ambition after 2014, despite all the scenario's trends being identical and near-zero in 2010. In SSP1-19 (a 1.5°C-compatible mitigation scenario) there is a much greater aerosol ERF trend change than in the less ambitious SSP2-45 scenario (+0.29 W/m^2/decade, compared to +0.19 W/m^2/decade). This is expected given the higher ambition policy SSP1-19 represents, achieving net zero CO_2 emissions around 2050 along with rapid aerosol and non-CO_2 GHG emissions reductions.

3.3 Observations as a constraint on aerosol forcing assumptions

Justification for the shapes of figure 3.2's ERFs are usually provided using emissions datasets. Figure 3.1 shows the CEDS SO_2 emissions dataset, with these chosen as SO_2 emissions, becoming SO_4^{2-} aerosols in the atmosphere, are the largest contributor to aerosol ERF today (*152*). In the figure SO_2 emissions peaked in 2005, while CO_2, CH_4 and N_2O concentrations have remained stable or continued to increase (*207*). With these emissions reductions, aerosol ERF trends become positive after 2010, leading to the substantial change in the overall anthropogenic ERF trend.

But what if figure 3.2's ERF trends are wrong? While global anthropogenic aerosol emissions are reported to be in decline since 2005 as a result of emissions reductions in South-East Asia, the spatial pattern of aerosol emissions has also redistributed towards the tropics from the northern hemisphere mid-latitudes over this period. This redistribution may influence cloud properties over the tropical pacific (*209*), with some research suggesting a greater response for aerosol ERF perturbations over the South-East Asian region compared to similar perturbations over other northern hemisphere mid-latitude regions (*210*), which may offset the ERF change expected following a reduction in anthropogenic aerosol emissions. A further concern is the impact of reporting biases and estimation errors in bottom-up emissions estimates, such as those produced by

CEDS, biasing ERF estimates produced with these global emissions timeseries. South-East Asian sulphate emissions may have been under-reported over the late 20th century, while since 2000 the surface dimming/brightening trends in the region are remarkably stable compared to corresponding emissions estimates (*154*).

Hence, there is reason to be cautious of figure 3.2's proposed ERF trend changes since 2000. To explore which ERF trends are representative of observed changes in the Earth system over the last two decades, below I use global surface temperature anomalies, TOA radiative flux anomalies, and AODs to derive observational constraints on the recent ERF trend change, focusing on the attribution of the aerosol contribution since 2000. Because the climate system is already in disequilibrium in 2000, downstream observables will be influenced both by variations in our present-day inputs (i.e. aerosol loading, GHG concentrations, internal variability), and the pre-2000 perturbation's influence on unforced variability. I compare the observed climate system's response since 2000 to modelled responses using the SSP2-45 ERF scenario shown in figure 3.2, and other scenarios with alternative aerosol ERF assumptions: SSP3-70, and a variant of SSP2-45 where no aerosol ERF trend change occurs (the 'no aerosol trend change' scenario shown with dashed orange and black lines in figure 3.2).

3.3.1 The global temperature anomaly

The first observation I investigate to determine confidence in figure 3.2's ERF trends is the GMST anomaly. The global mean surface temperature is defined using an average over several GMST products, following the approach of IPCC's SR1.5 (*16*). I consider four in-situ datasets which use statistical infilling to produce near-global coverage: HadCRUT5 (*43*), NOAA (*177*), Berkeley Earth (*167*) and GISTEMP (*211*). Although this means that datasets produced with different infilling approaches, data coverage and time periods are mixed, it is unlikely this will significantly skew results since differences between these datasets are much smaller than the assumed uncertainty within any single dataset (*16*).

Figure 3.4 shows the multi-dataset observed GMST anomaly (black scatterpoints), with warming contributions from natural (blue) and anthropogenic (black) ERFs plotted on top. The temperature attribution follows the Haustein *et al.* (2017) methodology

(*15*), as discussed in chapter 1. The FaIRv2.0 (*29*) model derives an ensemble of globally-averaged temperature responses using figure 3.2's anthropogenic and natural ERF timeseries as inputs. Physical response uncertainty is sampled by repeating the forced temperature response calculation with 20 different response parameter configurations, sampling the AR6 likely range of ECS (2.5-4.0 °C), TCR (1.4-2.2 °C), and thermal response timescales (d_1 = 1-10 yrs, d_2 = 100-800 yrs) as in refs. (*15*, *42*). Hence, each natural and anthropogenic forcing pair in the ensemble plotted in figure 3.2 corresponds to 20 temperature response pairs. The derived temperature response pairs are regressed onto the GMST anomaly as in equation 1.2, additionally sampling observational uncertainty (200-member ensemble (*43*)) and natural variability (102-member ensemble CMIP6 PIControl runs (*36*)) in the GMST timeseries. In total each forcing pair produces around 400,000 temperature response pairs, which are sampled to find the median and 5-95th percentile range temperature response attributable to the natural and anthropogenic ERFs for the figures.

The anthropogenic warming plume tracks the GMST anomaly over the historical record in panel a, confirming that the anthropogenic ERF changes are indeed responsible for the majority of observed warming to date (*16*). AGW reaches 1.04 °C averaged over the decade 2010-2019 (0.98-1.10 °C for 5-95th percentile range; re-baselined to the IPCC's near-term baseline of 0.85 °C in 2006-2015 above 1850-1900 levels (*16*)), consistent with the attribution studies discussed in chapter 1. Natural ERFs contribute very little to the multi-decade warming, with the only significant contributions visible following major volcanic eruptions.

The trend in GMST anomaly is plotted against attributed warming trends on panel b. The wider historical period correlates well with the AGW signal, with the GMST trend broadly reproduced by the anthropogenic warming trend in figure 3.4b. However, the anthropogenic contribution is not a perfect explanation of GMST trends. Over decade-long intervals the GMST trend can vary substantially away from the multi-decade mean, for example in the early-20th century with departures of around ±0.1-0.2 °C/decade away from the underlying anthropogenic warming trend. These deviations are typically explained as evidence of early Arctic warming or other exceptional

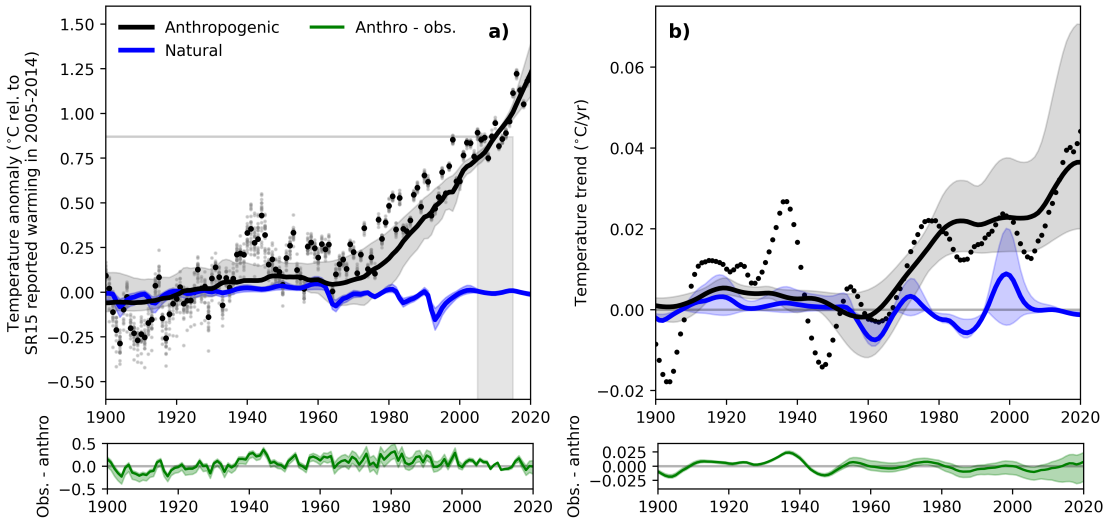

Figure 3.4: The level and rate of anthropogenic warming between 1900-2020. Panel a uses the methodology of Haustein et al. (2017) along with radiative forcing estimates from figure 3.2 to estimate the level of anthropogenic warming (black) compared to natural forcing (blue). Panel b plots the corresponding trend for each contribution to the global temperature anomaly. Plumes show the 5-95th percentile uncertainty range. Observed temperatures from a 4-dataset mean are plotted in black points (with individual ensemble uncertainty shown in grey); the level of warming is baselined to the SR1.5 reported warming over the period 2006-2015 inclusive (grey region in panel a). Green lines below each panel show the difference between the observed monthly temperature anomaly and anthropogenic temperature anomaly.

events tied to internal variability (*212*), along with the impact of reduced regional coverage of observations at that time.

Since 2000, the GMST record has again exhibited a trend substantially above the multi-decade warming rate, with the GMST trend averaging +0.18 °C/decade between 1980-2009, but reaching +0.35 °C/decade between 2010-2019. Internal variability (principally trends in cloudiness and SSTs in the tropical pacific) and anthropogenic forcing have both been suggested as possible explanations for this trend change (*173*). The largest internal variability contribution comes from ENSO over this two decade interval. Figure 3.6 shows the Niño3 index timeseries (*119*), a measure of ENSO variability, with a particularly strong El Niño event in 2015/16. It also shows PDO variability, which exhibits a general shift from negative-to-positive. Both these signals could play a role in explaining recent GMST trends (*3*).

Despite these potential contributions, the attribution in figure 3.4b determines anthropogenic forcing is the majority cause of recent GMST trends (black plume tracks

the black scatterpoints). The anthropogenic warming trend rises from +0.21 (+0.13 to +0.35) °C/decade between 2000-2009, to around +0.33 (+0.20 to +0.56) °C/decade between 2010-2019 (brackets show the 5-95th percentile range) — a 65% increase in the best-estimate anthropogenic warming rate. As was noted for the stylised scenario in figure 1.1, this highlights an issue with the standard Haustein attribution methodology: the methodology fails to account for internal variability which co-varies with a regressors shape. In this case the anthropogenic ERF and internal variability signals both contain a substantial trend change between 2000 and 2020 (see figures 3.2 and 3.6), but the attribution only considers the warming shapes in response to externally-applied forcings, and thus does not include internal variability as a regressor. Hence, the OLS regression determines that the anthropogenic ERF acceleration must be the cause of the recent GMST trend change, in the absence of an alternative explanation in the blue natural ERF timeseries.

3.3.1.1 Separating the aerosol and GHG contributions

Fortunately, although an internal variability signal is not explicitly regressed against GMST in Haustein's methodology, the residual in figure 3.4 provides additional information. If the anthropogenic and natural ERFs were a perfect description of the external forcing which is driving global temperature change, the residual between the GMST and the attributed AGW would only contain internal variability, and hence should be unbiased over a multi-decade interval. Considering figure 3.4, while in panel a the broad characteristics the GMST anomaly behaviour are reproduced, the residual remains positive throughout the second half of the 20th century. This bias bears the characteristics of overly strong aerosol forcing also found in some CMIP6 GCMs (e.g. refs. (*49*, *50*)). In these models anthropogenic warming is held artificially low until the mid-20th century when aerosol forcing peaks, and then accelerates more rapidly than observed GMST after 1980 as the overly negative aerosol forcing declines, potentially exaggerating the aerosol warming trend contribution since 2000. This implies that the aerosol ERF in figure 3.2 is too large.

Alternatively, it is possible that figure 3.4's residual is explained by a combination of changes in ocean heat uptake and other variability to the net feedback parameter

since the late-20th century. These explanations are less plausible: Zanna *et al.* (2019) does not observe a significant change in the rate of ocean heat uptake between the mid-20th century and present day (*213*), while internal variability is unlikely to bias the net feedback consistently low over a multi-decade interval. Other forced changes to the net feedback parameter, for example resulting from variation to global cloud radiative properties following a change in aerosol emissions, could contribute a low bias, particularly since 2000 when aerosol emissions have declined rapidly. This possibility requires further research (*161*, *162*).

Assuming these alternative explanations are not sufficient, the AGW attribution in figure 3.4 therefore suggests that the anthropogenic ERF shape does not contain the correct relative contribution from aerosols and GHGs. This possibility has been noted by others, including both warming attributions using CMIP6 model outputs (*17*) and using FaIR (*73*). To investigate this further, the attribution procedure can be repeated using a three-way regression, where the aerosol warming is rescaled separately to the GHG and natural warming. The attribution procedure is otherwise identical to the two-way attribution shown in figure 3.4.

The aerosol (orange), GHG (red), total anthropogenic (aerosol + GHG; black) and natural (blue) contributions to the GMST anomaly are shown in figure 3.5, with panel a showing the warming level and panel b the warming trend. Aerosol cooling lies around -0.35 °C (-0.20 to -0.65 °C) between 2010-2019, relative to 1850-1900. GHG warming is 1.50 °C (1.35-1.70 °C) between 2010-2019. Therefore, anthropogenic warming overall is 1.09 °C (1.00-1.30 °C) between 2010-2019, again consistent with the recent warming attribution studies discussed in table 1.1. The aerosol-induced warming is notably smaller than is suggested in AR6's best-estimate (*5*) since the aerosol forcing is downscaled, but it is consistent with other energy-balance-constrained warming attribution studies (e.g. refs. (*17*, *73*)).

Considering the residual of this three-way attribution, figure 3.5a appears to offer a better explanation of the aerosol, GHG and natural forced contributions to GMST over history. The aerosol warming is scaled down substantially (the best-estimate aerosol scaling factor is 0.62), while the GHG warming contribution remains closer to its

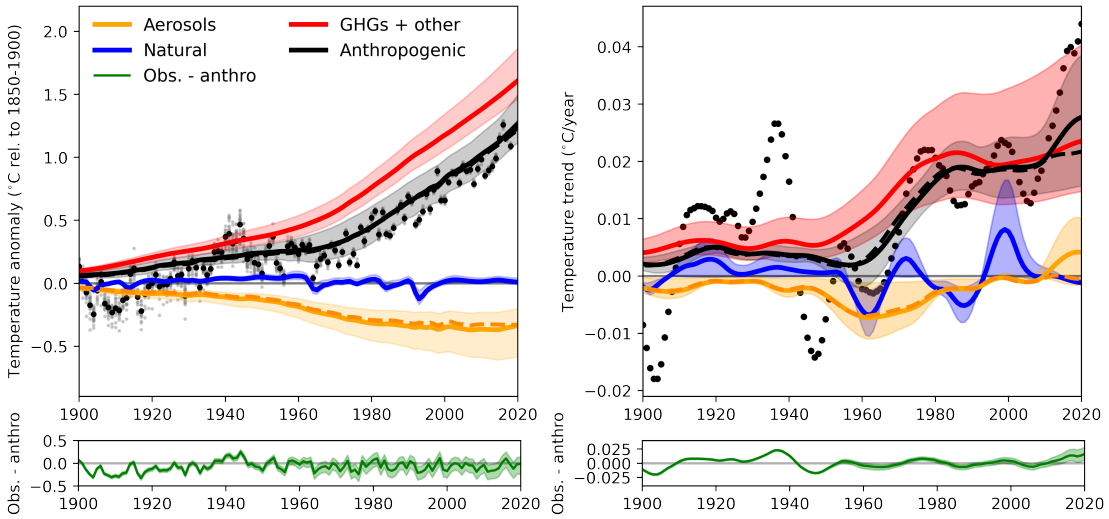

Figure 3.5: A three-way attribution of aerosols, greenhouse gases and natural ERF contributions onto GMST observations. The level and rate of anthropogenic warming between 1900-2020. Panel a again plots the level of human-induced warming using the methodology of Haustein *et al.* (2017), while panel b plots the warming trend for each contribution. Observed GMST from a 4-dataset mean are plotted in black (with individual ensemble uncertainty shown in grey). In both panels the orange line corresponds to the attributed aerosol contribution to global temperatures, blue shows the natural contribution, and red shows the GHG contribution; the black plume shows the total anthropogenic contribution. Plumes show the 5-95th percentile uncertainty range. Green lines below each panel show the difference between attributed anthropogenic warming and the observed GMST anomaly. Orange and black dashed lines show the alternative attribution result if the dashed zero-trend aerosol ERF scenario from figure 3.2 is used in the attribution instead.

original value in figure 3.4 (the best-estimate GHG scaling factor is 0.90). Downscaling the relative aerosol contribution like this has removed the bias in figure 3.5's AGW response, suggesting that the aerosol ERF was indeed too large in the anthropogenic ERF timeseries used in figure 3.5. Distributions of the scaling factors for aerosol, GHG and natural warming are shown in figure A.2 in appendix A. The aerosol and GHG scaling factors are correlated, as is expected given the energy-budget constraints set by GMST observations: a large negative aerosol ERF estimate must correspond to a large positive GHG ERF estimate in order to balance the historical energy budget. The level and rate of present-day anthropogenic warming are also somewhat correlated (figure A.3), with some of this likely arising from the ERF sampling methodology correlating ERF level with ERF trend, as was discussed in section 3.2.

3.3.1.2 Warming trends post-2000

Having established a three-way attribution produces a less-biased fit to the GMST record than a two-way attribution, and it does so by down-scaling the aerosol contribution, I now ask how this alters the assessed anthropogenic warming trend since 2000.

In figure 3.5, GMST trends rise from +0.18 °C/decade to +0.35 °C/decade between the first and second decade post-2000. The anthropogenic warming trend increases from +0.19 (0.14-0.24) °C/decade in 2000-2009 to +0.24 (0.15-0.32) °C/decade in 2010-2019. Aerosol-induced warming trends contribute the majority of this anthropogenic warming acceleration, increasing from +0.00 (-0.01 to 0.00) °C/decade in 2000-2009 to +0.03 (0.00 to +0.07) °C/decade.

Hence, although anthropogenic ERFs still cause a warming acceleration in figure 3.5b, the attribution determines substantially less of the post-2000 GMST trend change arises from anthropogenic origins. While figure 3.4's anthropogenic contribution explains more than 80% of the GMST acceleration since 2000, figure 3.5b only explains around 50% (5-95th percentile range is approximately 0 to 100%), with the remainder being attributed to natural variability. A small number of ensemble members do continue to attribute the full GMST trend change to an anthropogenic ERF trend change, although substantially less of the distribution considers this a plausible explanation compared to figure 3.4b, where much higher 2010-2019 anthropogenic warming trends were possible.

Reducing the aerosol ERF by around 40% in figure 3.5 results in a better fit to the GMST behaviour over the historical record as a whole. Figures 3.4 and 3.5 are trading-off using aerosol forcing to explain the post-2000 GMST behaviour (i.e. including a larger aerosol ERF trend change) vs. using aerosol forcing to explain mid-20th century GMST behaviour (i.e. including a smaller aerosol ERF trend change). Rescaling the aerosol warming to fit mid-20th century GMST, as in figure 3.5, automatically reduces the aerosol contribution to early 21st century GMST trends, since each component's ERF level correlates with its ERF trend.

In determining which of figures 3.4 and 3.5 better reflect historical aerosol contribution, we must weigh up the extent to which mid-20th century GMST provides relevant

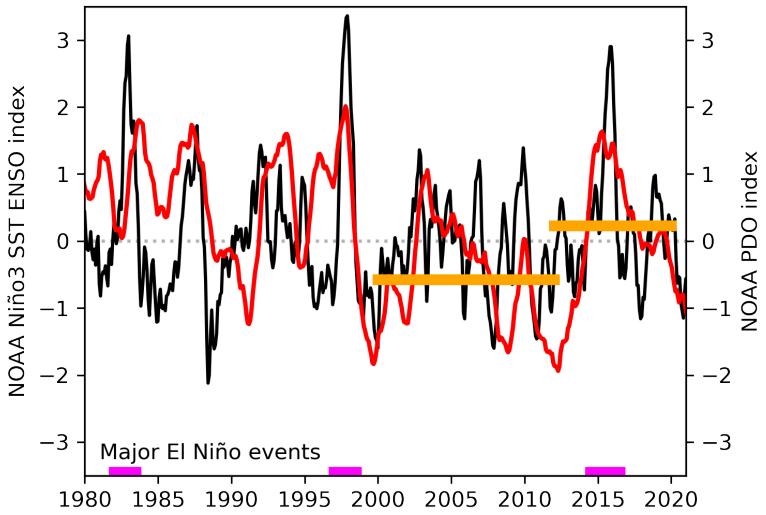

Figure 3.6: Timeseries of the relative ENSO state over the tropical pacific (black) from NOAA's Niño3 record (*119*). Significant positive El Niño events are highlighted with pink regions along the x-axis (defined as having a Niño3.0 index above 2.0). Timeseries of PDO state (*214*) (red) tracks significant deviations in the ENSO record, and has a lower mean value through the period of 'paused' global warming (2000-2012; -0.51), than afterwards (2012-2020; +0.22), marked with orange bar.

information for constraining the aerosol warming trend post-2000, particularly given mid-century forcing assessments are supported with substantially less observational evidence. For example, using aerosol ERF with zero-trend-change since 2000 (dashed lines in figure 3.2) to attribute warming contributions in figure 3.5 causes no substantial change in the quality of fit to GMSTs over the 20th century, suggesting it is an acceptable explanation for historical GMST behaviour, but substantially reduces the anthropogenic warming trend change since 2000 (orange and black dashed lines in figure 3.5). Conversely, ignoring the mid-20th century constraint entirely, figure 3.2's range of aerosol ERF trends support a wider range of hypotheses, including aerosol trends entirely explaining GMST post-2000, or much of the trend change arising in response to internal variability alone.

Clearly, internal variability plays an important role in determining the trend over decadal and shorter timescales — the residuals in figures 3.4b and 3.5b both show departures of around $\pm$0.1-0.2 °C/decade away from the anthropogenic decadal warming trend in the early-20th century (*212*), and in figure 3.5b 50% of the recent GMST trend change is again left unattributed to an external forcing source, suggesting an

important role of ENSO and PDO variability here (see figure 3.6, with the particularly strong El Niño event in 2015/16 highlighted) (*173*).

In summary, GMST observations have accelerated since 2000 (*215*), with around 80% of this change attributed to aerosol ERF trend changes if the attribution uses the bulk anthropogenic ERF shape from figure 3.2. However, this anthropogenic ERF shape may not be the best description of the energy imbalance contributing to historical GMSTs; in particular biasing the aerosol ERF negative causes the mid-20th century anthropogenic warming to be too low in figure 3.4. To correct for this, in figure 3.5 the aerosol and GHG contributions are separately attributed to the GMST anomaly. Figure 3.5 suggests around 50% of the post-2000 GMST acceleration is attributable to the anthropogenic ERF trend change (+0.05 °C/decade between 2000-2009 and 2010-2019; +0.03 °C/decade of which is due to aerosols and +0.02 °C/decade of which is due to GHGs). The remaining 50% of the GMST acceleration is attributed to unforced internal variability. This three-way attribution better fits the historical GMST anomaly compared to figure 3.4. The uncertainty on the anthropogenic warming rate estimates in both figures 3.4 and 3.5 is substantial. If the attribution focuses solely on determining the cause of the GMST trend increase since 2000 there is greater freedom, including both the recent acceleration originating from anthropogenic ERF trends in isolation, or from internal variability in isolation.

3.3.2 TOA radiative fluxes

Further assessing the extent of internal variability's influence on recent GMST requires separating these contributions from those arising from external forcing, or from temperature-mediated feedbacks. Studying the TOA flux trends in combination with GMST trends provides one means to separate these terms, following an energy balance framework like equation 3.1.

Figure 3.7 plots radiative flux anomalies from Earth observations since 2000, and from various simulations of the recent historical period using GCMs. All anomalies are calculated by removing the average seasonal cycle, defined as the mean monthly TOA flux value for the 20-year record. Additionally, all panels assume that a positive

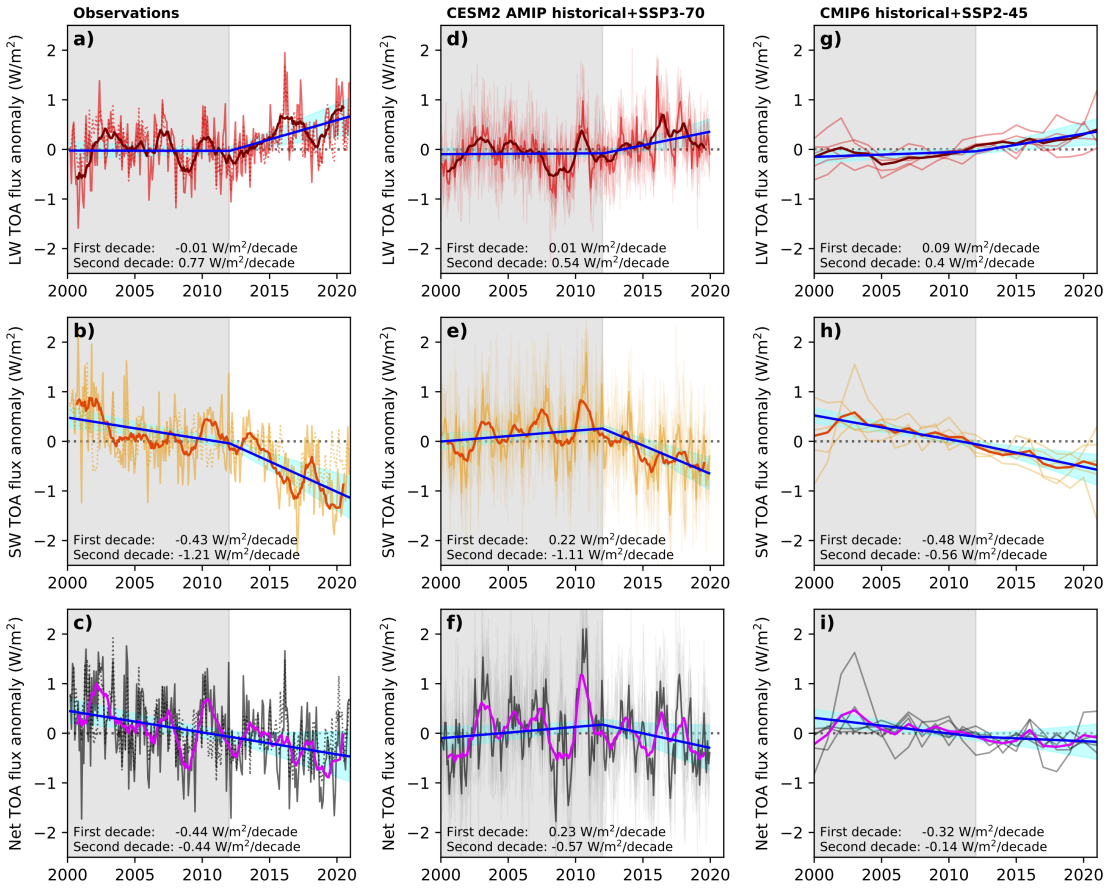

Figure 3.7: Comparing radiative flux anomalies in observations and GCMs. The left column plots TOA radiative flux anomalies from CERES EBAFv4.1 satellite observations product; the middle column plots a 10-member ensemble of CESM2 atmosphere-only (AMIP) runs with externally imposed SSTs; the right column shows the ensemble mean TOA flux anomaly from five CMIP6 models. The top row shows the LW flux anomaly (red), the middle row shows the SW flux anomaly (orange), and the bottom row shows the net flux anomaly (black). 12-month running means are shown in with a thick line over each timeseries, along with a decadal trend (blue plume). GLS regression estimates the decadal linear trends, assuming an AR(1) process in the residuals. Resulting decadal trend estimates are noted in the bottom left of each panel. CMIP6 TOA flux anomalies in the right column are found using a multi-model mean over individual TOA flux anomalies in historical+SSP2-45 experiments. 2000-2012 is shaded grey to denote the 'pause in global warming' period.

TOA flux anomaly is oriented radially outward from the Earth's surface, corresponding to radiative cooling, and thus negative anomalies correspond to additional heat being retained in the Earth system. The left column plots the observed globally-averaged outgoing flux anomaly recorded by the CERES EBAF4.1 product (*168*) between 2000 and 2020. Panel a shows the LW TOA flux anomaly in red, panel b the SW TOA flux anomaly in orange, and panel c net TOA flux anomaly in black; and in all panels dotted lines refer to clear sky anomalies, and solid lines to all sky anomalies. On all panels a shaded region (2000-2012) highlights the period commonly considered to exhibit the so-called 'pause in global warming' (*216*).

The middle column of figure 3.7 shows prescribed-SST atmosphere-only simulations with the CESM2 model (*90*) forced with historical+SSP3-70 concentrations and emissions precursors. Here, SST and sea-ice coverage from reanalysis products (*217*, *218*) drive the CAM6 atmospheric model between 2000-2020, while boundary conditions mimic observed SST variability over the past two decades. Hence, the decadal trends in timeseries shown on the central column of figure 3.7 contain realisations of the internal variability signal in observations driven by the underlying SSTs (assuming the cloud cover variability is largely driven by the SST boundary conditions (*173*)).

The right column shows an ensemble of coupled atmosphere-ocean simulations forced with historical+SSP2-45 concentrations and emissions precursors, following the RFMIP hist-all experiment protocol (*54*). The LW, SW and net TOA flux anomaly is calculated using runs of the historical+SSP2-45 experiment with five CMIP6 models for which I have corresponding ERF timeseries from RFMIP (*54*) (CanESM5, HadGEM3-GC31-LL, IPSL-CM6A-LR, GISS-E2-1-G and NorESM2-LM); the multi-model-mean flux anomaly is shown with a thick line in each panel, with individual models shown with thin lines. The historical+SSP2-45 experiment uses a coupled atmosphere-ocean setup, meaning the natural variability over the 20-year period is randomised for each model run. Plotting the ensemble average over each model (as is shown in the righthand column's panels) averages out the impact of historical unforced SST and cloud cover variability, isolating the model's response to external forcing changes. Hence the middle and right-hand

columns explore scenarios which have removed the externally-applied ERF trend change and internal variability contributions to TOA flux trend behaviour, respectively.

Across all panels in figure 3.7 the blue trend lines are fit to the flux anomalies to estimate the decadal linear trends using a generalised least squares (GLS) regression. This fit uses a fixed breakpoint piecewise linear regression combining three components: a constant term, a constant gradient line, and a split trend line (in 2012), and assumes auto-correlated residuals using an AR(1) process. The shaded uncertainty range on the linear fit is found using a 10,000-member ensemble produced by resampling the GLS fit parameter distributions. The uncertainty ranges show the 5-95th percentile range, with the central blue line showing the best-estimate fit.

3.3.2.1 The net TOA flux anomaly

The bottom row of figure 3.7 shows the net TOA flux anomaly. The observed net flux anomaly in figure 3.7c has a negative trend (-0.44 ($\pm$0.20) W/m^2/decade), which remains approximately constant over the two-decade interval. Since the net TOA flux anomaly relates approximately to the ocean heat uptake (ignoring small contributions from sea ice, land and atmospheric heat uptake), this supports Zanna *et al.* (2019)'s suggestion that the rate of ocean heat uptake has been steady since 2000 (*213*).

Compare this with the net TOA flux trends produced over the same 20-year interval in a prescribed-SST historical+SSP3-70 experiment using the CESM2 model (figure 3.7f), and with an ensemble of coupled-atmosphere-ocean models using historical+SSP2-45 forcing (figure 3.7i). These two experiments are chosen since they allow us to separate the key drivers of trends which were identified above: internal variability and aerosol forcing. The prescribed-SST historical+SSP3-70 experiment has minimal trend change induced by a change in aerosol emissions, since SSP3-70 has the smallest aerosol ERF trend change of the assessed SSPs (see figure 3.3), but does capture internal variability in the CERES record caused by the time-varying SST boundary conditions. On the other hand, the right column's CMIP6 simulations remove the trend variability arising due to SST boundary conditions over the 20-year period by averaging over an ensemble of coupled atmosphere-ocean simulations, but do include the aerosol ERF trends.

In figure 3.7, the decadal flux trends are larger for the observations (panel c), and for the atmosphere-only prescribed-SST experiments (panel f), than for the coupled-model ensemble (panel i). This is consistent with the notion that the net feedback parameter is biased by short-term variability processes (*74*). Clearly, the prescribed-SST experiment in panel f cannot perfectly reproduce observations (particularly noting the trend with the opposite sign identified in the first decade), although the key scale and locations of variability is captured more successfully (e.g. high TOA flux peak in 2010/11) and the experiment appears to approximately reproduce the behaviour of the net TOA flux anomaly (comparing the pink lines in panels c and f). The trend change in panel i (-0.2 W/m^2/decade between the first and second decade) describes the impact of the anthropogenic ERF trends on net TOA flux trends in isolation — substantially smaller than the variability contribution in panel f. The sum of responses in panels f and i approximately reproduces the observed net flux anomaly in panel c, as expected.

To determine if the trends identified in panels c, f and i are consistent with the anthropogenic forcing timeseries in figure 3.2 we can regress the forcing-adjusted TOA flux anomaly (F-N in equation 3.1, along with an additional stratospheric aerosol RF timeseries from GloSSACv2 (*219*)) against GMST. The gradient of this fit is an estimate of the net feedback parameter, which we can compare across the experiments and with alternative observational constraints to infer the influence of internal variability on the TOA flux record in the past two decades. The regression is bootstrapped to estimate uncertainty ranges following Dessler and Forster (2018)'s approach (sub-sampling the 20-year TOA flux anomaly record with replacement to account for correlation between datapoints) (*74*). Panel i's ensemble-mean net feedback parameter is +1.1 $W/m^2/°C$, consistent with the estimated feedback strength in 4xCO_2 experiments (*81*).

Estimating the net feedback parameter in this way using observations can introduce a bias because short-term internal variability influences the TOA flux anomaly trend (*74*), meaning the feedback parameter may not reflect the true value of the multi-century equilibrium climate sensitivity. An unbiased estimate of the net feedback strength over a short observational record using a total least squares regression would require an external estimate of the total variance in GMST and TOA flux observations, including partitioning

between the various sources of variability. This partitioning is extremely challenging to characterize over the historical record, with a poor understanding of drivers of the variability in surface- and deep-ocean heat uptake, and of key temperature-mediated feedbacks (such as cloud cover variability over the tropical pacific).

Despite this, many groups have attempted to estimate the net feedback parameter using short observational records with some success (*82*, *172*). Similarities between their results and the expected multi-century feedback parameter likely stem from fortuitous cancellations in the key internal variability signals over the first decade of CERES observations (see ENSO and PDO values between 2000-2010 in figure 3.6). This is not the case over the full period 2000-2020, which includes a strong El Niño event in 2015/16 and a negative-to-positive PDO shift.

I estimate the net feedback parameter for observations in panel c, λ_{net}, finding $\lambda_{net} = +0.74\ (\pm 0.34)\,W/m^2/°C$. This net feedback parameter estimate is likely biased low by short-term natural variability: $\lambda_{net} = +1.2\,W/m^2/°C$ produces an ECS around 3 °C, the best-estimate value in AR6 (*5*), assuming $F_{2\times}$, the forcing resulting to doubling CO_2 concentrations, is $3.74\,W/m^2$. Sherwood et al.'s recent reassessment of the ECS still includes substantial uncertainty ($\lambda_{net} = +1.3\ (\pm 0.44)\,W/m^2/°C$, with $F_{2\times} = +4.00\ (\pm 0.30)\,W/m^2$) (*151*). We can adjust our λ_{net} estimate using the mean CMIP5 relationship between decadal and multi-century feedback parameters, following Dessler and Forster (2018), to attempt to account for this bias. This finds a best-estimate $\lambda_{net} = +0.92\,W/m^2/°C$, which corresponds to an ECS around 4°C, in the upper half of the uncertainty range in the AR6, but consistent with other observationally constrained studies (*74*, *82*, *172*).

Another option to account for the variability signal uses a joint regression of NOAA's Niño3 index, PDO index (*199*) and surface temperature anomalies onto forcing-adjusted fluxes, with the aim of identifying the ENSO and PDO variability contributions to the feedback parameter. This finds $\lambda_{net} = +0.85\ (\pm 0.44)\,W/m^2/°C$, shifting in the correct direction but remaining lower than the multi-century feedback strength (similar to the CMIP5-adjusted response above). This joint regression approach finds relatively weak correlation between ENSO or PDO and the net flux anomaly, despite the impact of

ENSO on tropical pacific cloud cover being highlighted as a key driver of net TOA flux variability (*173*). This failure to correlate ENSO or PDO variability with the net flux trend change likely arises due to the large variability in figure 3.7c, which dominates over the scale of the ENSO/PDO trends, along with the fact that SST variability itself correlates well with the ENSO record over these intervals (*175*). This demonstrates the challenge in determining the partitioning of variances contributing the observed TOA flux anomaly, and means that the quality of feedback parameter fits do not in-and-of-themselves represent evidence supporting or refuting recent ERF trends.

3.3.2.2 Separating the SW and LW contributions

Additional insight can be gained by separating the TOA flux anomaly into SW and LW contributions, plotted in figures 3.7a and b. As with the net TOA flux record in panel c, the influence of internal variability on the measured LW and SW feedback parameters is used to gain an understanding of the likely contribution to trends in the LW and SW records over the last two decades. I expect the SW component trends to be a key indicator of the aerosol contribution, since aerosols principally interact with SW radiation both directly and through aerosol-cloud interactions.

Over the first decade (2000-2010), the LW flux anomaly exhibits a near-zero trend (0.0 ($\pm$0.1) W/m^2/decade), with the weak positive GMST trend and a steadily increasing LW ERF (principally from the ongoing CO_2 emissions radiative contribution; see figure 3.2). Over the second decade (2010-2020) the LW flux anomaly trend is positive (+0.9 ($\pm$0.2) W/m^2/decade), with continuing GHG ERF trends combining with a strong positive GMST trend.

A subset of the CERES dataset excluding particularly strong El Niño events (defined as having a Niño3 index greater than 2.0, highlighted in figure 3.6) produces a LW feedback parameter characteristic of the multi-decade 'noise-free' response ($\lambda_{LW,masked}$ = +2.2 ($\pm$0.3) W/m^2/°C), in agreement with Donohoe *et al.* (2014) who estimate the LW feedback parameter using CERES data up to Dec. 2013 (Donohoe's feedback parameter estimates use a period of CERES observations absent in major swings in ENSO and PDO variability, hence the estimates are generally more consistent with expected

multi-century values than those calculated over periods including the 2015/16 El Niño event) (*82*). A slightly larger feedback parameter is obtained if all data is included (λ_{LW} = +2.3 ($\pm$0.2) W/m^2/°C). Both of these estimates are consistent with previous efforts to deduce the LW feedback parameter using observations, but are slightly larger than those found using GCMs running a 4xCO_2 experiment (λ_{LW} = +1.8 ($\pm$0.5) W/m^2/°C) (*81*), or using the mean coupled-model response in panel g (λ_{LW} = +1.9 W/m^2/°C).

The observed SW flux anomaly has a similarly large trend change between the first and second decades in panel b, but in the opposite direction to the LW response (from -0.4 ($\pm$0.2) W/m^2/decade between 2000-2010 to -1.2 ($\pm$0.3) W/m^2/decade between 2010-2020). Estimates of the SW feedback parameter are more uncertain than their LW equivalent, principally due to a continued poor knowledge of how cloud-aerosol interactions vary under changing aerosol emissions pattern and under a changing background climate state (*5*).

Uncertainty in the measurement of the SW feedback is further confounded when combined with the co-varying natural variability signals in figure 3.7b. Since 2000, the PDO and ENSO have driven much of the variability in tropical cloud cover (*173*), key to the resulting SW flux trends (*175*). Observed reductions in sea ice cover (*220*) may also contribute to the trends observed in figure 3.7b, although the cloud fraction variability and major El Niño event in 2015/16 are the major drivers of SW flux variability (*173*). As with the LW anomaly, the SW feedback parameter can be estimated using the entire CERES SW record (2000-2020), or sub-setting to mask out the most significant ENSO variability. The full record's λ_{SW} = -1.6 ($\pm$0.3)/,W/m^2/°C, larger than the SW feedback measured in GCMs over multi-century intervals. Masking the prominent 2015/16 El Niño years finds $\lambda_{SW,masked}$ = -1.2 ($\pm$0.3) W/m^2/°C. A joint regression of ENSO, PDO and temperature anomalies onto the SW flux anomaly finds λ_{SW} = -1.4 ($\pm$0.4) W/m^2/°C. As with the LW feedback, this joint regression finds only a limited contribution from ENSO explicitly, predominantly because of the correlation between the global-averaged SSTs and ENSO variability (*173*). Removing the impact of internal variability using an ensemble of CMIP6 models finds λ_{SW} = -0.8 ($\pm$0.5) W/m^2/°C

using 4xCO_2 experiments (*81*), or λ_{SW} = -1.0 W/m^2/°C using the mean CMIP6-model response from historical experiments in panel h.

Compare the observed LW and SW flux anomaly behaviour in figure 3.7a and b with the *low-aerosol-trend-change SSP3-70 and prescribed-SSTs* experiment (panels d and e), and the *ensemble-mean SSP2-45* experiment which averages out the impact of SST and cloud cover variability (panels g and h). In the experiments where internal variability has been removed the decadal trends show much smaller trend changes than the CERES observations, while the prescribed-SST experiment continues to show a large change in the decadal trend despite having a small aerosol ERF trend change. This supports the assessment that trends in the left column's anomalies are significantly exaggerated in response to short-term variability signals, as is proposed in our analysis of observed feedback parameters and in the attribution of the aerosol ERF contribution to the GMST trend change above. The LW flux anomaly trend change is reasonably well reproduced in the multi-model ensemble average response, reinforcing the claim that the GHG contribution to the TOA flux anomaly is well understood over this period as a combination of the externally-forced response (including various LW temperature-mediated feedbacks) and internal variability (panel d). The SW trend change is almost entirely missed in the ensemble-average coupled model response of panel h, suggesting the vast majority of the SW trend change occurs due to natural variability (driven by SST variability) and not because of aerosol ERF trend changes. A wide range of aerosol ERF trend changes are therefore compatible with the observed SW trend change in panel b, including zero trend change over the interval.

CERES observations suggest a larger LW feedback over the past two decades than CMIP6 GCMs (compare the trends in panels a and g), although within the range of uncertainty (*81*). This may result from natural variability influencing LW fluxes in observations, by varying sea surface temperatures or the rate of ocean heat uptake. This does go against the notion that natural variability will principally bias SW feedbacks through variations in cloud cover (*173*), and recent updates to ocean heat uptake datasets which show a roughly constant trend over the past two decades (*213*). One alternative explanation for the discrepancy is that LW fluxes are partly increased since

2000 because of an additional LW cloud-ice feedback in response to the declining atmospheric aerosol burden as anthropogenic aerosol emissions decrease. LW fluxes have been demonstrated to increase in response to reduced upper tropospheric cloud ice content, which occurs following aerosol emissions reductions in regional CRM simulations (*221*, *222*). This additional LW feedback to aerosol emissions perturbations is not captured in GCM's parameterised convection schemes at present, hence the possibility for discrepancy between observations and coupled models. However, we also note that figure 3.7a's LW all-sky and clear-sky observations have remarkably similar trend changes, suggesting the LW cloud-ice feedback is not the culprit.

In summary, the decadal TOA flux trends assessed from CMIP6 models are consistent with the ERF trends in figure 3.2, and ensemble-averages over CMIP6 coupled model runs provide an assessment of the underlying forced response behaviour we should hunt for in observations. Much larger trend changes are identified in observed LW and SW TOA flux anomalies than those which are predicted with anthropogenic ERF trends alone (compare figure 3.7a and b to figure 3.7g and h). The observed trend changes are better explained as resulting from SST and cloud cover variability since 2000; CESM2's atmosphere-only historical+SSP3-70 ensemble supports this assessment (figure 3.7d and e), with larger trends appearing in the flux anomalies when the model is run with observed SSTs over the interval, despite the experiment also containing a much smaller anthropogenic ERF trend change. The best-estimate ERF timeseries does explain the TOA flux observations behaviour shown in the left column of figure 3.7. As was determined in the GMST analysis, a wide range of near-term ERF trends remains plausible since the principal driver of changes in the TOA flux trend since 2000 is likely SST and cloud cover variability, and not changes in the aerosol ERF trend.

3.3.3 Aerosol optical depths

AODs give the most direct observation of recent aerosol trend behaviour, but is also less clearly associated with the overall global energy imbalance/ERF. Sogacheva *et al.* (2020)'s AOD product combines several satellite records to produce a near-global AOD timeseries between 1995-2018 (*153*). From this synthesised AOD record globally-,

Region name	Latitude (°N/S)	Longitude (°E/W)
Northern Africa	5N:35N	20W:40E
Southern Africa	50S:10N	0E:60E
Europe	60S:35N	20W:40E
Middle East	10N:45N	20E:70E
Central Asia	30N:60N	40E:150E
South East Asia	0N:30N	60E:150E
Australia	60S:0N	110E:180E
North America	20N:60N	140W:60W
South America	70S:25N	110W:30W

Table 3.1: Latitudes and longitudes of AOD regions in figure 3.8.

hemispherically- and regionally-averaged anomalies (calculated by removing their mean seasonal cycle over the full record) are plotted in figure 3.8. Regional trends are calculated over geographical regions defined in table 3.1.

Global AOD observations (black) are remarkably stable since 2000 in figure 3.8 (the period 1995-2000 shows a residual trend caused by the 1991 Mt. Pinatubo eruption). Separating the northern hemisphere's (NH's) AOD trends isolates a slight peak-and-decline behaviour since 2000 (red), while the global average is dampened by a flatter and smaller southern hemisphere (SH) AOD contribution (blue). Since anthropogenic aerosol emissions are predominantly released in the NH, this weak SH trend reflects the near-constant natural AOD contribution over the two-decade period of AOD observations. Regional anomalies in panel b more clearly show emissions-induced trends in South-East Asia, which are to first order balanced by an accelerating trend in Northern Africa (and smaller contributions from Australia and South America). Regional SO_2 emissions timeseries in figure 3.1 support these South-East Asian AOD trends, but there is little evidence supporting an acceleration of Northern African AOD caused by anthropogenic emissions in emissions datasets. Limited in-situ observations and high variability in Aeronet AODs (*153*) mean validation remains challenging, and there are known retrieval issues for many satellite AOD products over reflective surfaces (deserts and ice sheets) and regions with high natural AOD burdens (*153*). Based on a global linear emissions-to-AOD relationship, since anthropogenic aerosol species have

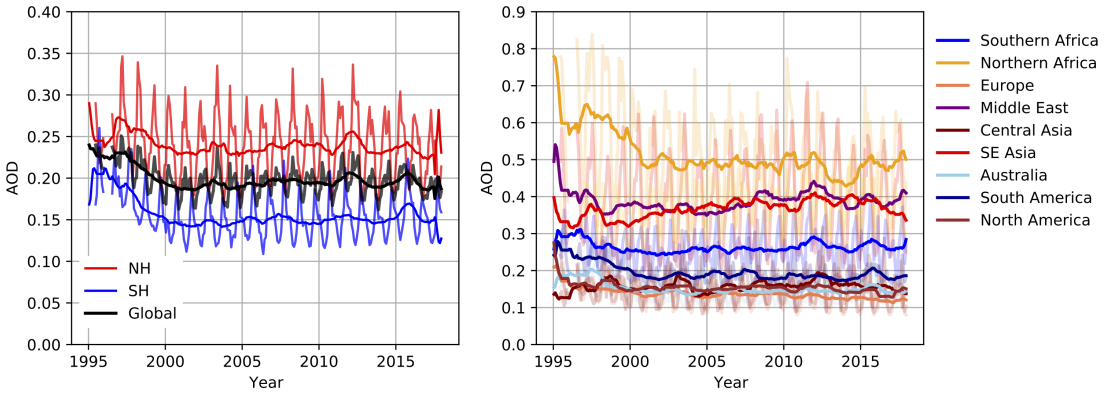

Figure 3.8: Aerosol optical depth (AOD) timeseries plotted from Sogacheva *et al.* (2020) between 1995 and 2018. Global and hemispheric averages are shown in panel a, while the AOD timeseries of several broad geographical regions are shown in panel b. In each panel, monthly anomalies are shown with their seasonal cycles, with thick lines on top plotting the annual anomaly (12-month rolling mean). In panel a the red line plots the northern hemispheric average, the blue line plots the southern hemispheric average, and a global average is shown in black. In the right panel key geographical regions include South East Asia (red), the Middle East (purple) and Northern Africa (yellow).

an extremely short atmospheric lifetime (*152*), figure 3.1's emissions trends suggests the anthropogenic AOD anomaly should have declined by around a third since 2000.

In figure 3.8, the difference between the NH (red) and SH (blue) AOD timeseries provides a rough estimate of the NH's anthropogenic AOD anomaly (assuming that the SH component contains a negligible anthropogenic component, and therefore acts as a proxy for the NH's natural AOD contribution). Differencing the NH and SH AOD timeseries finds a subtle peak-and-decline trend change, with a 10-30% decrease in the NH anthropogenic AOD anomaly between 2010 and 2018. Hence, this NH trend supports the SO_2 emissions behaviour exhibited in figure 3.1. The 10-30% reduction is approximately halved in the global-average AOD anomaly since little anthropogenic AOD is contributed by the SH, but the land area of the AOD average is doubled. GCMs replicate the observed emissions-to-AOD relationship in the global and hemispheric average (see for example the AOD anomalies produced from CMIP6 models historical experiments in figure A.4 of appendix A).

The fact that anthropogenic aerosol emissions are largely localised in the NH, and that AOD has substantial natural contributions globally, means there is a smaller percentage change in global AOD expected for a given percentage change in aerosol

emissions. This lack of coherency between observables along the aerosol chain from emissions to AOD to ERF could be indicative of a pattern dependence for aerosol emissions, where the spatial distribution of emissions impacts on their global-average ERF outcome. Some research suggests that the spatial distribution of aerosol emissions will alter the efficacy and lifetime of atmospheric aerosol perturbations, complicating the prospect of simple global emissions-to-AOD relationship described above (*209*, *223*, *224*). The size of this impact requires further research.

Despite these concerns there has been recent success working within a global and linear framework for the relationship between aerosol and precursor emissions and total aerosol ERF (*73*, *152*). Below I take advantage of this, looking to CMIP6 models to derive a globally-averaged relationship between AOD and aerosol ERF.

3.3.3.1 Trends in global AOD and ERF

To establish whether the gradient change in observed AOD is consistent with figure 3.2's global aerosol ERF trends, figure 3.9 plots the decadal linear trend change (2010-2020 minus 2000-2010) in AOD (panel a) and ERF (panel b). I again use a split decadal linear trendline fit using GLS regression onto individual model's AOD and ERF timeseries, as was used for figure 3.7 above. The figure shows the historical+SSP2-45 AOD and ERF trend in for CMIP6 models, and compares them with observed AODs and ERF trends from figure 3.2. When analysing the CMIP6 model AOD trends, I use the same five models as were presented in the right column of figure 3.7 (for which I have corresponding historical ERF timeseries to derive a global relationship between changes in AOD trend and corresponding changes in ERF trend from RFMIP's transient ERF experiment (*54*)). The individual CMIP6 model AOD and ERF trendline fits are shown in figure A.4 in appendix A. For the five CMIP6 models, the AOD trend change over the two decades since 2000 lies between -0.011 and -0.023 /decade (black scatter points in figure 3.9a; note AOD is unitless), while figure 3.8's observed AOD trends change is between -0.002 and -0.029 /decade. As expected, NH trend change dominates the global trend behaviour in both the CMIP6 models and the observations (shown in red in figure 3.9a). The trends are modulated by weaker SH trends (blue scatter points in figure 3.9a).

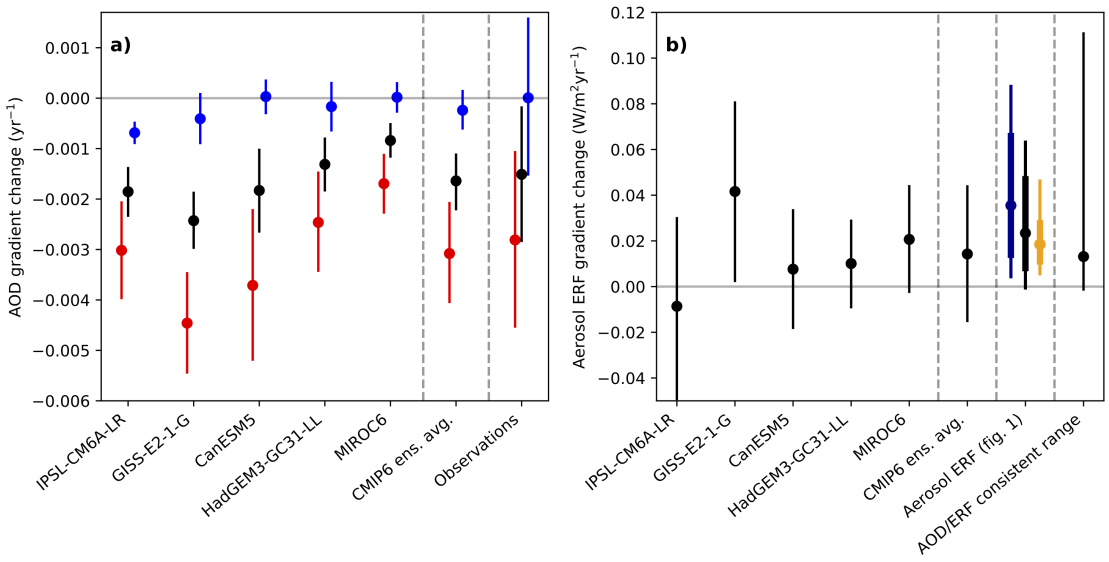

Figure 3.9: AOD and ERF gradient changes between 2000 and 2020 for CMIP6 models and satellite observations. Panel a shows the AOD gradient change, including averages over the Northern Hemisphere (red), Southern Hemisphere (blue) and Globe (black). Panel b plots the ERF trend changes using the RFMIP transient ERF experiment (*54*). All trend changes are measured using a linear trend which is split in 2010. This trend is fit using GLS regression onto each timeseries (assuming an AR(1) process autocorrelates the residual), and the process is identical to that in figure 3.7. In panel a the CMIP6 ensemble mean AOD trend change is shown, alongside the AOD gradient change measured in observations from figure 3.8. In panel b the ensemble mean CMIP6 ERF trend change is shown alongside the assessed gradient change in standard ERF timeseries from figure 3.2. The standard dataset's aerosol ERF trend change is assessed in three ways: 1) using decadal averages of the trends plotted in figure 3.2d (orange scatterpoint); 2) using GLS regression identical to that used for the CMIP6 models (blue scatterpoint); 3) using GLS regression and comparing the gradients over an extended historical period, i.e. gradient change between (1990-2010) and (2010-2020). Finally, the rightmost scatterpoint in panel b shows the implied aerosol ERF trend change, given the observed AOD trend change, calculated using the CMIP6-mean linear relationship between AOD trend changes and resulting aerosol ERF trend changes.

The relative change in CMIP6 ERF trends (shown in figure 3.9b) are more uncertain than their corresponding AOD trends, reflecting the greater difficulty in assessing the downstream properties of the climate system which become increasingly impacted by natural variability. Panel b compares the five-model-average CMIP6 ERF trend change with three estimates of the ERF trend change estimated from figure 3.2, labelled 'Aerosol ERF (fig. 2)'. The orange range shows the estimated ERF trend change directly lifted from figure 3.3 (the inner range shows SSP2-45's aerosol ERF trend change and the wider range the full range across all SSP variants). Black and blue bars show two

alternative estimates of figure 3.2's aerosol ERF trend change: blue is the difference between (2010-2019) – (2000-2009) linear trends (consistent with the method used to derive AOD trend change estimates for the CMIP6 models in figure 3.9); and black is the difference between (2010-2019) – (1990-2009) linear trends.

In general, the AOD-ERF relationship is negative, meaning a negative AOD trend change corresponds to a positive ERF trend change ($\sim -10\,\mathrm{Wm}^{-2}$/[AOD]). Figure 3.2's aerosol ERF trend change (orange) overlaps with the trend change calculated for the five CMIP6 models in figure 3.9b. However, while figure 3.2's ERF trend change consistently produces positive aerosol ERF trend changes since 2000, the five CMIP6 models often have aerosol ERF trend changes which overlap with zero, despite the model derived AOD trend change estimates all being negative over the same interval.

By assuming that a linear relationship exists between the AOD trend change and the aerosol ERF trend change as above (i.e. a single efficacy parameter governs the relationship between panels a and b, defined using the ensemble-mean CMIP6 response), we can estimate the ERF trend change expected given the observed AOD trend change since 2000. This 'AOD-ERF consistent range' in figure 3.9b finds a wider range of aerosol ERF trends is compatible with observed AODs since 2000, expanding beyond the estimates from the standard ERF trends assessed in figure 3.2 to include both near-zero trend change in the lower bound, and higher trend changes for the upper bound. While this higher limit is not supported by CMIP6 models themselves (the upper end of the range far exceeds the limits of the individual CMIP6 model fits), near-zero trend change is also observed in individual model outputs in figure 3.9b (e.g. IPSL-CM6A-LL, CanESM5), implying a *no-trend-change* aerosol ERF scenario is plausible in both modelled and observed AOD responses since 2000.

3.4 Discussion

Successive IPCC reports have given assessments of the level of anthropogenic global warming, but no equivalent assessment of the rate of human-induced warming has been made. To constrain the rate of anthropogenic warming, one also needs an accurate assessment of the anthropogenic ERF trend and how it has changed over the period of

interest. Recent studies have highlighted a potential acceleration in anthropogenic ERF, driven by reducing aerosol emissions since the mid-2000s (*163*, *164*). This chapter highlights the extent of this perceived acceleration in AR6's standard ERF timeseries, and uses observations of key climate system properties to assess observational evidence supporting this acceleration claim.

Global temperatures show a clear change in trend between 2000 and 2020, characterised by temperatures remaining stable at around +1.0 °C above preindustrial levels in the first decade, while in the second decade temperatures increase rapidly (with the rate of warming peaking at over +0.3 °C/decade). The reduced warming trend around 2000 has been discussed in the context of ocean heat uptake and natural variability contributions (*3*, *216*), but less research has focused on a possible warming acceleration in the following decade induced by aerosol ERF trend changes.

By attributing the temperature trends to anthropogenic and natural sources we show the forcing timeseries from figure 3.2 capture the broad warming contributions over the previous two decades (figure 3.4). Significant variations around the anthropogenic best-fit are still present, and alternative forcing trend change assumptions can be applied with little indication of a worse fit. A three-way regression isolates the aerosol contribution over history in figure 3.5, fitting the mid-20th century GMST more successfully by down-scaling the aerosol contribution to historical warming. This implies the both the aerosol and overall anthropogenic contributions are smaller, with the anthropogenic warming acceleration (+0.05 (+0.01 to +0.08) °C/decade between 2000-2009 and 2010-2019) representing 50% of the overall GMST trend change. The remainder of the GMST trend change is attributed to internal variability.

In the CERES record, LW TOA flux contributions are explained by recent GMST and forcing trends combined, while there is greater uncertainty in the contributors to the SW and net flux anomalies. In the SW anomaly, unforced variability in temperature and TOA flux timeseries precludes clear assessments of the aerosol ERF contribution, supporting the assessment that significant contributions from ENSO and PDO are present in recent TOA flux trend changes. Given this, TOA flux trends cannot rule out little-to-no anthropogenic ERF trend change over the two decades, despite the best-estimate

anthropogenic ERF timeseries agreeing well with both TOA fluxes and temperature anomalies. Figure 3.7's middle column (atmosphere-only TOA flux anomalies) and right column (coupled-model TOA flux anomalies) confirm the major role played by natural variability processes in these TOA flux records, demonstrating that the trend change induced in the SW TOA flux anomaly, where we expect to observe a large trend change induced by aerosols, (figure 3.7h) is small compared to the trend change caused by unforced variability over the previous two decades (figure 3.7e). Continued funding for new satellites to study the outgoing radiative balance of the Earth system (such as the recently announced FORUM mission (*225*)) is vitally important in order to maintain long-term records and constrain the properties of short-term radiative feedbacks with greater certainty.

Finally, satellite observations and CMIP6 models agree that a relatively small AOD trend change has occurred over the last two decades, despite significant reductions in anthropogenic aerosol emissions in the northern hemisphere. Exploring a linear relationship between AOD and aerosol ERF trends (based on the mean response of CMIP6 models) allows us to estimate the ERF trend change expected in response to the observed AOD trend change since 2000. This analysis again supports the best estimate ERFs in figure 3.2, but also suggests that little-to-no trend change remains a possible assessment for ERF trends since 2000 in observations. The spatial pattern of aerosol emissions also may play a role in determining the aerosol ERF level (*226*), causing non-linearities in the AOD and ERF responses to globally-averaged aerosol emissions reductions. Further research of ERF trends and feedbacks using their full spatiotemporal signal in atmopshere-only GCM experiments where forcing timeseries are known, and conducting regional aerosol perturbation experiments in coupled models (*162*), will provide greater insight. The spatiotemporal fingerprint of aerosols is the focus of chapter 4.

Overall, this chapter suggests that aerosol emissions reductions have contributed to an increase in the rate of anthropogenic warming since 2000, but with a substantial uncertainty range. The forced behaviour coincides with a period of considerable internal variability, meaning that isolating the aerosol-induced ERF trend change from

observations is challenging, and that a wide range of ERF scenarios offer plausible explanations of the past 20 years. Some of these possibilities are not well represented in the ERF ensemble shown in figure 3.2: for example, a zero-trend-change aerosol ERF scenario between 2000 and 2020 (shown in figure 3.2 as an dashed orange line, with the corresponding anthropogenic ERF a black dashed line), is considered possible in all three observation datasets, but is poorly represented in the ERF ensemble of figure 3.2. Using a zero-trend-change aerosol ERF to attribute anthropogenic global warming results in a similar quality fit to GMSTs over the wider historical period (see dashed orange and black lines in figure 3.5a), but substantially reduces the anthropogenic warming trend change which occurs since 2000 (orange and black dashed lines in figure 3.5b). A comprehensive ERF ensemble of the recent time-history of anthropogenic ERF should offer these alternative scenarios, including scenarios with reduced aerosol ERF trend change since 2000 and with alternative rescalings for all pollutants using global energy balance constraints (e.g. those in Smith *et al.* (2021) (*73*) or figure 3.5).

3.5 Chapter close

This chapter used observations to answer *'Is anthropogenic global warming accelerating?'*. I determined that, in the best-estimate attribution, AGW has accelerated since 2000, with aerosols contributing around 30% of the observed GMST trend increase, GHGs around 20%, and natural variability the remaining 50%. Because of the prominent role internal variability has played in observations over the past two decades, I also could not rule out natural variability causing the entirety of the recent GMST trend increase. This possibility is poorly sampled in current ERF ensembles.

It is not generally known that every individual has a peculiar arrangement [on] the grain of the skin... the impressions made from the fingers of different persons will produce different shapes.

— Robert Blake Overton (Letter to Scotland Yard, 1840)

4

Spatiotemporal fingerprinting a changing aerosol radiative forcing trend

This chapter discusses the spatiotemporal patterns in observations which provide evidence for a rapid change in the aerosol ERF trend since 2000. This work is based on a draft manuscript which will be submitted to ACP: *Spatiotemporal fingerprinting a changing aerosol radiative forcing trend.* Jenkins, S., Storelvmo, T., Sanderson, B., Stier, P. and Allen M. Atmospheric Chemistry and Physics.

Contents

4.1 Introduction

Over the near-present period (2000-2020) the spatial distribution and quantity of aerosol emissions have both varied substantially: SO_2 emissions have declined by a third, BC and OC emissions have stabilised, and all three species emissions have shifted towards South East Asia (*63*). Driven by these trends, AR6's headline ERF assessment (*5*) accelerates since 2000, implying an increased rate of anthropogenic warming. Chapter 3 identified observational evidence of this acceleration, determining 50% (10-80%) of the observed GMST trend increase, which rose to more than +0.3 °C/decade in the 2010s from +0.2 °C/decade the decade before, was attributable to anthropogenic ERF.

The uncertainty in the anthropogenic contribution is influenced by both internal variability and uncertainty in the size of the aerosol forcing trend change. The similarity of these two drivers' globally-averaged shapes mean that the GMST acceleration is consistent with both, and hence chapter 3's attribution could not easily separate them. Additional complexities, including the level of confidence in reported anthropogenic aerosol emissions over the late 20th century (*154*, *227*, *228*) and uncertainty in model-derived warming responses to decade-long ERF perturbations (*59*, *78*), further hamper efforts to assess the aerosol contribution to recent warming trends using GCMs.

To improve on the aerosol attribution described in chapter 3, in this chapter I apply a fingerprinting approach, where the full spatiotemporal pattern that aerosols imprint on observations is identified. This better separates the internal variability and the aerosol forcing fingerprints (since their spatial patterns differ), facilitating a more robust assessment of the recent aerosol-induced warming acceleration. Other studies have previously considered the spatial distribution of aerosol forcing and identified an 'aerosol fingerprint' in model outputs or observations. Chapter 1 discussed some of these attempts to constrain ACI in spatiotemporal observations using observed AOD, cloud droplet number concentration (CDNC), liquid water path (LWP) and cloud fraction observations (*134*, *136*, *137*). Gryspeerdt *et al.* (2016, 2019) and Quaas *et al.* (2020) use a mixture

of satellite observations and models to characterise these variables contributions to warm marine-cloud ACI, deriving observational constraints on ACI over the satellite record.

Similar fingerprinting approaches have been extended to the cloud controlling factors literature (e.g. see a recent example in Wall *et al.* (2022) (*229*)). In Wall's methodology a number of local meteorological factors (e.g. SST, wind shear, near-surface air pressure, relative humidity, SO_4^{2-} AOD) are correlated with daily-mean cloud optical properties (e.g. TOA SW radiative flux anomaly), to produce maps of correlation between the cloud field and each controlling factor. This is used to estimate ACI from the partial correlation between SO_4^{2-} AOD and the TOA SW radiative flux. However, in these assessments the underlying GMST trend can spuriously correlate with the various observables. To account for this, Wall *et al.* (2022) first removes any linear trend from each observable prior to estimating its contribution to the (de-trended) cloud response. This limits its applicability to the direct assessment of multi-decade and near-global aerosol trends.

Complementary studies have identified the spatiotemporal pattern of anthropogenic aerosols in models (*155*, *162*). RFMIP and AerChemMIP provide a series of standardised ERF perturbation experiments for CMIP6 models which have resulted in studies on the spatial distribution of aerosol ERF at present day (*54*, *55*). Wilcox *et al.* (2019) probes how anthropogenic aerosol emissions interact with the global climate system by exploring the boreal winter response to Asian aerosol emissions in HadGEM3-GC31-LL. They find Rossby waves form in the NH extratropics in simulations where Asian aerosol emissions are removed after 1980, and argue this is controlled by Chinese aerosol emissions influencing the strength of the Aleutian low (*155*). Tian, Dong *et al.* (2020) expanded on this work (*230*), using aerosol perturbation experiments to derive three processes by which aerosol emissions trends induce NH regional surface temperature responses in HadGEM3-GC31-LL:

- Increasing Asian emissions strengthen the wintertime Aleutian Low, inducing a Rossby wave response in NH extratropics, inducing local and non-local surface temperature patterns.

- Decreasing European emissions decrease AOD, both increasing clear-sky downwelling flux and decreasing CDNC, inducing local surface temperature pattern. Particularly in summertime, driven by greater downwelling insolation.

- Decreasing Eurasian emissions decrease AOD, both increasing clear-sky downwelling flux and decreasing CDNC, inducing a local surface temperature perturbation.

Experiments like these will be expanded in the Regional Aerosol Model Intercomparison Project (RAMIP) (*162*), where the global response to regional aerosol emissions trends will be explored using dedicated GCM experiments. These three processes for aerosol-induced surface temperature change will be discussed further in the analysis of observations below.

The IPCC combines several model and observational studies to produce a multi-dataset consensus estimate of aerosol ERF (*5*). Despite some recent success in constraining the aerosol ERF level, these efforts still struggle to constrain the aerosol ERF trend, as was highlighted in chapter 1. Forster *et al.* (2021) gives little attention to estimating the aerosol ERF trend in AR6, only noting that aerosol forcing estimates ending in 2019 are around 0.2 W/m^2 weaker (closer to zero) than estimates ending in 2014 "primarily due to recent emissions changes (medium confidence)".

More recently, Quaas *et al.* (2022) discusses observational evidence of aerosol ERF trends. They begin by estimating the model-derived aerosol ERF spatial pattern from RFMIP experiments, and then search for this spatiotemporal pattern in satellite observations. With this broad viewpoint, Quaas determines that there is "robust evidence for reversal of the trend in aerosol effective climate forcing" since 2000, based on co-varying trends in satellite records consistent with CMIP6 models aerosol-induced trends. Complementing that study, Bauer *et al.* (2022) diagnoses the aerosol ERF in the GISS-E2-1-G model under various historical and SSP scenarios, demonstrating that the aerosol ERF trend turns positive this decade in all SSPs, regardless of scenario ambition (*163*). These two studies present the first claim that we are entering the 'end of the aerosol era'. Despite this progress the Quaas study was limited for several reasons:

- it failed to consider any aerosol-induced trends other than a 20-year linear trend, despite the emissions, AOD and forcing ensembles suggesting other behaviour is equally important over the two-decade interval since 2000.

- it uses a coarse $5° \times 5°$ spatial resolution throughout, missing key spatiotemporal information from their fingerprint.

- it does not quantify consequences of the proposed aerosol ERF trend for recent warming rates, despite several model studies suggesting a global warming response may be quantifiable given recent regional emissions changes (*155*, *163*, *230*).

In this chapter I quantify the observational evidence for both a trend, and more importantly a change in trend, in aerosol ERF since 2000. Section 4.2 analyses the aerosol emissions datasets which are used to produce the global ERF estimates in AR6 (*72*) and CMIP6 models (*62*, *63*). Having identified the spatiotemporal patterns in emissions data, I "fingerprint" (meaning, in effect, regressing the temporal patterns in aerosol emissions onto downstream observations to identify regions of co-variance) observations of AOD, cloud optical properties, TOA radiative fluxes, and surface temperatures, searching for the aerosol-induced trends in each. Section 4.3 uses an ensemble of aerosol ERFs, produced using an emulator sampling CMIP6-derived aerosol forcing and constrained against the observational constraints from this and the previous chapter, to estimate the aerosol-induced warming trend since 2000, before section 4.4 concludes.

4.2 Identifying aerosol-induced trends

To identify the key patterns which may appear as a result of aerosol emissions, I first analyse the trend behaviour exhibited by gridded SO_2, BC and OC emissions inventories (*62*, *63*). Small contributions from other anthropogenic aerosol and precursor emissions (NO_x, VOCs etc.) are ignored.

4.2.1 Implied behaviour from emissions inventories

This analysis focuses on the Community Emissions Data System (CEDS) emissions database (*63*), which provides gridded anthropogenic aerosol emissions inputs for GCMs in CMIP6 (*231*). The CEDS inventory uses a bottom-up approach, where regional and source-specific emissions are estimated using reported activity data and location-dependent emissions factors (*63*). These inputs have been updated since CMIP6 (*232*) reflecting recent analyses which suggest that earlier data under-represented Asian aerosol emissions reductions since 2010 (*62*, *233*), and adding data collected between 2015-2020.

SO_2 emissions are the predominant source of anthropogenic aerosol pollution since the mid-20th century (*116*). CEDS SO_2 emissions, coloured by source region, are shown in figure 3.1 of chapter 3. They exhibit a double-peak structure, first in the 1980s (driven by subsequent emissions declines in North America, Europe and the former Soviet Union states), and a second, lower peak in the 2000s driven by East Asian emissions trends. Although the absolute emissions level does vary between datasets (see SI figure S6 in Zhong *et al.* (2020) (*234*)), SO_2 trends also dominate the overall aerosol emissions trend exhibited post-2000 (*63*, *64*, *234*).

I use a multivariate empirical orthogonal function (multivariate EOF) decomposition (*235*) to isolate the key spatiotemporal patterns in emissions inventories. For this, I deseasonalise and combine three aerosol emissions datasets (SO_2, BC and OC) into a single vector before decomposing it into principal components and EOFs. This approach highlights temporal patterns which are coherent across all three aerosol species together — important if I am to use these spatiotemporal patterns to identify the aerosol-fingerprint in downstream observations. Figure 4.1 shows the first two principal components and corresponding spatial correlation maps for SO_2, OC and BC emissions datasets. Together these two principal components (approximately a 20-year positive linear trend, PC1 in figure 4.1; and a 10-year peak-and-decline structure centred on 2010, PC2 in figure 4.1) describe around 90% of the emissions variance.

SO_2 emissions show the most extensive spatial correlation with both of these principal components, as expected given SO_2 emissions make up the majority of the anthropogenic aerosol perturbation (*152*). SO_2 emissions exhibit a declining 20-year trend over the

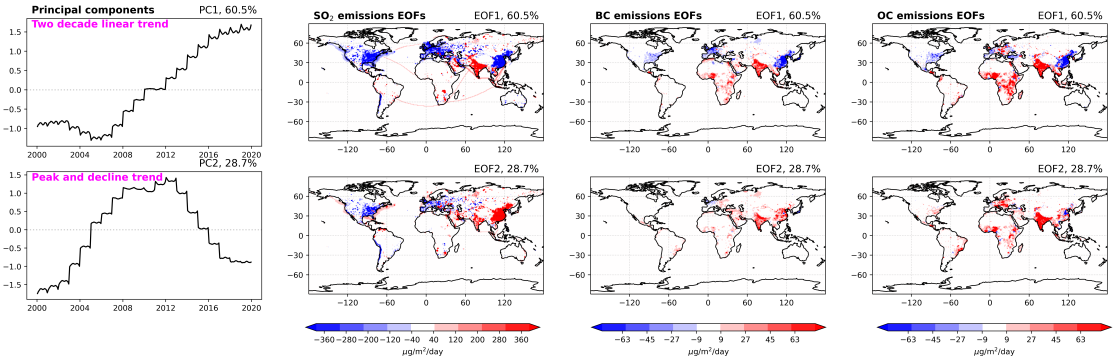

Figure 4.1: Multivariate EOF decomposition of three aerosol emissions species (SO_2, BC, and OC) between 2000–2019. CEDS emissions inventories, converted into a spatiotemporal dataset using the approach outlined in McDuffie *et al.* (2020), are deseasonalised and decomposed into their principal components and EOFs. The first two principal components (shown here) explain ~90% of the emissions datasets' variance. EOFs are plotted on a blue-to-red colourscale (corresponding to negative-to-positive correlation with the respective principal component).

east coast of the US, Europe and China, and a positive 20-year trend over India. They also show a prominent 10-year peak-and-decline structure for Chinese emissions, and, to a lesser extent, India. BC and OC have considerably weaker trends overall, but have similar structures to SO_2 in key emissions regions. Positive peak-and-decline trends over India dominate carbonaceous aerosol emissions since 2000 (but these are significantly weaker than the SO_2 trend change over China). Shipping SO_2 emissions are present on figure 4.1, but are of a much smaller magnitude compared to most land regions, and are therefore not highlighted on the trendmaps (except for 20-year positive SO_2 emissions trends over the India-Singapore strait shipping lane, the NH Atlantic shipping lanes, and around the South African coastline).

Regional aerosol emission trends in Europe and the US are consistent with the timing of the introduction of air quality legislation, and have been noted in several other studies (*236*, *237*). Surface sulphur deposition rates have declined by 50% across the US between the early 1990s and late 2000s (*238*), while estimated sulphate concentration of precipitation over Western Europe has declined by around 75% between 1980 and 2010 (*239*). Indian aerosol emissions uniformly increase over the two decades since 2000, with studies noting the impact of absorbing aerosols on the Indian monsoon over the satellite record (*148*, *240*). South East Asia is the only region where a major peak-and-decline structure is suggested, with the peak around 2007 coinciding with strict

air quality legislation being introduced in China (*241*). As discussed above, the extent of the emissions decline since 2010 in China is believed to have been under-reported for inputs to the CMIP6 experiments (*242*, *243*), meaning Chinese SO_2 emissions now exhibit a larger 20-year linear decline principal component (PC1, SO_2 emissions) in figure 4.1. This downward revision mirrors other evidence for the evolution of aerosol emissions trends, such as observed AOD trends (*244*).

The accuracy of China's recent SO_2 emissions estimates is particularly important as Chinese SO_2 emissions contribute the majority of the total anthropogenic aerosol perturbation over this period, and are also thought to be the primary source of any trend discontinuity. The minima around 2000 in figure 3.1's SO_2 emissions, caused by declining European and US emissions being replaced by rising Chinese emissions thereafter, is a particular area of uncertainty in records. Chinese SO_2 emissions between 1990 and 2005, which are estimated using coal consumption data split by coal grade and multiplied by emissions factors, have been the subject of much debate and have been revised upwards several times (*245*, *246*). The depth of this minima therefore remains uncertain. Its presence plays an important role in producing the peak-and-decline principal component discussed in figure 4.1. India's emissions also pose a significant accounting challenge for the Indian state, particularly for wood-based fuels which remain in widespread use domestically (*247*, *248*).

Despite these challenges, emissions inventories have proved to be reasonably successful measures of global aerosol pollution over the past two decades. Mortier *et al.* (2020) presents a helpful evaluation of CMIP6-derived AOD trends in comparison to AeroCom observations since 2000 (*233*). This work shows models driven with the CEDS emissions inventories generally reproduce the observed globally-averaged AOD trends, although are less successful over regions with large natural AOD variability (e.g. Northern Africa). Determining the portion of errors in model-derived AODs which reflect errors in input datasets, versus structural uncertainties in models themselves, remains an open challenge (*249*). Further analysis of uncertainties in the emissions datasets is beyond the scope of this work.

4.2.2 Evidence in the spatiotemporal patterns of observations

Having established the aerosol fingerprint in emissions inventories, I now consider the evidence for these spatiotemporal patterns in global satellite observations.

4.2.2.1 Aerosol optical depths

AODs are smoothed spatially compared to emissions, and transported downwind (predominantly eastwards in the northern hemisphere), but are otherwise expected to reflect the spatiotemporal patterns in emissions data due to the short lifetime of aerosol particulates (*164*).

To confirm this and explore the AOD fingerprint caused by figure 4.1's emissions trends, figure 4.2 projects the two principal components onto AOD. The colours indicate, for a unit change in the emissions principle components, how much local AOD is estimated to change. I use an AOD reanalysis as this provides a spatially-complete record, unlike in-situ or satellite-derived records, which can be split into individual aerosol species (allowing easier comparison against the emissions trends in figure 4.1). Figure 4.3 then compares this AOD fingerprint to the spatiotemporal patterns identified in satellite-observed AODs.

Figure 4.2 uses AOD from the CAMS reanalysis (*178*) product — a set of atmospheric composition datasets produced using the ECMWF's Integrated Forecasting System, with boundary conditions and inputs supplied from satellite observations and independent emissions inventories (*250*). The top of each column in figure 4.2 shows a principal component from figure 4.1, with projections onto the AOD550 variable (*178*) below: the total AOD, and the contributions to this total from SO_4^{2-}, BC and OC.

Reassuringly, these trendmaps demonstrate similar patterns to the emissions EOFs in figure 4.1. The green-ringed areas in figure 4.2 highlight regions of large anthropogenic aerosol emission trends from the previous figure. The SO_4^{2-} AOD contributes the majority of recent anthropogenic AOD trends in the CAMS reanalysis, particularly in the northern hemisphere, which is expected given the dominant role SO_2 emissions play in this region. BC contributes very little to the global spatiotemporal trend in AOD, although there are local trends present over Indian-subcontinent and northern China which align with the emissions maps. OC plays a larger role, with positive

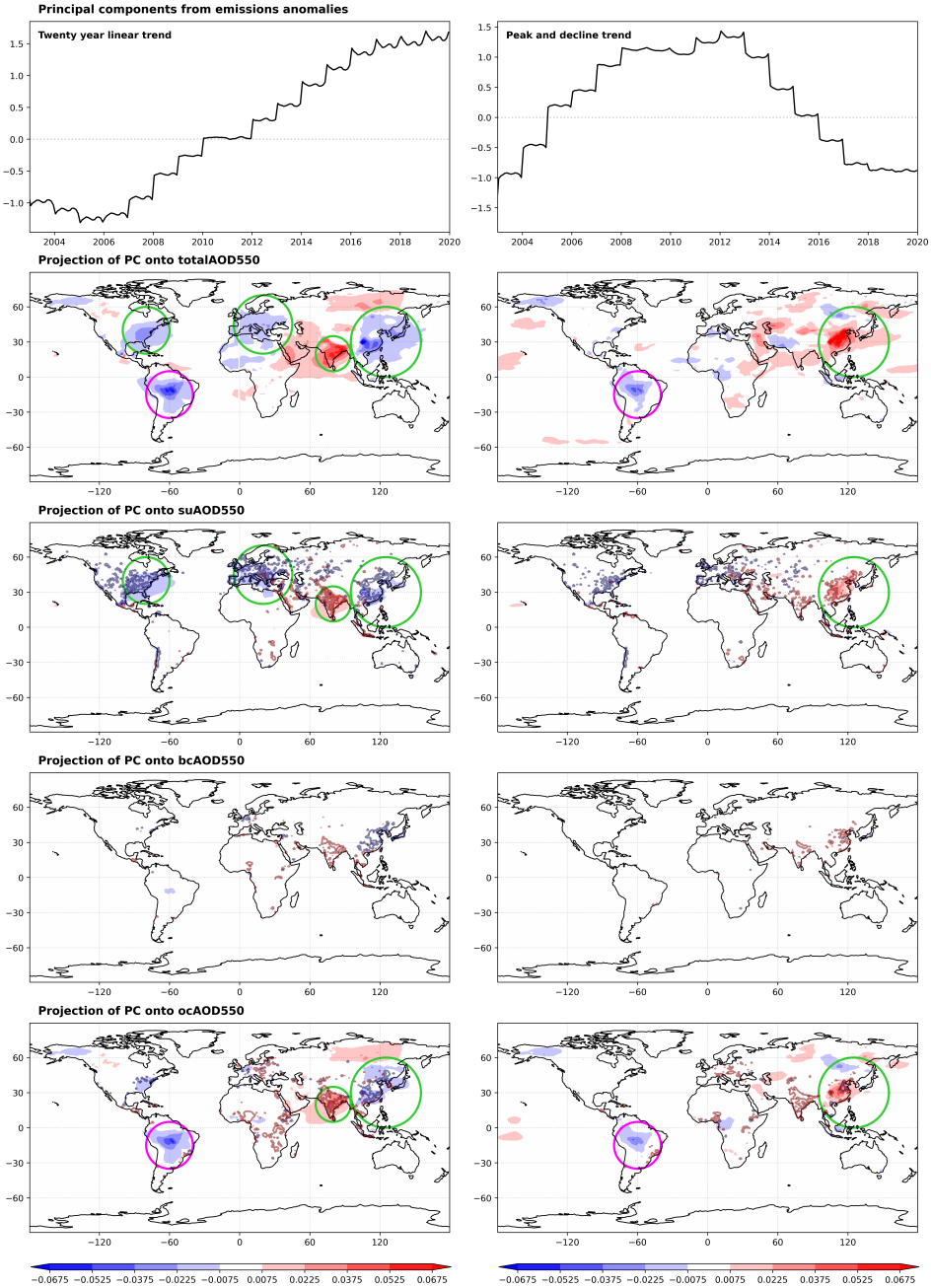

Figure 4.2: Projected EOFs onto the CAMS reanalysis AOD, sulphate AOD, black carbon AOD, and organic carbon AOD, using the first two principal components from emissions multivariate EOF decomposition (figure 4.3). First two principal components are shown at the top of figure, with the total AOD (totalAOD550) correlation below. Below that are the correlations with individual AOD species: sulphate AOD (suAOD550), black carbon AOD (bcAOD550), and organic carbon AOD (ocAOD550). All panels use the same blue-to-red colourbar, corresponding to negative-to-positive correlation with the projected principal component. The significant emissions trend regions from figure 4.1 are also plotted on the sulphate, black carbon and organic carbon AOD panels, outlined in blue-to-red colour scale. Green circles show regions where emissions spatial trends correlate well with the AOD spatial trends. Pink circles show regions where the anthropogenic aerosol emissions and CAMS AOD analysis spatial trends are poorly correlated.

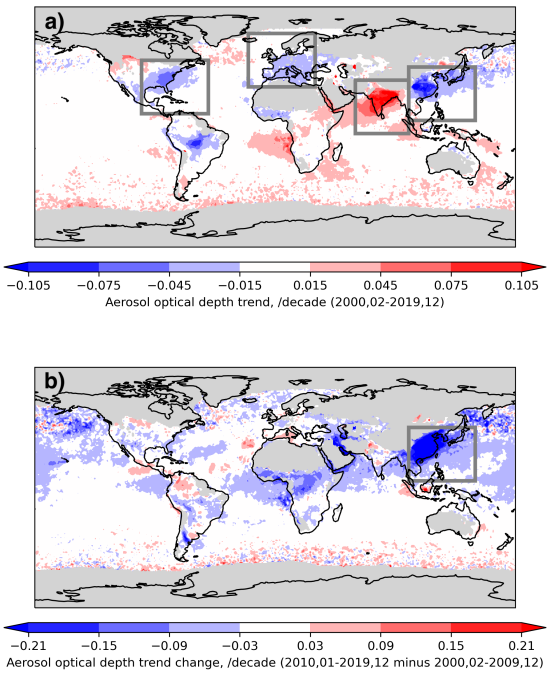

Figure 4.3: 20-year linear trends (panel a) and the 10-year trend change (panel b) of the MODIS AOD observations between 2000-2019. Red-to-blue colourbar shown below each panel, with units [AOD]/decade. Grey regions are where there are too few monthly observations to accurately determine a trend (fewer than 75 per decade). Grey boxes highlight regions of large anthropogenic aerosol emissions trends.

20-year trends over India, negative trends over China, and China also showing a large positive 10-year trend change contribution.

Pink-ringed regions highlight contributions to the total AOD which are not well-represented in the emissions fingerprints identified in figure 4.1. For example, the large negative trend region in South American OC AOD, and positive trends over Canada and Siberia (not ringed), which are absent in the corresponding OC emissions trendmap. These pink-ringed regions are also observed in AOD trends from other in-situ observations and satellite studies (*153*, *164*), and likely stem from fire emissions trends since 2000 (*251*–*253*). Fire emissions are treated separately to anthropogenic aerosol emissions in inventories (*254*, *255*), and are therefore not captured in emissions EOFs in figure 4.1 despite having a role in explaining the global AOD over this period. In this study I focus on anthropogenic aerosol emissions only, and do not include fire emissions and their downstream impacts on other observations.

Satellite-derived AOD trends

I now look to identify this fingerprint in satellite-derived AOD. Trends in satellite remote sensing observations can be challenging to interpret because the sensors are subject to orbital drift and degradation over the lifetime of missions. MODIS AOD observations have been carefully re-calibrated to reduce these issues (*176*, *256*). The co-observation of many cloud and atmospheric optical properties from MODIS and CERES on the same satellites further increases the comparability of their derived products. However, discrepancies still exist for areas with lower absolute emissions, e.g. remote ocean regions (*164*).

NASA's MODIS and MISR equipment, and EUMETSAT's METOPB, provide direct AOD observations from 2000 (*164*, *233*). All three records identify broadly consistent spatiotemporal patterns over the Eastern US, Europe, India and China, although disagree on the absolute AOD magnitude both at regional and global scales (*153*). AOD trends averaged from MODIS (*257*, *258*) and MISR (*259*) observations show 20-year linear trends of between $\pm 2\,\%$/year (see figure 2.9 in Gulev *et al.* (2021) (*260*)). In-situ observations (for example AERONET's (*261*) ground observation network), which compared to satellite remote sensing are far more sparse spatially but provide a more accurate measurement of near surface AOD, also report consistent trends to the satellite-derived products since 2000 (*260*).

Figure 4.3 shows AOD trends calculated from MODIS observations since 2000 (*176*). The trendmaps are calculated using a simplified version of the two principal components in figure 4.1: a 20-year linear trend and 10-year trend change (i.e. the linear trend between 2010-2019 minus the linear trend between 2000-2009) at each gridpoint. These two stylised trends replace the more complex principal components' shapes from earlier figures but keep their key characteristics, simplifying the fingerprints for the evaluation of downstream observations which are not spatially complete and for which there is greater temporal variability. The decadal trend change (m_2-m_1) can be thought of as a measure of the acceleration in the observation between the first and second decade since 2000. The greyed-out regions contain insufficient datapoints to assess the trend accurately (< 75 /decade), due to: high cloud fractions reducing

the availability of clear sky conditions, underlying surface reflectivity hampering the observation (e.g. the Sahara and ice sheets), or where insolation variability is high (near the poles). High latitudes are particularly poorly sampled by satellite equipment since they rely on back-scattered sunlight to estimate aerosol and cloud properties.

The boxed areas of figure 4.3 highlight the regions where anthropogenic aerosol emissions have varied substantially since 2000. 20-year declining AOD trends are visible in Europe and the US, along with increases over the Indian-subcontinent (panel a), and a peak-and-decline trend over China (panel b). MODIS AOD trends show good agreement with both the CAMS AOD reanalysis (figure 4.2) and emissions inventories (figure 4.1) across these regions, providing direct observational evidence of the regional emissions patterns identified above. Panel b's peak-and-decline trend structure is prominent over China with good correlation across much of the northern pacific, where emissions are advected by the jet stream.

Quaas *et al.* (2022) completes a similar analysis of the 20-year linear trend in fine-mode AOD (fAOD), using MODIS and MISR data (where fine-mode AOD refers to particles with radii $< 1\,\mu m$) (*164*). fAOD is considered a better assessment of anthropogenic aerosol pollution since anthropogenic emissions contribute the majority of particulates of this size. Hence, fAOD trends are also well-correlated with SO_2, BC, and OC emissions trends isolated in figure 4.1. In this study I focus on total AOD to analyse the total aerosol influence on climate, which is better described by total AOD than by either a sub-species of it (e.g. sulphate AOD from figure 4.2) or by a sub-component of it (e.g. fAOD in Quaas' study).

The patterns identified in figure 4.3 generally support the reported aerosol emissions, although at a pixel-by-pixel level the observed trends can still vary substantially. To identify regional trends, figure 4.4 averages figure 4.3's trends over the boxed regions, weighted by land surface area. Split-decadal trendlines are fitted onto each timeseries using an OLS regression, with the gradients of the trendlines reported at the top of each panel (m = 20-year trend, m_2-m_1 = 10-year trend change, both with units [ΔAOD]/decade).

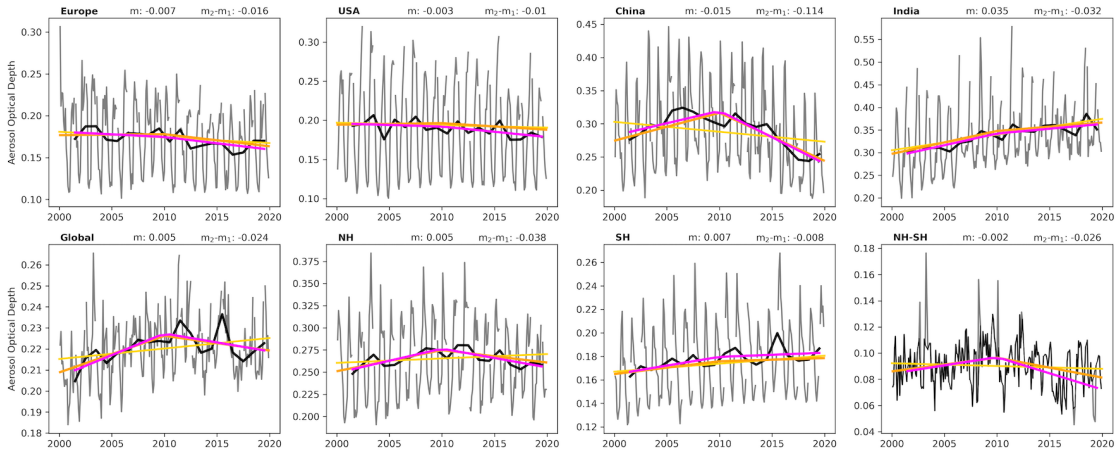

Figure 4.4: 20-year linear trends (gold) and the 10-year trend change (orange and pink) of the MODIS AOD observations 2000-2019. Each panel in the top row refers to a different boxed region in figure 4.3, and each panel in the bottom row refers to a broad regional average (e.g. northern hemisphere (NH), southern hemisphere (SH) or global). Black lines are the annual-average AOD over that spatial box, with the grey lines underneath the full record including sub-annual variability. 20-year trend and 10-year trend change are reported above each sub-panel (m and m_2-m_1), with units [AOD]/decade.

These regional decadal trends mirror the emissions inventory's trends in figure 4.3. Europe and US AOD show negative 20-year linear trends of -0.007 /decade and -0.003 /decade since 2000, with very little trend change signal (note that optical depth is a unitless quantity). These relatively weak trends reflect the fact that, by 2000, Europe and the US had already substantially reduced their particulate pollution (*228*, *239*). In contrast, Indian-subcontinent and China-and-far-eastern AOD trends are large in figure 4.4, as they have produced a combined 50% of global aerosol pollution since 2000. These are also subject to greater uncertainty than the US and European trends, as accurate retrieval of the AOD burden in a tropical atmospheric column is more challenging, and clear sky conditions are rarer. India's 20-year AOD trend (m $= +0.035$ /decade) is much larger than the European or US trends. This may reflect India's large emissions trends over all aerosol species, but could be biased higher by observational challenges in distinguishing aerosol haze from thin cloud in the tropics (particularly with an underlying global warming trend) (*262*, *263*). AOD trends over China show remarkable agreement with the emissions inventories (m $= -0.015$ /decade, m_2-m_1 $= -0.114$ /decade), although the same caveats exist regarding the biasing of AOD retrievals in the tropics as Indian observations above.

Local positive trends are also observed over the large marine stratocumulous decks off western continental coastlines, e.g. the prominent positive 20-year trend off the Angolan and Namibian coasts in figure 4.3 (*71*). Some of these trends correspond to large fractional increases in AOD (*164*), and hence may contribute non-negligible positive ACI trends. This effect could be responsible for the peak-and-decline structures visible in the stratocumulous decks in the all sky SW radiative flux variable plotted in figure 4.8. Partitioning these observed trends between: the true anthropogenic AOD trend; the erroneous retrieval of thin cloud surrounding the marine cloud deck; and the influence of co-varying meteorological factors (or warming-induced cloud-radiative feedbacks) remains an open challenge. Several studies have claimed an anthropogenic contribution to the radiative properties of marine stratocumulous cloud decks (*71*, *229*).

The bottom row of figure 4.4 plots the globally-averaged AOD, northern hemisphere (NH) AOD, southern hemisphere (SH) AOD, and (NH-SH) AOD difference. The NH AOD, which contains the majority of anthropogenic aerosol emissions, has a clear peak-and-decline structure (m $= +0.005$ /decade, m_2-m_1 $= -0.038$ /decade) reminiscent of the emissions fingerprint. The small positive 20-year trend is not explained by the emissions behaviour, although adding fire emissions may help (see CAMS reanalysis in figure 4.3). Similarly, the SH AOD displays a positive 20-year linear trend (m $= +0.007$ /decade, m_2-m_1 $= -0.008$ /decade). This behaviour somewhat aligns with the emissions in figure 4.1 (southern African BC and OC emissions have a positive 20-year trend), but the trend is too large and widely dispersed to have originated solely from emissions in the SH. It could instead highlight a bias in MODIS retrievals, where the observed AOD correlates with the local surface temperature trend in regions of low AOD. MODIS struggles to differentiate clear sky pixels from low-optical-depth cloudy sky pixels (*176*), and the optical thickness of low-optical-depth clouds has been shown to increase with GMST in many GCMs (*264*). This suggestion is further supported by Quaas *et al.* (2022)'s analysis showing MISR and METOPB satellite products contain little Southern Ocean AOD trend since 2000 (*164*), implying this is an issue with MODIS retrievals specifically. Regardless, in all three satellite products the NH trend behaviour dominates, and hence these issues do not bias the globally-averaged AOD trend significantly.

Globally-averaged AOD observed with MODIS is between 0.20-0.25, with around three quarters of this due to natural aerosols (Bellouin *et al.* (2020) estimates preindustrial AOD at around 0.17 using MODIS data (*71*)). The temporal evolution broadly follows the NH's peak-and-decline behaviour, which appears to be driven by Chinese SO_2 emissions trends in figure 4.4. If the southern hemisphere can be considered a clean 'preindustrial' atmosphere, then the (NH-SH) AOD difference on the bottom right panel of figure 4.4 isolates the anthropogenic AOD trend behaviour since 2000. Although this is clearly a first-order approximation, it goes some way to confirming the CEDS emissions above, with a prominent peak and decline structure centred on 2010. There is remarkable similarity between this shape and the SO_2 emissions in figure 3.1 — the peak in 2010 is +0.02 above the *hemispheric-average* AOD level in 2000, and declines back down to the 2000 level by 2020. This corresponds to a *global-average* anthropogenic AOD trend of +0.01 /decade in the first decade, and -0.01 /decade in the second; half the *hemispheric-average*). If anthropogenic AOD has indeed varied in this way, and SO_2 emissions are responsible for 80% of the anthropogenic AOD anomaly (*116*), the globally-averaged AOD/SO_2 emissions sensitivity parameter is approximately ~0.4 [AOD]/(GtSO_2/yr). This back-of-the-envelope calculation corresponds to the peak SO_2 emissions in the 1980s causing a +0.05 anthropogenic AOD perturbation, which aligns with other estimates in the literature (*71*, *153*).

4.2.2.2 Clear sky fluxes

The TOA radiative flux anomaly responds to perturbations in AOD, with greater SW scattering in an atmosphere with a higher aerosol burden. As in the previous chapter, flux anomalies are calculated from NASA's Clouds and Earth Radiation Energy System (CERES) EBAF4.1 dataset (*168*), which has been spatially-infilled, regridded ($1^\circ \times 1^\circ$ spatial grid), and time-averaged into a monthly-mean array. The timeseries of CERES EBAF TOA flux anomalies are shown on the left column of figure 3.7 for reference.

Figure 4.5 plots the spatiotemporal patterns exhibited in the clear sky SW TOA flux trends. Panels a and b show the 20-year trend and 10-year trend change for the deseasonalised clear sky SW TOA flux anomaly, respectively (grey regions are poorly

observed due to large insolation variability at high latitudes). Regional clear sky SW TOA flux trends, averaged over the boxed regions of figure 4.5, are plotted in figure 4.6 (the trendlines are fit identically to those in the regional AOD figure above). The 20-year linear trend and 10-year trend change are reported above each panel with units W/m^2/decade.

The clear sky SW flux trends have similar spatiotemporal patterns to those found in AODs over the four boxed regions. This suggests that, at least at a local level, clear sky fluxes are being directly perturbed by the aerosol emissions trends (*131*). This makes intuitive sense: the amount of reflected sunlight at a particular location in clear sky conditions is principally controlled by the aerosol burden in the atmospheric column. Other factors also contribute to the clear sky reflectivity, including the atmospheric ozone and water vapour concentrations, as well as the underlying surface albedo (*265*). Stephens *et al.* (2015, 2022) determined that atmospheric influences dominate over surface albedo contributions to SW flux trends (*131*, *266*), and that the majority of clear sky atmospheric reflection arises from AOD scattering (ozone and water vapour changes predominantly result in additional absorbed SW flux in the troposphere (*5*)). These atmospheric trends correlate well with anthropogenic aerosol emissions trends since 2000. US and European clear sky SW flux anomalies show declining trends over the last 20 years (m $= -0.55$ W/m^2/decade and m $= -0.70$ W/m^2/decade). Indian-subcontinent trends are positive (m $= +0.10$ W/m^2/decade, with little trend change), and China again displays the characteristic 10-year peak-and-decline trend structure which was prominent in AOD and emissions variables (m $= -0.49$ W/m^2/decade, m_2-m_1 $= -1.87$ W/m^2/decade).

These European and Asian trends are supported by both the trends in observed surface downwelling radiation (*228*, *267*, *268*), and Tian, Dong *et al.* (2020)'s HadGEM3-GC31-LL analysis that aerosol emissions reductions in the NH lead to local increases in clear sky downwelling SW radiation (and hence local surface temperature increases) (*230*).

Although the four high-emission regions are broadly well captured, there are some discrepancies between clear sky fluxes and AODs. Artifacts in the clear sky trendmaps between land and ocean retrievals (e.g. see Indian coastlines) result from CERES' use of different algorithms to estimate fluxes observed over oceans (so-called "dark-target")

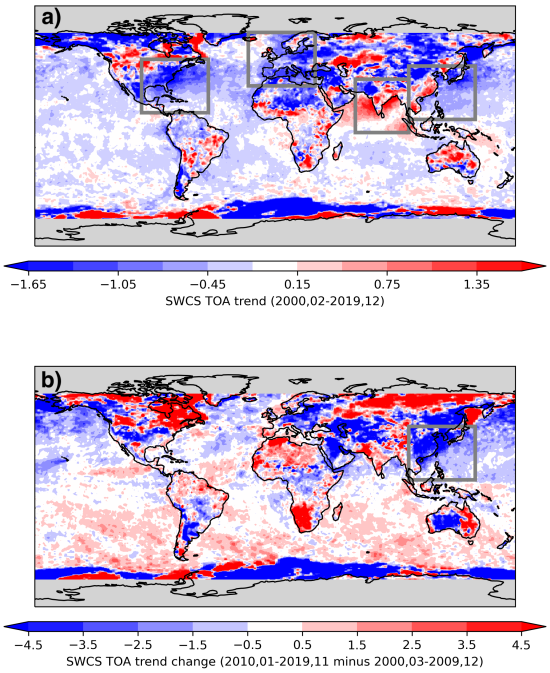

Figure 4.5: 20-year linear trends (panel a) and the 10-year trend change (panel b) of the CERES clear sky SW TOA flux observations 2000-2019 (from the EBAF4.1 product). Red-to-blue colourbar is shown below each panel, with units of W/m^2/decade. Greyed regions show where there is insufficient data to take a reliable trend measurement (< 75 /decade). Grey boxes highlight regions of large anthropogenic aerosol emissions trends.

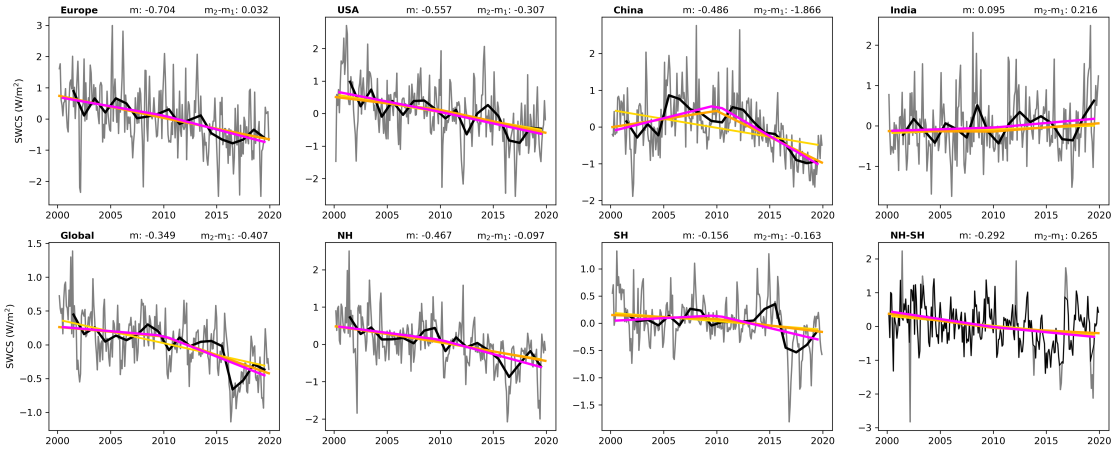

Figure 4.6: 20-year linear trends (gold) and the 10-year trend change (orange and pink) of the CERES SW clear sky TOA flux observations 2000-2019. Each panel in the top row refers to a different boxed region in figure 4.5, and each panel in the bottom row refers to a broad regional average (e.g. northern hemisphere, southern hemisphere or global). Black lines are the annual-average SW clear sky flux anomaly over that spatial box, with the grey lines underneath the full record including sub-annual variability. 20-year trend and 10-year trend change are reported above each sub-panel (m and m_2-m_1), with units W/m^2/decade.

and over land. The global oceans show a negative 20-year linear trend, except in high-latitude regions with substantial sea ice variability, and regions adjacent to land with rapidly increasing aerosol emissions (e.g. India and the Malay Archipelago; see figure 4.1). Western Canada, central Asia and South America also exhibit local clear sky SW flux trends consistent with the fire-induced AOD trends noted in figures 4.2 and 4.3.

Indian-subcontinent trends are weaker in the clear sky SW flux variable than is suggested in AOD. Some of this may be due to Indian-subcontinent AOD retrievals having higher BC and OC content compared to other NH emissions regions, resulting in relatively stronger absorption and weaker scattering of SW flux. Alternatively, it may again hint at challenges in separating low-optical-depth cloudy sky scenes from clear sky aerosol scenes in retrievals over the tropics. Trends over China continue to drive the shape of the wider NH and global trends in figure 4.6, as was found for AOD.

The hemispheric- and global-average clear sky SW flux trends also correlate with GMST trends. Examples of this include: the global oceans negative 20-year trend; the inflection in SH trends in 2010; and the correlation of the hemispheric- and global-average trends with ENSO variability. Over global oceans this correlation likely reflects rising GMST causing a moistening of the troposphere (*269*) which increases SW absorption. Recent ozone trends may also make a small contribution to increased clear sky SW absorption (*5*), predominantly concentrated around major anthropogenic emissions sources. Since the negative trend in clear sky flux is particularly prominent over global oceans, increased SSTs moistening the troposphere are the most likely explanation for the widespread correlation with GMST. All panels on the bottom row of figure 4.6 also show a reduction in clear sky SW flux between 2015-16, corresponding to the large El Niño event in figure 3.6. As ENSO principally impacts the cloudy sky observations (*173*), its presence in figure 4.6 is confusing and adds weight to the claim that the MODIS satellite retrievals struggle to distinguish clear sky aerosol pollution scenes from low-optical-depth cloudy sky scenes.

Despite this, many studies use regional trends in clear sky SW flux as evidence of the radiative response to AOD changes (*131*, *228*, *266*, *270*). To explore this, figure 4.7 plots the satellite-derived 20-year AOD trend vs. CERES clear sky SW flux trend

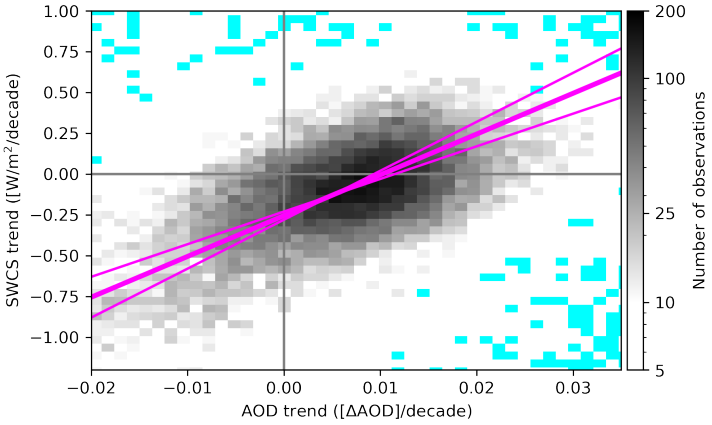

Figure 4.7: 2D histogram of the absolute trend in clear sky SW TOA flux anomaly (SWCS trend) and AOD (AOD trend) between 2000-2019. Coloured by number of datapoints underlying that pixel. Poles (70-90° N/S) are ignored, as they exhibit high clear sky SW flux variability due to insolation variability. AOD is derived from Sogacheva's multi-satellite AOD product (*153*). Pink lines show the AOD-clear sky SW flux sensitivity estimated by Aerocom II models in Myhre, Samset *et al.* (2013); $25 \pm 5\,\mathrm{W/m^2/[\Delta AOD]}$ (*200*). Blue bins contain no data.

in a 2D histogram. Shading indicates the density of observations in each pixel using a logarithmic colour scale to filter out extremes in trend observations, better sampling the large-scale correlation between the AOD and clear sky SW flux fields. The two variables are linearly dependent, with offsets from the origin reflecting the fact that both variables exhibit non-zero trends independently of one another (implying correlation with other variables, e.g. GMST, as discussed above).

The relationship between AOD trend and clear sky SW flux trend in figure 4.7 can be compared with the relationship derived from 16 GCMs in the AeroCOM phase II experiments by Myhre, Samset *et al.* (2013). They determined the sensitivity, $S_{\text{clear sky SW/AOD}}$, was $25 \pm 5\,\mathrm{W/m^2/[\Delta AOD]}$ (*200*) (plotted in pink in figure 4.7, centred on the grey plume). The agreement between the grey shaded plume's behaviour and Myhre's $S_{\text{clear sky SW/AOD}}$ parameter adds confidence that AOD trends are indeed causing the observed spatiotemporal patterns in clear sky flux. This is particularly prominent in the NH where the anthropogenic emissions trends are largest, despite biases in both variables moving the relationship away from the origin.

Given figure 4.7's implied $S_{\text{clear sky SW/AOD}}$ parameter and the observed AOD trend

change, I estimate the ARI ERF acceleration since 2000. This uses:

$$\Delta\left(\frac{\mathrm{dERF_{ARI}}}{\mathrm{dt}}\right) = \Delta\left(\frac{\mathrm{dAOD}}{\mathrm{dt}}\right) \times \mathrm{S_{clear\ sky\ SW/AOD}} \times (1 - \mathrm{c_{cloudy}}), \tag{4.1}$$

following the approach of Bellouin *et al.* (2020) (*71*). I assume the effective cloud fraction, c_{cloudy}, is ~0.65 (*71*), and that $\Delta\left(\frac{dAOD}{dt}\right)$ is -0.01/decade (half the [NH-SH] AOD trend change reported in figure 4.4 to account for area-weighting to a global-average). Together, this suggests the ARI ERF has accelerated, with its trend increasing by $+0.088 \pm 0.018\,W/m^2$/decade between the first and second decade since 2000. This supports both the ARI trend change in SSP scenarios explored in chapter 3, and the trend change exhibited in the observed globally-averaged SW TOA flux anomaly in figure 3.7 (this ARI ERF acceleration equates to clear sky SW flux trends decreasing by $-0.25\,W/m^2$/decade between the first and second decade since 2000).

Stephens *et al.* (2022) decompose the 20-year clear sky SW flux trend into contributions from the atmosphere and surface (*266*). They determined that trends arise predominantly due to changes in atmospheric reflectivity, and further that these clear sky trends contribute 50% of the overall all sky flux trend. This is more than is suggested by other analyses, which typically estimate closer to 30% (*173*, *270*). Stephens' result implies a larger ARI ERF and weaker ACI ERF in CERES observations, although, this is inconsistent with other observational studies (*5*, *71*) and with CMIP6 GCMs (*131*, *271*). Using an ARI-ACI ratio of between 30 and 50% (*5*) and the ARI ERF acceleration derived above implies total aerosol forcing has reduced by between $+0.2$ and $+0.3\,W/m^2$ since 2010.

In summary, the clear sky SW record offers evidence of a direct radiative effect induced by aerosol emissions since 2000. This behaviour is particularly prominent over high-emissions regions, as could be seen in figure 4.5, and is consistent with model predictions that the NH aerosol emissions trends produce localized clear sky radiative perturbations since 2000 (*230*). Correlation between AOD and clear sky SW fluxes implies a $S_{clear\ sky\ SW/AOD}$ parameter consistent with estimates from GCMs, which demonstrates causal co-variability driven by the underlying aerosol emissions behaviour. Combining this with an estimate of the AOD reduction over the last decade

suggests ARI ERF trend has increased by $+0.088 \pm 0.018\,W/m^2$/decade between 2000-2020. This supports AR6's estimate that total aerosol ERF has weakened by approximately $+0.2\,W/m^2$ over the last decade (*5*).

4.2.2.3 Cloud properties and all sky SW fluxes

All sky fluxes are less tightly correlated with the spatiotemporal pattern of aerosol emissions. This lack of correlation is for two reasons: 1) aerosols acting as CCN mean the radiative impact of the ACI may persist far away from the emissions source, and 2) local cloudiness is primarily controlled by other meteorological factors which can be highly variable over short intervals (*229*), dominating over the AOD-induced trends.

To identify whether any spatiotemporal patterns are consistent with aerosol emissions changes in observed all sky fluxes, figure 4.8 plots the trends in several local cloud optical properties (CDNC in panel a; cloud optical depth in panel b; cloud fraction in panel c). The CERES all sky SW flux anomaly is shown in panel d. All sub-figures use the same layout as earlier trendmaps, with the upper plot showing 20-year linear trends and the lower plot the 10-year trend change. Trends averaged over the boxed regions in all sky SW flux are plotted in the top row of figure 4.9, along with the global, NH, SH and (NH-SH) average trends, as for the variables above.

All sky SW flux trends are negative (corresponding to a negative SW feedback parameter (*81*)); and are larger and more dispersed than the corresponding clear sky trends in regional, hemispheric and global averages. These differences highlight the key role clouds are playing in driving regional all sky SW flux trends. Compare the spatial patterns in figure 4.8d to those exhibited in the cloud fraction (figure 4.8c) and cloud optical depth (figure 4.8b). Cloud location (panel c) and thickness (panel b) correlate closely with the spatial patterns exhibited by all sky fluxes. This makes sense: Stephens *et al.* (2015) demonstrates the importance of global clouds in setting the net planetary albedo (the presence of clouds doubles the net planetary albedo to ~0.3) (*266*). Loeb *et al.* (2019) demonstrates that cloud variability is a key variable for predicting the all sky flux in the CERES record (*173*).

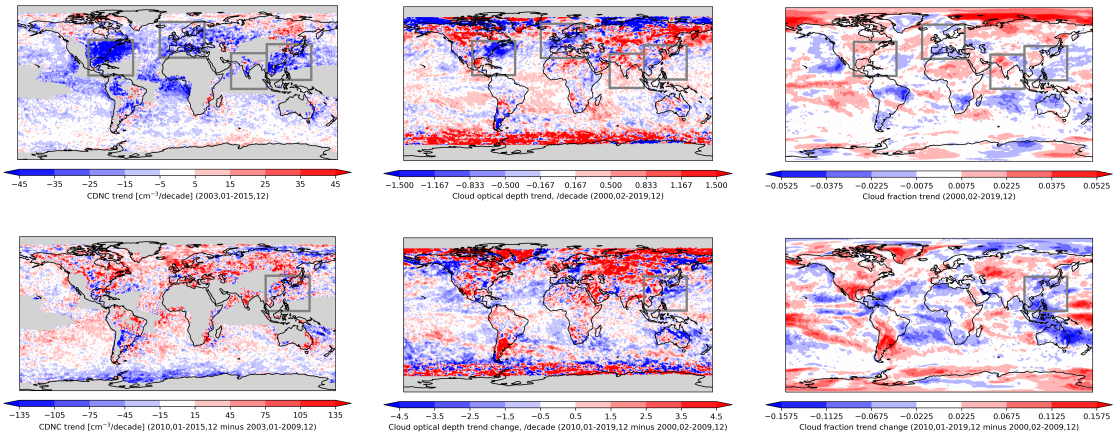

(a) CDNC **(b)** Cloud optical depth **(c)** Cloud fraction

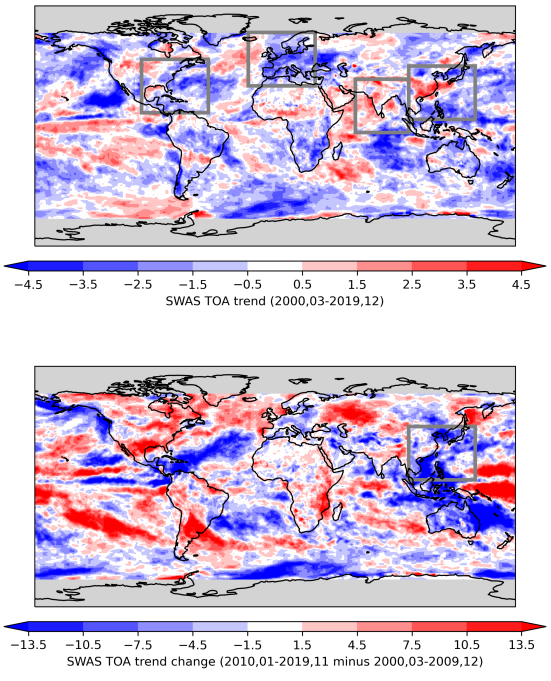

(d) All sky SW flux

Figure 4.8: Cloud optical properties and all sky SW TOA flux anomaly trends from MODIS and CERES observations. In panel a CNDC trends (cm^{-3}/decade), calculated from Grosvenor *et al.* (2018)'s CDNC variable are plotted. Panels b and c plot MODIS cloud optical depth (/decade) and cloud fraction trends (%/decade). Panel d plots CERES all sky SW flux trends (W/m^2/decade). Greyed out regions contain insufficient data to estimate a trend. All sub-panels are laid out in an identical way to previous figures, with the upper panel showing the 20-year linear trend, and lower panel the 10-year trend change. Red-to-blue colourbars are shown below each panel.

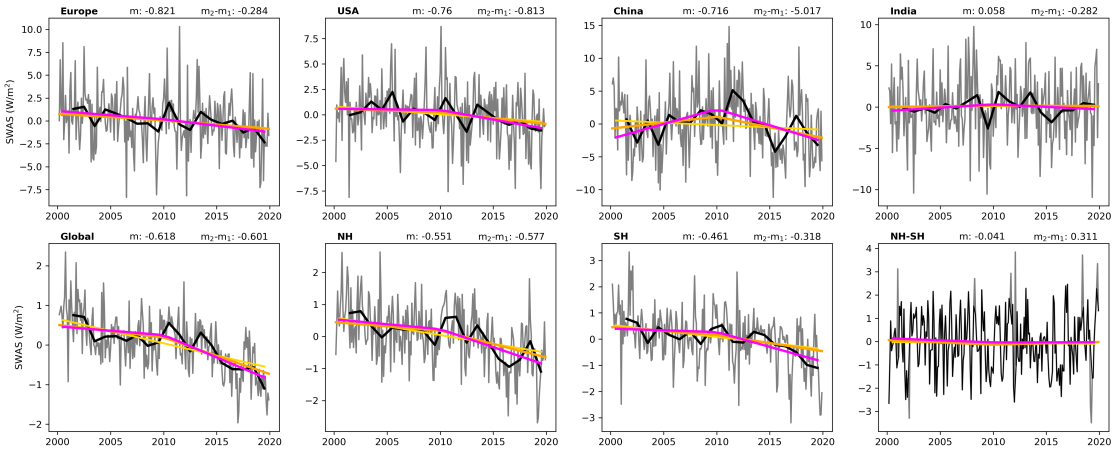

Figure 4.9: 20-year linear trends (gold) and the 10-year trend change (orange and pink) of the CERES all sky SW TOA flux observations 2000-2019. Each panel in the top row refers to a different boxed region in figure 4.8d, and each panel in the bottom row refers to a broad regional average (e.g. northern hemisphere (NH), southern hemisphere (SH) or global). Black lines are the annual-average anomaly over that spatial box, with the grey lines underneath the full record including sub-annual variability. 20-year trend and 10-year trend change are reported above each sub-panel (m and m_2-m_1), with units W/m^2/decade.

In turn, cloud fraction spatial patterns are primarily set by the underlying GMST spatial pattern (compare the cloud fraction's patterns to HadCRUT5's GMST patterns in figure 4.11) (*271*). Regions with warm surface temperature anomalies correspond to positive upwelling LW radiative flux anomalies, tropospheric temperature profiles which more readily promote free convection, and greater evaporation at the surface — all promoting cloud growth. These large-scale SST patterns driving the cloud fraction spatial structure are set by variability in the rate of ocean heat uptake. Hence, the spatial structures in the cloud fraction are readily influenced by and/or co-vary with the ENSO, PDO and AMV variability trends since 2000. Internal variability's influence on the cloud fraction poses a major barrier to isolating the aerosol contribution to all sky flux trends, since the spatial structure of the cloud fraction field is so important for driving the patterns observed in all sky flux trends over these short records. This challenge was also seen in the previous chapter, where the SST boundary conditions were the principal input necessary to reproduce recent all sky flux trend behaviour (see figure 3.7).

ENSO's influence on tropical deep-convective cloud structures makes it a particularly important driver of the spatial patterns in figure 4.8. ENSO's fingerprint is prominent in the Eastern Pacific (figure 4.8d) in both the 20-year and 10-year trend change patterns.

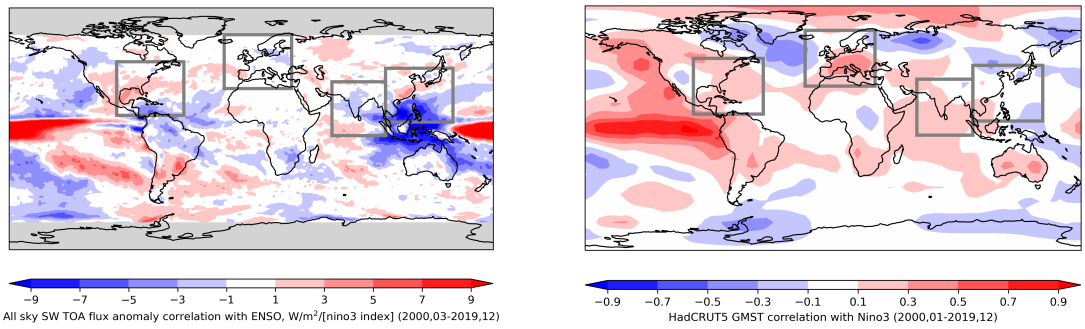

(a) ENSO-All sky SW flux correlation **(b)** ENSO-GMST correlation

Figure 4.10: Panel a shows the correlation between ENSO and the all sky SW flux anomaly at the TOA. Panel b shows the correlation between ENSO and the HadCRUT5 GMST anomaly. ENSO is measured using the Niño3 index (figure 3.6), and only non-zero ENSO months are considered (Niño3 index $> \pm 0.5$). A red-to-blue colourbar is shown below each panel. Grey boxes highlight regions of large anthropogenic aerosol emissions trends.

Loeb *et al.* (2021) demonstrates that for several CMIP6 models the model's ability to reproduce CERES all sky flux trends is tied to its ability to capture this tropical cloud variability, particularly in the Eastern Pacific (and hence to model the cloud response to ENSO) (*175*). The correlation between the Niño3 index and all sky flux in figure 4.10a highlights the ENSO influence on the Walker circulation and cloud structures in the tropics and Southern Ocean. Note that the all sky flux trends in the NH extratropics are less well correlated with ENSO, meaning more of these signals may originate from anthropogenic forcing instead (although other variability signals, AMV and PDO, likely also play a role here too).

Despite this link between the cloud fraction and internal variability complicating matters, figure 4.8 also hints at an aerosol contribution to the trends in the all sky SW flux. The cloud fraction has a near-zero temporal trend since 2000 (the globally-averaged rate of ocean heat uptake since 2000 is roughly constant (*213*)). Hence, the presence of multi-decade temporal trend in all sky SW flux in figure 4.9 is not explained by ENSO-induced cloud fraction variability. This temporal trend is instead explained by variations in the cloud optical properties and the clear sky SW reflectivity — both of which are driven more directly by aerosol emissions trends.

To demonstrate this, figure 4.8a plots the 20-year trend and 10-year trend change in CDNC (*142*) observed in global cloudy sky scenes since 2000. Since aerosols act

as CCN, one would expect areas with reducing AOD trends to also exhibit reducing CDNC trends (*272*). In turn, a reduction in CDNC would increase the cloud droplet effective radius (assuming a fixed liquid water path) (*134*), hence reduce the mean cloud brightness via the Twomey effect (*133*). This can be seen in European and US regional AOD trends in figure 4.8a. The four high-emissions regions display CDNC trends which are well correlated with AOD trends. This is particularly evident over the US, Europe and China, which all show strong negative 20-year declining trends in all sky SW flux, CDNC and AOD. This means anthropogenic aerosol emissions trends are visibly impacting the NH's cloud optical properties.

Figure 4.8b plots the trend and trend change in the cloud optical depth observed by MODIS, which includes both the CDNC trend and the LWP response to produce an overall picture of the trends in cloud reflectivity since 2000. The fact that CDNC and cloud optical depth records display similar trends to AOD in the four boxed regions further highlights the role of the anthropogenic aerosol perturbation in the NH cloud fields. This supports the link between reductions in aerosol emissions in these regions and a change in the ACI ERF trend. Combining these observations with the spatial structures of cloud fraction in figure 4.8c and the clear sky patterns in figure 4.5 reproduces the broad spatiotemporal patterns exhibited in the all sky flux trends (figure 4.8d).

The relationship between AOD changes and CDNC changes has previously been modelled with a log-log sensitivity parameter at a globally-averaged level (*71*), $\beta_{\ln(\mathrm{CDNC})/\ln(\mathrm{AOD})}$, meaning fractional changes in each variable are linearly related. McCoy *et al.* (2017) estimates $\beta_{\ln(\mathrm{CDNC})/\ln(\mathrm{AOD})}$ as between 0.3-0.8. With MODIS-derived preindustrial AOD averaging 0.17 (*71*), and $\Delta\left(\frac{\mathrm{dAOD}}{\mathrm{dt}}\right)$ = -0.01, the CDNC trend change is -3.5%/decade (-2 to -5%/decade) between the first and second decade since 2000. Since 2010, this is consistent with the roughly 7 %/decade trend exhibited in the globally-averaged CDNC observations by MODIS.

It is less consistent with the notion that, globally, AOD increased in the first decade since 2000, while CDNC trends are negative across the 20-year record. This challenges the interpretation of the CDNC behaviour as being solely 'aerosol-induced'. The difference highlights the role of other important cloud controlling feedbacks in the tropics (e.g.

GMST) acting to increase net radiative heating via cloud radiative feedbacks (*80*, *82*) and unforced variability. This analysis is supported by Cao *et al.* (2023), who determine aerosol emissions reductions significantly reduce the hemispheric contrast in CDNC since 2000 (*273*), and also find the hemispheric- and globally-averaged CDNC observations exhibit very little trend change signal between the first and second decade since 2000.

The spatiotemporal pattern in CDNC, reported by both Cao *et al.* (2023) and figure 4.8, support an aerosol emissions influence on cloud optical properties in the NH extratropics since 2000 (*273*). Using this evidence to further claim a global-scale ACI ERF acceleration since 2000 remains uncertain, since a trend change signal is not directly observed in cloud optical properties over China. This lack of observation may be for two reasons: 1) clouds are CCN-saturated over the tropics, and hence are less perturbed by a unit-size AOD perturbation; or 2) cloud optical properties are more influenced by variability in other meteorological factors over the tropics, hampering the observation of a trend change signal. If this lack of signal is due to the former reason, then the overall aerosol ERF acceleration may be substantially smaller (since it will not include an ACI contribution).

The reasoning that CDNC is harder to measure where natural variability is more pronounced, clouds are optically thick, or the clouds are already CCN-saturated, is supported by other studies of aerosol cloud interactions. Flight campaigns and models suggest cloud radiative responses saturate at high aerosol burdens, meaning they become insensitive to AOD perturbations if the cloud field is already optically thick (*274*). Because of this, tropical deep-convective clouds exhibit reduced ACI ERF changes for a given AOD change, and the NH extratropics cloud optical properties are more perturbed by changes to AOD in figure 4.8a and b. Re-normalising the observed AOD field by aerosol occurrence before correlating the AOD vs. CDNC could reduce this dependence, offering a means to better characterise the trendmaps as a function of anthropogenic aerosol emissions trends in the tropics (although the fundamental issue that cloud fields are saturated will persist). That analysis is beyond the scope of this research, but has been considered elsewhere (*274*).

Assuming that the AOD trend change is impacting global cloud optical properties, but is poorly observed in tropical clouds, I can estimate the resulting ACI ERF trend change. This uses a linear sensitivity parameter to relate fractional changes in CDNC to ACI ERF (as in Bellouin *et al.* (2020)) (*71*):

$$\Delta\left(\frac{\mathrm{dERF_{ACI}}}{\mathrm{dt}}\right) = \left[\beta_{\mathrm{ln(CDNC)/ln(AOD)}}\frac{\Delta\left(\frac{\mathrm{dAOD}}{\mathrm{dt}}\right)}{\mathrm{AOD_{PI}}}\right] \times S_{\mathrm{CDNC}} \times c_{\mathrm{CDNC}}. \quad (4.2)$$

Here, S_{CDNC} is the parameter relating fractional changes in CDNC to changes in ACI ERF (-26 to -27 $\mathrm{W/m^2}$ (*71*)), c_{CDNC} is the effective cloud fraction (0.19-0.29 (*71*); effective because it incorporates information on the co-variability of the variables in equation 4.2), and $\mathrm{AOD_{PI}}$, or the preindustrial AOD, is 0.17 (*71*). Combining these produces an estimated ACI ERF trend change of $+0.2 \pm 0.1\,\mathrm{W/m^2}$/decade between the first and second decade since 2000, assuming $\Delta\left(\frac{\mathrm{dAOD}}{\mathrm{dt}}\right) = -0.01$ /decade and ignoring second-order corrections from cloud fraction and LWP feedbacks. Adding this to the earlier ARI ERF trend change estimate ($+0.088 \pm 0.018\,\mathrm{W/m^2}$/decade), gives a total aerosol ERF trend change of $+0.3 \pm 0.1\,\mathrm{W/m^2}$/decade between the first and second decade since 2000.

An aerosol ERF trend change of $+0.3\,\mathrm{W/m^2}$/decade is likely too high given energy balance constraints over the historical record (*73*), and the fact that the CDNC observations do not clearly isolate a trend change signal in figure 4.8. The application of energy balance constraints on top of pure observational estimates downscales the aerosol ERF by around 20-40% (see refs. (*5*, *17*, *71*, *73*, *186*), and chapter 3). Therefore, my overall assessment is that the aerosol ERF trend has increased by $+0.2 \pm 0.1\,\mathrm{W/m^2}$/decade between the first and second decade since 2000. Since aerosol forcing was approximately zero in the first decade since 2000 (see figure 3.2, this is equivalent to claiming total aerosol ERF has weakened by $+0.2\,\mathrm{W/m^2}$ since 2010. The lower bound of my trend change estimate ($+0.1\,\mathrm{W/m^2}$/decade) reflects the possibility that AOD trends have caused an acceleration in ARI ERF, but not in ACI ERF, since 2000.

In summary, this analysis provides evidence that the trends in aerosol emissions are well supported in current observations of the climate system. The ARI ERF trend and trend change is directly observed in the satellite record, suggesting ARI ERF trends have

increased by $+0.09 \pm 0.02\,W/m^2$/decade since 2000. Confirming the ACI contribution to the total aerosol ERF trend is more challenging since the perturbation to the cloud fields is dominated by ENSO variability in the all sky SW flux. Some confidence can be taken from the direct observation of an aerosol influence on local cloud optical properties in figures 4.8a and b, and the fact that an aerosol-induced ARI trend change is observed in clear sky SW fluxes. Using Bellouin *et al.* (2020)'s approach relating global AOD to ACI ERF, and the estimated anthropogenic AOD trend change since 2010, I estimate CDNC trend has declined by 2-5%/decade, causing the ACI ERF trend to increase by $+0.2 \pm 0.1\,W/m^2$/decade since 2000. Combining this with the ARI ERF trend change estimate means total aerosol ERF trends have increased by +0.2 to $+0.3\,W/m^2$/decade between 2000-2020. Considering all lines of evidence, including energy balance constraints from the previous chapter, I assess the total aerosol ERF trend has increased by $+0.2 \pm 0.1\,W/m^2$/decade between the first and second decade since 2000.

4.3 The aerosol contribution to recent warming trends and acceleration

4.3.1 Trends in surface temperature observations

Although decadal trends in surface temperature are influenced by the full range of anthropogenic pollutants, aerosols are unique in having a spatially-distinct pattern. That means large enough trends in aerosol emissions could become visible in GMST observations, even if they are a small contribution to the overall multi-decadal warming behaviour. The derived aerosol forcing behaviour above implies a NH-led acceleration in globally-averaged GMST trends. On top of these anthropogenic influences are short-term trends introduced by internal variability.

Figure 4.11 shows the spatiotemporal trends in HadCRUT5 surface temperature anomaly observations since 2000. The 20-year linear trend (panel a) is influenced by GHG concentration changes (*166*), aerosol emissions trends, and the underlying ocean heat uptake variability. Key patterns, including the large warming trends visible over the Arctic (*275*) and the sub-polar Atlantic 'warming hole' (*276*), have all been studied extensively. Less well-studied is the pattern in the warming acceleration since 2000.

In the NH extratropics the surface temperature pattern shows a Rossby-wave-like response in the 10-year trend change signal. Wilcox *et al.* (2019) and Tian, Dong *et al.* (2020) argue that a rapid reduction in Chinese aerosol emissions would produce a Rossby-wave response in the NH extratropics by producing a western tropical pacific heating perturbation and strengthening the Aleutian low (*155*, *230*). This is certainly consistent with the pattern in the bottom panel in figure 4.11. Observed AOD trends over the northern Pacific highlight that Chinese AOD trends are advected around the NH extratropics (figure 4.3), implying a secondary role for anthropogenic aerosol trends in the NH's Rossby wave response in figure 4.11.

This pattern in NH surface temperature is also influenced by ENSO variability, where a shift from La Niña to El Niño conditions shifts the Walker circulation, causing a western tropical pacific heating perturbation. This coupling produces a very similar spatiotemporal pattern to that expected by Chinese aerosol emissions trends since 2000 (*173*). ENSO was the single largest contribution to the western tropical Pacific heating perturbation this decade. This conclusion combines the correlation of the Niño3 index with both all sky fluxes and surface temperatures in figure 4.10, the size of the El Niño event in 2015/16, and the results discussed in chapter 3. The SH also exhibits a warming acceleration since 2000, but this is even less likely to be aerosol-forced given the size of SH emissions trends in figure 4.1. Therefore, although GMST does accelerate since 2000, it is unlikely that this acceleration is majority aerosol-induced.

Tian, Dong *et al.* (2020) discusses another mechanism by which regional aerosol emissions trends induce surface temperature responses in HadGEM3-GC31-LL (*230*): local emissions reductions cause a direct clear sky radiative heating perturbation over both Europe and Central Asia. These clear sky perturbations are easier to identify in AOD and clear sky flux observations, and have also been noted in work quantifying surface SW flux trends using in-situ observations (*228*, *265*).

The corresponding local surface temperature responses are hard to isolate in observations, since they are typically smaller than local variability. Regional warming trends are plotted on the top row of figure 4.12. European and US warming trends are positive (m=0.20 °C/decade, m=0.18 °C/decade), with both additionally showing

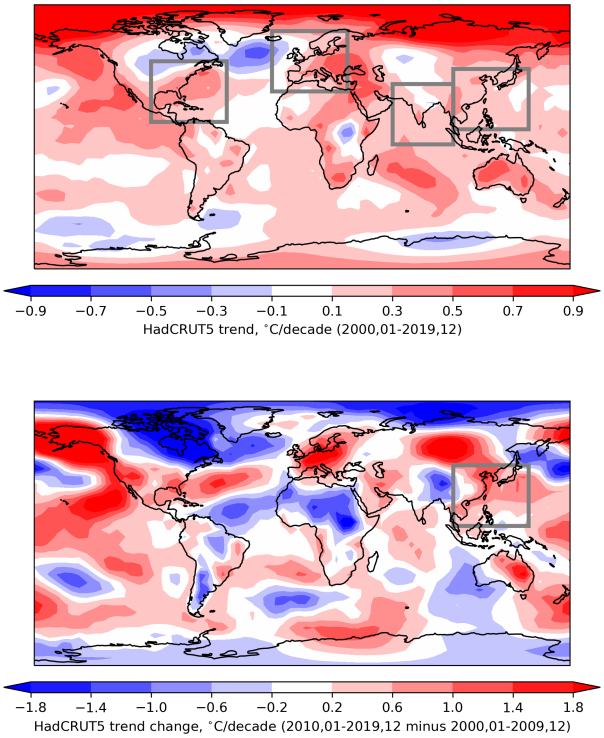

Figure 4.11: 20-year linear trends (top) and the 10-year trend change (bottom) of the HadCRUT5 surface temperature anomaly observations (2000-2019). Red-to-blue colourbar shown below each panel, with units of °C/decade. Grey boxes highlight regions of large anthropogenic aerosol emissions trends.

a positive acceleration signal. While the linear warming trend is consistent with the 20-year anthropogenic ERF trend, the acceleration is inconsistent with their local aerosol emissions trends. The acceleration behaviour is likely induced by ENSO, but may have an additional contribution from aerosol-induced cloud radiative effect trends advected around the NH from China (*155*). Further modelling of the impact of regional aerosol perturbations, like that done by Wilcox and Tian (*155*, *230*), is required to better isolate the aerosol vs. internal variability contribution to GMST trends. This is beyond the scope of this work, but has been proposed in a dedicated Regional Aerosol Model Intercomparison Project (RAMIP) (*162*). Overall, observational evidence for an aerosol-induced warming acceleration since 2000 is inconclusive.

4.3.2 Combined assessment of aerosol warming trends

Above, I established broad observational support for aerosol emissions inventories and their claim of a weakening aerosol ERF since 2010. Direct confirmation of this ERF

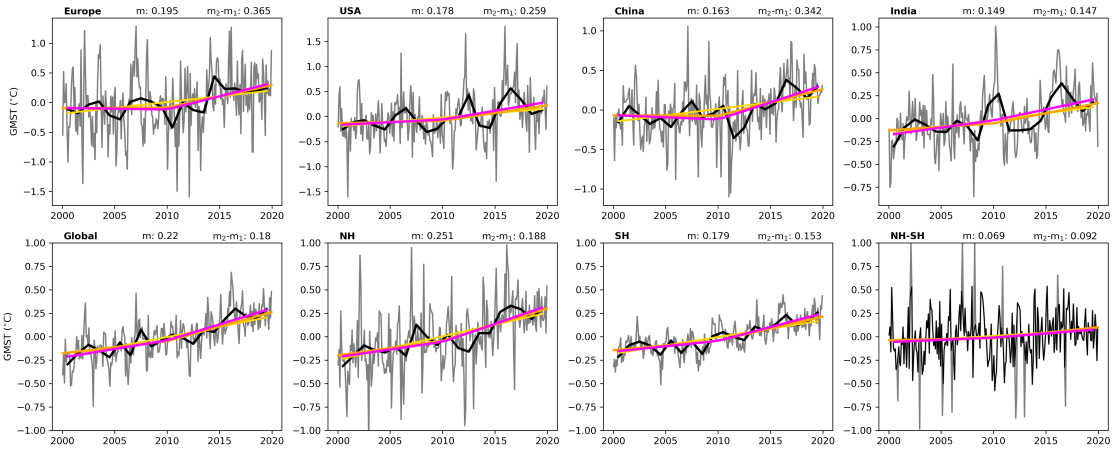

Figure 4.12: 20-year linear trends (gold) and the 10-year trend change (orange and pink) of the HadCRUT5 surface temperature anomaly observations 2000-2019. Each panel in the top row refers to a different boxed region in figure 4.10b, and each panel in the bottom row refers to a broad regional average (e.g. northern hemisphere, southern hemisphere or global). Here, NH and SH means are averaged up to $\pm 70°$, for consistency with SW flux trends, and because the poles contain strong warming trends due to so-called arctic amplification. Black lines are the annual-average surface temperature anomaly over that spatial box, with the grey lines underneath the full record including sub-annual variability. 20-year trend and 10-year trend change are reported above each sub-panel (m and m_2-m_1), with units °C/decade.

acceleration in the temperature record remains challenging. Its effect can, however, be inferred using a simple climate model. Below I use FaIRv2.0 to estimate the change in anthropogenic warming trend since 2000, following the approach used to estimate pollutants' contributions to historical warming in Forster *et al.* (2021) (*5*). This complements the attribution approach used in chapter 3.

Producing a model- and observationally-consistent aerosol ERF ensemble

I produce a globally-averaged aerosol ERF timeseries using the emissions-aerosol ERF expressions described in chapter 2. These equations use the CEDS aerosol emissions data from figure 4.1 to produce an ensemble of aerosol ERF shapes, using a 1000-member parameter ensemble based on CMIP6-emulated aerosol emissions-to-ERF relationships (see figure 2.2 in chapter 2). Figure 4.13 shows the parameter distributions which assume co-variability between each ACI parameter (β, s_{SO2} and s_{OC+BC}), and also between the OC and BC ARI radiative efficacies (α_{BC} and α_{OC}). The independent parameters (α_{OC}, α_{SO2} and β) are sampled using univariate kernel density estimation over the parameter distributions from 11 CMIP6 models (*73*). The co-varying parameters (α_{BC}, s_{SO2} and

s_{OC+BC}) are then sampled using a multivariate kernel density estimate between relevant pairs of parameters, again based on the CMIP6-model parameter distributions, as in Smith *et al.* (2021) (*73*). The co-variance in the 11 CMIP6 models' parameter sets could imply modelling groups have tuned outputs for consistency with total energy balance constraints — the ARI vs. ACI strength will correlate if model groups tune to achieve a set global energy balance overall, and the same is true for sub-components of ACI.

Note that the CMIP6 models display a bimodal structure, with two (NorESM2-LM and GFDL-ESM4) suggesting a significantly more linear emissions-to-ERF relationship. Assuming a random distribution over this bimodal structure is problematic, since the differences between sampled parameter sets may not be random but instead reflect fundamental differences in physical properties. Smith *et al.* (2021) overcame this by sampling a wide range of parameters and constraining them against GMST and ocean heat uptake observations, discarding members whose downstream properties did not conform to energy balance constraints. Further sampling of global and regional aerosol forcing properties in CMIP7 is required to understand if this bimodal structure reflects two possible 'aerosol schemes', or instead a single, poorly-sampled, smooth distribution.

Here, I use the 1000-member aerosol forcing parameter ensemble to produce a 1000-member ensemble of aerosol ERF shapes. These are then rescaled against observationally-constrained present-day aerosol ERF distribution (see refs. (*29*, *73*, *186*) for examples, and the three-way warming attribution in chapter 3) to produce an energy-balance-constrained aerosol ERF ensemble. Figure 4.14 shows the resulting ERF shapes (level on panel a, trend on panel b), with the energy-balance-constrained ensemble in blue, and the original CMIP6-model-constrained ensemble in orange. This rescaling is necessary because CMIP6 models typically exhibit larger historical aerosol ERF trends than is compatible with energy balance constraints of the climate system (*35*, *73*). Smith *et al.* (2021)'s analysis determined best-estimate aerosol ERF was -0.9 W/m^2 in 2019 relative to 1750 (5-95th percentile range spans -1.56 to -0.35 W/m^2; see table 4.1). For comparison, the pure CMIP6-model-derived aerosol ERF is -1.1 W/m^2 in 2019 relative to 1750 (5-95th percentile spans -1.78 to -0.50 W/m^2) in figure 4.14) (*5*). My energy-balance-constrained total aerosol ERF spans -0.90 W/m^2 (-1.45 to -0.41 W/m^2)

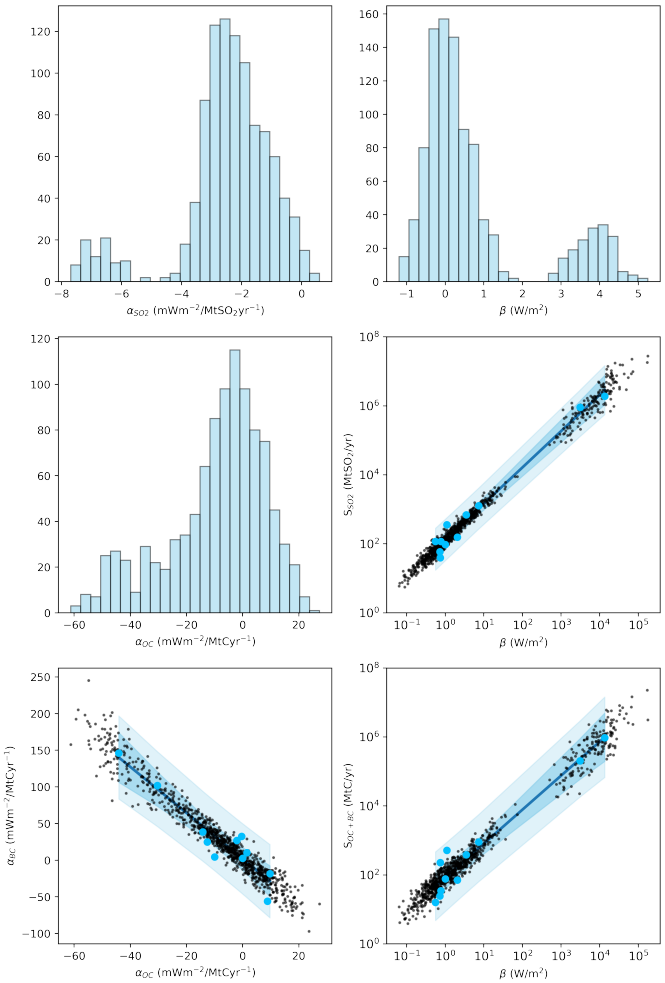

Figure 4.13: Parameter distributions for six parameters describing the aerosol emissions-to-ERF relationships defined in equations 2.22 and 2.23. α_{SO2}, α_{OC}, α_{BC} refer to ARI radiative efficacies for SO_2, organic carbon and black carbon, respectively. β is the ACI radiative efficiency, and s_{SO2} and s_{OC+BC} describe the size of non-linearities in the ACI response. Black scatterpoints show sampled co-varying distributions for this study, with emulated CMIP6 model parameters (blue scatterpoints) and OLS regressions between covarying parameters (blue lines and shaded regions). Histograms show sampled distributions for independently sampled parameters.

in 2019 relative to 1750. Various properties of the derived aerosol ERF distribution can be compared with Smith's and Forster's distributions in table 4.1.

Smith *et al.* (2021) argues that a rapid aerosol forcing recovery between 1980 and 2014 is unlikely and not consistent with the energy budget constraints, estimating the average ERF trend between 1980-2014 at around $+0.025\,W/m^2$/decade. They admit that it is not conclusive whether aerosol forcing has been strengthening, weakening, or stable in recent decades, since they did not assess the forcing trends since 2000

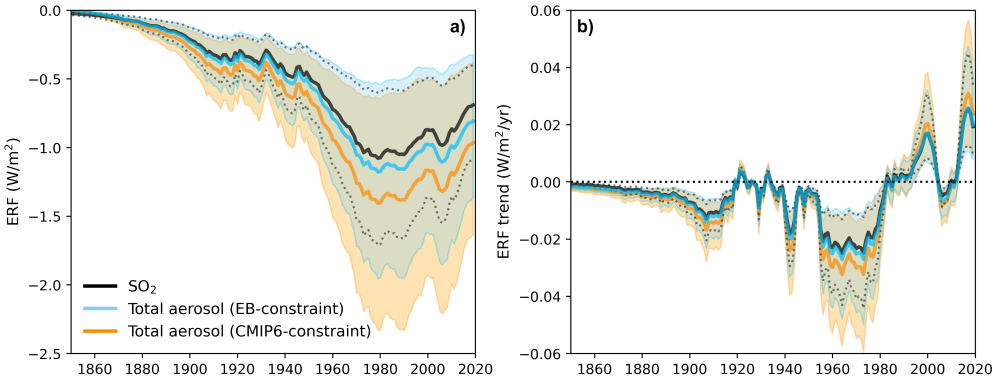

Figure 4.14: Aerosol ERF shapes between 1850 and 2020, derived using CEDS aerosol emissions inventories and the parameter ensemble in figure 4.13. Blue plume shows aerosol ERF rescaled to match an energy-balance constraint at present-day consistent with chapter 3 and Smith *et al.* (2021). Orange plume shows ERF rescaled to match CMIP6-constrained aerosol ERF at present-day. Black solid/dashed lines show the shape of SO_2-induced ERF (CMIP6-constrained). Trends in panel b are smoothed using a 10-year backward rolling mean.

in isolation. With the work in this chapter, I can go further. The ERF distribution in figure 4.14 shows similar trend structures over the wider historical period (1980-2014) — averaging +0.024 W/m^2/decade (5-95th percentile range spans -0.013 to +0.057 W/m^2/decade). Figure 4.14's (2000-2019) 20-year aerosol ERF trend is +0.078 (+0.027 to +0.154) W/m^2/decade, with the trend change between the 2010s and 2000s equal to +0.104 (+0.048 to +0.192) W/m^2/decade. The constructed ERF ensemble exhibits aerosol ERF weakening by 0.2 $\pm$ 0.1 W/m^2 since 2010, consistent with both the AR6 assessment and the satellite observations analysed above.

Aerosol-induced warming trends

I calculate the range of aerosol-induced warming using the FaIRv2.0 simple climate model (*29*), shown in figure 4.15. As outlined in chapter 2, FaIR's thermal response to ERF changes can be described by an arbitrary number of response timescales, depending on the experimental setup. In Leach *et al.* (2021) FaIR is presented with three thermal response timescales, two of which correspond to sub-decadal responses of the climate system (short-timescale land and shallow ocean heat uptake), and a third describing the multi-century thermal response (deep ocean). Earlier versions of FaIR used two timescales, with the third timescale added due to work suggesting an additional very short timescale ($d_1 \sim 1$ year) better captures the thermal response of more complex

ERF level (W/m^2) and trend (W/m^2/decade)	Interval	5th	17th	Mean	83rd	95th
Total Aerosol ERF	1750-2019	-1.45	-1.17	-0.90	-0.61	-0.41
ARI ERF	1750-2019	-0.54	-0.33	-0.18	-0.01	0.09
ACI ERF	1750-2019	-1.16	-0.90	-0.72	-0.49	-0.33
Total Aerosol ERF trend	1980-2014	-0.013	0.007	0.024	0.041	0.057
Total Aerosol ERF trend	2000-2019	0.027	0.049	0.078	0.113	0.154
Total Aerosol ERF trend change	2010s minus 2000s	0.048	0.069	0.104	0.145	0.192
Smith *et al.* (2021) Aerosol ERF	1750-2019	-1.56	-1.16	-0.90	-0.54	-0.35
Smith *et al.* (2021) Aerosol ERF trend	1980-2014	-0.074	–	0.025	–	0.111
IPCC AR6 aerosol ERF	1750-2019	-1.7	–	-1.1	–	-0.4
Total aerosol ERF (CMIP6)	1750-2019	-1.78	-1.43	-1.10	-0.75	-0.50

Table 4.1: Percentiles of the aerosol ERF level and trend distributions. First three rows refer to aerosol ERF sampled in this study and constrained using the energy-balance-constraint from Smith *et al.* (2021). Middle three rows refer to trends of energy-balance-constrained aerosol ERF from my study. Final four rows refer to Smith *et al.* (2021)'s results, the AR6 WG1 Chapter 7 aerosol ERF assessment, and the CMIP6-constrained aerosol ERF from this study. Forcing levels quoted here are reported in W/m^2 and the interval referenced refers to the span over which the ERF difference is calculated. Forcing trends quoted here are reported in W/m^2/decade averaged over the interval reported.

GCMs in fits to 4xCO_2 perturbation experiments (*189*). Forster *et al.* (2021) uses a two-box thermal model and samples parameter ranges which span the range of emulated fits to 4xCO_2 experiments in CMIP6 models. These experiments typically result in a short d_1 timescale (~1-5 years), since a very short timescale is necessary to capture the initial response in the first years following these large perturbations.

Despite the suggestion that idealised 4xCO_2 experiments are better emulated with this very short sub-decadal thermal response timescale, it is less clear this setup is best-suited for describing the response to transient ERF changes which persist over decadal timescales. In reality, relatively little is known about the $\mathbf{d}$ parameter distributions, or even the appropriate number of timescales needed to capture the multi-decadal response, as they refer to impulse response boxes which are not directly observable quantities.

The FaIR model can be setup to run identical TCR, ECS, $F_{2\times}$ parameters using *two or three* thermal timescales, allowing us to assess the warming response shape in

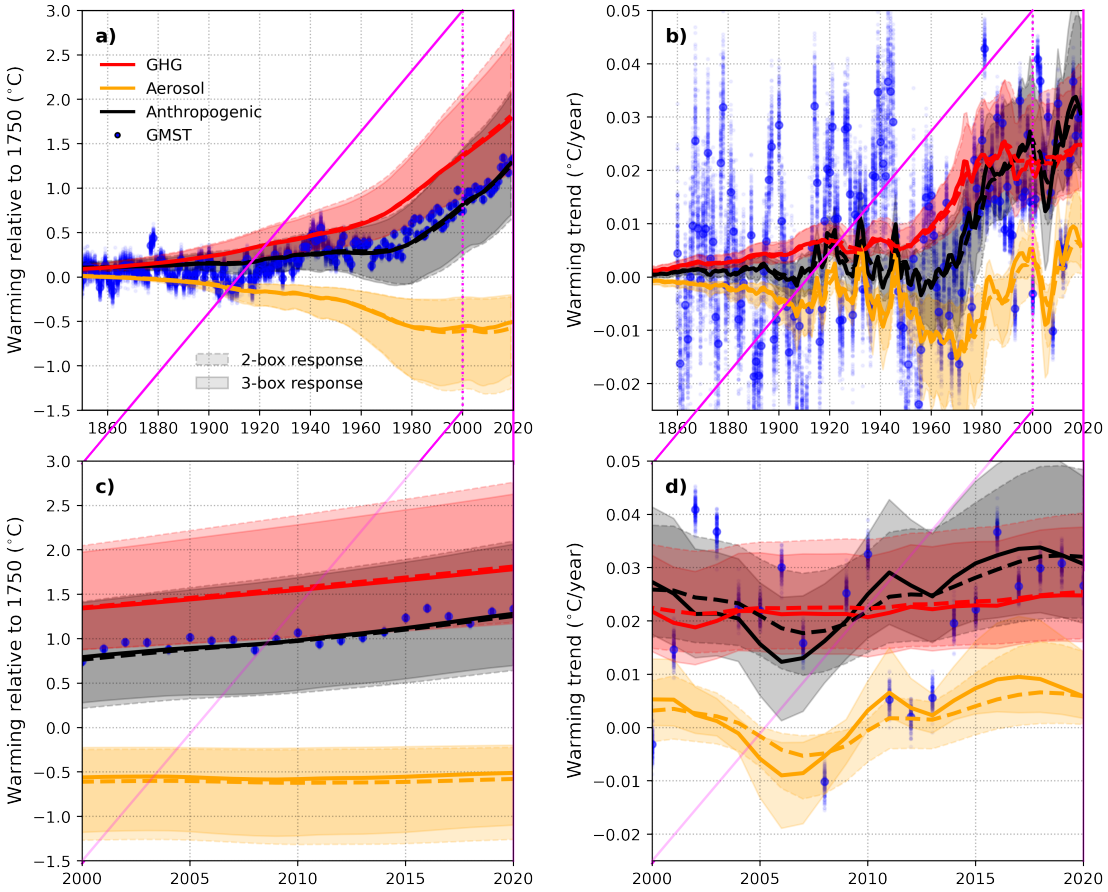

Figure 4.15: Warming attribution calculated with FaIRv2.0 using observationally-consistent and energy-balance constrained aerosol ERF distribution (see figure 4.14). GHG ERF is taken from the AR6 ERF ensemble (see figure 3.2 in chapter 3). Panels a and c show warming level, and panels b and d show the warming trend. Panels b and d zoom in on the period 2000-2020. Colours are consistent with figure 3.5 in chapter 3: red = GHG, orange = aerosols, black = anthropogenic. Blue scatterpoints show the HadCRUT5 GMST anomaly (small scatterpoints are a 200-member ensemble sampling HadCRUT5 uncertainty), with trends in all variables smoothed using a 10-year backward rolling mean in panels b and d. In the warming attribution, dashed/solid plumes use a two-/three-box thermal impulse response model in FaIRv2.0.

each case. For the three-box version of FaIR the c and d parameters are sampled using observationally-constrained distributions from Leach *et al.* (2021), whose underlying prior distributions are based on kernel density estimation of emulated CMIP6 model parameters. These produce likely distributions of TCR = 1.8 (1.4-2.2) °C, ECS = 3.2 (2.5-4.5) °C and $F_{2\times}$ = 3.75 (3.0-4.5) °C, consistent with the AR6 and Smith *et al.* (2021) assessments. The exception is the upper end of the ECS distribution sampled from FaIRv2.0 thermal cycle parameters. This is higher than the AR6 assessment, reflecting the 'medium confidence' interval placed on this upper bound by AR6 authors. The

two-box FaIR setup samples the same TCR, ECS and $F_{2\times}$ range, and uses a long thermal response timescale distribution based on fits to CMIP6 models, but exchanges the short timescale distribution for a Gaussian distribution centred on 8 years ($d_1 = \mathcal{N}(8, 2)$ years; consistent with the upper-end of samples drawn in Millar *et al.* (2015) (*277*)).

With these two FaIR parameter ensembles I compute the aerosol-induced warming response shown in figure 4.15. Table 4.2 shows percentiles of the warming response distributions for comparison against other studies. In each panel in figure 4.15 orange dashed/solid plumes show the two/three-box warming response. The level of warming in 2019 resulting from the time-history of aerosol emissions is -0.51 (-0.97 to -0.18) °C with the three-box setup, and -0.57 (-1.09 to -0.20) °C with the two-box setup, both relative to 1750. The three-box setup produces a very similar warming outcome to AR6's assessment of -0.50 (-0.96 to -0.22) °C aerosol warming in 2019 relative to 1750. In figure 4.15 the trend over the period (2000-2019) in panel d shows the importance of the choice of short timescale distribution when deriving decadal warming trends — these warming outcomes have identical ERF inputs, and identical TCR and ECS distributions, but display important differences in the decadal warming rates. This most prominently impacts on the aerosol-induced warming trend change between the 2000s and 2010s: where aerosols cause a mean warming trend change of +0.09 (+0.03 to +0.17) °C in the three-box setup, or +0.05 (+0.02 to +0.11) °C in the two-box setup. This results in a anthropogenic warming trend change of +0.11 (+0.05 to +0.20) °C/decade for the three-box setup, vs. +0.07 (+0.03 to +0.14) °C/decade for the two-box setup, despite the 20-year warming trends being nearly identical. The distributions of aerosol-induced warming levels, trends and trend changes using two- and three-box thermal models are summarised in table 4.2. There is currently no way of saying definitively which of the three-box or two-box setups are correct, however, both setups confirm the aerosol-induced warming acceleration is significantly positive.

4.4 Discussion

Emissions inventories report a dramatic reduction in anthropogenic aerosol emissions over the past two decades, causing aerosol ERFs to weaken since 2000 in globally-averaged

Warming (°C) or trend (°C/decade)	Interval	#[d]	5th	17th	Mean	83rd	95th
Aerosol-induced warming	1750-2019	3	-0.97	-0.71	-0.51	-0.29	-0.18
Aerosol-induced warming	1750-2019	2	-1.09	-0.79	-0.57	-0.32	-0.20
Aerosol warming trend	2000-2019	3	-0.006	0.007	0.024	0.041	0.059
Aerosol warming trend	2000-2019	2	-0.022	0.003	0.016	0.033	0.049
Aerosol warming trend change	2010s minus 2000s	3	0.030	0.050	0.087	0.122	0.165
Aerosol warming trend change	2010s minus 2000s	2	0.018	0.030	0.054	0.078	0.108
Anthropogenic warming	1750-2019	3	0.72	0.95	1.33	1.71	2.09
Anthropogenic warming	1750-2019	2	0.68	0.91	1.32	1.72	2.12
Anthropogenic warming trend	2000-2019	3	0.160	0.193	0.252	0.310	0.360
Anthropogenic warming trend	2000-2019	2	0.162	0.196	0.256	0.316	0.366
Anthropogenic warming trend change	2010s minus 2000s	3	0.048	0.069	0.112	0.151	0.200
Anthropogenic warming trend change	2010s minus 2000s	2	0.031	0.045	0.074	0.101	0.137
IPCC AR6 Ch7 aerosol warming	1750-2019	2 (4xCO_2)	-0.96	-	-0.50	-	-0.22
IPCC AR6 Ch7 anthropogenic warming	1750-2019	2 (4xCO_2)	1.00	-	1.29	-	1.65
HadCRUT5 GMST warming	1750-2019 (+0.09 °C)	-	1.30	1.32	1.34	1.35	1.36
HadCRUT5 GMST trend	2000-2019	-	0.262	0.271	0.280	0.291	0.294
HadCRUT5 GMST trend change	2010s minus 2000s	-	0.003	0.024	0.056	0.088	0.107

Table 4.2: Properties of the distribution of warming responses in the attribution shown in figure 4.15. Two- and three-box thermal models are used (#[d] refers to the number of thermal timescales used in FaIRv2.0), and the interval defines the period over which the warming level/trend is reported. Distributions 5th, 17th, mean, 83rd and 95th values are reported. HadCRUT5 reports GMST beginning in 1850. To shift this to the GMST anomaly relative 1750 AR6 recommends adding +0.09 °C.

timeseries produced for warming attribution studies (5). AR6 suggested a +0.2 W/m^2 increase in aerosol ERF since 2014, but did not quantify the uncertainty, or assess the impact of this change on the rate of warming this decade.

Global observations of the climate system support anthropogenic aerosol emissions trends since 2000. These emissions trends imply a positive aerosol ERF trend globally over the two decades since 2000, with a significant trend change since 2010, and major contributions from the US, European, Chinese and Indian emissions. This can be seen in several satellite observations, including in the spatiotemporal patterns of AOD, TOA SW flux anomaly and cloud optical properties. The agreement is strongest for observations which have local spatiotemporal patterns directly influenced by the aerosol burden at that location, such as AOD and the clear sky SW flux anomaly. All sky SW flux patterns are principally informed by meteorological boundary conditions and the natural variability of the climate system since 2000, but do also display regional trends in CDNC which are consistent with anthropogenic influences since 2000. CNDC has good correlation with AOD trends in the NH extratropics, particularly over regions with significant anthropogenic aerosol emissions trends since 2000. This implies a direct ACI trend contribution in the NH extratropics, despite other factors driving many of the spatiotemporal patterns in all sky flux. Combining this result with the observed clear sky SW flux trends (which support the estimated size of ARI trends since 2000), there is good support for both a positive trend and trend change contribution from aerosol ERF since 2000. I assess that the ARI ERF trend has increased by +0.09 $\pm$ 0.02 W/m^2/decade between the first and second decade since 2000, and the ACI ERF trend has increased by +0.2 $\pm$ 0.1 W/m^2/decade over the same period (both assuming a -0.01 /decade AOD trend change). Combining this with energy balance constraints (from chapter 3 and other studies (71, 73)) implies total aerosol ERF trend has increased by +0.2 $\pm$ 0.1 W/m^2/decade between the first and second decade since 2000. The low end of this uncertainty range reflects the weaker observational evidence of an aerosol-induced acceleration signal in cloud structures since 2000.

The importance of the choice of poorly-constrained thermal response timescales in simple climate models is underappreciated in the IPCC's standard attribution procedures.

In FaIR this uncertainty is sufficient to alter the decadal warming trend by ±50%. This, along with the accuracy of underlying aerosol emissions inventories, highlight two key weaknesses for the assessment of the current warming trend in AR6 (*8*).

4.5 Chapter close

This chapter used observations to evaluate evidence for an aerosol ERF acceleration since 2000. I determined that aerosol forcing trend has likely increased by $+0.2 \pm 0.1\,\mathrm{W/m^2}$/decade between 2000-2020, causing the AGW trend to increase by +0.07 (+0.03 to +0.14) °C/decade between 2000-2009 and 2010-2019. The exact aerosol contribution to the GMST trend depends on the assumed short-timescale thermal response of the climate system. The aerosol-induced acceleration is temporary, only existing while aerosol emissions are declining, but could continue to have a contribution to warming trend assessments over the next two decades.

The future depends on what you do today.

— Mahatma Gandhi

5

Quantifying non-CO_2 contributions to remaining carbon budgets

This chapter discusses an observational constraint on the TCRE parameter, and uses the CO_2-forcing-equivalent metric to include non-CO_2 pollutants in the remaining carbon budget framework. This work is based on the publication *Quantifying non-CO_2 contributions to remaining carbon budgets.* Jenkins, S., Cain, M., Friedlingstein, P., Gillett, N., Walsh, T. and Allen, M. (2021). NPJ Climate and Atmospheric Science. See ref. (*278*).

Contents

5.1 Introduction

In the previous two chapters I derived constraints on the level and rate of warming at present day. I focused on aerosols, since these contribute the largest uncertainty to the warming rate assessment over the recent historical period. I estimated the level of warming was 1.1 °C over the decade 2010-2019, rising to 1.3 °C by 2020, with the rate of anthropogenic warming around +0.3 °C/decade since 2010. Building from this assessment, I now discuss the physical constraints on future policy design. This chapter focuses on quantifying the contributions from CO_2 and non-CO_2 pollutants to the remaining warming budget between now and the 1.5 °C temperature threshold set out in the Paris Agreement (*39*).

The basis for this discussion is the carbon budget framing I introduced in chapter 1, which defines a total quantity of CO_2 emissions available until a given warming threshold is exceeded. This approach relies on the TCRE parameter (*99*, *100*) defining a linear proportionality between cumulative CO_2 emissions and CO_2-induced warming. Defining a remaining carbon budget makes sense for policymakers because most warming to date has been caused by CO_2 (*93*, *279*, *280*), and CO_2, of all major pollutants, has the most permanent impact on the climate system (*42*, *93*, *281*). Chapter 1 noted several complications (*14*, *42*, *47*, *282*) in the use of TCRE to derive the remaining carbon budget, including the estimate of the historical anthropogenic warming level; the size and sign of the ZEC; possible contributions of Earth System Feedbacks to future warming; uncertainty in the estimated value of the TCRE; and the future contribution of non-CO_2 climate pollutants. Of these, the contribution of non-CO_2 pollutants is unique in that it depends on future policy decisions, not simply scientific uncertainty.

In this chapter I focus on carbon budgets corresponding to increases in GMST. This is different to the IPCC's AR6 report, whose headline outputs are GSAT budgets. Previous studies have suggested that changing sea-ice cover precludes the use of GMST in projections (*283*). However, figure 3f of Tokarska *et al.* (2019) indicates very limited impact of sea-ice retreat on GMST under ambitious mitigation scenarios (*283*),

while under sustained warming the impact would correspond to a couple of years of warming at most. Therefore, changing sea-ice cover does not present any fundamental impediment to the use of GMST. Further, recent updates to GMST datasets have largely accounted for differences against GSAT using statistical infilling approaches (*43*). As in the previous chapters, I use a global temperature anomaly calculated from a 4-dataset mean of these statistically infilled GMST products: HadCRUT5 (*43*), NOAA (*177*), GISTEMP (*211*) and BerkeleyEarth (*167*) (similar to the approach taken in Allen *et al.* (2018) (*16*)) to reduce the impact of any individual dataset, and to ensure that conclusions are consistent with the estimates of the current level and rate of increase of anthropogenic global warming in chapters 3 and 4.

Figure 1.1 in chapter 1 showed how the recent updates to these GMST datasets (relating to the improvement of statistical infilling approaches), along with updated ERF datasets, have revised the present decade's warming level and rate up compared to earlier products. This presents a hazard for policymakers: using different indices to report observed warming (e.g. the reference period chosen in the Structured Expert Dialogue (*284*) informing the Paris Agreement) and to calculate carbon budgets (*283*) raises the possibility of the carbon budget being exhausted well before a temperature threshold is reached, potentially undermining confidence in the entire construct. Following SR1.5 and AR6, this chapter focuses on remaining carbon budgets consistent with halting warming to 1.5 °C or 2.0 °C over a *multi-decade period*, relative to 1850-1900. In the derivation of the TCRE concept in chapter 2 I discussed how the multi-decadal ZEC behaviour and TCRE are related by the properties of the multi-century thermal and carbon cycle responses. This introduced the RAZE parameter, which determines the precise conditions for warming stabilisation over mutli-decadal timescales. In this chapter the RAZE term is ignored (equivalent to setting the ZEC to zero) — this is the standard approach used in recent assessments of the remaining carbon budget (*47*). The exact requirements for warming stabilisation, having included the RAZE behaviour, are studied in chapter 6.

Rogelj *et al.* (2019)'s approach to calculating the remaining carbon budget relies on subtracting a distribution of warming responses to non-CO_2 sources from the target total warming and estimating a CO_2 budget for the remainder (*14*, *41*, *47*). However, a

predetermined quantity of non-CO_2 warming should not simply be subtracted from the total remaining warming without considering the accompanying impact of co-varying physical climate uncertainty implicit in the choice of TCRE. Despite this, most headline assessments of the remaining budget (*3*, *14*, *47*, *84*) all remove a quantity of warming attributed to non-CO_2 pollutants independent of the sampled TCRE percentile.

A more transparent treatment of non-CO_2 climate drivers uses CO_2-fe emissions (*94*), meaning the CO_2 emissions timeseries that would give precisely the same impact on ERF and thence GMST. This is similar to the approach of Mengis *et al.* (2018), although they use a single representative non-CO_2 forcing scenario (*285*). By doing this I can explicitly sample the physical climate response uncertainty for both CO_2 and non-CO_2 contributions identically, and more clearly separate scenario and physical response uncertainties in non-CO_2 contributions.

5.2 CO_2-forcing-equivalent emissions in ambitious mitigation scenarios

CO_2-fe emissions (*124*) express an emissions timeseries of any climate pollutant in terms of the timeseries of CO_2 emissions that would have an identical impact on ERF, and hence GMST, on all timescales. They are obtained by converting the ERF associated with that pollutant to a timeseries of change in CO_2-equivalent concentrations, and then computing the CO_2 emissions required to produce that CO_2 concentration perturbation using a carbon cycle model (*94*). Chapter 2 gives a full explanation of the CO_2-fe methodology.

The principal benefit of using the CO_2-fe metric is that it allows direct comparison between the CO_2 and non-CO_2 contributions in a complex multi-gas emissions scenario. Figure 5.1a plots a number of scenarios for future CO_2 emissions from the IIASA SR1.5 scenario database (*280*), which were also used in AR6. They are coloured by ambition according to their label in the database; dark blue corresponds to scenarios tagged as '1.5 °C-compatible', light orange corresponds to 'lower-2 °C-compatible', and dark orange corresponds to 'higher-2 °C-compatible'. Panel b below shows the cumulative CO_2 emissions relative to 2018, which can be translated into the CO_2 warming contributions by multiplying by the TCRE. Panel c shows the corresponding

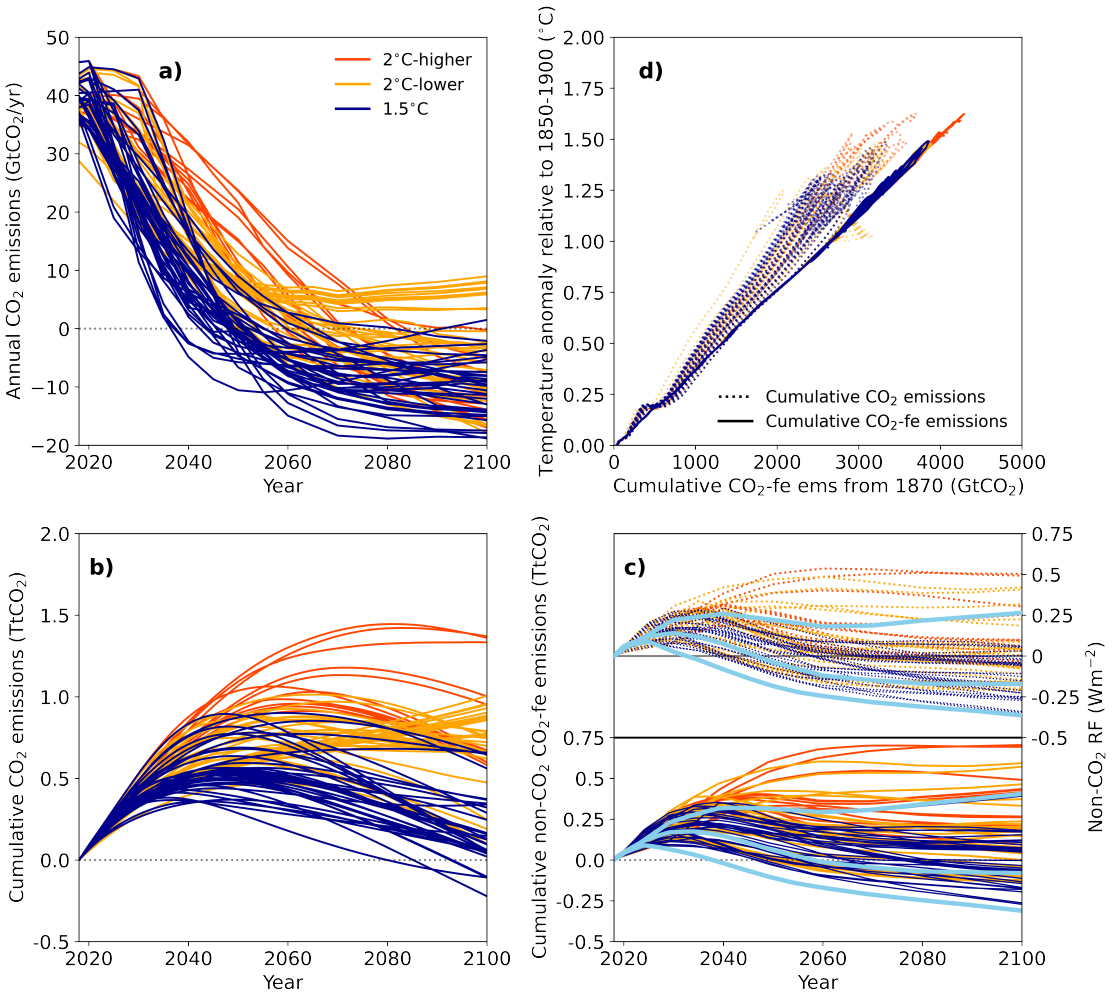

Figure 5.1: IIASA IAMC database of scenarios in the IPCC Special Report on the Global Warming of 1.5 °C. Panel a plots the annual CO_2 emissions. Panel b (below a) shows the running sum (or cumulative) CO_2 emissions from 2018. Panel c (bottom right) shows the non-CO_2 radiative forcing for each scenario (dotted lines, right hand axis). Also on panel c are the cumulative non-CO_2 CO_2-fe emissions from 2018 corresponding to each non-CO_2 RF line (solid lines, left hand axis). The axes of panels b and c are scaled so the cumulative emissions from CO_2 and non-CO_2 are directly comparable. Panel d plots the FaIRv2.0-derived temperature response against the diagnosed cumulative CO_2-fe emissions (solid lines) and against the cumulative CO_2-only emissions (dotted lines). For FaIR temperature response TCR=1.8 °C, ECS=3.0 °C. Scenarios are coloured by category in the IAMC database: red for 2 °C-higher, orange for 2 °C-lower and blue for 1.5 °C-compatible. Light blue scenarios in panel c highlight some example non-CO_2 pathways (lower bound, upper bound and a central scenario from 1.5 °C-compatible dark blue plume) with the central light-blue scenario (P3 scenario from SR15 SPM.3b) also used in figures 5.2 and 5.3.

non-CO_2 ERFs for each CO_2 emissions pathway (dotted lines, right axis), which describe the net energy imbalance contributed by the multi-gas non-CO_2 mitigation scenarios. To compare these non-CO_2 scenarios to the CO_2 emissions one cannot simply multiply their emissions by the TCRE as was done for CO_2, since the non-CO_2 warming response is non-linear and species dependent. Because of this the total warming to the CO_2+non-CO_2 mitigation scenario is also non-linear when plotted against cumulative CO_2 emissions alone (dotted lines in panel d).

If, instead, the non-CO_2 ERFs are expressed as cumulative CO_2-fe emissions, they are now physically equivalent quantities and the cumulative CO_2/CO_2-fe emissions timeseries in panels b and c (solid lines, left axis) can be directly compared. This would not be possible with CO_2-equivalent emissions calculated using the GWP or GTP metrics which were introduced in chapter 1, since these do not accurately reproduce the warming outcome for a complex multi-gas emissions pathway involving pollutants with very different efficacies and lifetimes (*129*).

To calculate the CO_2-fe emissions attributable to a subset of the total anthropogenic ERF time series, e.g. the non-CO_2 component or $\Delta F(t)$, I difference the annual CO_2-fe emissions calculated from the total forcing (i.e. using $F_{anthro}(t)$), and the annual CO_2-fe emissions calculated from the total forcing minus the forcing component of interest: (i.e. using $F_{anthro}(t) - \Delta F(t)$). This differencing approach is suggested in Jenkins *et al.* (2018) when calculating subsets of the total CO_2-fe emissions timeseries, as this best accounts for non-linearities in the carbon cycle response to under high ERF perturbations (*94*). The similarity of the dotted and solid lines in figure 5.1c shows that, over these scenarios and timescales, a $1\,W/m^2$ change in ERF is approximately equivalent to $1000\,GtCO_2$-fe, consistent with fig. 8.29 of Myhre *et al.* (2013) (*68*).

By converting the full range of pollutants into cumulative CO_2-fe emissions the TCRE can now be used in the same way as would be done for CO_2 alone. Figure 5.1d shows global temperatures plotted against cumulative total CO_2-fe emissions (solid lines). Cumulative total CO_2-fe emissions multiplied by the TCRE predicts the temperature response just as in a pure-CO_2 scenario (a linearity exists between cumulative emissions and temperature on panel d). If non-CO_2 radiative forcing were

correlated with cumulative CO_2 emissions in these scenarios, then the latter would also predict the response with a simple scaling factor, or 'effective TCRE', to account for a constant fractional contribution to warming from non-CO_2 drivers (*92*, *105*, *286*). Figure 5.1d shows this is not always the case (nor is there any physical reason for it to be the case in complex multi-gas future scenarios) (*287*): hence the impact of non-CO_2 forcing needs to be treated explicitly.

5.2.1 The non-CO_2 contributions to a 1.5 °C-compatible scenario

Having explained the utility of the CO_2-fe metric for assessing the relative CO_2 and non-CO_2 contributions to warming in mitigation scenarios, I now turn to a single scenario and explore the contributions from individual pollutants in greater detail. The three light blue scenarios in figure 5.1 display the range of non-CO_2 ERF pathways exhibited in 1.5 °C-compatible scenarios, with the central light blue pathway highlighting the P3 scenario from SR1.5's SPM figure 3b (*14*) (a middle of the road scenario which achieves 1.5 °C ambition). Figure 5.2 shows a breakdown of the total CO_2-fe emissions timeseries for this central light blue scenario in figure 5.1c. The mitigation scenario (2015-2100) chosen is extended back to preindustrial using the historical ERF timeseries from Dessler and Forster (2018) (*74*) (the same as shown in figure 3.2). In figure 5.2's scenario aerosol ERF averages -0.90 W/m^2 over the decade prior to 2020 (consistent with energy-balance studies (*29*, *73*), and the results of chapters 3 and 4). I calculate individual CO_2-fe emissions contributions using a differencing approach used above to estimate the non-CO_2 CO_2-fe emissions in figure 5.1, and described in chapter 2. These individual contributions are stacked and coloured by pollutant, with panel a showing the annual CO_2-fe emissions, and panel b showing the same cumulatively. In contrast to CO_2-equivalent emissions, whether computed with GWP_{100} or any other conventional metric, CO_2-fe emissions reflect the impact of individual climate drivers on global temperature (panel c), allowing them to be compared objectively. CO_2-fe provides a transparent and easily implementable approach which translates readily to warming: cumulative emissions contributions in panel 5.2b correspond to warming levels

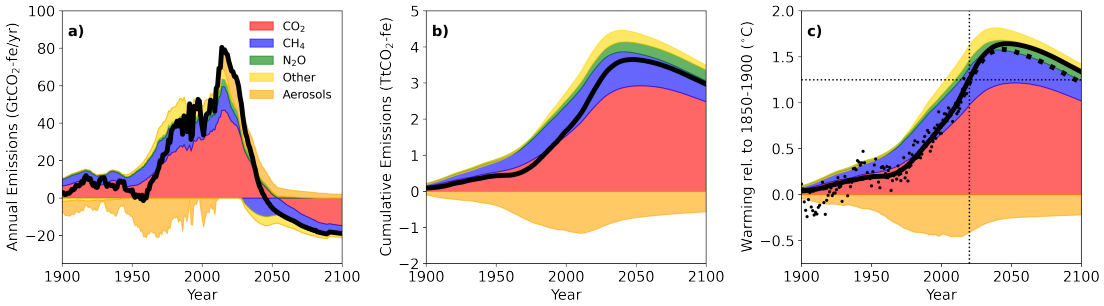

Figure 5.2: Central light-blue 1.5 °C-compatible scenario from figure 5.1 displayed showing component contributions to warming. Panel a plots the annual CO_2 emissions and CO_2-fe emissions for each of the major contributing pollutant (red = CO_2, blue = CH_4+Ozone+Strat. H_2O, green = N_2O, gold = Other, and orange = Aerosols). Panel b shows the corresponding cumulative CO_2 and CO_2-fe emissions timeseries (stacked by contribution to total). Panel c plots the temperature response for each component. Black solid lines show the total annual (panel a) and cumulative (panels b and c) CO_2-fe emissions, while the total temperature response is shown with a black dotted line (all calculated from total ERF). Small back scatter points on panel c show the annual temperature observations using 4-dataset mean observations updated from SPM.1, SR1.5. FaIR-derived temperatures (panel c) use thermal parameters chosen to best emulate historical temperatures (TCR=1.8 °C, ECS=3.0 °C). ERFs before 2020 are taken for individual components from Dessler and Forster (2018)'s ERF dataset, with future ERF components from SR1.5's figure SPM.3b's P3 scenario, rescaled to match the best-estimate historical ERF in 2020. CH_4 forcing is scaled by 1.65 to account for Ozone and stratospheric H_2O contributions, following refs. (*68*, *125*). Aerosol forcing is approximately -0.9 W/m^2 in the decade 2010-2019, consistent with energy-balance-constrained estimates from chapters 3 and 4 and literature estimates (e.g. refs. (*5*, *68*, *73*)). Thin dotted lines show the best-estimate anthropogenic warming level from chapters 3 and 4 (~1.3 °C in 2020).

in panel 5.2c (I have used a TCRE of 0.4 °C/$TtCO_2$ — the best estimate TCRE found using an observationally-constrained methodology described in section 5.4 below).

Note that the calculation of CO_2-fe emissions is not model specific: with a linear CO_2 impulse response function (as used for the calculation of GWPs) one can calculate CO_2-fe emissions with a simple matrix inversion and get very similar results (see Allen *et al.* (2021) (*288*)). The accuracy of CO_2-fe emissions for representing the radiative forcing and therefore temperature impacts of long- and short-lived pollutants gives it clear advantages over GWP_{100} for presenting mitigation scenarios aimed at limiting global warming (*129*).

On figure 5.2 LLCPs like N_2O behave similarly CO_2: cumulative LLCP emissions are proportional to warming. Contrasting this, SLCPs like CH_4 make a net positive contribution to annual CO_2-fe emissions until they begin to rapidly decline in the 2030s.

Thereafter, the short atmospheric residence time of CH_4 (*125*) means that falling CH_4 emissions give a declining ERF, equivalent to negative CO_2-fe emissions in figure 5.2a. Aerosol cumulative CO_2-fe emissions in figure 5.2b are negative (corresponding to their negative ERF and warming contributions), but show a sharp increase towards zero in the 2020s and 2030s, corresponding to a high associated CO_2-fe emissions rate (orange in figure 5.2a), and consequently a rapid removal of the cooling effect that aerosols have contributed over history.

Remember that the positive aerosol CO_2-fe emissions in panel a occur while real aerosol emissions are declining. Hence, according to the analysis of chapters 3 and 4, the aerosol CO_2-fe emissions should be positive in the 2010s as well. The fact that figure 5.2's scenario does not show this behaviour highlights that SR1.5's scenarios did not include the rapid aerosol mitigation assumptions over the period 2015-2020. Figure 5.2 also highlights the 'co-mitigation assumption' used in 1.5 °C scenarios, where positive future aerosol CO_2-fe emissions are offset by negative CH_4 CO_2-fe emissions, reducing the net non-CO_2-induced warming. This is not what has occurred in reality in the 2010s, where instead aerosol emissions have reduced but CH_4 emissions have not. If this co-mitigation assumption remains invalid in the 2020s the rate of warming will continue to lie well above +0.2 °C/decade, resulting in '1.5 °C-compatible' scenarios according to SR1.5 exceeding 1.5 °C peak warming (see figure 5.2c).

Figure 5.2 acts as a useful schematic revealing the relative contributions from individual pollutants between present decade and net zero in an ambitious mitigation scenario. Total cumulative CO_2-fe emissions and total anthropogenic warming are approximately proportional to the combined warming impact of CO_2 and CH_4, as indicated by cumulative CO_2-plus-CH_4 CO_2-fe emissions, up to the present day (red and blue in figures 5.2b,c), but diverge rapidly over the coming decades as aerosol forcing declines (orange). Strikingly, this aerosol decline contributes almost as much to future warming as remaining CO_2 emissions in this central 1.5 °C-compatible scenario (panel c), highlighting the importance of common and comparable presentations of all climate drivers in the remaining budget framework. Aerosols are often not included

in figures showing multi-gas emission scenarios (*158*) because of the lack of a non-arbitrary way of displaying them on a common axis. This problem is resolved by CO_2-fe. Individual contributions to CO_2-fe emissions from 2020 to the time of peak warming under this scenario are: CO_2: 555 $GtCO_2$; CH_4: -65 $GtCO_2$-fe; N_2O: 65 $GtCO_2$-fe; aerosols: 290 $GtCO_2$-fe; other forcings: -45 $GtCO_2$-fe; giving a total CO_2-fe budget of 800 $GtCO_2$-fe.

This total CO_2-fe budget produces approximately +0.3 °C additional warming from 2020 (again using a TCRE of 0.4 °C/$TtCO_2$). As highlighted above, whether this is '1.5 °C-consistent' depends on the assessed present-day warming level. SR1.5 and AR6 produced very similar assessments of the 2010-2019 decade-average warming (~1.1 °C). The SR1.5 scenarios analysed here did not contain the rapid aerosol emissions decline in the 2010s which is now suggested in CEDS aerosol emissions inventories (*63*). Without this aerosol emissions decline in the 2010s, attributed anthropogenic warming was approximately 1.2 °C in 2020 (see table 1.1), and consequently the 800 $GtCO_2$-fe remaining carbon budget would be consistent with limiting warming to 1.5 °C. Instead, if the more recent aerosol emissions updates are included, as is the case in figure 5.2, the 2020 warming was approximately 1.3 °C (see chapters 3 and 4). This alters the requirements for 1.5 °C-compatibility for these high-ambition mitigation scenarios (see the stylised example in figure 1.1 in chapter 1) — figure 5.2's scenario now exceeds 1.5 °C at peak warming. Revised 1.5 °C budgets which are compatible with the previous chapters' present-day warming attribution are estimated below.

5.3 Observational constraints on the TCRE

Having demonstrated how the TCRE can be extended to multi-gas scenarios using CO_2-fe emissions, I now consider how CO_2-fe emissions can be used to investigate the TCRE itself. Previous TCRE estimates (*107*) have compared cumulative pure-CO_2 emissions with warming attributable to CO_2 alone, but the fractional uncertainty in the latter is higher than uncertainty in total anthropogenic warming. Comparing total anthropogenic warming with total cumulative CO_2-fe emissions over the historical record presents a useful complementary approach.

I estimate the TCRE in figure 5.3 using an observationally-constrained methodology. To estimate anthropogenic warming over the historical period I again use the Haustein *et al.* (2017) (*15*) attribution approach. As was done in figures 3.4 and 3.5 of chapter 3, this attribution uses the FaIRv2.0 simple climate model in a two-timescale thermal impulse response model configuration (*29*, *42*, *78*). I use an ensemble of physical response parameters (20 members; sampling the AR6 range of TCR and ECS parameters, and several short and long thermal response timescales, identically to Haustein (*15*)) to estimate temperature responses to the 1000-member anthropogenic and natural ERF ensemble (*74*) from chapter 3. These FaIR-derived temperature response ensembles are then regressed against GMST observations, with added CMIP6 PIControl simulations (104 members (*36*)) and observed GMST uncertainty (200 members (*43*)) included to account for internal variability. Based on this, estimated anthropogenic warming is 1.1 °C (1.0-1.2 °C) between 2010-2019 relative to 1850-1900, consistent with both the SR1.5 and AR6 estimates (*3*, *14*). To avoid the uncertainty introduced by very recent warming rate assessments the anthropogenic warming estimates used to calculate the TCRE are averaged over the decade 2010-2019.

I express the 1000 anthropogenic ERF timeseries as CO_2-fe emissions pathways by inverting FaIRv2.0's carbon cycle (as derived in chapter 2), with carbon cycle response parameters determined by best-estimate fits to the historical relationship between carbon emissions and concentrations from Jenkins *et al.* (2018). I account for uncertainty in cumulative CO_2 airborne fraction to date (0.40 ± 0.04 (*289*)), and the carbon cycle feedbacks due to the raised warming level (*94*), by sampling the feedback parameters setting the dynamics of the carbon cycle impulse response model (r_0, r_C and r_T; see equation 2.21), using their distributions derived in Jenkins *et al.* (2018) (*94*). This assessment determines present day total anthropogenic CO_2-fe emissions were around 2900 ± 600 $GtCO_2$-fe for the decade 2010-2019, relative to 1850-1900 (*94*).

Dots in figure 5.3a show estimates of the total anthropogenic warming and cumulative all-pollutant CO_2-fe emissions, coloured by decade. For example, pink dots in figure 5.3a sample the resulting joint distribution of cumulative anthropogenic CO_2-fe emissions 2015 relative to 1875, and human-induced warming to the decade 2010-2019 relative

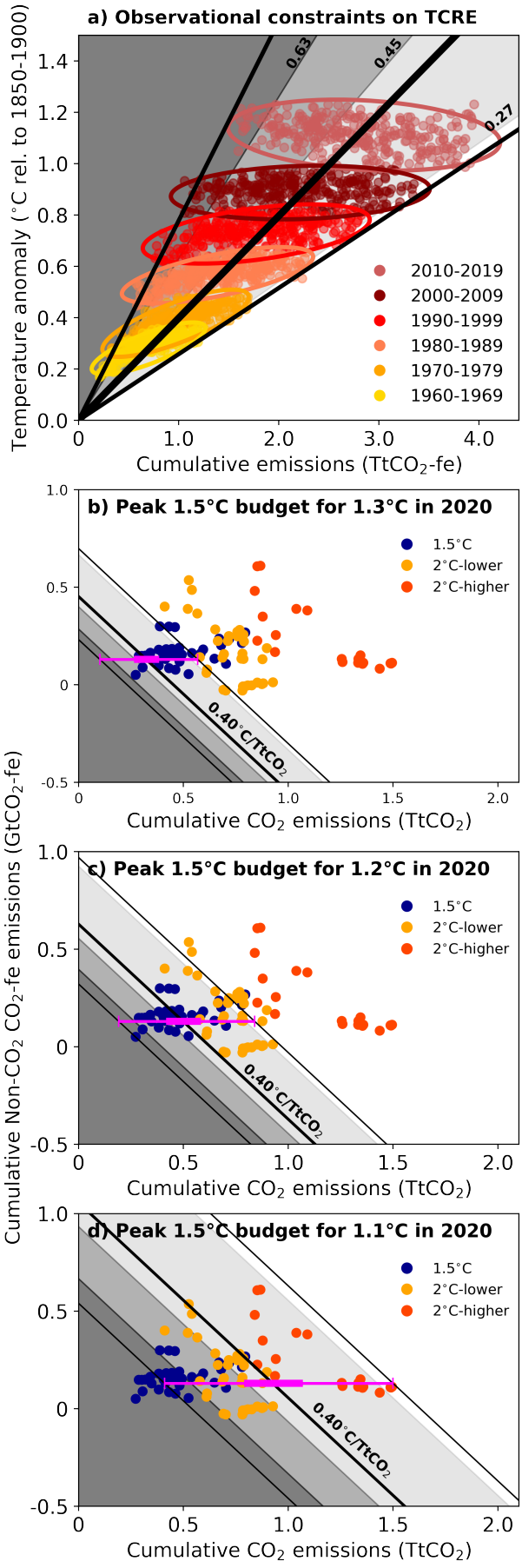
a) Observational constraints on TCRE
0.63
0.45
0.27
2010-2019
2000-2009
1990-1999
1980-1989
1970-1979
1960-1969
Temperature anomaly (°C rel. to 1850-1900)
Cumulative emissions (TtCO2-fe)
b) Peak 1.5°C budget for 1.3°C in 2020
c) Peak 1.5°C budget for 1.2°C in 2020
d) Peak 1.5°C budget for 1.1°C in 2020
1.5°C
2°C-lower
2°C-higher
0.40°C/TtCO2
Cumulative Non-CO2 CO2-fe emissions (GtCO2-fe)
Cumulative CO2 emissions (TtCO2)

Figure 5.3 ***(previous page)*****:** Observational constraints on the TCRE and consequences for design of Paris Agreement-compatible scenarios. Panel a plots attributed human-induced warming against cumulative emissions of CO_2. The space is shaded by the value of the TCRE (gaussian distribution in best-estimate and likely range in AR6) and the points are coloured by decade in which the temperature (relative to 1850-1900 baseline) and cumulative CO_2-fe emissions (relative to 1875) are diagnosed. An ellipse is drawn around central 90% of points. Black lines in panel a depict the 5th, 50th and 95th percentile of the overall observationally-constrained TCRE distribution based on the 2010-2019 decade. Panels b, c and d show the remaining CO_2 and non-CO_2 CO_2-fe budgets to peak warming from 2020 for each scenario in figure 5.1, coloured by category in the IIASA SR15 database. In all three panels shading shows budgets compatible with limiting warming to 1.5 °C for the AR6 Gaussian TCRE likely range, as in panel a. The solid black lines show the corresponding remaining total CO_2-fe budgets instead using our observationally-constrained TCRE 5-95th percentile range. Each panels shading corresponds to budgets for a set quantity of residual warming: +0.2 °C remaining warming to 1.5 °C (panel b), +0.3 °C (panel c), or +0.4 °C (panel d). Pink horizontal box-whisker plots in panels b, c and d show estimates of remaining CO_2 budgets for each assumed present-day warming level, assuming a mid-range non-CO_2 budget to peak warming (130 $GtCO_2$-fe) and plotting the 5th, 33rd, 66th and 95th percentiles.

to 1850-1900. The cumulative anthropogenic CO_2-fe emissions and human-induced warming estimate for each dot correspond to the same ERF timeseries to account for any covariance, while CO_2 airborne fraction and internal climate variability are sampled independently. Shading shows the AR6 gaussian TCRE distribution (0.27-0.63 °C/$TtCO_2$), with the likely range and median values highlighted on the figure. Ellipses are drawn around each decade's scatter of co-varying temperature anomaly and cumulative CO_2-fe emissions, encompassing the central 90% of the distribution, also coloured by decade, using a similar approach to that used in fig. 1 in Otto *et al.* (2013) (*87*). The observationally-constrained range of TCREs found in figure 5.3 is 0.26-0.78 °C/$TtCO_2$ (central 90 percent of distribution) with a best-estimate value of 0.40 °C/$TtCO_2$, marked with black lines in panel a. These could be interpreted as median and 5-95th percentiles of a probability distribution if the input ERF pathways are assumed to be equiprobable, but more research characterising the distribution of uncertainty in radiative forcing to date is needed (*71*). Note that, because CO_2-fe remains physically coherent irrespective of time horizon, previous decades' TCRE estimates (the other ellipses in figure 5.3a) also align with the estimated TCRE range from only the most recent decade. The observationally-constrained TCRE distribution

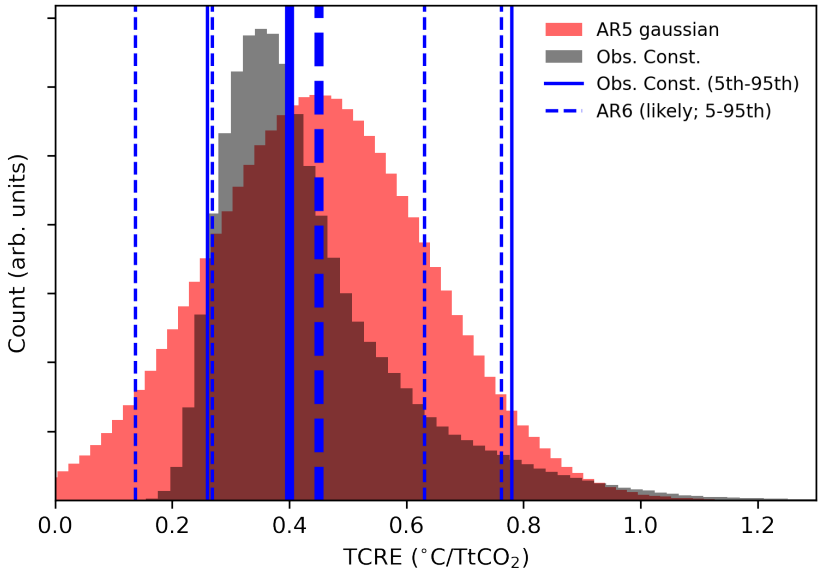

Figure 5.4: TCRE distribution derived in figure 5.3 (black) and the AR6 Gaussian distribution (red). Solid blue lines show the best-estimate and 5-95th percentile range of the observationally-constrained distribution from this study; dotted blue lines show the best-estimate, 17th-83rd and 5-95th range of the AR6 Gaussian TCRE distribution for comparison.

has a log-normal shape and is plotted in figure 5.4.

For comparison, SR1.5 used a likely TCRE range of 0.22-0.68 °C/TtCO$_2$ and also includes a 100-200 GtCO$_2$ budget correction accounting for differences between gaussian and log-normal TCRE distributions. TCREs derived from the CMIP6 1%/yr CO$_2$ concentration increase experiment lie in the range 0.36-0.63 °C/TtCO$_2$ (*104*). Other groups (*290*) have additionally noted that the inter-model spread in TCRE is strongly affected by cloud feedbacks, particularly in high sensitivity models. Mengis and Matthews (2020) uses the CO$_2$-fe metric to demonstrate the bias introduced by assuming a constant fractional non-CO$_2$ contribution to warming in TCRE assessments, and estimate the TCRE using a single warming pathway (~0.5 °C/TtCO$_2$) (*287*). Matthews *et al.* (2021) estimates an observationally-constrained TCRE by removing a fractional warming contribution attributed to non-CO$_2$ pollutants, finding a median TCRE of 0.44 °C/TtCO$_2$ (0.32-0.62 °C/TtCO$_2$ 5-95th percentile range) (*291*). Both these approaches could be considered adaptations of the 'effective TCRE' approach I critiqued above (since the fractional non-CO$_2$ contribution is time varying). I argue that the contribution from non-CO$_2$ pollutants should be determined explicitly using the CO$_2$-fe methodology.

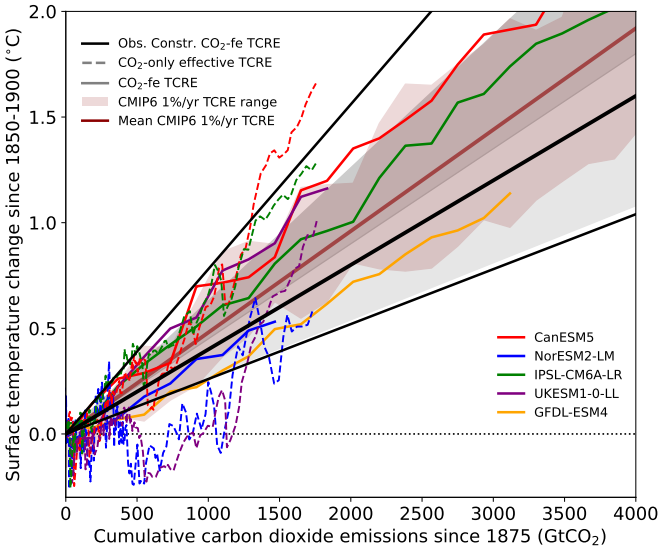

Figure 5.5: TCREs calculated for a range of CMIP6 models. FaIRv2.0 simple climate model used to emulate the carbon cycle and thermal responses of each GCM with parameters from Leach *et al.* (2021); forced with ERF timeseries diagnosed from ERF experiments completed as part of RFMIP. UKESM1-0-LL and GFDL-ESM4 calculated GCM diagnosed aerosol ERF timeseries over 1850-2014; NorESM2-LM, IPSL-CM6A-LR and CanESM5 calculated using transient anthropogenic ERFs from RFMIP runs (1850-2100). Solid lines show individual CMIP6 model TCREs calculated with CO_2-fe over historical experiments (coloured by model), while dashed lines show CMIP6 models if the effective TCRE is plotted (1850-2014) from Liddicoat *et al.* (2021). Brown plume shows the CMIP6 TCRE range calculated with 1%/yr concentration increase experiment (from Arora *et al.*, 2020). Grey shading shows the AR6 Gaussian TCRE range, and black lines shows the observationally-constrained TCRE range from figure 5.3.

5.3.1 Model-derived CO_2-fe TCRE estimates

To complement the observational assessment, the TCREs for a subset of CMIP6 GCMs can be calculated over history directly using CO_2-fe emissions to account for the impact of non-CO_2 pollutants. Leach *et al.* (2021) demonstrates the FaIRv2.0 (*29*) model emulates the thermal and carbon cycle properties of CMIP6 GCMs, and provide parameter sets for several CMIP6 models. RFMIP experiments (*54*) allow for the calculation of ERF timeseries over history (UKESM1-0-LL, NorESM2-LM, GFDL-ESM4) and extended up to 2100 where data is available (CanESM5, IPSL-CM6A-LR).

Using these, I diagnose the TCREs from estimates of the cumulative CO_2-fe emissions budgets and associated warming for each GCM, plotted in figure 5.5 (coloured solid lines). Compare these to the dashed lines on the same figure, which show the total

warming plotted against historical CO_2 emissions alone, diagnosed from individual CMIP6-model historical experiments (following Liddicoat *et al.* (2021) (*197*)). These CO_2-only effective TCREs are non-linear over the historical period, as was found for the dotted lines of figure 5.1d. In contrast, the solid lines are straight, showing the CO_2-fe emissions have correctly reproduced the TCRE relationship for each GCM. I find a CMIP6 TCRE range of 0.35-0.68 °C/TtCO_2 based on the five models sampled, consistent with the range of TCREs from figure 5.3a (black lines in figure 5.5).

Further, the five models' TCREs estimated using CO_2-fe emissions can also be compared against their TCREs calculated from the 1%/yr CO_2 concentration increase experiment in CMIP6 (*36*) (brown plume in figure 5.5), calculated by Arora *et al.* (2020) (*104*). CMIP6 TCREs estimated with CO_2-fe are near-identical to the estimates in Arora *et al.* (2020) using pure-CO_2 1%/yr experiments, indicating the CO_2-fe methodology is indeed identifying the true CO_2-only TCRE parameter. I present all calculated TCREs in table 5.1 for comparison against the observationally-constrained estimates and against estimates using the 1%/yr experiment (*104*).

Overall, both CMIP6 TCRE ranges (calculated from CO_2-fe emissions or 1%/yr experiments) appear to be consistent with the 5-95th percentile TCRE found from historical observations. The mean response (0.48 °C/TtCO_2 in CMIP6 models assessed) is somewhat higher than the observationally-constrained result (0.40 °C/TtCO_2). Extremes of the CMIP6 ensemble slightly under-sample the observationally-constrained upper and lower bounds. Even UKESM1-0-LL and CanESM5, both of which have equilibrium climate sensitivities that are above the range consistent with historical observations (*80*) show high but not out-of-range TCRE estimates, lying around the 83rd percentile of the TCRE distribution in figure 5.5. Because the CMIP6 distribution does not sample the full TCRE range suggested by observations, simply using the CMIP6 range in isolation is potentially problematic, despite the range implying no significant bias. A better approach would use observations to constrain the CMIP6 ensemble TCRE range, such as the yes/no exclusion for models based on historical temperature gradient reconstruction as suggested in Tokarska *et al.* (2020) (*84*).

Source	Model	TCRE (°C/TtCO$_2$)	Uncertainty range
1%/yr CMIP6	ACCESS-ESM1.5	0.55	-
1%/yr CMIP6	BCC-CSM2-MR	0.36	-
1%/yr CMIP6	**CanESM5**	**0.57**	-
1%/yr CMIP6	CESM2	0.58	-
1%/yr CMIP6	CNRM-ESM2-1	0.44	-
1%/yr CMIP6	**IPSL-CM6A-LR**	**0.58**	-
1%/yr CMIP6	MIROC-ES2L	0.38	-
1%/yr CMIP6	MPI-ESM1.2-LR	0.45	-
1%/yr CMIP6	**NOAA-GFDL-ESM4**	**0.39**	-
1%/yr CMIP6	**NorESM2-LM**	**0.36**	-
1%/yr CMIP6	**UKESM1-0-LL**	**0.63**	-
1%/yr CMIP6	ENSEMBLE MEAN	0.48	0.28-0.68 (5^{th}-95^{th}percentile)
Historical CO_2-fe CMIP6	**CanESM5**	**0.58**	-
Historical CO_2-fe CMIP6	**IPSL-CM6A-LR**	**0.57**	-
Historical CO_2-fe CMIP6	**NOAA-GFDL-ESM4**	**0.36**	-
Historical CO_2-fe CMIP6	**NorESM2-LM**	**0.35**	-
Historical CO_2-fe CMIP6	**UKESM1-0-LL**	**0.64**	-
Historical CO_2-fe CMIP6	ENSEMBLE MEAN	0.50	-
Obs. constrained (fig. 5.3)	Observations/FaIRv2.0	0.40	0.26-0.78 (5^{th}-95^{th}percentile)
SR1.5 gaussian TCRE	SR1.5	0.45	0.22-0.68 (likely range)
AR6 gaussian TCRE	AR6	0.45	0.27-0.63 (likely range)

Table 5.1: TCRE estimates used in this study. 1%/yr results are taken from Arora *et al.* (2020). CO_2-fe results are calculated from OLS regression of individual model's (1850-2014) cumulative CO_2-fe emissions and GSAT anomaly in figure 5.5. The observationally-constrained TCRE range uses statistically-infilled GMST to mimic GSAT with full spatial coverage. Models highlighted bold have their TCRE estimated using both the CO_2-fe and 1%/yr concentration increase experiment approaches.

5.3.2 Calculating the remaining carbon budget

Rogelj *et al.* (2019) identifies the present-day warming level, the TCRE value, and the contribution of non-CO_2 pollutants as the three largest contributors to the uncertainty of the remaining carbon budget. The first two of these have already been studied in this thesis: the level of warming in chapters 3 and 4, and the TCRE value in the previous section. As noted above, differences between the assessed warming rate in SR1.5/AR6 and in this thesis will substantially alter the remaining carbon budget assessment. SR1.5/AR6 suggest the 2020 warming level is 1.2 °C (1.0-1.4 °C) based on a warming rate of +0.2 °C/decade (*15*, *17*, *18*). The 2020 warming level rises to 1.3 °C (1.1-1.5 °C) if the increased warming rate in chapter 3 and 4 is used instead (e.g. see figure 3.5 or figure 4.15).

To account for how these assessments impact on the remaining budget, figure 5.3b, c and d show the remaining total budget compatible with various quantities of remaining warming (0.2, 0.3 or 0.4 °C additional warming, respectively), calculated

with the Gaussian TCRE distribution reported in AR6 (grey shading), or using the observationally-constrained TCRE distribution from panel a (solid black lines). The 0.2 °C target corresponds to 1.3 °C warming in 2020 (consistent with chapters 3 and 4); 0.3 °C corresponds to 1.2 °C warming in 2020 (consistent with SR1.5/AR6); and 0.4 °C corresponds to 1.1 °C in 2020 (consistent with the assessment that warming reached 0.85 °C in the decade 2005-2014 above the preindustrial baseline, used in the Structured Expert Dialogue to support the writing of the Paris Agreement text (*284*)).

Diagonal lines on each panel define the total remaining total CO_2-fe emissions budgets for a set quantity of additional warming (sampling uncertainty in the TCRE). For example, panel c's remaining total CO_2-fe budgets range between:

- 5^{th} percentile: (1.5-1.2) $\times$ 1000/0.26 = 1150 $GtCO_2$,
- 50^{th} percentile: (1.5-1.2) $\times$ 1000/0.40 = 750 $GtCO_2$,
- 95^{th} percentile: (1.5-1.2) $\times$ 1000/0.78 = 380 $GtCO_2$.

A detailed breakdown by percentile for each remaining warming quantity are shown in table 5.2 (see table 5.3 for equivalent budgets to 2 °C). For each remaining warming quantity, the wide range of remaining total CO_2-fe budgets I find here are largely a result of the range of present-day ERF in the 1000-member total anthropogenic ERF ensemble, which hampers tighter constraints on the TCRE despite AR6's reductions in the TCR value. Reducing ERF component uncertainty and accounting for correlations between component ERFs would better constrain this range, and is a focus for future research.

Given this total remaining CO_2-fe budget range, the question now becomes what fraction of this budget is used by CO_2 and non-CO_2 pollutants respectively. Figures 5.3b, c and d show the proportions of the future total CO_2-fe budget allocated to CO_2 and non-CO_2. Scatter points indicate the cumulative CO_2 and non-CO_2 CO_2-fe emissions to peak warming in 1.5 °C-compatible, 2 °C-lower and 2 °C-higher scenarios from figure 5.1, with the colours indicating the scenario category as in figure 5.1. In these scenarios, the non-CO_2 contribution to the total remaining budget ranges from 50-300 $GtCO_2$-fe, exactly the range determined in SR1.5 (where 250 $GtCO_2$ budget uncertainty was

attributed to non-CO_2 scenario uncertainty). Depending on the TCRE, this means non-CO_2 scenario uncertainty contributes between 0.01 °C and 0.23 °C warming in these scenarios (using the observationally-constrained TCRE 5th-95th percentile range). Importantly, if an SR1.5-consistent present-day warming rate estimate is used (panel c), dark blue 1.5 °C-compatible scenarios are consistent with their 1.5 °C peak warming categorisation — the scatter of blue dots sits over my best estimate TCRE.

Scenario categories are less well suited if the budget is based on other assessments of present-day warming. Scenario categorisation appears overly conservative if the remaining budget is allocated based on 1.1 °C warming at present day (i.e. re-baselining anthropogenic warming to be consistent with the assessment that 0.85 °C warming occurred up to the 2006-2015 decade relative to 1850-1900 (*284*, *292*)), with around half of the 1.5 °C-consistent scenarios lying outside the lower bound of the likely range in panel d, and several scenarios classified as 'lower-2 °C' becoming 1.5 °C-consistent. Conversely, scenarios are overly optimistic if 1.3 °C warming at present day is used, where now nearly all dark blue 1.5 °C-compatible scenarios unlikely to limit peak warming to 1.5 °C (lie to the right of the black best-estimate line in panel b). Further, the evident lack of correlation between cumulative CO_2 and non-CO_2 emissions budgets to peak warming in all sub-panels of figure 5.3 again undermines the use of an 'effective' (multi-gas) TCRE (*291*). Since CO_2 and non-CO_2 emissions are affected by different policies, it is potentially misleading to present them using a single index such as percentage aggregate CO_2-equivalent emission reductions by a given date (*293*). A two-dimensional presentation, separating CO_2 and non-CO_2 contributions to warming (as in panels b, c and d here), is the minimum required to ensure both indicators are on track to achieve a temperature goal. The sum of cumulative CO_2 and non-CO_2 CO_2-fe emissions, multiplied by the TCRE accurately, determines long-term warming.

Since the scenarios explored here do not represent a random distribution that can be sampled for a particular percentile (the distribution depends on the Integrated Assessment Model used to generate individual scenarios), accounting for non-CO_2 contributions to remaining CO_2-only budget estimates is more challenging. Subtracting a representative mid-range scenario's non-CO_2 contribution from estimated total CO_2-fe budgets gives

indicative pure-CO_2 budgets, indicated by horizontal box-whisker symbols in pink in figure 5.3 (using the central non-CO_2 ERF scenario highlighted in figure 5.1 and used in figure 5.2). The range of non-CO_2 contributions implied by the non-CO_2 forcing scenarios as a whole indicates the potential for trade-offs between CO_2 and non-CO_2 warming.

Using GMST warming of 1.2 °C in 2020 (for consistency with the SR1.5 scenarios) and the mid-range non-CO_2 forcing from figure 5.1 (130 $GtCO_2$-fe; range spans 50-300 $GtCO_2$-fe), I find the remaining carbon budget to 1.5 °C corresponding to different TCRE percentiles as follows:

- 5th percentile: (0.3 × 1000/0.26) - 130 = 1020 $GtCO_2$ (range: 850-1100 $GtCO_2$)
- 33rd percentile: (0.3 × 1000/0.35) - 130 = 730 $GtCO_2$ (range: 560-810 $GtCO_2$)
- 50th percentile: (0.3 × 1000/0.40) - 130 = 620 $GtCO_2$ (range: 450-700 $GtCO_2$)
- 66th percentile: (0.3 × 1000/0.46) - 130 = 520 $GtCO_2$ (range: 350-600 $GtCO_2$)
- 95th percentile: (0.3 × 1000/0.78) - 130 = 250 $GtCO_2$ (range: 80-330 $GtCO_2$)

This methodology is followed to find remaining CO_2-only budgets for other remaining warming quantities in tables 5.2 and 5.3 and for the pink error bars in figure 5.3b, c and d.

I re-emphasise this is just one possible pathway for future non-CO_2 forcing, which will be determined by policy choices, some but not all of which also involve trade-offs and synergies with CO_2 policy. Exploring these trade-offs is a matter for policymakers. CO_2-fe emissions, or warming-equivalent emissions (*125*) that are very similar and easier to calculate, provide the necessary framework. SR1.5 gave 33rd, 50th and 66th percentile remaining carbon budgets for 1.5 °C GMST warming from 2018 of 1080, 770, 570 $GtCO_2$ respectively. This chapter's best-estimate remaining carbon budget for 0.3 °C additional warming from 2020, 620 $GtCO_2$, is therefore consistent with SR1.5 having accounted for recent updates to the level of GMST and an additional two years of warming. These remaining carbon budgets are also consistent with AR6 remaining budget estimates, since those budgets were based off 1.1 °C warming over the historical period until 2010-2019, and assumed a warming rate of 0.2 °C/decade thereafter, shown in table 5.2. Discrepancies with the AR6 budgets relate to the accounting of non-CO_2

Percentile	TCRE (GMST) (°C/TtCO_2)	0.2 °C CO_2-fe budget (TtCO_2-fe)	0.3 °C CO_2-fe budget (TtCO_2-fe)	0.4 °C CO_2-fe budget (TtCO_2-fe)	0.2 °C CO_2-only budget (TtCO_2): *130 GtCO_2-fe (50-300) GtCO_2-fe non-CO_2 budget*	0.3 °C CO_2-only budget (TtCO_2): *130 GtCO_2-fe (50-300) GtCO_2-fe non-CO_2 budget*	0.4 °C CO_2-only budget (TtCO_2): *130 GtCO_2-fe (50-300) GtCO_2-fe non-CO_2 budget*	SR1.5 1.5 °C CO_2 budget (TtCO_2)	AR6 1.5 °C CO_2 budget (TtCO_2)
5th	0.26	0.77	1.15	1.54	0.64 (0.47-0.72)	1.02 (0.85-1.10)	1.41 (1.24-1.49)	-	-
17th	0.31	0.65	0.97	1.29	0.52 (0.35-0.60)	0.84 (0.67-0.92)	1.16 (0.99-1.24)	-	-
33rd	0.35	0.57	0.86	1.14	0.44 (0.27-0.52)	0.73 (0.56-0.81)	1.01 (0.84-1.09)	0.84	0.65
50th	0.40	0.50	0.75	1.00	0.37 (0.20-0.45)	0.62 (0.45-0.70)	0.87 (0.70-0.95)	0.58	0.50
66th	0.46	0.43	0.65	0.87	0.30 (0.13-0.38)	0.52 (0.35-0.60)	0.74 (0.57-0.82)	0.42	0.40
83rd	0.57	0.35	0.53	0.70	0.22 (0.05-0.30)	0.40 (0.23-0.48)	0.57 (0.40-0.65)	-	-
95th	0.78	0.26	0.38	0.51	0.13 (-0.04,+0.21)	0.25 (0.08-0.33)	0.38 (0.21-0.46)	-	-

Table 5.2: TCRE percentiles and corresponding remaining carbon budgets to 1.5 °C. Percentiles of the TCRE found in this study shown in column 2. CO_2-fe budgets for 0.2 °C additional warming (1.5 °C-compatible using chapter 3 and 4 assessment), 0.3 °C additional warming (1.5 °C-compatible according to SR1.5/AR6), and 0.4 °C additional warming (1.5 °C-compatible using GMST re-baselined to 0.85 °C over the decade up to 2015) shown in columns 3, 4 and 5, respectively. Corresponding CO_2-only budgets to 1.5 °C are shown in columns 6, 7 and 8, with mid-range non-CO_2 contribution (range shown in brackets). For comparison, headline remaining budget estimates in SR1.5 and AR6 are shown in columns 9 and 10.

Percentile	TCRE (GMST) (°C/TtCO_2)	0.7 °C CO_2-fe budget (TtCO_2-fe)	0.8 °C CO_2-fe budget (TtCO_2-fe)	0.9 °C CO_2-fe budget (TtCO_2-fe)	0.7 °C CO_2-only budget (TtCO_2): *150 GtCO_2-fe (-30,+610) GtCO_2-fe non-CO_2 budget*	0.8 °C CO_2-only budget (TtCO_2): *150 GtCO_2-fe (-30,+610) GtCO_2-fe non-CO_2 budget*	0.9 °C CO_2-only budget (TtCO_2): *150 GtCO_2-fe (-30,+610) GtCO_2-fe non-CO_2 budget*	AR6 2.0 °C CO_2 budget (TtCO_2)
5th	0.26	2.69	3.08	3.46	2.54 (2.08-2.72)	2.93 (2.47-3.11)	3.31 (2.85-3.49)	-
17th	0.31	2.26	2.58	2.90	2.11 (1.65-2.29)	2.43 (1.97-2.61)	2.75 (2.29-2.93)	-
33rd	0.35	2.00	2.29	2.57	1.85 (1.39-2.03)	2.14 (1.68-2.32)	2.42 (1.96-2.60)	1.70
50th	0.40	1.75	2.00	2.25	1.60 (1.14-1.78)	1.85 (1.39-2.03)	2.10 (1.64-2.28)	1.35
66th	0.46	1.52	1.74	1.95	1.37 (0.91-1.55)	1.59 (1.13-1.77)	1.80 (1.34-1.98)	1.15
83rd	0.57	1.23	1.40	1.58	1.08 (0.62-1.26)	1.25 (0.79-1.43)	1.43 (0.97-1.61)	-
95th	0.78	0.90	1.03	1.15	0.75 (0.29-0.93)	0.88 (0.42-1.06)	1.00 (0.54-1.18)	-

Table 5.3: TCRE percentiles and corresponding remaining carbon budgets to 2.0 °C. Percentiles of the TCRE found in this study shown in column 2. CO_2-fe budgets for 0.7 °C additional warming (2.0 °C-compatible using chapter 3 and 4 assessment), 0.8 °C additional warming (2.0 °C-compatible according to SR1.5/AR6), and 0.9 °C additional warming (2.0 °C-compatible using GMST re-baselined to 0.85 °C over the decade up to 2015) shown in columns 3, 4 and 5, respectively. Corresponding CO_2-only budgets to 2.0 °C are shown in columns 6, 7 and 8, with mid-range non-CO_2 contribution (range shown in brackets). For comparison, headline remaining budget estimates in AR6 are shown in column 9.

warming. AR6 chose a non-CO_2 warming range of 0.1-0.2 °C for budget estimates, towards the upper half of the non-CO_2 CO_2-fe budgets used here.

If GMST warming of 1.3 °C in 2020 is used (reflecting the updated warming trend assessment in this thesis), along with a mid-range non-CO_2 forcing from figure 5.1 (130 $GtCO_2$), the remaining budgets are reduced compared to AR6's assessment. In this case a 33, 50 and 66% chance of limiting warming to below 1.5 °C requires CO_2-only budgets of 440, 370, 300 $GtCO_2$, respectively. The full ranges of estimated remaining CO_2-fe and CO_2-only budgets are given in tables 5.2, along with comparable budgets from SR1.5 and AR6.

5.4 Discussion

This chapter analysed mitigation scenarios informing the IPCC's SR1.5 and AR6 report, deconstructing them to highlight the relative contributions from CO_2 and non-CO_2 pollutants (figures 5.1 and 5.2). CO_2-fe emissions provide a means to quantify non-CO_2 contributions to future scenarios, without relying on traditional metrics which do not translate readily into a corresponding warming response. Further, I demonstrated that a simple scaling factor, or 'effective TCRE', doesn't adequately account for the warming contribution from non-CO_2 drivers (*92*, *105*, *286*) as future non-CO_2 radiative forcing isn't tightly correlated with cumulative CO_2 emissions in these scenarios. Using CO_2-fe emissions to constrain the TCRE distribution based on historical temperature observations and radiative forcing estimates, I produced an observationally-constrained remaining carbon budget estimate based on central non-CO_2 ERF estimates, along with highlighting the co-varying uncertainty in the physical climate response to CO_2 and non-CO_2 pollutants. A two-dimensional presentation which separates CO_2 and non-CO_2 contributions to warming (figure 5.3b, c and d) is recommended as the most transparent approach when displaying the physical constraints of remaining budgets.

A remaining carbon budget for 1.5 °C of 400 $GtCO_2$ from 2020 (the most widely quoted 66th percentile AR6 remaining carbon budget) is consistent with a current level of warming of 1.2 °C (in 2020 relative to 1850-1900) (*17*), given an observationally-constrained TCRE (0.40 °C/$TtCO_2$; 0.26-0.78 °C/$TtCO_2$), unless we experience a

sudden increase in the TCRE or future non-CO_2 climate forcing above the upper end of the range in the SR1.5 1.5 °C-compatible scenarios (see figure 5.3b and table 5.2).

Recent updates to datasets of observed CH_4 and N_2O mixing ratios suggest these are tracking a path higher than most future scenarios suggest (*122*, *294*), while aerosol emissions have declined more rapidly than scenarios suggested, meaning the level and rate of anthropogenic warming is higher than the assessment in AR6. Using 1.3 °C as the present-day warming level reduces the remaining carbon budget by 1/3rd and means '1.5 °C-compatible' scenarios are inconsistent with this categorisation. For 1.3 °C warming, 0.2 °C additional warming has an associated total CO_2-fe budget of 570, 500 and 430 $GtCO_2$-fe (33rd, 50th and 66th percentiles). This gives representative CO_2-only budgets of 440, 370 and 300 $GtCO_2$, assuming a non-CO_2 budget of 130 $GtCO_2$. Uncertainty in the non-CO_2 contribution adds approximately $\pm$130 $GtCO_2$-fe to these estimates.

The decision on what index will be used to determine when 1.5 °C is reached has substantial policy implications and hence should not be determined by scientists alone. As long as observed warming continues to be reported in terms of GMST, reporting remaining carbon budgets in terms of GMST baselined to several periods (for example: both 0.85 °C over the decade prior to 2015; 1850-1900 preindustrial baseline), as well as for alternative assessments of the near-present warming rate, seems the simplest and least policy-prescriptive option available. Regardless, CO_2-fe emissions are the most transparent method to analyse the relative contributions from individual pollutants to remaining warming, particularly in order to disentangle scenario from physical climate uncertainty.

5.5 Chapter close

This chapter used the CO_2-forcing-equivalent metric to estimate the CO_2 and non-CO_2 contributions to the remaining carbon budget. I first demonstrated the utility of the CO_2-fe metric for comparing CO_2 and non-CO_2 emissions timeseries, including determining their relative contributions to a 1.5 °C-compatible scenario. I then used them to estimate the TCRE, using an attribution of historical anthropogenic warming from GMST observations and cumulative CO_2-fe emissions (to account for warming

contributions from all pollutants). This produced a TCRE estimate of 0.40 (0.26-0.78) °C/TtCO_2. The exact remaining carbon budget depends on the assessed present day anthropogenic warming level, the chosen non-CO_2 emissions scenario, and other factors (the ZEC and Earth System Feedbacks).

Adopt the pace of nature, her secret is patience.

— Ralph Waldo Emerson

6

The multi-decadal response to net zero CO_2 emissions

This chapter discusses the conditions for warming stabilisation following net zero CO_2 emissions using the RAZE framework derived in chapter 2. This work is based on the publication *The multi-decadal response to net zero CO_2 emissions and implications for emissions policy.* Jenkins, S., Sanderson, B., Peters, G., Frölicher, T., Friedlingstein, P. and Allen, M. (2022). Geophysical Research Letters. See ref. (*187*).

Contents

6.1 Introduction

Over the last decade the ambition of global, regional and national climate policy has increasingly become defined by the date of net zero (*3*, *14*, *295*, *296*). In chapter 1 I discussed the properties of the CO_2 warming response which facilitate this net zero framing: the realisation that the CO_2-induced warming response is determined by the cumulative CO_2 emissions released (*98*, *100*), and that CO_2-induced warming only stops when CO_2 emissions reach net zero. That formed the basis for the discussion in chapter 5, where I showed how non-CO_2 pollutants can be brought into this framework using the CO_2-forcing-equivalent emissions metric. CO_2-fe emissions allowed me to estimate total CO_2-fe remaining budgets across all pollutants, and compare pollutants' contributions to this total, simplifying the analysis of complex multi-gas emissions scenarios. All of the work in chapter 5 derives budgets assuming that net zero is a condition to halt anthropogenic warming. In this chapter I consider the robustness of this assumption.

SR1.5 noted that "reaching and sustaining net zero global anthropogenic CO_2 emissions and declining net non-CO_2 radiative forcing would halt anthropogenic global warming on inter-decadal timescales (high confidence)" (*14*). AR6 (*3*) made a much stronger statement: "from a physical science perspective, limiting human-induced global warming to a specific level *requires* limiting cumulative CO_2 emissions, reaching *at least* net zero CO_2 emissions, along with *strong reductions* in other greenhouse gas emissions", and more specifically, "achieving global net zero CO_2 emissions, . . . , is a *requirement* for stabilizing CO_2-induced global surface temperature increase" (emphasis has been added where language differs from SR1.5).

The AR6 statement implies that net zero CO_2 emissions is a necessary condition to stabilise warming, while SR1.5 instead argued that net zero and declining net non-CO_2 radiative forcing is sufficient to halt warming on inter-decadal timescales. This distinction is important: while both reports emphasise that halting warming requires at least an order of magnitude reduction in CO_2 emissions, SR1.5 leaves open the possibility that stabilising warming may not require strictly net zero CO_2 emissions.

AR6's statement is approximately correct (cumulative CO_2 emissions have a near-linear relationship with global warming (*98*)), but the 'requirement' language may be problematic if it later transpires substantial non-zero residual CO_2 emissions are consistent with stabilising warming over multi-decade intervals. Even if net zero is the best-estimate requirement for warming stabilisation today, the lack of an uncertainty qualifier on the AR6 statement presents a second risk: if uncertainty in the conditions for warming stabilisation is large then society must maintain the capacity to adjust carbon sinks to the emergent conditions for warming stabilisation. Presenting the condition for warming stabilisation as an unqualified 'requirement' today implies that achieving said condition will always halt warming.

Given these concerns, I ask which of these statements is best supported by our current understanding of the physical climate system? Both refer to a physical science perspective, and are not restricted to specific scenarios. SR1.5's and AR6's scenario databases both show that the bulk of scenarios halting warming in the middle of the 21st century reach net zero CO_2 emissions, which then become net negative, along with declining net non-CO_2 radiative forcing (*280*). But most of these scenarios deliver net zero GHG emissions (evaluated with GWP_{100}), later in the century, causing net-negative CO_2-fe emissions and therefore achieving a "peak and decline" global temperature pathway. Here I focus on the physical requirements for stabilizing temperatures, a necessary condition for limiting warming to any level.

Answering this question requires probing the amount of "warming in the pipeline" (*47*, *291*) following net zero CO_2 emissions, often referred to as the ZEC (*57*). In chapter 5 I explicitly set the ZEC to zero, meaning that policy reaching net zero CO_2-fe emissions was automatically successful in halting warming. Including the ZEC, the condition for warming stabilisation becomes less clear.

The range of the ZEC in the century following net zero can be quantified using GCMs. In chapter 1 I introduced the Zero Emissions Commitment Model Intercomparison Project (ZECMIP) (*57*), which explored ESM and EMIC responses in the century following net zero (*113*). ZECMIP's A-type experiments followed an emissions pathway where CO_2 concentrations increased at 1 %/yr until a set quantity of CO_2 had been released,

and thereafter emissions were set to net zero and models allowed to re-equilibrate. These experiments suggest that ZEC is approximately $\pm 0.2\,^{\circ}C$, and depends on small differences in the carbon and thermal cycle response following net zero. If ZEC does lie between $\pm 0.2\,^{\circ}C$, a wide range of post-net zero CO_2 emissions are theoretically compatible with stable temperatures (*113*), but to date no study has focused on diagnosing them. Drawing on these experiments, this chapter explores the physical conditions for warming stabilisation.

6.2 Characteristics of the response to net zero

The impulse response framework describing the surface temperature anomaly in response to an ERF timeseries is written in equation 2.2 in chapter 2. Here, c_i and d_i define the efficacies and thermal response timescales for the individual impulse response boxes (*78*). In FaIRv2.0 there are three boxes, with d_i values broadly split between sub-decadal and multi-century timescales (d_1=0.903 years, d_2=7.92 years, d_3=355 years) (*29*). Noting this, and following Seshadri (2017) (*191*), chapter 2 expands equation 2.2 for the multi-decade warming response to an ERF perturbation F(t), finding

$$\Delta T = \kappa_F(\Delta F + \rho \bar{F} \Delta t). \tag{6.1}$$

In equation 6.1 ΔT is the temperature change, ΔF the change in ERF over the period Δt, and $\bar{F}$ is the average ERF over the period Δt (compared to preindustrial). Chapter 2 defined ρ as the fractional rate of adjustment to constant forcing (RACF, in units per year) (*125*), and κ_F as the Transient Climate Response to Forcing (TCRF, in units of $^{\circ}C/Wm^{-2}$) (*103*). Note that RACF is small and positive, such that a constant positive ERF (as would occur if CO_2 concentrations were stabilised) results in slow residual warming due to the multi-century climate adjustment.

Also in chapter 2, equation 2.4 defines the corresponding four-pool impulse response representation (*93*, *297*) of the carbon cycle. In it, τ_j are the carbon cycle response timescales and μ_j are forcing efficacies (in units $W/m^2/GtCO_2$). Assuming that the τ_j can also be split into sub-decadal and multi-century response timescales in

the same way as the thermal cycle parameters, I expanded equation 2.4 over multi-decadal timescales. This found an expression for the cumulative CO_2 emissions, ΔG, in terms of the ERF perturbation

$$\Delta G = \frac{1}{\mu_2}\left(\Delta F + \frac{1}{\tau_2}\bar{F}\Delta t\right). \tag{6.2}$$

In equation 6.2 τ_2 and μ_2 refer to the multi-century response timescale and multi-century forcing efficacy, respectively. Note the similarity between this expression and equation 6.1, with one term proportional to the change in ERF over a time interval Δt, and the other proportional to the average ERF over the interval Δt (relative to preindustrial).

Combining equations 6.1 and 6.2 derived equation 2.15 in chapter 2

$$\Delta T = \kappa_E(\Delta G + o\bar{G}\Delta t) \tag{6.3}$$

where $o = \rho - \tau_2^{-1}$ is the RAZE in units %/year, κ_E is the TCRE parameter ($=\mu_2\kappa_F$), ΔG is the cumulative CO_2 emissions change over the interval Δt, and $\bar{G}$ is the cumulative CO_2 emissions released since preindustrial averaged over the interval Δt. In equation 6.3 the RAZE parameter is a measure of the difference between the multi-century response rate of the thermal cycle, ρ, and the multi-century response rate in the carbon cycle, $1/\tau_2$. A positive RAZE corresponds to residual warming post-net zero, and can arise as a result of either slow carbon sinks post-net zero, or because of a fast thermal cycle supplying excess heat from the deep ocean (e.g. with both the TCR/ECS ratio (*42*) and d_2 small). Tarshish, Jeevanjee and Fung (2022) discusses a similar framework describing the cause of post-net zero temperature trends to characterise the carbon and thermal cycle contributions to the spread in ZEC between ESMs (*298*), although they work over different timescales and infer a more qualitative result than this study.

The RAZE defines the fractional rate at which the temperature adjust over multi-decadal timescales in response to net zero CO_2 emissions. As the difference of two small quantities, $\rho \sim 0.3\,\%$/yr (*127*) and $\tau_2^{-1} \sim 0.3\,\%$/yr (*93*), the RAZE can be positive or negative with typical values of order $\pm 0.1\,\%$/yr (*103*).

Setting ΔG to zero in equation 6.3 gives an expression for the rate of residual warming after net zero

$$\frac{\Delta T}{\Delta t} = \kappa_E o\bar{G} = \kappa_E o G(t = t_{\text{net zero}}), \tag{6.4}$$

where $\kappa_E o \approx \pm 4 \times 10^{-4}\,^{\circ}\mathrm{C\,yr^{-1}/TtCO_2}$ (assuming the best-estimate TCRE value derived in chapter 5, and the RAZE range above). Hence the RAZE parameter determines the development of ZEC_H over a multi-decade interval, H,

$$ZEC_H = \kappa_E o G(t = t_{\text{net zero}})H. \tag{6.5}$$

For $\kappa_E o \approx \pm 4 \times 10^{-4}\,^{\circ}\mathrm{C\,yr^{-1}/TtCO_2}$, $G(t = t_{\text{net zero}}) = 3.75\,\mathrm{TtCO_2}$ (approximately 1.5 °C-compatible) and H = 100 years, $ZEC_{100} = \pm 0.15\,^{\circ}\mathrm{C}$ (i.e. consistent with the magnitude of ZEC in ZECMIP experiments).

Equation 6.5's mathematical framing is similar to how the transient warming in response to an emissions scenario can be characterised using a scenario-independent TCR parameter (*103*): ZEC_H (a scenario-dependent and time-dependent quantity) can be deconstructed into the RAZE × TCRE (scenario independent), multiplied by $G(t = t_{\text{net zero}}) \times$ H (scenario dependent).

Since the RAZE determines the multi-decadal warming following net zero, equation 6.3 can also be used to derive a level of CO_2 emissions compatible with approximately constant temperatures

$$E_{\text{halt}} = \frac{\Delta G}{\Delta t} = -o\bar{G} \approx -oG(t = t_{\text{net zero}}), \tag{6.6}$$

assuming any additional emissions after temperatures halt are small relative to cumulative emissions prior to that time, as will be the case on multi-decadal timescales (*109*). Typical values of RAZE and cumulative emissions released over history suggest that $oG(t = t_{\text{net zero}})$ is approximately $1/20^{\text{th}}$ the size of anthropogenic CO_2 emissions released in 2020 (*299*).

6.3 Emissions consistent with halting warming

The framework presented in equations 6.3, 6.5 and 6.6 allows me to probe the requirements of emissions policy aiming to halt global warming. I now explore constraints on the RAZE parameter and E_{halt} using ESMs and the FaIRv2.0 simple climate model.

6.3.1 RAZE and E_{halt} distributions from the Zero Emissions Commitment Intercomparison Project

RAZE parameters estimated directly from 9 ESMs and 9 EMICs from ZECMIP are shown in table 6.1. These are calculated using the linear gradient in the temperature response following net zero (following equation 6.4), ignoring the first decade to allow adjustments from the sub-decadal timescale responses in the carbon and thermal cycles. The mean RAZEs are -0.077, -0.108 and -0.015 %/yr in net zero experiments where CO_2 concentrations are first increased by 1 %/yr until 2750, 3670 and 7330 $GtCO_2$ (750, 1000 and 2000 GtC) has been released. The RAZE appears weakly scenario dependent, although this is less pronounced than in the ZEC which, as expected, scales with cumulative emissions prior to the date of net zero (*113*). In ESMs, a negative average RAZE is observed for the 3670 $GtCO_2$ experiment, but positive average RAZE for 7330 $GtCO_2$, both based on small samples and due to a mixture of strong positive carbon-climate feedbacks and slower carbon sinks in ACCESS-ESM1.5, UKESM1-0-LL and GFDL-ESM2M (such feedbacks are observed in other large perturbation experiments (*29*, *58*, *92*, *278*, *300*)). In the EMICs the RAZE is consistently negative, but still weakens as the perturbation size increases. Fortunately, policy consistent with achieving the temperature goals of Paris Agreement demands substantially lower than 7330 $GtCO_2$ cumulative emissions until the time of net zero (7330 $GtCO_2 \sim 3\,^{\circ}C$ CO_2-induced warming for a TCRE = $0.4\,^{\circ}C/TtCO_2$, the best-estimate value from chapter 5), increasing the likelihood of a small negative RAZE according to the results of ZECMIP experiments.

Table 6.1 also shows estimates of the emissions consistent with no further warming over multi-decadal intervals (E_{halt}) for each experiment. For 3670 $GtCO_2$, the mean E_{halt} is +4.0 $GtCO_2$ across all models (+2.1 $GtCO_2$ for ESMs only) — between $1/10^{th}$ and $1/20^{th}$ of the anthropogenic CO_2 emissions released in 2020. E_{halt} scales with the size of the perturbation: higher emissions prior to net zero result in lower E_{halt}, including negative E_{halt} if the RAZE becomes positive. The mean ESM and EMIC responses suggest E_{halt} is positive following both 2750 and 3670 $GtCO_2$ perturbations (with the latter representing an approximately $1.5\,^{\circ}C$-compatible emissions budget). In all experiments E_{halt} is an

Model	RAZE (%/yr)	$E_{halt,\ 2750}$ ($GtCO_2$/yr)	$E_{halt,\ 3670}$ ($GtCO_2$/yr)	$E_{halt,\ 7330}$ ($GtCO_2$/yr)
ACCESS-ESM1.5	-0.056 (-0.073, +0.339)	2.0	2.1	-24.9
CanESM5	-0.083 (–, -0.035)	–	3.0	2.6
CESM2	-0.164 (–, –)	–	6.0	–
CNRM-ESM2-1	+0.126 (–, –)	–	-4.6	–
GFDL-ESM2M	+0.004 (+0.010, +0.085)	-0.3	-0.1	-6.3
MIROC-ES2L	-0.227 (-0.177, -0.170)	4.9	8.3	12.5
MPI-ESM1.2-LR	-0.145 (–, –)	–	5.3	–
NorESM2-LM	-0.045 (–, –)	–	1.7	–
UKESM1-0-LL	+0.070 (-0.030, +0.228)	-2.6	0.8	-16.7
ESM MEAN	**-0.058 (-0.028, +0.089)**	**1.9**	**2.1**	**-6.6**
Bern3D-LPX	-0.135 (-0.122, -0.020)	3.4	5.0	1.4
CLIMBER-2	-0.116 (–, –)	–	4.3	–
DCESS	-0.124 (-0.108, -0.094)	3.0	4.5	6.9
IAPRAS	-0.329 (-0.276, -0.327)	7.6	12.1	23.9
LOVECLIM 1.2	-0.008 (+0.128, –)	-3.5	0.3	–
MESM	-0.100 (-0.115, -0.011)	3.2	3.7	0.8
MIROC-lite/JUMP-LCM	-0.095 (-0.121, -0.092)	3.3	3.5	6.7
PLASIM-GENIE	-0.504 (-0.129, -0.290)	3.6	18.5	23.1
Uvic ESCM 2.10	-0.017 (-0.066, +0.203)	1.8	0.6	-14.9
EMIC MEAN	**-0.159 (-0.101, -0.090)**	**2.8**	**5.8**	**6.6**
ESM + EMIC MEAN	**-0.108 (-0.077, -0.015)**	**2.1**	**4.0**	**1.1**

Table 6.1: Estimated RAZE and E_{halt} parameters using A-type experiments from ZECMIP study (*113*). A-type experiments consist of ESM and EMICs run with 1 %/yr CO_2 concentration increase experiments until 2750, 3670 or 7330 $GtCO_2$ (750, 1000 or 2000 GtC) have been emitted in total. Thereafter, emissions are set to net zero and the climate response is simulated for the following 100 years. RAZE is estimated using a linear OLS fit to years 10-100 following the cessation of emissions, using the models' reported TCRE values in the ZECMIP study (*113*). RAZE values are reported as $RAZE_{3670\,GtCO2}$ ($RAZE_{2750\,GtCO2}$, $RAZE_{7330\,GtCO2}$), respectively. Dashes are inputted where experiments were not completed with a given model.

order of magnitude smaller than present-day emissions, and will likely become smaller still once models routinely include additional under-represented Earth System feedbacks.

Over multi-decadal timescales, additional non-linear effects may result from predominantly positive feedbacks which are missing from current iterations of ESMs and EMICs. These include the potential release of non-CO_2 GHGs (e.g., CH_4, N_2O) from the ocean and land biosphere, wildfire dynamics, ice-sheet-albedo feedbacks and others. IPCC's SR1.5 suggested that 100 $GtCO_2$ be removed from their remaining carbon budget estimates for 1.5 °C and 2 °C to account for unmodelled Earth system feedbacks over the remainder of the 21st century, largely due to permafrost thawing (*109*, *301*), corresponding to additional emissions of up to +2 $GtCO_2$/year after 2050. AR6 gave a best estimate of +26 ± 97 $GtCO_2$ per °C of warming, less than half the SR1.5 estimate, albeit with a large uncertainty. In the context of the ZECMIP experiments, including these unmodelled feedbacks (*109*) would increase the ensemble-average

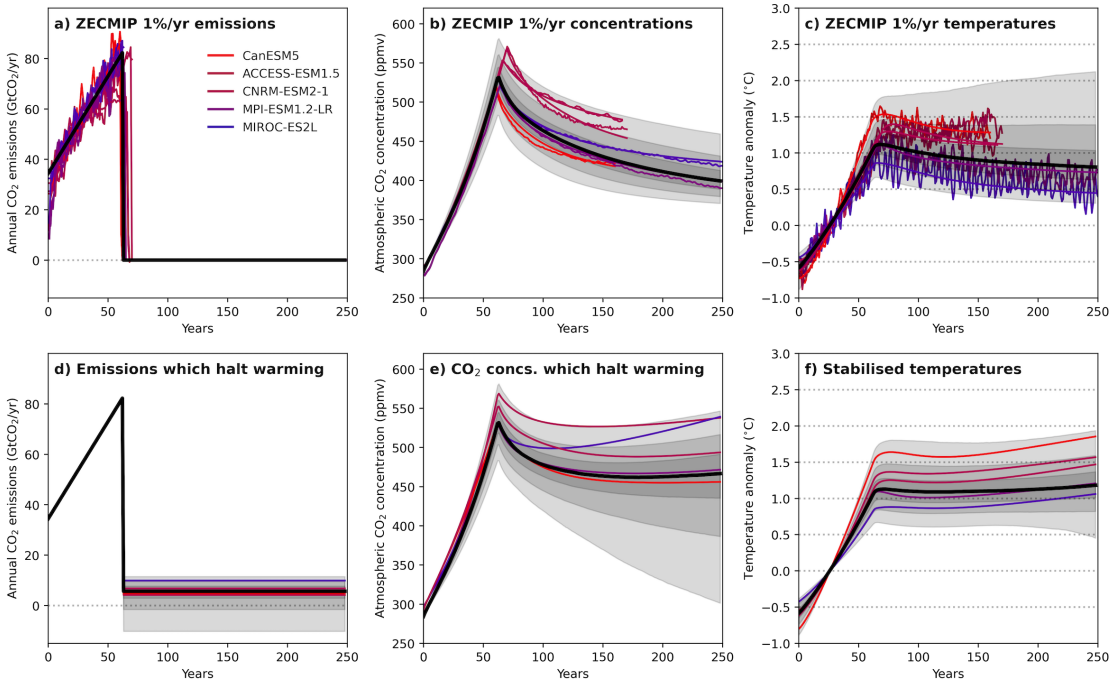

Figure 6.1: Response to net zero following an idealised 1%/yr concentration increase experiment. CO_2 emissions (panel a), atmospheric CO_2 concentrations (panel b) and temperature anomalies (panel c) from five ESMs contributing A-type experiments to the ZECMIP study. Line colours correspond to individual model's TCRE values (see colourbar range below figure 6.3, and individual model values to right of figure 6.4b). FaIRv2.0 emulations are shown on top of individual model outputs in grey. An ensemble of FaIR model runs using the black emissions timeseries (plotted in panel a) is shown in panels b and c, with shaded regions showing the 5-95th, 17-83rd, 33-66th percentiles of the distribution (solid black line shows the 50th percentile response). In panel d the CO_2 emissions are identical to the black emissions in panel a before net zero, but after they include the emissions which are consistent with no further warming (E_{halt}), for both the FaIR ensemble response (in grey) and individual ESM emulations. The CO_2 concentrations and temperature anomaly for the CO_2 emissions in panel d are plotted in panels e and f.

RAZE distribution from negative towards zero, but not enough to make it positive, at least for 1.5 °C-compatible scenarios. There remains substantial uncertainty in these underrepresented feedbacks at various cumulative emissions levels (*111*). Additional non-linearities may also arise over centennial-or-longer timescales where the assumptions used in deriving the RAZE response break down (*113*, *302*).

6.3.2 Emulating the ESM response to net zero

Using the FaIRv2.0 simple climate model I can emulate individual model responses to the ZECMIP experiments to confirm these direct RAZE estimates, as well as extend

the analysis to a probabilistic treatment of uncertainties. Figure 6.1 shows five ESM responses to the ZECMIP A-type 3670 $GtCO_2$ experiment, where CO_2 concentrations rise at 1 %/yr until 3670 $GtCO_2$ has been emitted, and thereafter emissions are set to net zero (ACCESS-ESM1.5, CanESM5, CNRM-ESM2-1, MIROC-ES2L, MPI-ESM1.2-LR; coloured according to their TCRE value). Panel a plots the CO_2 emissions, panel b the CO_2 concentrations, and panel c the global surface temperature anomaly. On the same panels smooth lines show the FaIRv2.0 emulated response to the same experiment for each ESM, using Leach *et al.* (2021)'s derived thermal parameter set for each ESM (*29*) and tuning the carbon cycle using the approach outlined in Jenkins *et al.* (2018) (i.e. by adjusting the r_0, r_C and r_T parameters estimating the integrated Impulse Response Function in FaIRv2.0 to reproduce the ESMs emissions-to-concentrations relationship, see equation 2.21 in chapter 2, and refs. (*29*, *94*)). As part of the carbon cycle tuning it was decided to alter the 'pool fractions' parameter (a_i in equation 2.19): in the standard FaIRv2.0 setup $a = [0.2173, 0.2240, 0.2824, 0.2763]$ (ordered longest-to-shortest timescale); while the revised setup uses $a = [0.1173, 0.1240, 0.3824, 0.3763]$. This adjustment is justified since the former setup is inconsistent with our understanding of the multi-millennial ocean carbon cycle response to an emissions perturbation. Estimates of the Revelle buffer factor, which sets the fraction of an atmospheric CO_2 perturbation which can dissolve in water at standard temperature and pressure (*303*), suggests that only 10-15% of a CO_2 emission will remain in the atmosphere over multi-millennial timescales (*304*) (hence the reduction of the two long-timescale a values above). A revisiting of Joos *et al.* (2013)'s study to refit FaIRv2.0's a parameters using CMIP6 ESMs would aid the analysis of RAZE, but is beyond the scope of this work. For each model plotted in figure 6.1 the temperature anomaly behaviour after net zero is successfully captured in FaIRv2.0.

Alongside the individual ESM emulations, I use FaIRv2.0 to produce an ensemble of responses to the black CO_2 emissions timeseries in figure 6.1a. The responses are derived with a 10,000-member ensemble of thermal and carbon cycle parameter sets, constrained on the range of CMIP6 model responses and temperature observations (*29*). FaIR carbon cycle sampling varies the integrated Impulse Response Function parameters,

following the approach of Jenkins *et al.* (2018) (*94*). Parameters are sampled from an ensemble of FaIR-emulated CMIP6 models (*29*), translating to distributions

$$r_0 \sim 33.90 \times \mathcal{N}(1,\, 0.154)\,\text{years},$$

$$r_C \sim 0.0188 \times \exp(\mathcal{N}(0,\, 0.442))\,\text{years/GtC},$$

$$r_T \sim 2.67 \times \mathcal{N}(1,\, 0.615)\,\text{years/°C}.$$

Following Leach *et al.* (2021), I use FaIRv2.0 with a three box thermal impulse response setup, sampling $\ln(d_1)$, $\ln(d_2)$ and c_1 parameters as a multi-variate normal distribution, and $\ln(d_3)$ with an independent normal distribution. The underlying distribution shapes are taken from parameter sets which emulate individual CMIP6 models (see Leach *et al.* (2021) (*29*)). The thermal-box efficacy parameters in equation 2.2 (c_1, c_2 and c_3) are then set such that, with the chosen d_is, the corresponding distributions of TCR and ECS parameters satisfy

$$\text{TCR} \sim \mathcal{N}(1.8,\, 0.2)\,°\text{C},$$

$$\text{TCR/ECS ratio} \sim \mathcal{N}(0.55,\, 0.15),$$

$$F_{2\times} \sim \mathcal{N}(3.74,\, 0.56)\,\text{W/m}^2,$$

where $F_{2\times}$ is the ERF from doubling CO_2 concentrations. These distributions produce an ECS = 3.2 °C (2.5-4.5°C; likely range), consistent with Forster *et al.* (2021) (*5*) and the observationally-constrained FaIRv2.0 ensemble produced in Leach *et al.* (2021) (*29*). Clearly, the choice of parameter distribution shapes will impact on the derived distributions of RAZE and hence ZEC, particularly if there is correlation between the multi-century carbon and thermal cycle response timescales, which is not accounted for in FaIRv2.0. Quantifying this effect requires further research.

With this parameter sampling I produce a 10,000-member set of CO_2 concentrations and temperature response timeseries for the black CO_2 emissions timeseries in panel a. These emissions are designed to produce a 1%/yr CO_2 concentration increase until 3670 $GtCO_2$ have been emitted, followed by a century of net zero CO_2 emissions

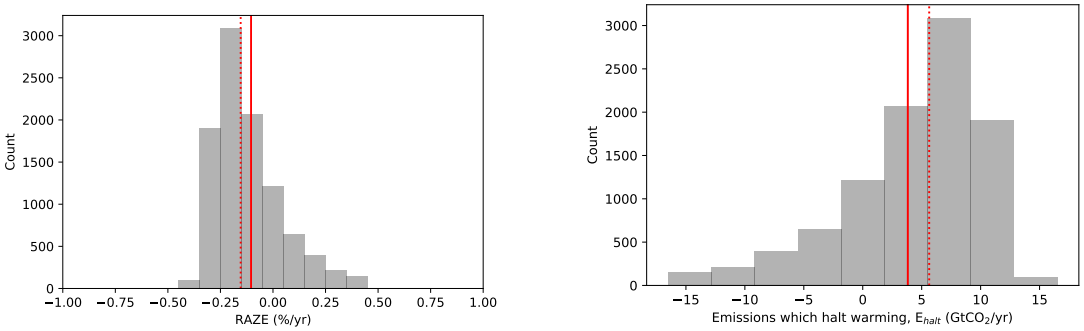

(a) RAZE distribution **(b)** E_{halt} distribution

Figure 6.2: Panel a shows the RAZE distribution produced in FaIRv2.0 using a 1 %/yr CO_2 experiment releasing 3670 $GtCO_2$ prior to net zero, following the A-type setup in MacDougall *et al.* (2020) (*113*). Panel b shows the corresponding E_{halt} distribution. Red lines show median (dotted) and mean (solid) values for each panel: RAZE = -0.15 %/yr, -0.10 %/yr; E_{halt} = +5.5 $GtCO_2$/yr, +3.7 $GtCO_2$/yr, respectively. 5-95th percentile ranges span -0.31 to +0.28 %/yr (RAZE), and -10.3 to +11.4 $GtCO_2$/yr (E_{halt}).

thereafter (following ZECMIP's A-type experiment protocol). The 5-95th, 17-83rd, 33-66th percentiles, and median responses for CO_2 concentrations and temperature anomaly are plotted in grey in figures 6.1b and c. The RAZE is estimated by fitting a linear relationship using OLS regression onto the temperature response between 10-100 years after net zero. I ignore the first decade following net zero where rapid adjustments take place resulting from imbalances between the sub-decadal carbon and thermal cycle timescales (*305*). This is appropriate given the expression for RAZE in equation 6.3 is linearised over multi-decade intervals. The RAZE distribution spans -0.31 %/yr to +0.28 %/yr, with a mean value of -0.10 %/yr (shown in figure 6.2a), overlapping with the RAZE estimated with individual ESMs and EMICs in table 6.1. Parameter sets corresponding to a smaller TCR/ECS ratio typically result in a more positive RAZE (*302*), and vice versa, supporting the findings of the derivation in chapter 2.

In the FaIRv2.0 ensemble the mean E_{halt} is +3.7 $GtCO_2$/yr, with the distribution's 5-95th percentile spanning -10.3 and +11.4 $GtCO_2$/yr (figure 6.1d and 6.3). The distribution is skewed towards positive residual emissions but with a tail reaching well into negative residual emissions, resulting from log-normal distributions sampled when estimating the multi-century response timescales in FaIRv2.0. Individual RAZE and E_{halt} distributions are shown in figure 6.2. Figure 6.3 highlights that E_{halt} is poorly constrained

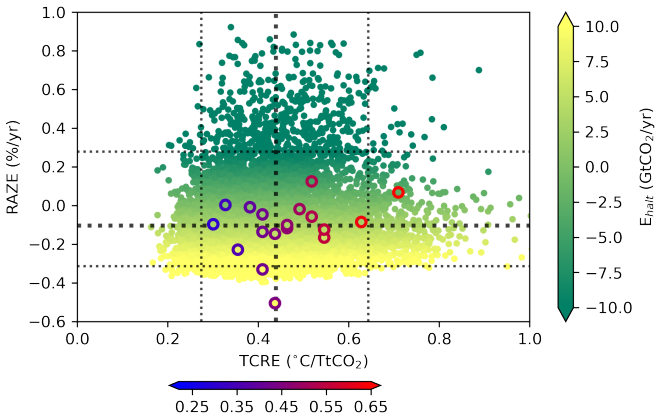

Figure 6.3: Characteristics of the distribution in RAZE, TCRE and E_{halt} parameters. Individual ESM and EMIC estimates using the 3670 $GtCO_2$ (1000 GtC) 1%/yr experiment in ZECMIP are plotted with edges coloured blue-to-red depending on the TCRE parameter. The 10,000-member FaIRv2.0 distribution is shown shaded by E_{halt} value (green refers to large negative E_{halt}, yellow to large positive E_{halt}). Means and 5-95th percentiles of RAZE and TCRE values in the FaIRv2.0 distribution are shown with dotted lines. The colourbar below the figures show the AR6 range for TCRE (0.27-0.63 °C/$TtCO_2$), with the same colouring used for all ZECMIP ESM models shown in figures 6.1 and 6.4.

by the TCRE, with no correlation existing between the TCRE and RAZE parameters. As in the ZECMIP ESM responses, net zero is not necessarily a requirement of halting CO_2-induced warming in the mean FaIRv2.0 response; around three quarters of the E_{halt} distribution lies above zero (see figure 6.2b). But it is possible that net negative emissions will prove necessary — for a quarter of the ensemble negative emissions are required to halt further warming (95th percentile of -10.3 $GtCO_2$/yr, around a quarter of present-day positive emissions).

I can demonstrate that warming does indeed halt over multi-decadal intervals by rerunning the FaIRv2.0 ensemble, but now including the E_{halt} in figure 6.2 after net zero, with resulting plumes shown in panels d, e and f. Over multi-decadal intervals the E_{halt} are successfully stabilising warming in figure 6.1f. Over multi-century timescales some residual warming or cooling may occur once the RAZE approximation begins to break down (see beyond 100 years following net zero in panel f). For an individual scenario the level of E_{halt} depends on the chosen thermal and carbon cycle parameters, however only in ensemble members where the TCR/ECS ratio is very small, or where the multi-century carbon cycle response is substantially slower than the thermal

cycle, are substantial negative emissions required to halt warming. The inclusion of additional unmodelled Earth System feedbacks will push the RAZE distribution (and hence E_{halt}) closer to centring on zero.

6.3.3 The response to net zero in real-world scenarios

The RAZE distribution suggests that small residual positive emissions may be consistent with halting global warming over multi-decadal intervals in idealised CO_2-only experiments. Next, I look at how this result changes in real-world scenarios, with both a more realistic time history of CO_2 emissions and the inclusion of non-CO_2 warming.

Figure 6.4a shows the best-estimate CO_2 emissions timeseries from the Global Carbon Project (*299*) between 1850 and 2020. Beyond present day, CO_2 emissions are reduced linearly to net zero by 2050 and remain zero thereafter (black line). CO_2-induced warming is shown in figure 6.4b with a grey plume, calculated using FaIRv2.0 and the same 10,000-member parameter set as in figure 6.1. The CO_2-induced warming reaches approximately 1.0 $\pm$ 0.2 °C) between 2010-2019, consistent with AR6 estimates for the CO_2 contribution to historical warming (see fig. 7.8 of Forster *et al.* (2021) (*5*)). After net zero CO_2-induced warming stabilises (if RAZE $\sim$ 0 %/yr) or exhibits a small quantity of residual warming or cooling. From this ensemble I again estimate the RAZE (derived from the gradient in CO_2-induced temperature in years 10-100 following net zero in figure 6.4b; mean = -0.09 %/yr, 5-95th percentile range -0.24 to +0.17 %/yr) and infer the CO_2 emissions consistent with no further CO_2 induced warming, $E_{halt,\ CO2}$. Halting CO_2-induced warming after 2050 requires residual emissions reduced to +2.6 $GtCO_2$/yr, with a 5-95% range of -5.1 to +7.3 $GtCO_2$/yr. Compare this to the E_{halt} estimated in figure 6.1, E_{halt} = +3.7 (-10.3 to +11.4) $GtCO_2$/yr, calculated from a very different CO_2 emissions scenario (a sudden cessation of emissions following a period of 1 %/yr CO_2 concentration increase). The difference between these two E_{halt} estimates arises predominantly because, at the time of net zero, figure 6.1's climate system is perturbed further from equilibrium than in figure 6.4, where CO_2 emissions are reduced to zero over a 30-year period (which gives the climate system some time

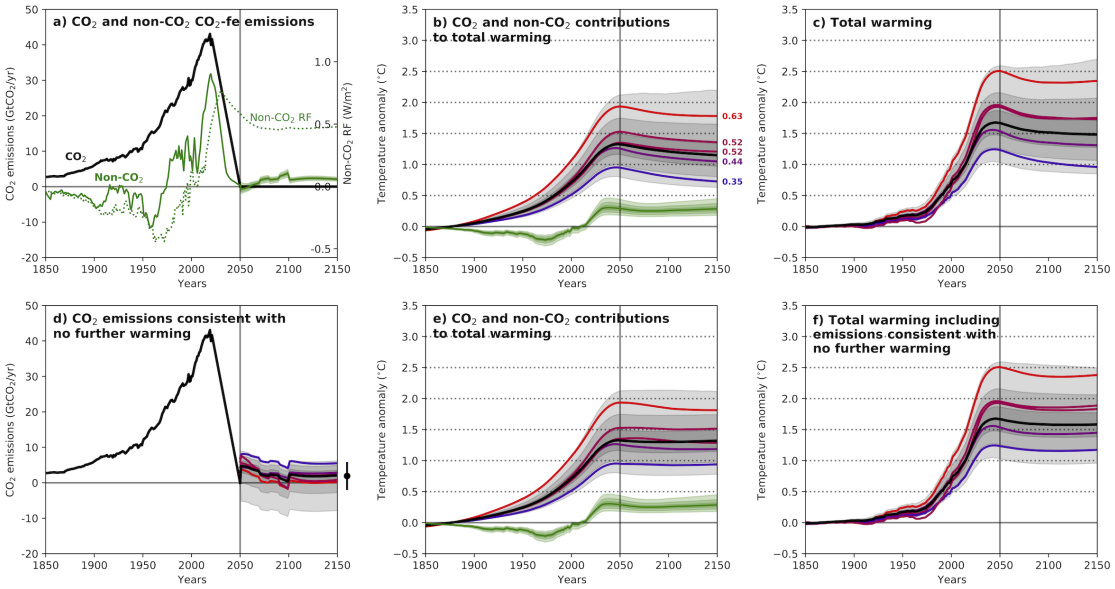

Figure 6.4: The response to net zero in a real-world 1.5 °C-consistent scenario. Panel a shows the best-estimate annual CO_2 emissions timeseries from the Global Carbon Project in black, which is reduced to net zero in 2050, and the best-estimate historical+SSP1-19 non-CO_2 ERF timeseries (green dotted line), also expressed in CO_2-forcing-equivalent terms (green solid line). For these, panel b shows the diagnosed CO_2 and non-CO_2 warming responses in grey and green respectively, and panel c shows the combined total warming plume. Panels d, e and f then repeat panels a, b and c, but include the additional emissions consistent with no further warming ($E_{halt,\ total}$). Panel d shows the black CO_2 emissions from panel a until 2050, and thereafter a plume of $E_{halt,\ total}$. Panel e shows the corresponding CO_2 and non-CO_2 warming plumes (and the SSP1-19 non-CO_2 ERF warming response in green). Panel f shows the corresponding total warming, which stabilises over multi-decade intervals after net zero. In all panels the coloured lines show five responses in FaIRv2.0 which emulate individual ESMs, for which we have appropriate parameter sets tuned to the ESM's carbon and thermal cycle properties (colour represents the relative TCRE value, noted to the right of panel b, with the colourbar shown below figure 6.3 and model names from figure 6.1a). A nominal missing Earth system feedback is shown for scale to the right of panel d, with magnitude +2.2 GtCO $\pm$ 3.7 $GtCO_2$/yr. In all panels, warming response plumes have 5-95th, 17-83rd and 33-66th percentile ranges along with the median response, all relative to 1850-1900.

to adjust). Therefore, residual heating or cooling from historical emissions manifests to a greater extent in figure 6.1, inflating the estimated E_{halt}.

Panel b also shows the warming response to the *historical+SSP1-19* non-CO_2 ERF timeseries (*44*, *72*) (dotted line in panel a), which I include to model the warming contribution from non-CO_2 pollutants over the 21st century (green plume). SSP1-19 is chosen since it has similar policy ambition to a "net zero by 2050" CO_2 pathway. Total anthropogenic warming (the sum of CO_2 and non-CO_2 contributions) is shown

in panel c. Alongside the plumes, five ESM emulations of this scenario (using the FaIRv2.0 parameter sets derived for figure 6.1) are shown in panels b and c (colour represents TCRE value, noted to right of panel b).

Stabilising the CO_2-induced warming in panel b does not guarantee that total warming is halted — residual emissions must also account for non-CO_2 warming. To help visualise this requirement, the green plume in panel a plots the non-CO_2 ERF converted into CO_2-fe emissions (*94*) (as defined in chapter 2 and used in chapter 5). In the SSP1-19 scenario, non-CO_2 ERF increases until 2030 before declining, corresponding to CO_2-fe emissions which increase to a peak around present day, and then decline to near-zero by 2030 (see the non-CO_2 CO_2-fe emissions in a 1.5 °C-compatible scenario in figure 5.2a). Expressing this as CO_2-fe emissions tells us the additional CO_2 emissions that must be removed from $E_{halt,\ CO2}$ in order to additionally cancel out the non-CO_2 warming after net zero.

Heavy and sustained reliance on offsetting between LLCPs and SLCPs present specific policy challenges (*4*, *125*, *127*). Fortunately, this is less of an issue in ambitious mitigation scenarios like SSP1-19, where the SLCP contribution to non-CO_2 ERF has largely stabilised by 2050 (*67*). Hence, CO_2-fe emissions reduce to near-zero in figure 6.4a by the time of net zero, and thereafter are composed of residual long-lived pollutants and the multi-century response to stabilised SLCP emissions. It is appropriate to offset these positive CO_2-fe emissions with negative CO_2 emissions.

The sum of $E_{halt,\ CO2}$ and the inverted CO_2-fe emissions from non-CO_2 pollutants gives us the CO_2 emissions required to stabilise total warming after net zero, $E_{halt,\ total}$. These are plotted in figure 6.4d in the grey plume. Larger TCR/ECS ratios and/or $d_2 < \tau_2$ are associated with more negative RAZE and more positive $E_{halt,\ total}$; smaller TCR/ECS ratios and/or $d_2 > \tau_2$ are associated with more positive RAZE and more negative $E_{halt,\ total}$. Around two thirds of the $E_{halt,\ total}$ distribution remains above zero after 2050, with best-estimate $E_{halt,\ total} = +2.2\ GtCO_2/yr$ (5-95th percentile range of -7.3 and +6.2 $GtCO_2/yr$). The error bar to the right of figure 6.4d indicates unrepresented feedbacks causing $+2.2 \pm 3.7\ GtCO_2/yr$ emissions (equivalent to $\sim 180\ GtCO_2$ released 2020-2100 (*14*), or +0.1 °C warming using the best-estimate TCRE from chapter

5), approximately the size of the permafrost thawing feedback (*14*, *109*). Including unrepresented feedbacks such as this would mean that $E_{halt,\ total}$ will approximately centre on zero, but still with a substantial range of uncertainty.

Finally, figure 6.4e and f show the warming response to figure 6.4d's CO_2 emissions and the SSP1-19 non-CO_2 ERF. Since CO_2 emissions are used to offset non-CO_2 warming after net zero, CO_2-induced warming does not quite stabilise in figure 6.4e. Total warming (figure 6.4f) does halt in the decades following net zero: see for example the edges of the warming plume after 2050 in panel c in comparison to the warming plume after 2050 in panel f (similar behaviour can be seen in the individual ESM emulations using FaIRv2.0, where the warming trends in the 10-100 years after 2050 are now approximately zero in panel f).

6.4 Discussion

Since the initial experiments identifying the linear TCRE relationship between cumulative CO_2 emissions and the global surface temperature anomaly in the early 2000s, the policymaking process has quickly adopted net zero as a focal point of mitigation policy. This rapid translation of an academic concept into policy reflects the considerable simplification the net zero framing offers. This work is not refuting the value of net zero as a headline target for global CO_2 emissions (the best-estimate condition for warming stabilisation is very close to net zero in figures 6.1 and 6.4). However, the precise conditions for warming stabilisation are uncertain at present, and still include the possibility of requiring gigatonne-scale positive or negative CO_2 emissions over multi-decadal intervals.

Hence, contrary to the perception in policy, current evidence does not indicate that net zero CO_2 emissions are necessarily a requirement to produce no further warming over multi-decadal timescales, and both positive or negative emissions can be consistent with halting warming. This supports SR1.5's statement that "reaching and sustaining net zero CO_2 emissions and declining net non-CO_2 RF" is sufficient to halt warming, and not the stronger "requirement" of "reaching at least net zero CO_2 emissions" in AR6. In IPCC lexicon, the uncertainty qualifier which should be placed on the AR6 statement

is "as likely as not", with at least 50% of the E_{halt} distribution lying above net zero in figures 6.1 and 6.4. Of course, the exact requirements for warming stabilisation will not be known for many decades after CO_2 emissions have been reduced by at least an order of magnitude below their current levels — the principle requirement of policy today must remain on achieving that order-of-magnitude reduction. RAZE provides additional context for policymakers on the requirements for mid-century policy: if the value of RAZE remains uncertain, then policy must maintain sufficient capacity to adjust carbon sinks to the emergent conditions for warming stabilisation.

Residual emissions consistent with no further warming over multi-decadal intervals may be positive or negative, depending on the exact balance of multi-century carbon and thermal cycle responses, even having accounted for the residual warming from non-CO_2 pollutants, and the impact of unrepresented Earth System feedbacks.

6.5 Chapter close

This chapter discussed an extension to the TCRE framework to model the multi-decadal response to net zero CO_2 emissions. I first demonstrated that the RAZE framework, derived in chapter 2, captured the ESM and EMIC response to net zero, and produced an ensemble of net zero responses using FaIRv2.0. I then investigated the requirements of 'net zero' if policymakers target a multi-decadal period of warming stabilisation. With RAZE between -0.09 (-0.24 to +0.17) %/yr, and non-CO_2 ERF following a 1.5 °C-compatible scenario, corresponding E_{halt} are +2.2 (-7.3 to +6.2) $GtCO_2$/yr, meaning small positive residual CO_2 emissions may be consistent with warming stabilisation. The exact conditions required depend on the magnitude of Earth System feedbacks and the non-CO_2 ERF pathway.

You're braver than you believe, stronger than you seem,
and smarter than you think.

— Winnie the Pooh

7 Conclusions

Contents

7.1 An overview of this thesis

This thesis began with an overview of the methodologies used to define the level and rate of anthropogenic global warming. These have grown more complex over the past decades, from the early WMO definition considering the trend in the 30-year average GMST anomaly (*14*), to the statistical attribution methodologies used today (*15*, *17*, *18*). The most recent IPCC report estimated the current level and rate of anthropogenic warming to be around 1.1 °C, rising at +0.2 °C/decade (see table 1.1). Chapter 1 discussed how the various methodologies for this attribution provide consensus on the level of warming, but are less consistent on the warming rate. This is despite the rate of warming being the more important variable for policymaking in the next decade, given our proximity to the 1.5 °C warming threshold.

The defining question of my thesis is: *what is the anthropogenic contribution to the rate of warming?* I framed this question over multiple timeframes: what controls the warming rate today?; how does this assessment impact on the design of policy between now and net zero?; and what are the requirements for warming stabilisation at the time of net zero? Below I summarise how these questions were addressed in chapters 3–6.

Chapter 3: The present-day rate of anthropogenic warming

Constraining the current rate of warming requires an accurate estimate of the anthropogenic ERF trend, whose recent uncertainty arises primarily from the aerosol component. Although GHGs contribute the majority of the overall ERF trend, rapid trend changes are more readily controlled by changes in the emissions rate of short-lived climate pollutants. In chapter 3 I demonstrated that aerosols drive an acceleration in anthropogenic ERF, causing the trend to rise by roughly $+0.2\,W/m^2$/decade between 2000-2020 in the IPCC's standard historical ERF timeseries (figure 3.2). This has caused an increase in the anthropogenic warming rate since 2010 (figures 3.5 and 4.15), which is not communicated in the AR6 headline assessment. These standard ERF timeseries rely on evidence from GCMs and simple climate models, with less input from direct observational evidence of the recent ERF trend. Chapters 3 and 4 identified observational evidence of an aerosol-induced ERF acceleration and determined the consequences for the rate of warming.

Chapter 3 focused on constraining the overall anthropogenic ERF trend using GMST, TOA flux, and AOD observations. First, I showed that the GMST record displays an apparent acceleration; increasing in trend by $+0.1\,°C$/decade since 2000. To isolate the anthropogenic contribution, I extended the attribution approach of Haustein *et al.* (2017) (*15*) to separate the aerosol and GHG contributions. I determined that AGW accelerated, increasing the trend by +0.05 (+0.01 to +0.08) °C/decade between the first and second decade since 2000, primarily due to aerosol forcing changes (~+0.03 °C/decade), with a smaller contribution from GHGs (~+0.02 °C/decade). The remainder of the GMST trend change (~+0.05 °C/decade) was attributed to internal variability of the climate system. This internal variability contribution, principally from ENSO, is a substantial

contributor to the trend variability over the two-decade interval and hampers efforts to better constrain the AGW trend.

Chapter 3 also analysed CERES TOA flux (*168*) and AOD trends (*153*), which both supported a small acceleration in the anthropogenic ERF trend since 2000. They also both included the possibility of a *little-to-no-acceleration* scenario, which was less well sampled by figure 3.2's ERFs. In the TOA flux data this arose because globally-averaged trends exhibit substantial variability over the two-decade interval, predominantly due to ENSO's influence on tropical cloud structures (see Loeb *et al.* (2019) (*173*) and figure 3.7). This variability is large enough to induce spurious TOA flux trends that overwhelmed the anthropogenic contribution, biasing the estimated feedback parameters. Similarly, in AODs the annual variability in the observed record means I could not rule out very low trend change since 2000 despite the best-estimate supporting the claim that aerosol emissions reductions had caused an anthropogenic ERF acceleration.

In summary, a wide range of anthropogenic ERF behaviour is supported by the globally-averaged observations. This includes both the best-estimate scenario of an aerosol-induced ERF acceleration of $+0.2\,W/m^2$/decade between 2000-2020, and a *little-to-no-acceleration* scenario that is less well sampled by the standard ERF ensemble.

Chapter 4: The aerosol ERF's spatiotemporal pattern

Chapter 3's difficulty in attributing the GMST acceleration exists primarily because the internal variability and anthropogenic ERF trends share similar globally-averaged shapes. To constrain the aerosol ERF trend, chapter 4 used a multi-decade and multi-dataset spatiotemporal pattern analysis. This built on Quaas *et al.* (2022)'s study of the linear trends present in aerosol, cloud, and TOA radiative flux satellite observations. Quaas concluded that aerosol ERF peaked between 2000-2020 (*164*), but only considered the 20-year linear trend in this analysis. Chapter 4 looked to improve on Quaas' study by specifically targeting the aerosol *acceleration* signal.

The spatiotemporal patterns exhibited by AOD and clear sky SW TOA flux correlate remarkably well with the location of prominent aerosol emissions trends since 2000. In the northern hemisphere the observed clear sky SW flux trends appear to be majority

aerosol-induced since 2000, with secondary contributions from relative humidity and surface albedo changes. AOD observations imply a -0.01 AOD trend change between the first and second decade since 2000, coinciding with the peak in anthropogenic aerosol emissions (*63*). This AOD trend change results in ARI ERF trends increasing by $+0.09 \pm 0.02\,W/m^2$/decade between 2000-2020, consistent with AR6's standard ERF dataset in figure 3.2.

With a constraint on the aerosol radiation interactions (ARI) ERF, chapter 4 then estimated the aerosol cloud interactions (ACI) ERF trend. This is more challenging; figures 4.8 and 4.10 showed that all sky SW TOA fluxes were strongly influenced by ENSO variability since 2000, with ENSO playing an important role setting the location and optical thickness of global cloud fields (*173*). Over most of the globe the all sky flux trendmaps are poorly correlated with AOD. Further, where the correlation does exist it is difficult to determine the aerosol contribution: as ENSO mimics the western tropical pacific SST perturbation that arises from a rapid reduction in Chinese aerosol emissions, limiting the direct observational evidence available in this key region.

Despite these complications the all sky flux record is compatible with a small ACI acceleration since 2000. ENSO-induced patterns principally manifest as changes in the location and prevalence of cloud fields, and less in their optical properties. Hence, by separating the cloud optical properties from cloud location trends, I better separated the variability and aerosol-induced patterns in figure 4.8. Local trends in CDNC retrievals implied an aerosol perturbation to the cloud fields in the northern hemisphere extratropics. These are entirely consistent with AOD trends over these regions, providing clear observational evidence of the impact of aerosol emissions trends on global cloud fields since 2000. Combining the cloud optical depth trends, cloud fraction trends, and clear sky flux trends provides a good explanation of the all sky flux trends in figure 4.8. I estimated aerosol-emissions-driven AOD trends have caused CDNC to reduce by 2-5%/decade since 2000, corresponding to an ACI ERF trend increase of $+0.2 \pm 0.1$ W/m^2/decade between the first and second decade since 2000.

Combining this observational analysis with energy-balance constraints (Smith *et al.* (2021) (*73*) and chapter 3), I estimated that aerosol ERF trends has increased

by $+0.2 \pm 0.1\,W/m^2$/decade between the first and second decade since 2000. Hence, chapter 4 supports Forster *et al.* (2021)'s claim that aerosol ERF has weakened by $+0.2\,W/m^2$ between 2014-2019 (*5*). It also supports the SSP ERF trends analysed in figure 3.2, but excludes the *little-to-no-acceleration* scenario which remained plausible after chapter 3's analysis.

With this aerosol ERF trend constraint I once again estimated the aerosol-induced warming acceleration, this time using a FaIRv2.0-ensemble methodology similar to that outlined in Forster *et al.* (2021) and Smith *et al.* (2021) (*5*, *73*). This concluded aerosol emissions trends have accelerated anthropogenic global warming by +0.05 (+0.02 to +0.11) °C/decade between the first and second decade since 2000. This is slightly larger than the result in chapter 3 reflecting the differing attribution methodologies used in each chapter; with the energy-balance constraint downscaling the historical aerosol contribution more strongly in chapter 3 than in chapter 4.

Taken together, chapters 3 and 4 support the attributed warming level of AR6 (+1.1 °C between 2010-2019 relative to 1850-1900). Both chapters additionally suggested an increased anthropogenic warming rate in the 2010s compared to the 2000s, driven by aerosol emissions reductions since their peak. Overall, I estimated the 2010-2019 warming level was 1.1 °C (relative to 1850-1900; for comparison with AR6), the 2020 warming level was 1.3 °C (relative to 1850-1900), and the current anthropogenic warming rate is around +0.3 °C/decade. These estimates are consistent with the uncertainty ranges in AR6, but higher than that implied by their best-estimates.

Chapter 5: Quantifying CO_2 and non-CO_2 contributions to ambitious climate policy

In the remainder of the thesis I looked at the implications of the warming rate attribution on the physical requirements of mitigation policy. Chapter 5 explored the physical requirements of mitigation scenarios consistent with 1.5 °C based on a reassessment of the remaining carbon budget.

Rogelj *et al.* (2019) described the standard approach used in the IPCC to estimate the remaining carbon budget. This depends principally on the TCRE distribution, present-day warming level, and the estimated warming contribution from non-CO_2 pollutants

(*47*). Using the anthropogenic warming attribution in chapters 3 and 4, chapter 5 focused on quantifying both the TCRE and the contribution of non-CO_2 pollutants to the remaining carbon budget. These estimates took advantage of the novel CO_2-fe metric to account for non-CO_2 contributions to warming, with this approach shown to provide a physically-coherent comparison of pollutants with widely-varying atmospheric properties.

In chapter 5 I estimated the TCRE at 0.40 (0.26-0.78) °C/TtCO_2 by combining assessments of the present-day cumulative CO_2-fe emissions, and anthropogenic warming level (*15*, *94*). This is consistent with other observationally-constrained estimates (*92*), but is slightly below the best-estimate TCRE quoted in AR6 (0.45 °C/TtCO_2; likely because the best-estimate TCRE in AR6 included assessments using CMIP6 models). In figure 5.3 I estimated the total remaining CO_2-fe budgets compatible with 1.5 °C warming, using the CO_2-fe metric to produce a 2D representation of the CO_2 and non-CO_2 contributions. This facilitated a physically-coherent comparison of scenario categorisations from recent IPCC reports. In 1.5 °C-compatible scenarios the non-CO_2 CO_2-fe budgets spanned 50-300 GtCO_2. Based on this range, I estimated the remaining carbon budget for a 66% chance of limiting warming to 1.5 °C was 300 GtCO_2. This is smaller than AR6's equivalent budget (400 GtCO_2 (*3*)). Differences were primarily due to the choice of present-day warming level and non-CO_2 warming contribution: I assumed non-CO_2 pollutants contribute 130 GtCO_2 until peak warming, and that present-day warming is 1.3 °C.

Chapter 6: The physical requirements for warming stabilisation

Building on chapter 5's analysis of the size of the remaining carbon budget, chapter 6 studied the physical conditions required to achieve a multi-decade period of warming stabilisation once the remaining budget is exhausted. This property of the physical climate system has received remarkably little research attention to date, beyond the IPCC statement that net zero CO_2 emissions are a condition to halting CO_2-induced warming. More precise conditions for warming stabilisation are unclear, with even the two most recent IPCC reports posing net zero CO_2 emissions as either a sufficient (SR1.5) or a necessary (AR6) condition for halting CO_2-induced warming. Chapter

6 looked to quantify the requirements of CO_2 emissions policy to halt anthropogenic warming over multi-decade intervals.

This discussion relates to the size and sign of the zero emissions commitment (ZEC) — a physical property which has, until now, been separated from other physical properties relevant to the CO_2 warming response (e.g. Rogelj *et al.* (2019) set the ZEC to zero when estimating the remaining carbon budget (*47*)). In chapter 6 I began by analysing the behaviour exhibited in ESMs and EMICs in the ZECMIP experiments (*57*), where the ZEC spans $\pm 0.2\,^{\circ}C$ in the 100 years after net zero. Macdougall *et al.* (2020) demonstrated that the spread in the ZECs across ZECMIP-contributing models were driven by differences between the carbon cycle and thermal cycle relaxation timescales between individual models (*113*).

I modelled the ZEC behaviour using a simplified mathematical framework derived from FaIRv2.0's impulse response representation of the carbon and thermal cycle. This framework defined the rate of decline of the temperature anomaly once emissions cease using a new parameter: the rate of adjustment to zero emissions (RAZE). The RAZE relates the difference between the multi-century relaxation rates for the carbon and thermal cycles (see equation 6.3). Whilst this framing aligns well with the results in Macdougall *et al.* (2020), it has the advantage of allowing the ZEC behaviour to be separated into a scenario-dependent term (the cumulative emissions budget), and scenario-independent physical properties (the TCRE and RAZE parameters). I noted that the RAZE itself is independent of the TCRE, but that the ZEC is correlated with both parameters and is scenario-dependent. Using a large ensemble in FaIRv2.0, I estimated that the RAZE parameter spans -0.09 (-0.24 to +0.17) %/yr, meaning at net zero the temperature anomaly declines at -0.9 (-2.4 to +1.7) %/decade. Combined with the TCRE, this corresponds to emissions consistent with warming stabilisation, E_{halt}, equal to +2.2 (-7.3 to +6.2) $GtCO_2$/yr for the decades following net zero in a $1.5\,^{\circ}C$-compatible mitigation scenario.

Hence, chapter 6 determined SR1.5's statement that reaching and sustaining net zero is 'sufficient' to achieve warming stabilisation is better supported than AR6's 'requirement'. These findings align with other recent research on the properties of

ZEC. Tarshish *et al.* (2023, in press) discussed the multi-century response to net zero CO_2 emissions using a simplified framework which balances the properties of the carbon cycle and thermal cycle (*298*). They derived a similar constraint on the long-term ZEC behaviour shown in equation 6.3 and described by Allen *et al.* (2022) (*103*). Koven *et al.* (2023) (*306*) showed that 50% of the multi-century ZEC is already present in CESM2 at the time of net zero. The RAZE framework in equation 6.3 also supports this result: adopting their experimental setup results in 50% of the ZEC_{100} being realised by the year of net zero in equation 6.3. The combined TCRE and RAZE framework in chapter 6 therefore provides a robust physical description of the multi-decadal response to CO_2 emissions.

7.2 Future research directions

This thesis has benefited from the availability of calibrated and co-observed — hence, highly inter-comparable — satellite observations over the near-present period. The quality and extent of these observations has improved markedly since 2000, with products today extending in excess of 20 years with near-global coverage. The upkeep of these products is vital to continue to reap the benefits of the previous two decades of investment. Chapter 3 showed that 20-years of observations are the minimum required to separate the anthropogenic and natural contributions to trends, with significant uncertainty remaining primarily because of the lack of long-term observations in key variables. An additional decade of TOA flux or cloud optical properties observations would substantially improve the derived observational constraints in chapters 3 and 4. The upkeep and replacement of this satellite equipment, as well as projects analysing the multi-decadal trends in their observations, should remain high on the agenda of policymakers and climate scientists alike. The upcoming ESA FORUM mission (*307*) is a significant step towards maintaining the CERES TOA flux records into the next decade, but other records remain at risk. The multi-decadal trends in satellite records are an underutilised data source to constrain key physical climate response parameters, and will become more useful as records mature.

An extension of chapter 3 would analyse an ensemble of atmosphere-only experiments produced using CMIP6 GCMs to emulate the CERES TOA flux products. CERESMIP (*308*) proposes these experiments using updated historical ERFs, SSTs, and emissions from 1990-2021. This protocol includes outputs from the COSP satellite-simulator to directly compare CERES fluxes and GCM outputs (*309*). Better still would be extending the analysis to run counterfactual scenarios where aerosol/precursor emissions were held fixed at 2000s levels, allowing the direct attribution of aerosols on the TOA flux record. Similar experiments where regional aerosol emissions are fixed were proposed by Wilcox *et al.* (2022) in RAMIP (*162*). These were discussed in chapter 4 to identify processes by which regional aerosol emissions impact on the wider climate system, and will build on the work in this thesis deriving the downstream spatiotemporal patterns imposed by large regional aerosol emissions trends. Finally, the ERF and warming trend attributions in this thesis offer a novel observational constraint for the TCR parameter, extending the approach taken in Tokarska *et al.* (2020) (*86*). This is of great value for constraining near-term climate projections.

The importance of continuing to track the early 21st century's forcing trends is underappreciated, and future work should focus on providing better estimates of near-term forcing trends as well as their levels. This is the subject of the ongoing FORCeS Horizon2020 project. Short-term ERF trends are vital to accurately assess this decade's warming rate, with tangible, real-time impacts for global mitigation policy. Several chapters in this thesis rely on the standardised ERF timeseries produced in AR6. The uncertainty in this ERF ensemble places a key limitation on the ability of this thesis to constrain policy relevant parameters (aerosol forcing, anthropogenic warming rate, TCRE). The methodology for combining individual pollutant's ERFs to produce a total anthropogenic ERF timeseries assumes no correlation between individual pollutants. This is a conservative assumption and requires further study, particularly as GCMs in fact suggest an overall correlation (or anti-correlation) between major forcing components. This is potentially due to modelling groups tuning model parameters to reproduce key observable quantities (e.g. globally-averaged TOA energy imbalance) or otherwise to balance the model and reduce drift. Another issue in the forcing ensemble production

is the failure to account for the pattern effect — where different spatial patterns of warming with the same global average can correspond to different transient and equilibrium climate sensitivities, and hence correspond to different underlying forcings (*310*). A similar issue is apparent with AR6's use of globally-averaged emissions-to-forcing relationships for producing individual pollutants' ERF timeseries. Such an approach misses any non-linearities introduced by the changing spatial pattern of emissions. Regional emissions-to-forcing metrics would be better placed to account for these, particularly for the prominent regional patterns seen for aerosol pollutants. The scale of this impact requires further research.

Work to better understand the physical processes underlying the carbon and thermal cycle response timescales in ESMs may help constrain the RAZE parameter estimated in chapter 6. This builds on the research of Macdougall *et al.* (2020) and Tarshish *et al.* (2023, in press), who were limited by the idealised nature of ZECMIP's experimental setups. Future research would benefit from coordinated experiments using more realistic net zero scenarios computed with emissions-driven ESMs in CMIP7. The newly developed Adaptive Emission Reduction Approach (*311*) provides another source of model data to constrain the RAZE parameter, allowing future studies to conduct emissions-driven ESM simulations that vary CO_2 emissions to stabilize surface temperature at a pre-specified level. The emissions derived from these experiments could be compared against the expected temperature stabilisation conditions derived from the RAZE framework to provide further insights on the applicability of the simplified framework derived in this thesis.

A final piece of future research that would build on this thesis' work is reassessing the pool fractions which are used in FaIR's carbon cycle. This requires repeating Joos *et al.* (2013)'s study analysing the multi-century and multi-millennial response timescales and 'pool fractions' for a four-pool impulse response representation of the carbon cycle (*93*). In chapter 6 I found that the standard pool fractions used in FaIR needed to be adjusted to capture the correct Revelle buffer fraction (the fraction of CO_2 emissions that are not dissolved into the oceans over multi-millennial timescales). This result needs revisting — Joos' study was the last to systematically constrain both

the pool fractions and timescales, and the exercise could be repeated using CMIP6/7-iteration ESMs and updated simple climate models. Further studies on the carbon cycle response to mitigation scenarios should also consider the role of mixed temporary, semi-permanent and permanent CO_2 removals in the context of warming stabilisation pathways, and the role of non-CO_2 uncertainty and Earth system feedbacks to assess the true conditions for warming stabilisation.

7.3 Concluding remarks

This thesis focused on developing a constraint on the current rate of warming using observational evidence of the anthropogenic ERF trend. I then analysed the physical guide rails required to achieve ambitious climate policy. This included quantifying the relative contribution of CO_2, non-CO_2 GHGs, and aerosols to future global warming, and determining the precise conditions for warming stabilisation.

These topics provide an array of questions across a wide range of overlapping research disciplines, such as Economics and Geography, but ultimately are all guided by the underlying properties of the physical climate system. I hope to have contributed to our understanding of the physical climate system and its response to anthropogenic pollution in this thesis, and look forward to the ongoing appraisal of global climate policy as we make progress towards net zero and the halting of anthropogenic global warming.

Appendices

A

Attributing trend changes in globally-averaged observables

Contents

A.1 ERF trend estimates

The ERF timeseries shown in figure 3.2 are taken from Smith *et al.* (2020)(*44*), with the methodology from Dessler and Forster (2018) used to sample individual timeseries to produce an ensemble(*74*). Smith *et al.* (2020) produces aerosol ERF timeseries using the approach outlined in Smith *et al.* (2021)(*73*), where energy budget constraints are used to produce an observationally-constrained aerosol ERF timeseries. GHG and other minor contributing ERFs are produced by averaging ERF timeseries outputted using concentration timeseries using the global relationships and approach outlined in the Supplementary Material of Chapter 7 in IPCC's AR6(*72*).

Aerosol forcing is sub-split into aerosol-radiation interactions (direct interactions

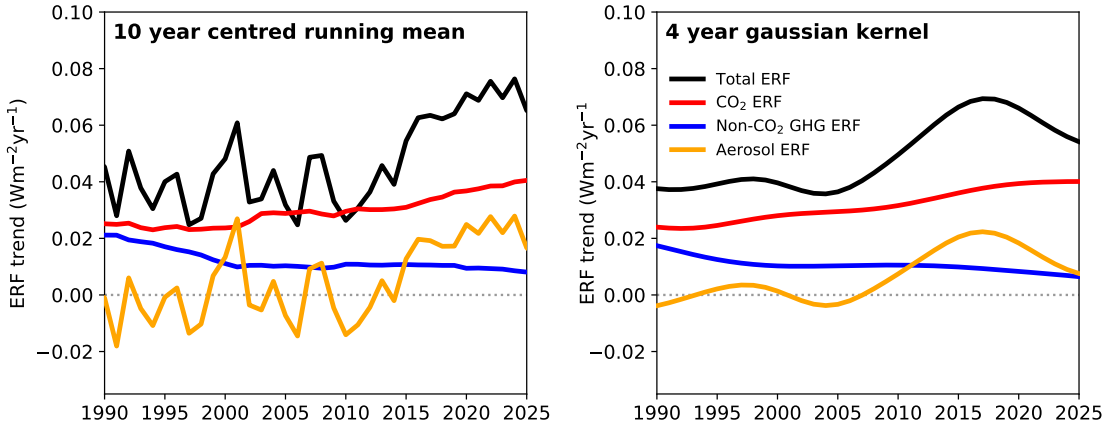

Figure A.1: Alternative estimates of the trends in ERF components, presented in same way as figure 3.2d of chapter 3. Alternative trend estimates here are smoothed using a 10-year centred mean (left panel) or using Gaussian kernel smoothing with a 4-year kernel (right panel), producing similar trends to those in figure 3.2.

between aerosol particulates and radiation; ARI) and aerosol-cloud interactions (aerosol induced changes to cloud properties; ACI). While ARI are approximately linear to first order, ACI have saturation effects that mean globally averaged estimates require different relationships between aerosol precursor emissions and resulting forcing for regions with low/high aerosol loading(*71*). While this saturation must occur locally where aerosol loading is particularly high, higher concentrations still can result in higher aerosol levels further away, offsetting some of the local saturation. Bellouin *et al.* (2020) considered these saturation effects in estimates of aerosol radiative forcing(*71*).

In the Dessler and Forster (2018) methodology individual best-estimate timeseries of ERF components are sampled to cover an assessed present day likely range for each component. Then the individual components are combined to produce an ensemble of anthropogenic ERFs using linear combinations of the individual components, assuming no correlation between individual ERFs. The present-day likely range for each ERF component is taken from AR6. Trends in ERF components are estimated in the main text using a 10-year rolling linear regression. Figure A.1 shows an alternative methodology for deriving the trends (gaussian smoothing with a 5-year kernel). We also consider a forward-differencing gradient, (X[n] – X[n-1])/(t[n]-t[n-1]), averaged over a 12-month centred mean (not shown). All the derived trends show the same approximate form,

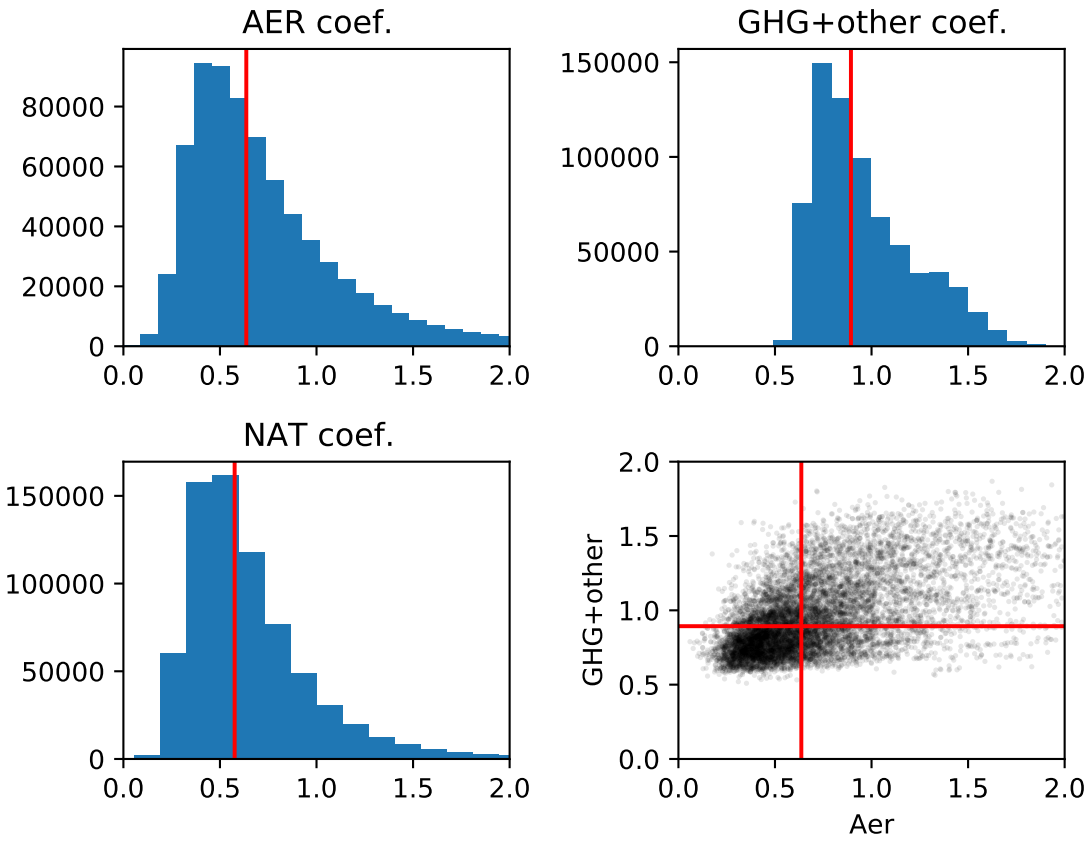

Figure A.2: Histograms of the scaling factors for aerosol, GHG and natural temperature response fits to GMST using OLS regression in figure 3.5 in chapter 3. Red line shows the median value. Bottom right panel shows the correlation between GHG and aerosol scaling factors.

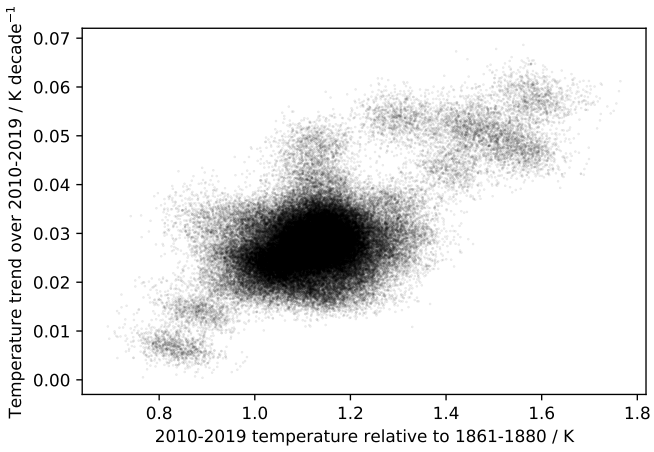

Figure A.3: Present-day anthropogenic warming level and trend correlation. Each point is taken from a fit using three-way attribution of aerosols, GHGs and natural forcings onto observed GMST, plotted in figure 3.5 in chapter 3.

with the increase in anthropogenic trends over the two decades since 2000 arising primarily as a result of aerosol trend changes.

A.2 Three-way warming attribution

In chapter 3 a three-way attribution is completed to determine likely contributions to the historical GMST anomaly timeseries. Additional information on the outcome of that attribution is provided by figures A.2 and A.3.

Figure A.2 shows the scaling factors for the aerosol, GHG and natural ERF's warming responses, calculated using the three-way attribution described in chapter 3. Correlation between the GHG and aerosol scaling factors is also shown. This correlation is expected since, for a given climate response parameter set, the GHG warming and aerosol cooling at present day must offset to best reproduce historical warming.

Figure A.3 then shows the correlation between anthropogenic warming level and rate in the three-way warming attribution, which arises due to the correlation in the ERF level and trend because of the sampling methodology described by Dessler and Forster (2018)(*74*).

A.3 CMIP6 model AOD trends

Figure A.4 shows estimation of five CMIP6 model globally-averaged AOD and ERF trends which are displayed on figure 3.9. Hemispherically averaged AOD trends are also shown. These are estimated using a split decadal trendline in the same way as the TOA flux trend estimates on figure 3.7.

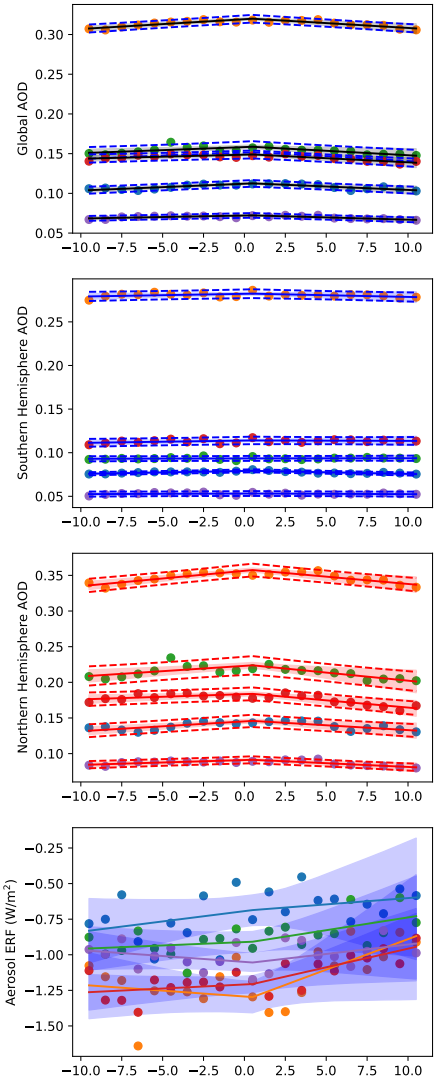

Figure A.4: AOD anomalies (top three panels) and ERF anomalies (bottom panel) for the 5 CMIP6 models considered in figure 3.9 of chapter 3. Years are relative to 2010.

If I have seen further [than others], it is by standing on the shoulders of giants...

— Issac Newton, 1675

Bibliography

[1] S. Arrhenius, "On the Influence of Carbonic Acid in the Air upon the Temperature of the Ground", Philosphical Magazine and Journal of Science, 5th ser. **41** (1896) (p. 2).

[2] "Hint to coal consumers", The Selma Morning Times (1902) (p. 2).

[3] V. Masson-Delmotte, P. Zhai, A. Pirani, S. Connors, C. Péan, S. Berger, N. Caud, Y. Chen, L. Goldfarb, M. I. Gomis, M. Huang, K. Leitzell, E. Lonnoy, J. B. R. Matthews, T. K. Maycock, T. Waterfield, O. Yelekçi, R. Yu, and B. Zhou, *Summary for Policymakers. In: Climate Change 2021: The Physical Science Basis. Contribution of Working Group I to the Sixth Assessment Report of the Intergovernmental Panel on Climate Change*. Tech. rep. 6 (IPCC, Cambridge University Press, 2021) (pp. 2, 3, 9, 25, 27, 75, 96, 143, 150, 165, 187).

[4] M. R. Allen, G. P. Peters, K. P. Shine, C. Azar, P. Balcombe, O. Boucher, M. Cain, P. Ciais, W. Collins, P. M. Forster, D. J. Frame, P. Friedlingstein, C. Fyson, T. Gasser, B. Hare, S. Jenkins, S. P. Hamburg, D. J. A. Johansson, J. Lynch, A. Macey, J. Morfeldt, A. Nauels, I. Ocko, M. Oppenheimer, S. W. Pacala, R. Pierrehumbert, J. Rogelj, M. Schaeffer, C. F. Schleussner, D. Shindell, R. B. Skeie, S. M. Smith, and K. Tanaka, "Indicate separate contributions of long-lived and short-lived greenhouse gases in emission targets", npj Climate and Atmospheric Science **5**, 1–4 (2022) (pp. 2, 19, 30, 31, 55, 179).

[5] P. Forster et al., *The Earth's Energy Budget, Climate Feedbacks, and Climate Sensitivity. In: Climate Change 2021: The Physical Science Basis. Contribution of Working Group 1 to the Sixth Assessment Report of the Intergovernmental Panel on Climate Change*, tech. rep. (IPCC, Cambridge University Press, 2021) (pp. 2–4, 20, 23, 27, 30, 32–34, 36–38, 41, 43, 65, 70, 77, 86, 88, 100, 102, 115, 117, 119, 120, 126, 130, 131, 138, 147, 174, 177, 186).

[6] S. C. Herring, N. Christidis, A. Hoell, and P. A. Stott, "Explaining Extreme Events of 2020 from a Climate Perspective", Bulletin of the American Meteorological Society **103**, S1–S117 (2022) (p. 2).

[7] H.-O. Pörtner et al., *Summary for Policymakers In Climate Change 2022: Impacts, Adaptation and Vulnerability. Contribution of Working Group II to the Sixth Assessment Report of the Intergovernmental Panel on Climate Change*. Tech. rep. (IPCC, Cambridge University Press, 2022), pp. 3–33 (p. 2).

[8] V. Eyring, N. P. Gillett, K. M. Achuta Rao, R. Barimalala, M. Barreiro Parrillo, N. Bellouin, C. Cassou, P. J. Durack, S. Kosaka, S. McGregor, S. Min, O. Morgenstern, and Y. Sun, *Human Influence on the Climate System. In: Climate Change 2021: The Physical Science Basis. Contribution of Working Group I to the Sixth Assessment Report of the Intergovernmental Panel on Climate Change*, tech. rep. 6 (IPCC, Cambridge University Press, 2021) (pp. 2, 3, 9, 19, 39, 43, 139).

[9] K. Hasselmann, "Optimal Fingerprints for the Detection of Time-dependent Climate Change", Journal of Climate **6**, 1957–1971 (1993) (pp. 2, 6).

[10] G. C. Hegerl, H. von Storch, K. Hasselmann, B. D. Santer, U. Cubasch, and P. D. Jones, "Detecting Greenhouse-Gas-Induced Climate Change with an Optimal Fingerprint Method", Journal of Climate **9**, 2281–2306 (1996) (p. 2).

[11] K. Hasselmann, "Multi-pattern fingerprint method for detection and attribution of climate change", Climate Dynamics **13**, 601–611 (1997) (p. 2).

[12] M. R. Allen and P. A. Stott, "Estimating signal amplitudes in optimal fingerprinting, part I: theory", Climate Dynamics **21**, 477–491 (2003) (p. 2).

[13] P. A. Stott, M. R. Allen, and G. S. Jones, "Estimating signal amplitudes in optimal fingerprinting. Part II: application to general circulation models", Climate Dynamics **21**, 493–500 (2003) (p. 2).

[14] IPCC, "Summary for Policymakers of the Special Report on the Global Warming of 1.5°C", (2018) (pp. 3, 9, 15, 18, 26, 27, 141–143, 146, 150, 165, 179, 180, 182).

[15] K. Haustein, M. R. Allen, P. M. Forster, F. E. L. Otto, D. M. Mitchell, H. D. Matthews, and D. J. Frame, "A real-time Global Warming Index", Scientific Reports **7**, 15417 (2017) (pp. 3, 74, 150, 156, 182, 183, 187).

[16] Allen et al., *Chapter 1: Framing and Context. In: Special Report on the Global Warming of 1.5°C*. Tech. rep. (IPCC, 2018) (pp. 3, 10, 73, 74, 142).

[17] N. P. Gillett, M. Kirchmeier-Young, A. Ribes, H. Shiogama, G. C. Hegerl, R. Knutti, G. Gastineau, J. G. John, L. Li, L. Nazarenko, N. Rosenbloom, Ø. Seland, T. Wu, S. Yukimoto, and T. Ziehn, "Constraining human contributions to observed warming since the pre-industrial period", Nature Climate Change, 1–6 (2021) (pp. 3, 6, 13, 21, 77, 126, 156, 161, 182).

[18] A. Ribes, S. Qasmi, and N. P. Gillett, "Making climate projections conditional on historical observations", Science Advances **7**, eabc0671 (2021) (pp. 3, 7, 8, 13, 21, 156, 182).

[19] K. S. Carslaw, H. Gordon, D. S. Hamilton, J. S. Johnson, L. A. Regayre, M. Yoshioka, and K. J. Pringle, "Aerosols in the Pre-industrial Atmosphere", Current Climate Change Reports **3**, 1–15 (2017) (p. 3).

[20] *World Meteorological Organization*, https://public.wmo.int/en (visited on 12/21/2022) (p. 4).

[21] *UNFCCC*, https://unfccc.int/ (visited on 12/21/2022) (p. 4).

[22] *IPCC — Intergovernmental Panel on Climate Change*, https://www.ipcc.ch/ (visited on 12/21/2022) (p. 4).

[23] S. Institution, *Global Volcanism Program | Hunga Tonga-Hunga Ha'apai*, (2022) https://volcano.si.edu/volcano.cfm?vn=243040 (visited on 06/29/2022) (p. 4).

[24] R. S. Matoza, D. Fee, J. D. Assink, A. M. Iezzi, D. N. Green, K. Kim, L. Toney, T. Lecocq, S. Krishnamoorthy, J.-M. Lalande, K. Nishida, K. L. Gee, M. M. Haney, H. D. Ortiz, Q. Brissaud, L. Martire, L. Rolland, P. Vergados, A. Nippress, J. Park, S. Shani-Kadmiel, A. Witsil, S. Arrowsmith, C. Caudron, S. Watada, A. B. Perttu, B. Taisne, P. Mialle, A. Le Pichon, J. Vergoz, P. Hupe, P. S. Blom, R. Waxler, S. De Angelis, J. B. Snively, A. T. Ringler, R. E. Anthony, A. D. Jolly, G. Kilgour, G. Averbuch, M. Ripepe, M. Ichihara, A. Arciniega-Ceballos, E. Astafyeva, L. Ceranna, S. Cevuard, I.-Y. Che, R. De Negri, C. W. Ebeling, L. G. Evers, L. E. Franco-Marin, T. B. Gabrielson, K. Hafner, R. G. Harrison, A. Komjathy, G. Lacanna, J. Lyons, K. A. Macpherson, E. Marchetti,

K. F. McKee, R. J. Mellors, G. Mendo-Pérez, T. D. Mikesell, E. Munaibari, M. Oyola-Merced, I. Park, C. Pilger, C. Ramos, M. C. Ruiz, R. Sabatini, H. F. Schwaiger, D. Tailpied, C. Talmadge, J. Vidot, J. Webster, and D. C. Wilson, "Atmospheric waves and global seismoacoustic observations of the January 2022 Hunga eruption, Tonga", Science **0**, 10.1126/science.abo7063 (2022) (p. 4).

[25] NASA, *Global Sulfur Dioxide Monitoring Home Page*, (2022) https://so2.gsfc.nasa.gov/ (visited on 06/29/2022) (p. 4).

[26] L. Millán, M. L. Santee, A. Lambert, N. J. Livesey, F. Werner, M. J. Schwartz, H. C. Pumphrey, G. L. Manney, Y. Wang, H. Su, L. Wu, W. G. Read, and L. Froidevaux, "The Hunga Tonga-Hunga Ha'apai Hydration of the Stratosphere", Geophysical Research Letters **49**, e2022GL099381 (2022) (pp. 4, 5).

[27] S. Guo, G. Bluth, W. Rose, M. Watson, and A. Prata, "Re-evaluation of SO2 release of the 15 June 1991 Pinatubo eruption using ultraviolet and infrared satellite sensors", AGU Publications **5**, 10.1029/2003GC000654 (2004) (p. 4).

[28] J. M. Edwards and A. Slingo, "Studies with a flexible new radiation code. I: Choosing a configuration for a large-scale model", Quarterly Journal of the Royal Meteorological Society **122**, 689–719 (1996) (p. 4).

[29] N. J. Leach, S. Jenkins, Z. Nicholls, C. J. Smith, J. Lynch, M. Cain, T. Walsh, B. Wu, J. Tsutsui, and M. R. Allen, "FaIRv2.0.0: a generalized impulse response model for climate uncertainty and future scenario exploration", Geoscientific Model Development **14**, 3007–3036 (2021) (pp. 5, 17, 18, 21, 24, 26, 48–51, 56–59, 74, 131, 133, 146, 150, 154, 167, 170, 173, 174).

[30] WMO, *WMO update: 50:50 chance of global temperature temporarily reaching 1.5°C threshold in next five years*, (May 2022) https://public.wmo.int/en/media/press-release/wmo-update-5050-chance-of-global-temperature-temporarily-reaching-15%C2%B0c-threshold (visited on 06/29/2022) (p. 5).

[31] S. Jenkins, C. Smith, M. Allen, and R. Grainger, "Tonga eruption increases chance of temporary surface temperature anomaly above 1.5°C", Nature Climate Change (2022) (p. 5).

[32] *FAQs - Climate*, (May 2016) https://public.wmo.int/en/about-us/frequently-asked-questions/climate (visited on 12/21/2022) (p. 5).

[33] J. Fox and S. Weisberg, *Appendix: Nonparametric Regression in R. An R Companion to Applied Regression*. 3rd (SAGE, 2018) (p. 5).

[34] D. C. Clarke and M. Richardson, "The Benefits of Continuous Local Regression for Quantifying Global Warming", Earth and Space Science **8**, e2020EA001082 (2021) (p. 5).

[35] C. J. Smith and P. M. Forster, "Suppressed Late-20th Century Warming in CMIP6 Models Explained by Forcing and Feedbacks", Geophysical Research Letters **48**, e2021GL094948 (2021) (pp. 6, 23, 131).

[36] V. Eyring, S. Bony, G. A. Meehl, C. A. Senior, B. Stevens, R. J. Stouffer, and K. E. Taylor, "Overview of the Coupled Model Intercomparison Project Phase 6 (CMIP6) experimental design and organization", Geoscientific Model Development **9**, 1937–1958 (2016) (pp. 6, 17, 18, 74, 150, 155).

[37] P. J. Green and B. W. Silverman, *Nonparametric Regression and Generalized Linear Models: A roughness penalty approach.* (Chapman and Hall., 1994) (p. 7).

[38] M. L. Eaton, *Multivariate Statistics: a Vector Space Approach* (John Wiley and Sons, 1983) (p. 7).

[39] UNFCCC, *Paris Agreement text*, (2015) https://treaties.un.org/Pages/ViewDetails.aspx?src=IND&mtdsg_no=XXVII-7-d&chapter=27&clang=_en (visited on 08/09/2019) (pp. 9, 141).

[40] IPCC, *AR4 Climate Change 2007: The Physical Science Basis*, tech. rep. (2007) (p. 9).

[41] IPCC, *AR5 Synthesis Report: Climate Change 2014 — IPCC*, (2013) https://www.ipcc.ch/report/ar5/syr/ (visited on 12/16/2019) (pp. 9, 27, 142).

[42] R. J. Millar, Z. R. Nicholls, P. Friedlingstein, and M. R. Allen, "A modified impulse-response representation of the global near-surface air temperature and atmospheric concentration response to carbon dioxide emissions", Atmospheric Chemistry and Physics **17**, 7213–7228 (2017) (pp. 10, 17, 21, 24, 48, 50, 51, 57, 74, 141, 150, 168).

[43] C. P. Morice, J. J. Kennedy, N. A. Rayner, J. P. Winn, E. Hogan, R. E. Killick, R. J. H. Dunn, T. J. Osborn, P. D. Jones, and I. R. Simpson, "An Updated Assessment of Near-Surface Temperature Change From 1850: The HadCRUT5 Data Set", Journal of Geophysical Research: Atmospheres **126**, e2019JD032361 (2021) (pp. 11, 40, 42, 73, 74, 142, 150).

[44] C. Smith et al., *SSP ERF timeseries*, (Sept. 2020) 10.5281/zenodo.3973015 (pp. 11, 20, 68, 71, 178, 194).

[45] P. M. Forster, T. Richardson, A. C. Maycock, C. J. Smith, B. H. Samset, G. Myhre, T. Andrews, R. Pincus, and M. Schulz, "Recommendations for diagnosing effective radiative forcing from climate models for CMIP6", Journal of Geophysical Research: Atmospheres **121**, 12, 460–12, 475 (2016) (pp. 11, 20, 65).

[46] J. Lee, J. Marotzke, G. Bala, L. Cao, S. Corti, J. P. Dunne, F. Engelbrecht, E. Fischer, J. C. Fyfe, C. Jones, T. A. Maycock, J. Mutemi, O. Ndiaye, S. Panickal, and T. Zhou, *Future Global Climate: Scenario-Based Projections and Near-Term Information. In: Climate Change 2021: The Physical Science Basis. Contribution of Working Group I to the Sixth Assessment Report of the Intergovernmental Panel on Climate Change*, tech. rep. 6 (IPCC, Cambridge University Press, 2021) (p. 13).

[47] J. Rogelj, P. M. Forster, E. Kriegler, C. J. Smith, and R. Séférian, "Estimating and tracking the remaining carbon budget for stringent climate targets", Nature **571**, 335 (2019) (pp. 14, 25, 27, 28, 141–143, 166, 187, 188).

[48] K. D. Williams, D. Copsey, E. W. Blockley, A. Bodas-Salcedo, D. Calvert, R. Comer, P. Davis, T. Graham, H. T. Hewitt, R. Hill, P. Hyder, S. Ineson, T. C. Johns, A. B. Keen, R. W. Lee, A. Megann, S. F. Milton, J. G. L. Rae, M. J. Roberts, A. A. Scaife, R. Schiemann, D. Storkey, L. Thorpe, I. G. Watterson, D. N. Walters, A. West, R. A. Wood, T. Woollings, and P. K. Xavier, "The Met Office Global Coupled Model 3.0 and 3.1 (GC3.0 and GC3.1) Configurations", Journal of Advances in Modeling Earth Systems **10**, 357–380 (2018) (p. 16).

[49] A. A. Sellar, C. G. Jones, J. P. Mulcahy, Y. Tang, A. Yool, A. Wiltshire, F. M. O'Connor, M. Stringer, R. Hill, J. Palmieri, S. Woodward, L. d. Mora, T. Kuhlbrodt, S. T. Rumbold, D. I. Kelley, R. Ellis, C. E. Johnson, J. Walton, N. L. Abraham, M. B. Andrews, T. Andrews, A. T. Archibald, S. Berthou, E. Burke, E. Blockley, K. Carslaw, M. Dalvi, J. Edwards, G. A. Folberth, N. Gedney, P. T. Griffiths, A. B. Harper, M. A. Hendry, A. J. Hewitt, B. Johnson, A. Jones, C. D. Jones, J. Keeble, S. Liddicoat, O. Morgenstern, R. J. Parker, V. Predoi, E. Robertson, A. Siahaan, R. S. Smith, R. Swaminathan, M. T. Woodhouse, G. Zeng, and M. Zerroukat, "UKESM1: Description and Evaluation of the U.K. Earth System Model", Journal of Advances in Modeling Earth Systems **11**, 4513–4558 (2019) (pp. 16, 36, 76).

[50] N. C. Swart, J. N. S. Cole, V. V. Kharin, M. Lazare, J. F. Scinocca, N. P. Gillett, J. Anstey, V. Arora, J. R. Christian, S. Hanna, Y. Jiao, W. G. Lee, F. Majaess, O. A. Saenko, C. Seiler, C. Seinen, A. Shao, M. Sigmond, L. Solheim, K. v. Salzen, D. Yang, and B. Winter, "The Canadian Earth System Model version 5 (CanESM5.0.3)", Geoscientific Model Development **12**, 4823–4873 (2019) (pp. 16, 36, 76).

[51] O. Boucher, J. Servonnat, A. L. Albright, O. Aumont, Y. Balkanski, V. Bastrikov, S. Bekki, R. Bonnet, S. Bony, L. Bopp, P. Braconnot, P. Brockmann, P. Cadule, A. Caubel, F. Cheruy, F. Codron, A. Cozic, D. Cugnet, F. D'Andrea, P. Davini, C. de Lavergne, S. Denvil, J. Deshayes, M. Devilliers, A. Ducharne, J.-L. Dufresne, E. Dupont, C. Éthé, L. Fairhead, L. Falletti, S. Flavoni, M.-A. Foujols, S. Gardoll, G. Gastineau, J. Ghattas, J.-Y. Grandpeix, B. Guenet, E. Guez Lionel, E. Guilyardi, M. Guimberteau, D. Hauglustaine, F. Hourdin, A. Idelkadi, S. Joussaume, M. Kageyama, M. Khodri, G. Krinner, N. Lebas, G. Levavasseur, C. Lévy, L. Li, F. Lott, T. Lurton, S. Luyssaert, G. Madec, J.-B. Madeleine, F. Maignan, M. Marchand, O. Marti, L. Mellul, Y. Meurdesoif, J. Mignot, I. Musat, C. Ottlé, P. Peylin, Y. Planton, J. Polcher, C. Rio, N. Rochetin, C. Rousset, P. Sepulchre, A. Sima, D. Swingedouw, R. Thiéblemont, A. K. Traore, M. Vancoppenolle, J. Vial, J. Vialard, N. Viovy, and N. Vuichard, "Presentation and Evaluation of the IPSL-CM6A-LR Climate Model", Journal of Advances in Modeling Earth Systems **12**, e2019MS002010 (2020) (p. 16).

[52] H. Tatebe, T. Ogura, T. Nitta, Y. Komuro, K. Ogochi, T. Takemura, K. Sudo, M. Sekiguchi, M. Abe, F. Saito, M. Chikira, S. Watanabe, M. Mori, N. Hirota, Y. Kawatani, T. Mochizuki, K. Yoshimura, K. Takata, R. O'ishi, D. Yamazaki, T. Suzuki, M. Kurogi, T. Kataoka, M. Watanabe, and M. Kimoto, "Description and basic evaluation of simulated mean state, internal variability, and climate sensitivity in MIROC6", Geoscientific Model Development **12**, 2727–2765 (2019) (p. 16).

[53] WCRP, *CMIP*, (2023) `https://www.wcrp-climate.org/wgcm-cmip` (visited on 01/18/2023) (p. 16).

[54] R. Pincus, P. M. Forster, and B. Stevens, "The Radiative Forcing Model Intercomparison Project (RFMIP): experimental protocol for CMIP6", Geoscientific Model Development **9**, 3447–3460 (2016) (pp. 17, 18, 20, 35, 68, 83, 93, 94, 101, 154).

[55] W. J. Collins, J.-F. Lamarque, M. Schulz, O. Boucher, V. Eyring, M. I. Hegglin, A. Maycock, G. Myhre, M. Prather, D. Shindell, and S. J. Smith, "AerChemMIP: quantifying the effects of chemistry and aerosols in CMIP6", Geoscientific Model Development **10**, 585–607 (2017) (pp. 17, 18, 20, 35, 58, 101).

[56] N. P. Gillett, H. Shiogama, B. Funke, G. Hegerl, R. Knutti, K. Matthes, B. D. Santer, D. Stone, and C. Tebaldi, "The Detection and Attribution Model Intercomparison Project (DAMIP v1.0) contribution to CMIP6", Geoscientific Model Development **9**, 3685–3697 (2016) (pp. 17, 36).

[57] C. D. Jones, T. L. Frölicher, C. Koven, A. H. MacDougall, H. D. Matthews, K. Zickfeld, J. Rogelj, K. B. Tokarska, N. P. Gillett, T. Ilyina, M. Meinshausen, N. Mengis, R. Séférian, M. Eby, and F. A. Burger, "The Zero Emissions Commitment Model Intercomparison Project (ZECMIP) contribution to C4MIP: quantifying committed climate changes following zero carbon emissions", Geoscientific Model Development **12**, 4375–4385 (2019) (pp. 17, 26, 166, 188).

[58] M. Meinshausen, S. C. B. Raper, and T. M. L. Wigley, "Emulating coupled atmosphere-ocean and carbon cycle models with a simpler model, MAGICC6 – Part 1: Model description and calibration", Atmospheric Chemistry and Physics **11**, 1417–1456 (2011) (pp. 17, 170).

[59] C. J. Smith, P. M. Forster, M. Allen, N. Leach, R. J. Millar, G. A. Passerello, and L. A. Regayre, "FAIR v1.3: a simple emissions-based impulse response and carbon cycle model", Geoscientific Model Development **11**, 2273–2297 (2018) (pp. 17, 48, 49, 100).

[60] M. Sandstad, R. B. Skeie, and B. H. Samset, "The updated CICERO Simple Climate Model – an open-source emulator contribution to the AR6 process", in (Apr. 2022) (p. 17).

[61] P. Friedlingstein, M. W. Jones, M. O'Sullivan, R. M. Andrew, D. C. E. Bakker, J. Hauck, C. Le Quéré, G. P. Peters, W. Peters, J. Pongratz, S. Sitch, J. G. Canadell, P. Ciais, R. B. Jackson, S. R. Alin, P. Anthoni, N. R. Bates, M. Becker, N. Bellouin, L. Bopp, T. T. T. Chau, F. Chevallier, L. P. Chini, M. Cronin, K. I. Currie, B. Decharme, L. Djeutchouang, X. Dou, W. Evans, R. A. Feely, L. Feng, T. Gasser, D. Gilfillan, T. Gkritzalis, G. Grassi, L. Gregor, N. Gruber, Ö. Gürses, I. Harris, R. A. Houghton, G. C. Hurtt, Y. Iida, T. Ilyina, I. T. Luijkx, A. K. Jain, S. D. Jones, E. Kato, D. Kennedy, K. Klein Goldewijk, J. Knauer, J. I. Korsbakken, A. Körtzinger, P. Landschützer, S. K. Lauvset, N. Lefèvre, S. Lienert, J. Liu, G. Marland, P. C. McGuire, J. R. Melton, D. R. Munro, J. E. M. S. Nabel, S.-I. Nakaoka, Y. Niwa, T. Ono, D. Pierrot, B. Poulter, G. Rehder, L. Resplandy, E. Robertson, C. Rödenbeck, T. M. Rosan, J. Schwinger, C. Schwingshackl, R. Séférian, A. J. Sutton, C. Sweeney, T. Tanhua, P. P. Tans, H. Tian, B. Tilbrook, F. Tubiello, G. van der Werf, N. Vuichard, C. Wada, R. Wanninkhof, A. Watson, D. Willis, A. J. Wiltshire, W. Yuan, C. Yue, X. Yue, S. Zaehle, and J. Zeng, "Global Carbon Budget 2021", Earth System Science Data Discussions, 1–191 (2021) (pp. 18, 20, 25, 68, 70, 71).

[62] P. O'Rourke, S. Smith, A. Mott, H. Ahsan, E. Mcduffie, M. Crippa, Z. Klimont, B. Mcdonald, S. Wang, M. Nicholson, R. Hoesly, and L. Feng, *CEDS v_2021_04_21 Gridded emissions data*, (2021) https://www.osti.gov/servlets/purl/1779095/ (visited on 02/03/2023) (pp. 18, 20, 103, 104).

[63] E. E. McDuffie, S. J. Smith, P. O'Rourke, K. Tibrewal, C. Venkataraman, E. A. Marais, B. Zheng, M. Crippa, M. Brauer, and R. V. Martin, "A global anthropogenic emission inventory of atmospheric pollutants from sector- and fuel-specific sources (1970–2017): an application of the Community Emissions Data System (CEDS)", Earth System Science Data **12**, 3413–3442 (2020) (pp. 18, 32, 37, 38, 41, 60, 65, 66, 68, 100, 103, 104, 149, 185).

[64] EDGAR4-database, *Emission Database for Global Atmospheric Research (EDGAR), release version 4.0. http://edgar.jrc.ec.europa.eu, 2009* (2009) (pp. 18, 20, 104).

[65] K. Riahi, D. P. van Vuuren, E. Kriegler, J. Edmonds, B. C. O'Neill, S. Fujimori, N. Bauer, K. Calvin, R. Dellink, O. Fricko, W. Lutz, A. Popp, J. C. Cuaresma, S. Kc, M. Leimbach, L. Jiang, T. Kram, S. Rao, J. Emmerling, K. Ebi, T. Hasegawa, P. Havlik, F. Humpenöder, L. A. Da Silva, S. Smith, E. Stehfest, V. Bosetti, J. Eom, D. Gernaat, T. Masui, J. Rogelj, J. Strefler, L. Drouet, V. Krey, G. Luderer, M. Harmsen, K. Takahashi, L. Baumstark, J. C. Doelman, M. Kainuma, Z. Klimont, G. Marangoni, H. Lotze-Campen, M. Obersteiner, A. Tabeau, and M. Tavoni, "The Shared Socioeconomic Pathways and their energy, land use, and greenhouse gas emissions implications: An overview", Global Environmental Change **42**, 153–168 (2017) (pp. 18, 68).

[66] S. Jenkins, E. Mitchell-Larson, M. C. Ives, S. Haszeldine, and M. Allen, "Upstream decarbonization through a carbon takeback obligation: An affordable backstop climate policy", Joule **0**, 10.1016/j.joule.2021.10.012 (2021) (p. 19).

[67] M. Meinshausen, Z. R. J. Nicholls, J. Lewis, M. J. Gidden, E. Vogel, M. Freund, U. Beyerle, C. Gessner, A. Nauels, N. Bauer, J. G. Canadell, J. S. Daniel, A. John, P. B. Krummel, G. Luderer, N. Meinshausen, S. A. Montzka, P. J. Rayner, S. Reimann, S. J. Smith, M. van den Berg, G. J. M. Velders, M. K. Vollmer, and R. H. J. Wang, "The shared socio-economic pathway (SSP) greenhouse gas concentrations and their extensions to 2500", Geoscientific Model Development **13**, 3571–3605 (2020) (pp. 19, 20, 179).

[68] G. Myhre, D. Shindell, F.-M. Bréon, W. Collins, J. Fuglestvedt, J. Huang, D. Koch, J.-F. Lamarque, D. Lee, B. Mendoza, T. Nakajima, A. Robock, G. Stephens, H. Zhang, B. Aamaas, O. Boucher, S. B. Dalsøren, J. S. Daniel, P. Forster, C. Granier, J. Haigh, Ø. Hodnebrog, J. O. Kaplan, G. Marston, C. J. Nielsen, B. C. O'Neill, G. P. Peters, J. Pongratz, V. Ramaswamy, R. Roth, L. Rotstayn, S. J. Smith, D. Stevenson, J.-P. Vernier, O. Wild, P. Young, D. Jacob, A. R. Ravishankara, and K. Shine, *Chapter 8–Anthropogenic and Natural Radiative Forcing, In IPCC AR5 WG1 - The Physical Science Basis.* Tech. rep. (IPCC, 2013), p. 82 (pp. 19, 20, 28, 30, 32, 37, 48, 50, 56, 65, 145, 147).

[69] M. Etminan, G. Myhre, E. J. Highwood, and K. P. Shine, "Radiative forcing of carbon dioxide, methane, and nitrous oxide: A significant revision of the methane radiative forcing", Geophysical Research Letters **43**, 12, 614–12, 623 (2016) (pp. 20, 24, 28, 50, 51, 56, 58).

[70] M. D. Zelinka, T. Andrews, P. M. Forster, and K. E. Taylor, "Quantifying components of aerosol-cloud-radiation interactions in climate models", Journal of Geophysical Research: Atmospheres **119**, 7599–7615 (2014) (p. 20).

[71] N. Bellouin, J. Quaas, E. Gryspeerdt, S. Kinne, P. Stier, D. Watson-Parris, O. Boucher, K. S. Carslaw, M. Christensen, A.-L. Daniau, J.-L. Dufresne, G. Feingold, S. Fiedler, P. Forster, A. Gettelman, J. M. Haywood, U. Lohmann, F. Malavelle, T. Mauritsen, D. T. McCoy, G. Myhre, J. Mülmenstädt, D. Neubauer, A. Possner, M. Rugenstein, Y. Sato, M. Schulz, S. E. Schwartz, O. Sourdeval, T. Storelvmo, V. Toll, D. Winker, and B. Stevens, "Bounding global aerosol radiative forcing of climate change", Reviews of Geophysics **n/a**, 10.1029/2019RG000660 (2020) (pp. 20, 32, 33, 37, 43, 66, 113, 114, 119, 124, 126, 138, 152, 195).

[72] C. Smith, Z. R. J. Nicholls, K. C. Armour, W. D. Collins, P. Forster, M. Meinshausen, M. D. Palmer, and M. Watanabe, *The Earth's Energy Budget, Climate Feedbacks, and Climate Sensitivity Supplementary Material. In: Climate Change 2021: The Physical Science Basis. Contribution of Working Group I to the Sixth Assessment Report of the Intergovernmental Panel on Climate Change*, tech. rep. (2021) (pp. 20, 58, 63, 68, 103, 178, 194).

[73] C. J. Smith, G. R. Harris, M. D. Palmer, N. Bellouin, W. Collins, G. Myhre, M. Schulz, J.-C. Golaz, M. Ringer, T. Storelvmo, and P. M. Forster, "Energy Budget Constraints on the Time History of Aerosol Forcing and Climate Sensitivity", Journal of Geophysical Research: Atmospheres **126**, e2020JD033622 (2021) (pp. 20, 24, 48, 58–60, 77, 93, 98, 126, 130, 131, 138, 146, 147, 185, 186, 194).

[74] A. E. Dessler and P. M. Forster, "An Estimate of Equilibrium Climate Sensitivity From Interannual Variability", Journal of Geophysical Research: Atmospheres **123**, 8634–8645 (2018) (pp. 20, 41, 65, 85, 86, 146, 150, 194, 197).

[75] G. L. Stephens, "Cloud Feedbacks in the Climate System: A Critical Review", Journal of Climate **18**, 237–273 (2005) (p. 21).

[76] B. J. Soden and I. M. Held, "An Assessment of Climate Feedbacks in Coupled Ocean–Atmosphere Models", Journal of Climate **19**, 3354–3360 (2006) (p. 21).

[77] J. A. Curry, J. L. Schramm, and E. E. Ebert, "Sea Ice-Albedo Climate Feedback Mechanism", Journal of Climate **8**, 240–247 (1995) (p. 21).

[78] O. Geoffroy, D. Saint-Martin, D. J. L. Olivié, A. Voldoire, G. Bellon, and S. Tytéca, "Transient Climate Response in a Two-Layer Energy-Balance Model. Part I: Analytical Solution and Parameter Calibration Using CMIP5 AOGCM Experiments", Journal of Climate **26**, 1841–1857 (2012) (pp. 21, 48, 49, 100, 150, 167).

[79] I. M. Held, M. Winton, K. Takahashi, T. Delworth, F. Zeng, and G. K. Vallis, "Probing the Fast and Slow Components of Global Warming by Returning Abruptly to Preindustrial Forcing", Journal of Climate **23**, 2418–2427 (2010) (pp. 21, 48).

[80] M. D. Zelinka, T. A. Myers, D. T. McCoy, S. Po-Chedley, P. M. Caldwell, P. Ceppi, S. A. Klein, and K. E. Taylor, "Causes of Higher Climate Sensitivity in CMIP6 Models", Geophysical Research Letters **47**, e2019GL085782 (2020) (pp. 22, 23, 36, 40, 125, 155).

[81] C. M. Flynn and T. Mauritsen, "On the climate sensitivity and historical warming evolution in recent coupled model ensembles", Atmospheric Chemistry and Physics **20**, 7829–7842 (2020) (pp. 22, 23, 85, 88, 89, 120).

[82] A. Donohoe, K. C. Armour, A. G. Pendergrass, and D. S. Battisti, "Shortwave and longwave radiative contributions to global warming under increasing CO2", Proceedings of the National Academy of Sciences **111**, 16700–16705 (2014) (pp. 22, 41, 65, 86, 88, 125).

[83] J. e. a. Charney, *Carbon Dioxide and Climate: A Scientific Assessment*, tech. rep. (1979) (p. 22).

[84] K. B. Tokarska, V. K. Arora, N. P. Gillett, F. Lehner, J. Rogelj, C.-F. Schleussner, R. Séférian, and R. Knutti, "Uncertainty in carbon budget estimates due to internal climate variability", Environmental Research Letters **15**, 104064 (2020) (pp. 23, 143, 155).

[85] L. L. Huusko, F. A.-M. Bender, A. M. L. Ekman, and T. Storelvmo, "Climate sensitivity indices and their relation with projected temperature change in CMIP6 models", Environmental Research Letters **16**, 064095 (2021) (p. 23).

[86] K. B. Tokarska, M. B. Stolpe, S. Sippel, E. M. Fischer, C. J. Smith, F. Lehner, and R. Knutti, "Past warming trend constrains future warming in CMIP6 models", Science Advances **6**, eaaz9549 (2020) (pp. 23, 190).

[87] A. Otto, F. E. L. Otto, O. Boucher, J. Church, G. Hegerl, P. M. Forster, N. P. Gillett, J. Gregory, G. C. Johnson, R. Knutti, N. Lewis, U. Lohmann, J. Marotzke, G. Myhre, D. Shindell, B. Stevens, and M. R. Allen, "Energy budget constraints on climate response", Nature Geoscience **6**, 415–416 (2013) (pp. 23, 152).

[88] Z. Hausfather, K. Marvel, G. A. Schmidt, J. W. Nielsen-Gammon, and M. Zelinka, "Climate simulations: recognize the 'hot model' problem", Nature **605**, 26–29 (2022) (p. 23).

[89] C. J. Smith, R. J. Kramer, G. Myhre, K. Alterskjær, W. Collins, A. Sima, O. Boucher, J.-L. Dufresne, P. Nabat, M. Michou, S. Yukimoto, J. Cole, D. Paynter, H. Shiogama, F. M. O'Connor, E. Robertson, A. Wiltshire, T. Andrews, C. Hannay, R. Miller, L. Nazarenko, A. Kirkevåg, D. Olivié, S. Fiedler, A. Lewinschal, C. Mackallah, M. Dix, R. Pincus, and P. M. Forster, "Effective radiative forcing and adjustments in CMIP6 models", Atmospheric Chemistry and Physics **20**, 9591–9618 (2020) (pp. 23, 36).

[90] A. Gettelman, C. Hannay, J. T. Bacmeister, R. B. Neale, A. G. Pendergrass, G. Danabasoglu, J.-F. Lamarque, J. T. Fasullo, D. A. Bailey, D. M. Lawrence, and M. J. Mills, "High Climate Sensitivity in the Community Earth System Model Version 2 (CESM2)", Geophysical Research Letters **46**, 8329–8337 (2019) (pp. 23, 36, 83).

[91] D. Watson-Parris and C. J. Smith, "Large uncertainty in future warming due to aerosol forcing", Nature Climate Change **12**, 1111–1113 (2022) (pp. 24, 37).

[92] R. J. Millar and P. Friedlingstein, "The utility of the historical record for assessing the transient climate response to cumulative emissions", Philosophical Transactions of the Royal Society A: Mathematical, Physical and Engineering Sciences **376**, 20160449 (2018) (pp. 24, 25, 146, 161, 170, 187).

[93] F. Joos, R. Roth, J. S. Fuglestvedt, G. P. Peters, I. G. Enting, W. v. Bloh, V. Brovkin, E. J. Burke, M. Eby, N. R. Edwards, T. Friedrich, T. L. Frölicher, P. R. Halloran, P. B. Holden, C. Jones, T. Kleinen, F. T. Mackenzie, K. Matsumoto, M. Meinshausen, G.-K. Plattner, A. Reisinger, J. Segschneider, G. Shaffer, M. Steinacher, K. Strassmann, K. Tanaka, A. Timmermann, and A. J. Weaver, "Carbon dioxide and climate impulse response functions for the computation of greenhouse gas metrics: a multi-model analysis", Atmospheric Chemistry and Physics **13**, 2793–2825 (2013) (pp. 24, 48, 50, 141, 167, 168, 191).

[94] S. Jenkins, R. J. Millar, N. Leach, and M. R. Allen, "Framing Climate Goals in Terms of Cumulative CO2-Forcing-Equivalent Emissions", Geophysical Research Letters **45**, 2795–2804 (2018) (pp. 24, 26, 30, 48, 51, 55, 143, 145, 150, 173, 174, 179, 187).

[95] M. J. E. van Marle, D. van Wees, R. A. Houghton, R. D. Field, J. Verbesselt, and G. R. van der Werf, "New land-use-change emissions indicate a declining CO2 airborne fraction", Nature **603**, 450–454 (2022) (p. 24).

[96] M. Bennedsen, E. Hillebrand, and S. J. Koopman, *Is there evidence of a trend in the CO2 airborne fraction?*, (Apr. 2022) `http://arxiv.org/abs/2204.11651` (visited on 01/17/2023) (p. 24).

[97] R. J. Kramer, H. He, B. J. Soden, L. Oreopoulos, G. Myhre, P. M. Forster, and C. J. Smith, "Observational Evidence of Increasing Global Radiative Forcing", Geophysical Research Letters **48**, e2020GL091585 (2021) (pp. 24, 41, 67).

[98] M. R. Allen, D. J. Frame, and C. F. Mason, "The case for mandatory sequestration", Nature Geoscience **2**, 813–814 (2009) (pp. 25, 165, 166).

[99] M. R. Allen, D. J. Frame, C. Huntingford, C. D. Jones, J. A. Lowe, M. Meinshausen, and N. Meinshausen, "Warming caused by cumulative carbon emissions towards the trillionth tonne", Nature **458**, 1163–1166 (2009) (pp. 25, 141).

[100] H. D. Matthews, N. P. Gillett, P. A. Stott, and K. Zickfeld, "The proportionality of global warming to cumulative carbon emissions", Nature **459**, 829–832 (2009) (pp. 25, 141, 165).

[101] K. Zickfeld, V. K. Arora, and N. P. Gillett, "Is the climate response to CO2 emissions path dependent?", Geophysical Research Letters **39**, 10.1029/2011GL050205 (2012) (p. 25).

[102] A. H. MacDougall, "The Transient Response to Cumulative CO2 Emissions: a Review", Current Climate Change Reports **2**, 39–47 (2016) (p. 25).

[103] M. R. Allen, P. Friedlingstein, C. A. Girardin, S. Jenkins, Y. Malhi, E. Mitchell-Larson, G. P. Peters, and L. Rajamani, "Net Zero: Science, Origins, and Implications", Annual Review of Environment and Resources **47**, 849–887 (2022) (pp. 25, 27, 50, 53–55, 167–169, 189).

[104] V. K. Arora, A. Katavouta, R. G. Williams, C. D. Jones, V. Brovkin, P. Friedlingstein, J. Schwinger, L. Bopp, O. Boucher, P. Cadule, M. A. Chamberlain, J. R. Christian, C. Delire, R. A. Fisher, T. Hajima, T. Ilyina, E. Joetzjer, M. Kawamiya, C. D. Koven, J. P. Krasting, R. M. Law, D. M. Lawrence, A. Lenton, K. Lindsay, J. Pongratz, T. Raddatz, R. Séférian, K. Tachiiri, J. F. Tjiputra, A. Wiltshire, T. Wu, and T. Ziehn, "Carbon–concentration and carbon–climate feedbacks in CMIP6 models and their comparison to CMIP5 models", Biogeosciences **17**, 4173–4222 (2020) (pp. 25, 56, 153, 155).

[105] H. D. Matthews, J.-S. Landry, A.-I. Partanen, M. Allen, M. Eby, P. M. Forster, P. Friedlingstein, and K. Zickfeld, "Estimating Carbon Budgets for Ambitious Climate Targets", Current Climate Change Reports **3**, 69–77 (2017) (pp. 25, 146, 161).

[106] P. Goodwin, A. Katavouta, V. M. Roussenov, G. L. Foster, E. J. Rohling, and R. G. Williams, "Pathways to 1.5 °C and 2 °C warming based on observational and geological constraints", Nature Geoscience **11**, 102–107 (2018) (p. 25).

[107] N. P. Gillett, V. K. Arora, D. Matthews, and M. R. Allen, "Constraining the Ratio of Global Warming to Cumulative CO2 Emissions Using CMIP5 Simulations", Journal of Climate **26**, 6844–6858 (2013) (pp. 25, 149).

[108] K. Schaefer, H. Lantuit, V. E. Romanovsky, E. A. G. Schuur, and R. Witt, "The impact of the permafrost carbon feedback on global climate", Environmental Research Letters **9**, 085003 (2014) (p. 25).

[109] A. H. MacDougall, "Estimated effect of the permafrost carbon feedback on the zero emissions commitment to climate change", Biogeosciences **18**, 4937–4952 (2021) (pp. 26, 169, 171, 180).

[110] H.-O. Pörtner, D. C. Roberts, V. Masson-Delmotte, P. Zhai, M. Tognor, E. Poloczanska, K. Mintenbeck, A. Alegría, M. Nicolai, A. Okem, J. Petzold, B. Rama, and N. M. Weyer, *Summary for Policymakers. In: IPCC Special Report on the Ocean and Cryosphere in a Changing Climate*, tech. rep. (IPCC, 2019) (p. 26).

[111] J. G. Canadell, P. M. S. Monteiro, M. H. Costa, L. Cotrim da Cunha, P. Cox, A. V. Eliseev, S. Henson, M. Ishii, S. L. Jaccard, C. Koven, A. Lohila, P. K. Patra, S. Piao, J. Rogelj, S. Syampungani, S. Zaehle, and K. Zickfeld, *Global Carbon and other Biogeochemical Cycles and Feedbacks. In: Climate Change 2021: The Physical Science Basis. Contribution of Working Group I to the Sixth Assessment Report of the Intergovernmental Panel on Climate Change*, tech. rep. (IPCC, Cambridge University Press, 2021) (pp. 26, 172).

[112] G.-K. Plattner, R. Knutti, F. Joos, T. F. Stocker, W. von Bloh, V. Brovkin, D. Cameron, E. Driesschaert, S. Dutkiewicz, M. Eby, N. R. Edwards, T. Fichefet, J. C. Hargreaves, C. D. Jones, M. F. Loutre, H. D. Matthews, A. Mouchet, S. A. Müller, S. Nawrath, A. Price, and A. Sokolov, "Long-term climate commitments projected with climate-carbon cycle models", Journal of Climate **21**, 2721–2751 (2008) (p. 26).

[113] A. H. MacDougall, T. L. Frölicher, C. D. Jones, J. Rogelj, H. D. Matthews, K. Zickfeld, V. K. Arora, N. J. Barrett, V. Brovkin, F. A. Burger, M. Eby, A. V. Eliseev, T. Hajima, P. B. Holden, A. Jeltsch-Thömmes, C. Koven, N. Mengis, L. Menviel, M. Michou, I. I. Mokhov, A. Oka, J. Schwinger, R. Séférian, G. Shaffer, A. Sokolov, K. Tachiiri, J. Tjiputra, A. Wiltshire, and T. Ziehn, "Is there warming in the pipeline? A multi-model analysis of the Zero Emissions Commitment from CO_2", Biogeosciences **17**, 2987–3016 (2020) (pp. 26, 27, 166, 167, 170–172, 175, 188).

[114] M. Saunois, A. R. Stavert, B. Poulter, P. Bousquet, J. G. Canadell, R. B. Jackson, P. A. Raymond, E. J. Dlugokencky, S. Houweling, P. K. Patra, P. Ciais, V. K. Arora, D. Bastviken, P. Bergamaschi, D. R. Blake, G. Brailsford, L. Bruhwiler, K. M. Carlson, M. Carrol, S. Castaldi, N. Chandra, C. Crevoisier, P. M. Crill, K. Covey, C. L. Curry, G. Etiope, C. Frankenberg, N. Gedney, M. I. Hegglin, L. Höglund-Isaksson, G. Hugelius, M. Ishizawa, A. Ito, G. Janssens-Maenhout, K. M. Jensen, F. Joos, T. Kleinen, P. B. Krummel, R. L. Langenfelds, G. G. Laruelle, L. Liu, T. Machida, S. Maksyutov, K. C. McDonald, J. McNorton, P. A. Miller, J. R. Melton, I. Morino, J. Müller, F. Murguia-Flores, V. Naik, Y. Niwa, S. Noce, S. O'Doherty, R. J. Parker, C. Peng, S. Peng, G. P. Peters, C. Prigent, R. Prinn, M. Ramonet, P. Regnier, W. J. Riley, J. A. Rosentreter, A. Segers, I. J. Simpson, H. Shi, S. J. Smith, L. P. Steele, B. F. Thornton, H. Tian, Y. Tohjima, F. N. Tubiello, A. Tsuruta, N. Viovy, A. Voulgarakis, T. S. Weber, M. van Weele, G. R. van der Werf, R. F. Weiss, D. Worthy, D. Wunch, Y. Yin, Y. Yoshida, W. Zhang, Z. Zhang, Y. Zhao, B. Zheng, Q. Zhu, Q. Zhu, and Q. Zhuang, "The Global Methane Budget 2000–2017", Earth System Science Data **12**, 1561–1623 (2020) (pp. 28, 29).

[115] M. Cain, S. Jenkins, M. R. Allen, J. Lynch, D. J. Frame, A. H. Macey, and G. P. Peters, "Methane and the Paris Agreement temperature goals", Philosophical Transactions of the Royal Society A: Mathematical, Physical and Engineering Sciences **380**, 20200456 (2022) (pp. 28, 30).

[116] S. Szopa, V. Naik, B. Adhikary, P. Artaxo, T. K. Berntsen, W. Collins, S. Fuzzi, L. Gallardo, A. Kiendler-Scharr, Z. Klimont, H. Liao, N. Unger, and P. Zanis, *Short-Lived Climate Forcers. In Climate Change 2021: The Physical Science Basis. Contribution of Working Group I to the Sixth Assessment Report of the Intergovernmental Panel on Climate Change*, tech. rep. (IPCC, 2021), pp. 817–922 (pp. 28–31, 104, 114).

[117] G. Thornhill, W. Collins, D. Olivié, R. B. Skeie, A. Archibald, S. Bauer, R. Checa-Garcia, S. Fiedler, G. Folberth, A. Gjermundsen, L. Horowitz, J.-F. Lamarque, M. Michou, J. Mulcahy, P. Nabat, V. Naik, F. M. O'Connor, F. Paulot, M. Schulz, C. E. Scott,

R. Séférian, C. Smith, T. Takemura, S. Tilmes, K. Tsigaridis, and J. Weber, "Climate-driven chemistry and aerosol feedbacks in CMIP6 Earth system models", Atmospheric Chemistry and Physics **21**, 1105–1126 (2021) (pp. 28, 29).

[118] S. Abernethy, F. M. O'Connor, C. D. Jones, and R. B. Jackson, "Methane removal and the proportional reductions in surface temperature and ozone", Philosophical Transactions of the Royal Society A: Mathematical, Physical and Engineering Sciences **379**, 20210104 (2021) (p. 28).

[119] NOAA, *Climate Timeseries: Nino 3: NOAA Physical Sciences Laboratory*, https://psl.noaa.gov/data/timeseries/monthly/NINO3/ (visited on 06/08/2021) (pp. 29, 43, 75, 80).

[120] J. Tollefson, "Scientists raise alarm over 'dangerously fast' growth in atmospheric methane", Nature, 10.1038/d41586-022-00312-2 (2022) (p. 29).

[121] Z. Zhang, N. E. Zimmermann, A. Stenke, X. Li, E. L. Hodson, G. Zhu, C. Huang, and B. Poulter, "Emerging role of wetland methane emissions in driving 21st century climate change", Proceedings of the National Academy of Sciences **114**, 9647–9652 (2017) (p. 29).

[122] H. Tian, R. Xu, J. G. Canadell, R. L. Thompson, W. Winiwarter, P. Suntharalingam, E. A. Davidson, P. Ciais, R. B. Jackson, G. Janssens-Maenhout, M. J. Prather, P. Regnier, N. Pan, S. Pan, G. P. Peters, H. Shi, F. N. Tubiello, S. Zaehle, F. Zhou, A. Arneth, G. Battaglia, S. Berthet, L. Bopp, A. F. Bouwman, E. T. Buitenhuis, J. Chang, M. P. Chipperfield, S. R. S. Dangal, E. Dlugokencky, J. W. Elkins, B. D. Eyre, B. Fu, B. Hall, A. Ito, F. Joos, P. B. Krummel, A. Landolfi, G. G. Laruelle, R. Lauerwald, W. Li, S. Lienert, T. Maavara, M. MacLeod, D. B. Millet, S. Olin, P. K. Patra, R. G. Prinn, P. A. Raymond, D. J. Ruiz, G. R. van der Werf, N. Vuichard, J. Wang, R. F. Weiss, K. C. Wells, C. Wilson, J. Yang, and Y. Yao, "A comprehensive quantification of global nitrous oxide sources and sinks", Nature **586**, 248–256 (2020) (pp. 29, 162).

[123] W. J. Collins, M. M. Fry, H. Yu, J. S. Fuglestvedt, D. T. Shindell, and J. J. West, "Global and regional temperature-change potentials for near-term climate forcers", Atmospheric Chemistry and Physics **13**, 2471–2485 (2013) (p. 30).

[124] T. M. L. Wigley, "The Kyoto Protocol: CO2 CH4 and climate implications", Geophysical Research Letters **25**, 2285–2288 (1998) (pp. 30, 55, 143).

[125] M. Cain, J. Lynch, M. R. Allen, J. S. Fuglestvedt, D. J. Frame, and A. H. Macey, "Improved calculation of warming-equivalent emissions for short-lived climate pollutants", npj Climate and Atmospheric Science **2**, 1–7 (2019) (pp. 30, 50, 55, 147, 148, 159, 167, 179).

[126] J. Lynch, M. Cain, R. Pierrehumbert, and M. Allen, "Demonstrating GWP\ast: a means of reporting warming-equivalent emissions that captures the contrasting impacts of short- and long-lived climate pollutants", Environmental Research Letters **15**, 044023 (2020) (pp. 30, 31).

[127] M. Allen, M. Cain, and J. Lynch, *Climate metrics for ruminant livestock*, (2018) (pp. 30, 55, 168, 179).

[128] J. Rogelj and C.-F. Schleussner, "Unintentional unfairness when applying new greenhouse gas emissions metrics at country level", Environmental Research Letters **14**, 114039 (2019) (p. 30).

[129] M. R. Allen, K. P. Shine, J. S. Fuglestvedt, R. J. Millar, M. Cain, D. J. Frame, and A. H. Macey, "A solution to the misrepresentations of CO 2 -equivalent emissions of short-lived climate pollutants under ambitious mitigation", npj Climate and Atmospheric Science **1**, 16 (2018) (pp. 30, 145, 147).

[130] M. A. Smith, M. Cain, and M. R. Allen, "Further improvement of warming-equivalent emissions calculation", npj Climate and Atmospheric Science **4**, 1–3 (2021) (p. 31).

[131] G. L. Stephens, M. Z. Hakuba, S. Kato, A. Gettelman, J.-L. Dufresne, T. Andrews, J. N. S. Cole, U. Willen, and T. Mauritsen, "The changing nature of Earth's reflected sunlight", Proceedings of the Royal Society A: Mathematical, Physical and Engineering Sciences **478**, 20220053 (2022) (pp. 32, 41, 115, 117, 119).

[132] T. Tang, D. Shindell, Y. Zhang, A. Voulgarakis, J.-F. Lamarque, G. Myhre, G. Faluvegi, B. H. Samset, T. Andrews, D. Olivié, T. Takemura, and X. Lee, "Distinct surface response to black carbon aerosols", Atmospheric Chemistry and Physics **21**, 13797–13809 (2021) (p. 33).

[133] S. Twomey, "Pollution and the planetary albedo", Atmospheric Environment (1967) **8**, 1251–1256 (1974) (pp. 33, 124).

[134] J. Quaas, A. Arola, B. Cairns, M. Christensen, H. Deneke, A. M. L. Ekman, G. Feingold, A. Fridlind, E. Gryspeerdt, O. Hasekamp, Z. Li, A. Lipponen, P.-L. Ma, J. Mülmenstädt, A. Nenes, J. E. Penner, D. Rosenfeld, R. Schrödner, K. Sinclair, O. Sourdeval, P. Stier, M. Tesche, B. van Diedenhoven, and M. Wendisch, "Constraining the Twomey effect from satellite observations: issues and perspectives", Atmospheric Chemistry and Physics **20**, 15079–15099 (2020) (pp. 33, 100, 124).

[135] E. Gryspeerdt, A. C. Povey, R. G. Grainger, O. Hasekamp, N. C. Hsu, J. P. Mulcahy, A. M. Sayer, and A. Sorooshian, "Uncertainty in aerosol-cloud radiative forcing is driven by clean conditions", Atmospheric Chemistry and Physics Discussions, 1–13 (2022) (p. 34).

[136] E. Gryspeerdt, T. Goren, O. Sourdeval, J. Quaas, J. Mülmenstädt, S. Dipu, C. Unglaub, A. Gettelman, and M. Christensen, "Constraining the aerosol influence on cloud liquid water path", Atmospheric Chemistry and Physics **19**, 5331–5347 (2019) (pp. 34, 100).

[137] E. Gryspeerdt, J. Quaas, and N. Bellouin, "Constraining the aerosol influence on cloud fraction", Journal of Geophysical Research: Atmospheres **121**, 3566–3583 (2016) (pp. 34, 100).

[138] B. A. Albrecht, "Aerosols, Cloud Microphysics, and Fractional Cloudiness", Science **245**, 1227–1230 (1989) (p. 34).

[139] K. Suzuki, G. L. Stephens, and M. D. Lebsock, "Aerosol effect on the warm rain formation process: Satellite observations and modeling", Journal of Geophysical Research: Atmospheres **118**, 170–184 (2013) (p. 34).

[140] A. S. Ackerman, M. P. Kirkpatrick, D. E. Stevens, and O. B. Toon, "The impact of humidity above stratiform clouds on indirect aerosol climate forcing", Nature **432**, 1014–1017 (2004) (p. 34).

[141] H. Xue, G. Feingold, and B. Stevens, "Aerosol Effects on Clouds, Precipitation, and the Organization of Shallow Cumulus Convection", Journal of the Atmospheric Sciences **65**, 392–406 (2008) (p. 34).

[142] D. P. Grosvenor, O. Sourdeval, P. Zuidema, A. Ackerman, M. D. Alexandrov, R. Bennartz, R. Boers, B. Cairns, J. C. Chiu, M. Christensen, H. Deneke, M. Diamond, G. Feingold, A. Fridlind, A. Hünerbein, C. Knist, P. Kollias, A. Marshak, D. McCoy, D. Merk, D. Painemal, J. Rausch, D. Rosenfeld, H. Russchenberg, P. Seifert, K. Sinclair, P. Stier, B. van Diedenhoven, M. Wendisch, F. Werner, R. Wood, Z. Zhang, and J. Quaas, "Remote Sensing of Droplet Number Concentration in Warm Clouds: A Review of the Current State of Knowledge and Perspectives", Reviews of Geophysics **56**, 409–453 (2018) (pp. 34, 123).

[143] J. Quaas, B. Stevens, P. Stier, and U. Lohmann, "Interpreting the cloud cover – aerosol optical depth relationship found in satellite data using a general circulation model", Atmospheric Chemistry and Physics **10**, 6129–6135 (2010) (p. 34).

[144] D. Rosenfeld, Y. Zhu, M. Wang, Y. Zheng, T. Goren, and S. Yu, "Aerosol-driven droplet concentrations dominate coverage and water of oceanic low-level clouds", Science **363**, eaav0566 (2019) (p. 34).

[145] V. Toll, M. Christensen, J. Quaas, and N. Bellouin, "Weak average liquid-cloud-water response to anthropogenic aerosols", Nature **572**, 51–55 (2019) (p. 35).

[146] T. S. L'Ecuyer, W. Berg, J. Haynes, M. Lebsock, and T. Takemura, "Global observations of aerosol impacts on precipitation occurrence in warm maritime clouds", Journal of Geophysical Research: Atmospheres **114**, 10.1029/2008JD011273 (2009) (p. 35).

[147] S. Jose, V. S. Nair, and S. S. Babu, "Anthropogenic emissions from South Asia reverses the aerosol indirect effect over the northern Indian Ocean", Scientific Reports **10**, 18360 (2020) (p. 35).

[148] L. Wei, Z. Lu, Y. Wang, X. Liu, W. Wang, C. Wu, X. Zhao, S. Rahimi, W. Xia, and Y. Jiang, "Black carbon-climate interactions regulate dust burdens over India revealed during COVID-19", Nature Communications **13**, 1839 (2022) (pp. 35, 105).

[149] P. Dave, M. Bhushan, and C. Venkataraman, "Aerosols cause intraseasonal short-term suppression of Indian monsoon rainfall", Scientific Reports **7**, 17347 (2017) (p. 35).

[150] R. Herbert, P. Stier, and G. Dagan, "Isolating Large-Scale Smoke Impacts on Cloud and Precipitation Processes Over the Amazon With Convection Permitting Resolution", Journal of Geophysical Research: Atmospheres **126**, e2021JD034615 (2021) (p. 35).

[151] S. C. Sherwood, M. J. Webb, J. D. Annan, K. C. Armour, P. M. Forster, J. C. Hargreaves, G. Hegerl, S. A. Klein, K. D. Marvel, E. J. Rohling, M. Watanabe, T. Andrews, P. Braconnot, C. S. Bretherton, G. L. Foster, Z. Hausfather, A. S. v. d. Heydt, R. Knutti, T. Mauritsen, J. R. Norris, C. Proistosescu, M. Rugenstein, G. A. Schmidt, K. B. Tokarska, and M. D. Zelinka, "An Assessment of Earth's Climate Sensitivity Using Multiple Lines of Evidence", Reviews of Geophysics **58**, e2019RG000678 (2020) (pp. 37, 41, 86).

[152] B. Stevens, "Rethinking the Lower Bound on Aerosol Radiative Forcing", Journal of Climate **28**, 4794–4819 (2015) (pp. 37, 58, 59, 72, 92, 93, 104).

[153] L. Sogacheva, T. Popp, A. M. Sayer, O. Dubovik, M. J. Garay, A. Heckel, N. C. Hsu, H. Jethva, R. A. Kahn, P. Kolmonen, M. Kosmale, G. de Leeuw, R. C. Levy, P. Litvinov, A. Lyapustin, P. North, O. Torres, and A. Arola, "Merging regional and global aerosol optical depth records from major available satellite products", Atmospheric Chemistry and Physics **20**, 2031–2056 (2020) (pp. 37, 42, 90, 91, 109, 110, 114, 118, 184).

[154] K. O. Moseid, M. Schulz, T. Storelvmo, I. R. Julsrud, D. Olivié, P. Nabat, M. Wild, J. N. S. Cole, T. Takemura, N. Oshima, S. E. Bauer, and G. Gastineau, "Bias in CMIP6 models as compared to observed regional dimming and brightening", Atmospheric Chemistry and Physics **20**, 16023–16040 (2020) (pp. 37, 73, 100).

[155] L. J. Wilcox, N. Dunstone, A. Lewinschal, M. Bollasina, A. M. L. Ekman, and E. J. Highwood, "Mechanisms for a remote response to Asian anthropogenic aerosol in boreal winter", Atmospheric Chemistry and Physics **19**, 9081–9095 (2019) (pp. 38, 101, 103, 128, 129).

[156] B. H. Samset, M. T. Lund, M. Bollasina, G. Myhre, and L. Wilcox, "Emerging Asian aerosol patterns", Nature Geoscience **12**, 582–584 (2019) (p. 38).

[157] B. Dong, L. J. Wilcox, E. J. Highwood, and R. T. Sutton, "Impacts of recent decadal changes in Asian aerosols on the East Asian summer monsoon: roles of aerosol–radiation and aerosol–cloud interactions", Climate Dynamics **53**, 3235–3256 (2019) (p. 38).

[158] H. D. Matthews and K. Zickfeld, "Climate response to zeroed emissions of greenhouse gases and aerosols", Nature Climate Change **2**, 338–341 (2012) (pp. 38, 149).

[159] C. J. Smith, P. M. Forster, M. Allen, J. Fuglestvedt, R. J. Millar, J. Rogelj, and K. Zickfeld, "Current fossil fuel infrastructure does not yet commit us to 1.5 °C warming", Nature Communications **10**, 101 (2019) (p. 38).

[160] B. H. Samset, M. Sand, C. J. Smith, S. E. Bauer, P. M. Forster, J. S. Fuglestvedt, S. Osprey, and C.-F. Schleussner, "Climate Impacts From a Removal of Anthropogenic Aerosol Emissions", Geophysical Research Letters **45**, 1020–1029 (2018) (p. 38).

[161] G. G. Persad, B. H. Samset, and L. J. Wilcox, "Aerosols must be included in climate risk assessments", Nature **611**, 662–664 (2022) (pp. 39, 77).

[162] L. Wilcox, R. Allen, S. Bauer, M. Bollasina, A. Ekman, J. Keeble, A. Lewinschal, M. Lund, J. Merikanto, D. O'Donnell, D. Paynter, G. Persad, S. Rumbold, B. Samset, T. Takemura, K. Tsigaridis, S. Undorf, and D. Westervelt, "Regional Aerosol Model Intercomparison Project", in (Mar. 2022) (pp. 39, 77, 97, 101, 102, 129, 190).

[163] S. E. Bauer, K. Tsigaridis, G. Faluvegi, L. Nazarenko, R. L. Miller, M. Kelley, and G. Schmidt, "The Turning Point of the Aerosol Era", Journal of Advances in Modeling Earth Systems **14**, e2022MS003070 (2022) (pp. 39, 45, 96, 102, 103).

[164] J. Quaas, H. Jia, C. Smith, A. L. Albright, W. Aas, N. Bellouin, O. Boucher, M. Doutriaux-Boucher, P. M. Forster, D. Grosvenor, S. Jenkins, Z. Klimont, N. G. Loeb, X. Ma, V. Naik, F. Paulot, P. Stier, M. Wild, G. Myhre, and M. Schulz, "Robust evidence for reversal of the trend in aerosol effective climate forcing", Atmospheric Chemistry and Physics **22**, 12221–12239 (2022) (pp. 39, 40, 43, 45, 96, 107, 109–111, 113, 184).

[165] N. J. L. Lenssen, G. A. Schmidt, J. E. Hansen, M. J. Menne, A. Persin, R. Ruedy, and D. Zyss, "Improvements in the GISTEMP Uncertainty Model", Journal of Geophysical Research: Atmospheres **124**, 6307–6326 (2019) (pp. 40, 42).

[166] N. US Department of Commerce, *NOAA Global Monitoring Laboratory - THE NOAA ANNUAL GREENHOUSE GAS INDEX (AGGI)*, `https://gml.noaa.gov/aggi/aggi.html` (visited on 01/08/2023) (pp. 40, 65, 127).

[167] R. A. Rohde and Z. Hausfather, "The Berkeley Earth Land/Ocean Temperature Record", Earth System Science Data **12**, 3469–3479 (2020) (pp. 40, 42, 73, 142).

[168] N. G. Loeb, D. R. Doelling, H. Wang, W. Su, C. Nguyen, J. G. Corbett, L. Liang, C. Mitrescu, F. G. Rose, and S. Kato, "Clouds and the Earth's Radiant Energy System (CERES) Energy Balanced and Filled (EBAF) Top-of-Atmosphere (TOA) Edition-4.0 Data Product", Journal of Climate **31**, 895–918 (2017) (pp. 40, 42, 66, 67, 83, 114, 184).

[169] B. Barkstrom and J. Hall, "The Earth Radiation Budget Experiment /ERBE/ - An overview", in *Sensor Systems for the 80's Conference* (American Institute of Aeronautics and Astronautics, 1982) (p. 40).

[170] B. R. Barkstrom, E. F. Harrison, and R. B. Lee, "Earth Radiation Budget Experiment", Eos, Transactions American Geophysical Union **71**, 297–304 (1990) (p. 40).

[171] J. M. Gregory, W. J. Ingram, M. A. Palmer, G. S. Jones, P. A. Stott, R. B. Thorpe, J. A. Lowe, T. C. Johns, and K. D. Williams, "A new method for diagnosing radiative forcing and climate sensitivity", Geophysical Research Letters **31**, 10.1029/2003GL018747 (2004) (p. 40).

[172] D. M. Murphy, S. Solomon, R. W. Portmann, K. H. Rosenlof, P. M. Forster, and T. Wong, "An observationally based energy balance for the Earth since 1950", Journal of Geophysical Research: Atmospheres **114**, 10.1029/2009JD012105 (2009) (pp. 41, 65, 86).

[173] N. G. Loeb, H. Wang, F. G. Rose, S. Kato, W. L. Smith, and S. Sun-Mack, "Decomposing Shortwave Top-of-Atmosphere and Surface Radiative Flux Variations in Terms of Surface and Atmospheric Contributions", Journal of Climate **32**, 5003–5019 (2019) (pp. 41, 75, 81, 83, 87–89, 117, 119, 120, 128, 184, 185).

[174] S. P. Raghuraman, D. Paynter, and V. Ramaswamy, "Anthropogenic forcing and response yield observed positive trend in Earth's energy imbalance", Nature Communications **12**, 4577 (2021) (pp. 41, 67).

[175] N. G. Loeb, G. C. Johnson, T. J. Thorsen, J. M. Lyman, F. G. Rose, and S. Kato, "Satellite and Ocean Data Reveal Marked Increase in Earth's Heating Rate", Geophysical Research Letters **48**, e2021GL093047 (2021) (pp. 41, 67, 87, 88, 123).

[176] R. C. Levy, S. Mattoo, L. A. Munchak, L. A. Remer, A. M. Sayer, F. Patadia, and N. C. Hsu, "The Collection 6 MODIS aerosol products over land and ocean", Atmospheric Measurement Techniques **6**, 2989–3034 (2013) (pp. 42, 110, 113).

[177] T. M. Smith, R. W. Reynolds, T. C. Peterson, and J. Lawrimore, "Improvements to NOAA's Historical Merged Land–Ocean Surface Temperature Analysis (1880–2006)", Journal of Climate **21**, 2283–2296 (2008) (pp. 42, 73, 142).

[178] M. Giusti, *CAMS Reanalysis*, (May 2022) https://www.ecmwf.int/en/research/climate-reanalysis/cams-reanalysis (visited on 02/06/2023) (pp. 42, 107).

[179] S. Wu, Z.-Y. Liu, J. Cheng, and C. Li, "Response of North Pacific and North Atlantic decadal variability to weak global warming", Advances in Climate Change Research, Including special topic on mitigation for 1.5 °C: Scenarios and options **9**, 95–101 (2018) (p. 43).

[180] R. A. Madden and P. R. Julian, "Detection of a 40–50 Day Oscillation in the Zonal Wind in the Tropical Pacific", Journal of the Atmospheric Sciences **28**, 702–708 (1971) (p. 43).

[181] B. Trewin, "Assessing Internal Variability of Global Mean Surface Temperature From Observational Data and Implications for Reaching Key Thresholds", Journal of Geophysical Research: Atmospheres **127**, e2022JD036747 (2022) (p. 43).

[182] NOAA, *The Walker Circulation: ENSO's atmospheric buddy | NOAA Climate.gov*, (2023) http://www.climate.gov/news-features/blogs/enso/walker-circulation-ensos-atmospheric-buddy (visited on 03/30/2023) (p. 44).

[183] P. T. Brown, W. Li, and S.-P. Xie, "Regions of significant influence on unforced global mean surface air temperature variability in climate models", Journal of Geophysical Research: Atmospheres **120**, 480–494 (2015) (p. 44).

[184] G. Beobide-Arsuaga, T. Bayr, A. Reintges, and M. Latif, "Uncertainty of ENSO-amplitude projections in CMIP5 and CMIP6 models", Climate Dynamics **56**, 3875–3888 (2021) (p. 44).

[185] S.-W. Yeh, W. Cai, S.-K. Min, M. J. McPhaden, D. Dommenget, B. Dewitte, M. Collins, K. Ashok, S.-I. An, B.-Y. Yim, and J.-S. Kug, "ENSO Atmospheric Teleconnections and Their Response to Greenhouse Gas Forcing", Reviews of Geophysics **56**, 185–206 (2018) (p. 44).

[186] S. Jenkins, A. Povey, A. Gettelman, R. Grainger, P. Stier, and M. Allen, "Is Anthropogenic Global Warming Accelerating?", Journal of Climate -**1**, 1–43 (2022) (pp. 47, 64, 126, 131).

[187] S. Jenkins, B. Sanderson, G. Peters, T. L. Frölicher, P. Friedlingstein, and M. Allen, "The Multi-Decadal Response to Net Zero CO2 Emissions and Implications for Emissions Policy", Geophysical Research Letters **49**, e2022GL101047 (2022) (pp. 47, 54, 164).

[188] R. J. Millar, J. S. Fuglestvedt, P. Friedlingstein, J. Rogelj, M. J. Grubb, H. D. Matthews, R. B. Skeie, P. M. Forster, D. J. Frame, and M. R. Allen, "Emission budgets and pathways consistent with limiting warming to 1.5 °C", Nature Geoscience **10**, 741–747 (2017) (p. 48).

[189] J. Tsutsui, "Diagnosing Transient Response to CO2 Forcing in Coupled Atmosphere-Ocean Model Experiments Using a Climate Model Emulator", Geophysical Research Letters **47**, e2019GL085844 (2020) (pp. 49, 134).

[190] B. Sanderson, "The role of prior assumptions in carbon budget calculations", Earth System Dynamics **11**, 563–577 (2020) (p. 49).

[191] A. K. Seshadri, "Fast–slow climate dynamics and peak global warming", Climate Dynamics **48**, 2235–2253 (2017) (pp. 50, 167).

[192] M. R. Allen, J. S. Fuglestvedt, K. P. Shine, A. Reisinger, R. T. Pierrehumbert, and P. M. Forster, "New use of global warming potentials to compare cumulative and short-lived climate pollutants", Nature Climate Change **6**, 773–776 (2016) (p. 55).

[193] A. R. Lauder, I. G. Enting, J. O. Carter, N. Clisby, A. L. Cowie, B. K. Henry, and M. R. Raupach, "Offsetting methane emissions — An alternative to emission equivalence metrics", International Journal of Greenhouse Gas Control **12**, 419–429 (2013) (p. 55).

[194] M. Manning and A. Reisinger, "Broader perspectives for comparing different greenhouse gases", Philosophical Transactions of the Royal Society A: Mathematical, Physical and Engineering Sciences **369**, 1891–1905 (2011) (p. 55).

[195] K. Zickfeld, M. Eby, H. D. Matthews, and A. J. Weaver, "Setting cumulative emissions targets to reduce the risk of dangerous climate change", Proceedings of the National Academy of Sciences **106**, 16129–16134 (2009) (p. 55).

[196] P. Friedlingstein, P. Cox, R. Betts, L. Bopp, W. Von Bloh, V. Brovkin, P. Cadule, S. Doney, M. Eby, I. Fung, G. Bala, J. John, C. Jones, F. Joos, T. Kato, M. Kawamiya, W. Knorr, K. Lindsay, H. D. Matthews, T. Raddatz, P. Rayner, C. Reick, E. Roeckner, K.-G. Schnitzler, R. Schnur, K. Strassmann, A. J. Weaver, C. Yoshikawa, and N. Zeng, "Climate-carbon cycle feedback analysis: Results from the C4MIP model intercomparison", Journal of Climate **19**, 3337–3353 (2006) (p. 56).

[197] S. K. Liddicoat, A. J. Wiltshire, C. D. Jones, V. K. Arora, V. Brovkin, P. Cadule, T. Hajima, D. M. Lawrence, J. Pongratz, J. Schwinger, R. Séférian, J. F. Tjiputra, and T. Ziehn, "Compatible Fossil Fuel CO2 Emissions in the CMIP6 Earth System Models' Historical and Shared Socioeconomic Pathway Experiments of the Twenty-First Century", Journal of Climate **34**, 2853–2875 (2021) (pp. 56, 155).

[198] J. Fuglestvedt, J. Rogelj, R. J. Millar, M. Allen, O. Boucher, M. Cain, P. M. Forster, E. Kriegler, and D. Shindell, "Implications of possible interpretations of 'greenhouse gas balance' in the Paris Agreement", Philosophical Transactions of the Royal Society A: Mathematical, Physical and Engineering Sciences **376**, 20160445 (2018) (p. 58).

[199] NOAA, *Climate at a Glance | National Centers for Environmental Information (NCEI)*, (Oct. 2019) `https://www.ncdc.noaa.gov/cag/global/time-series` (visited on 10/04/2019) (pp. 58, 86).

[200] G. Myhre, B. H. Samset, M. Schulz, Y. Balkanski, S. Bauer, T. K. Berntsen, H. Bian, N. Bellouin, M. Chin, T. Diehl, R. C. Easter, J. Feichter, S. J. Ghan, D. Hauglustaine, T. Iversen, S. Kinne, A. Kirkevåg, J.-F. Lamarque, G. Lin, X. Liu, M. T. Lund, G. Luo, X. Ma, T. van Noije, J. E. Penner, P. J. Rasch, A. Ruiz, Ø. Seland, R. B. Skeie, P. Stier, T. Takemura, K. Tsigaridis, P. Wang, Z. Wang, L. Xu, H. Yu, F. Yu, J.-H. Yoon, K. Zhang, H. Zhang, and C. Zhou, "Radiative forcing of the direct aerosol effect from AeroCom Phase II simulations", Atmospheric Chemistry and Physics **13**, 1853–1877 (2013) (pp. 59, 118).

[201] L. J. Wilcox, E. J. Highwood, B. B. B. Booth, and K. S. Carslaw, "Quantifying sources of inter-model diversity in the cloud albedo effect", Geophysical Research Letters **42**, 1568–1575 (2015) (p. 59).

[202] Y. Dong, K. C. Armour, C. Proistosescu, T. Andrews, D. S. Battisti, P. M. Forster, D. Paynter, C. J. Smith, and H. Shiogama, "Biased Estimates of Equilibrium Climate Sensitivity and Transient Climate Response Derived From Historical CMIP6 Simulations", Geophysical Research Letters **48**, e2021GL095778 (2021) (p. 65).

[203] C. Justice, E. Vermote, J. Townshend, R. Defries, D. Roy, D. Hall, V. Salomonson, J. Privette, G. Riggs, A. Strahler, W. Lucht, R. Myneni, Y. Knyazikhin, S. Running, R. Nemani, Z. Wan, A. Huete, W. van Leeuwen, R. Wolfe, L. Giglio, J. Muller, P. Lewis, and M. Barnsley, "The Moderate Resolution Imaging Spectroradiometer (MODIS): land remote sensing for global change research", IEEE Transactions on Geoscience and Remote Sensing **36**, 1228–1249 (1998) (p. 66).

[204] M. Meinshausen, E. Vogel, A. Nauels, K. Lorbacher, N. Meinshausen, D. M. Etheridge, P. J. Fraser, S. A. Montzka, P. J. Rayner, C. M. Trudinger, P. B. Krummel, U. Beyerle, J. G. Canadell, J. S. Daniel, I. G. Enting, R. M. Law, C. R. Lunder, S. O'Doherty, R. G. Prinn, S. Reimann, M. Rubino, G. J. M. Velders, M. K. Vollmer, R. H. J. Wang, and R. Weiss, "Historical greenhouse gas concentrations for climate modelling (CMIP6)", Geoscientific Model Development **10**, 2057–2116 (2017) (p. 68).

[205] S. Rao, Z. Klimont, S. J. Smith, R. Van Dingenen, F. Dentener, L. Bouwman, K. Riahi, M. Amann, B. L. Bodirsky, D. P. van Vuuren, L. Aleluia Reis, K. Calvin, L. Drouet, O. Fricko, S. Fujimori, D. Gernaat, P. Havlik, M. Harmsen, T. Hasegawa, C. Heyes, J. Hilaire, G. Luderer, T. Masui, E. Stehfest, J. Strefler, S. van der Sluis, and M. Tavoni, "Future air pollution in the Shared Socio-economic Pathways", Global Environmental Change **42**, 346–358 (2017) (p. 68).

[206] C. Le Quéré, R. B. Jackson, M. W. Jones, A. J. P. Smith, S. Abernethy, R. M. Andrew, A. J. De-Gol, D. R. Willis, Y. Shan, J. G. Canadell, P. Friedlingstein, F. Creutzig, and G. P. Peters, "Temporary reduction in daily global CO 2 emissions during the COVID-19 forced confinement", Nature Climate Change **10**, 647–653 (2020) (p. 70).

[207] N. US Department of Commerce, *Global Monitoring Laboratory - Carbon Cycle Greenhouse Gases*, https://www.esrl.noaa.gov/gmd/ccgg/trends/ (visited on 03/10/2021) (pp. 70, 72).

[208] Q. Zhang, Y. Zheng, D. Tong, M. Shao, S. Wang, Y. Zhang, X. Xu, J. Wang, H. He, W. Liu, Y. Ding, Y. Lei, J. Li, Z. Wang, X. Zhang, Y. Wang, J. Cheng, Y. Liu, Q. Shi, L. Yan, G. Geng, C. Hong, M. Li, F. Liu, B. Zheng, J. Cao, A. Ding, J. Gao, Q. Fu, J. Huo, B. Liu, Z. Liu, F. Yang, K. He, and J. Hao, "Drivers of improved PM2.5 air quality in China from 2013 to 2017", Proceedings of the National Academy of Sciences **116**, 24463–24469 (2019) (p. 70).

[209] M. Kasoar, D. Shawki, and A. Voulgarakis, "Similar spatial patterns of global climate response to aerosols from different regions", npj Climate and Atmospheric Science **1**, 1–8 (2018) (pp. 72, 93).

[210] D. T. Shindell, A. Voulgarakis, G. Faluvegi, and G. Milly, "Precipitation response to regional radiative forcing", Atmospheric Chemistry and Physics **12**, 6969–6982 (2012) (p. 72).

[211] NASA Goddard Institute for Space Studies., *GISS Surface Temperature Analysis (GISTEMP), version 4*, (2018) https://data.giss.nasa.gov/gistemp (visited on 01/05/2018) (pp. 73, 142).

[212] G. C. Hegerl, S. Brönnimann, A. Schurer, and T. Cowan, "The early 20th century warming: Anomalies, causes, and consequences", WIREs Climate Change **9**, e522 (2018) (pp. 75, 80).

[213] L. Zanna, S. Khatiwala, J. M. Gregory, J. Ison, and P. Heimbach, "Global reconstruction of historical ocean heat storage and transport", Proceedings of the National Academy of Sciences **116**, 1126–1131 (2019) (pp. 77, 84, 89, 123).

[214] NOAA, *Pacific Decadal Oscillation (PDO) | National Centers for Environmental Information (NCEI)*, (2023) https://www.ncei.noaa.gov/access/monitoring/pdo/ (visited on 03/24/2023) (p. 80).

[215] M. Office, *The recent pause in global warming(2): What are the potential causes?*, tech. rep. (July 2013) (p. 81).

[216] B. D. Stocker, R. Roth, F. Joos, R. Spahni, M. Steinacher, S. Zaehle, L. Bouwman, Xu-Ri, and I. C. Prentice, "Multiple greenhouse gas feedbacks from the land biosphere under future climate change scenarious", Nature Climate Change **3**, 666–672 (2013) (pp. 83, 96).

[217] B. Huang, P. W. Thorne, V. F. Banzon, T. Boyer, G. Chepurin, J. H. Lawrimore, M. J. Menne, T. M. Smith, R. S. Vose, and H.-M. Zhang, "Extended Reconstructed Sea Surface Temperature, Version 5 (ERSSTv5): Upgrades, Validations, and Intercomparisons", Journal of Climate **30**, 8179–8205 (2017) (p. 83).

[218] N. A. Rayner, D. E. Parker, E. B. Horton, C. K. Folland, L. V. Alexander, D. P. Rowell, E. C. Kent, and A. Kaplan, "Global analyses of sea surface temperature, sea ice, and night marine air temperature since the late nineteenth century", Journal of Geophysical Research: Atmospheres **108**, https://doi.org/10.1029/2002JD002670 (2003) (p. 83).

[219] M. Kovilakam, L. W. Thomason, N. Ernest, L. Rieger, A. Bourassa, and L. Millán, "The Global Space-based Stratospheric Aerosol Climatology (version 2.0): 1979–2018", Earth System Science Data **12**, 2607–2634 (2020) (p. 85).

[220] D. Notz and J. Stroeve, "Observed Arctic sea-ice loss directly follows anthropogenic CO2 emission", Science **354**, 747–750 (2016) (p. 88).

[221] G. Dagan, P. Stier, M. Christensen, G. Cioni, D. Klocke, and A. Seifert, "Atmospheric energy budget response to idealized aerosol perturbation in tropical cloud systems", Atmospheric Chemistry and Physics **20**, 4523–4544 (2020) (p. 90).

[222] P. J. Marinescu, S. C. v. d. Heever, M. Heikenfeld, A. I. Barrett, C. Barthlott, C. Hoose, J. Fan, A. M. Fridlind, T. Matsui, A. K. Miltenberger, P. Stier, B. Vie, B. A. White, and Y. Zhang, "Impacts of Varying Concentrations of Cloud Condensation Nuclei on Deep Convective Cloud Updrafts—A Multimodel Assessment", Journal of the Atmospheric Sciences **78**, 1147–1172 (2021) (p. 90).

[223] G. G. Persad and K. Caldeira, "Divergent global-scale temperature effects from identical aerosols emitted in different regions", Nature Communications **9**, 3289 (2018) (p. 93).

[224] M. Sand, T. K. Berntsen, A. M. L. Ekman, H.-C. Hansson, and A. Lewinschal, "Surface temperature response to regional black carbon emissions: do location and magnitude matter?", Atmospheric Chemistry and Physics **20**, 3079–3089 (2020) (p. 93).

[225] ESA, *A new satellite to understand how Earth is losing its cool*, (Dec. 2021) https://www.esa.int/Applications/Observing_the_Earth/A_new_satellite_to_understand_how_Earth_is_losing_its_cool (p. 97).

[226] P. Stier, N. a. J. Schutgens, N. Bellouin, H. Bian, O. Boucher, M. Chin, S. Ghan, N. Huneeus, S. Kinne, G. Lin, X. Ma, G. Myhre, J. E. Penner, C. A. Randles, B. Samset, M. Schulz, T. Takemura, F. Yu, H. Yu, and C. Zhou, "Host model uncertainties in aerosol radiative forcing estimates: results from the AeroCom Prescribed intercomparison study", Atmospheric Chemistry and Physics **13**, 3245–3270 (2013) (p. 97).

[227] T. Storelvmo, U. K. Heede, T. Leirvik, P. C. B. Phillips, P. Arndt, and M. Wild, "Lethargic Response to Aerosol Emissions in Current Climate Models", Geophysical Research Letters **45**, 9814–9823 (2018) (p. 100).

[228] M. Wild, "Decadal changes in radiative fluxes at land and ocean surfaces and their relevance for global warming", Wiley Interdisciplinary Reviews: Climate Change **7**, 91–107 (2016) (pp. 100, 112, 115, 117, 128).

[229] C. J. Wall, J. R. Norris, A. Possner, D. T. McCoy, I. L. McCoy, and N. J. Lutsko, "Assessing effective radiative forcing from aerosol–cloud interactions over the global ocean", Proceedings of the National Academy of Sciences **119**, e2210481119 (2022) (pp. 101, 113, 120).

[230] F. Tian, B. Dong, J. Robson, R. Sutton, and L. Wilcox, "Processes shaping the spatial pattern and seasonality of the surface air temperature response to anthropogenic forcing", Climate Dynamics **54**, 3959–3975 (2020) (pp. 101, 103, 115, 119, 128, 129).

[231] *input4MIPs - Home | ESGF-CoG*, https://esgf-node.llnl.gov/projects/input4mips/ (visited on 02/03/2023) (p. 104).

[232] R. M. Hoesly, S. J. Smith, L. Feng, Z. Klimont, G. Janssens-Maenhout, T. Pitkanen, J. J. Seibert, L. Vu, R. J. Andres, R. M. Bolt, T. C. Bond, L. Dawidowski, N. Kholod, J.-i. Kurokawa, M. Li, L. Liu, Z. Lu, M. C. P. Moura, P. R. O'Rourke, and Q. Zhang, "Historical (1750–2014) anthropogenic emissions of reactive gases and aerosols from the Community Emissions Data System (CEDS)", Geoscientific Model Development **11**, 369–408 (2018) (p. 104).

[233] A. Mortier, J. Gliß, M. Schulz, W. Aas, E. Andrews, H. Bian, M. Chin, P. Ginoux, J. Hand, B. Holben, H. Zhang, Z. Kipling, A. Kirkevåg, P. Laj, T. Lurton, G. Myhre, D. Neubauer, D. Olivié, K. von Salzen, R. B. Skeie, T. Takemura, and S. Tilmes, "Evaluation of climate model aerosol trends with ground-based observations over the last 2 decades – an AeroCom and CMIP6 analysis", Atmospheric Chemistry and Physics **20**, 13355–13378 (2020) (pp. 104, 106, 110).

[234] Q. Zhong, H. Shen, X. Yun, Y. Chen, Y. Ren, H. Xu, G. Shen, W. Du, J. Meng, W. Li, J. Ma, and S. Tao, "Global Sulfur Dioxide Emissions and the Driving Forces", Environmental Science & Technology **54**, 6508–6517 (2020) (p. 104).

[235] T. DelSole and M. Tippett, *Statistical Methods for Climate Scientists* (Cambridge University Press, Cambridge, 2022) (p. 104).

[236] V. Vestreng, G. Myhre, H. Fagerli, S. Reis, and L. Tarrasón, "Twenty-five years of continuous sulphur dioxide emission reduction in Europe", Atmospheric Chemistry and Physics **7**, 3663–3681 (2007) (p. 105).

[237] K. Tørseth, W. Aas, K. Breivik, A. M. Fjæraa, M. Fiebig, A. G. Hjellbrekke, C. Lund Myhre, S. Solberg, and K. E. Yttri, "Introduction to the European Monitoring and Evaluation Programme (EMEP) and observed atmospheric composition change during 1972–2009", Atmospheric Chemistry and Physics **12**, 5447–5481 (2012) (p. 105).

[238] J. E. Sickles II and D. S. Shadwick, "Air quality and atmospheric deposition in the eastern US: 20 years of change", Atmospheric Chemistry and Physics **15**, 173–197 (2015) (p. 105).

[239] M. Engardt, D. Simpson, M. Schwikowski, and L. Granat, "Deposition of sulphur and nitrogen in Europe 1900–2050. Model calculations and comparison to historical observations", Tellus B: Chemical and Physical Meteorology **69**, 1328945 (2017) (pp. 105, 112).

[240] P. Sherman, M. Gao, S. Song, A. T. Archibald, N. L. Abraham, J.-F. Lamarque, D. Shindell, G. Faluvegi, and M. B. McElroy, "Sensitivity of modeled Indian monsoon to Chinese and Indian aerosol emissions", Atmospheric Chemistry and Physics **21**, 3593–3605 (2021) (p. 105).

[241] L. Yan, "Legislation of air pollution control in China", IOP Conference Series: Earth and Environmental Science **512**, 012029 (2020) (p. 106).

[242] *JGCRI/CEDS*, (Feb. 2021) https://github.com/JGCRI/CEDS (visited on 03/18/2021) (p. 106).

[243] N. Elguindi, C. Granier, T. Stavrakou, S. Darras, M. Bauwens, H. Cao, C. Chen, H. a. C. Denier van der Gon, O. Dubovik, T. M. Fu, D. K. Henze, Z. Jiang, S. Keita, J. J. P. Kuenen, J. Kurokawa, C. Liousse, K. Miyazaki, J.-F. Müller, Z. Qu, F. Solmon, and B. Zheng, "Intercomparison of Magnitudes and Trends in Anthropogenic Surface Emissions From Bottom-Up Inventories, Top-Down Estimates, and Emission Scenarios", Earth's Future **8**, e2020EF001520 (2020) (p. 106).

[244] S. Ramachandran, M. Rupakheti, and R. Cherian, "Insights into recent aerosol trends over Asia from observations and CMIP6 simulations", Science of The Total Environment **807**, 150756 (2022) (p. 106).

[245] T. A. P. Journal, *The Revision of China's Energy and Coal Consumption Data: A preliminary analysis*, (2023) https://apjjf.org/-John_A_-Mathews/4398 (visited on 02/06/2023) (p. 106).

[246] S. Su, B. Li, S. Cui, and S. Tao, "Sulfur Dioxide Emissions from Combustion in China: From 1990 to 2007", Environmental Science & Technology **45**, 8403–8410 (2011) (p. 106).

[247] V. Karthik, B. Vijay Bhaskar, S. Ramachandran, and A. W. Gertler, "Quantification of organic carbon and black carbon emissions, distribution, and carbon variation in diverse vegetative ecosystems across India", Environmental Pollution **309**, 119790 (2022) (p. 106).

[248] C. Granier, B. Bessagnet, T. Bond, A. D'Angiola, H. Denier van der Gon, G. J. Frost, A. Heil, J. W. Kaiser, S. Kinne, Z. Klimont, S. Kloster, J.-F. Lamarque, C. Liousse, T. Masui, F. Meleux, A. Mieville, T. Ohara, J.-C. Raut, K. Riahi, M. G. Schultz, S. J. Smith, A. Thompson, J. van Aardenne, G. R. van der Werf, and D. P. van Vuuren, "Evolution of anthropogenic and biomass burning emissions of air pollutants at global and regional scales during the 1980–2010 period", Climatic Change **109**, 163 (2011) (p. 106).

[249] A. Zhao, C. L. Ryder, and L. J. Wilcox, "How well do the CMIP6 models simulate dust aerosols?", Atmospheric Chemistry and Physics **22**, 2095–2119 (2022) (p. 106).

[250] *ACCENT emissions*, http://accent.aero.jussieu.fr/MACC_metadata.php (visited on 02/06/2023) (p. 107).

[251] M. W. Jones, J. T. Abatzoglou, S. Veraverbeke, N. Andela, G. Lasslop, M. Forkel, A. J. P. Smith, C. Burton, R. A. Betts, G. R. van der Werf, S. Sitch, J. G. Canadell, C. Santín, C. Kolden, S. H. Doerr, and C. Le Quéré, "Global and Regional Trends and Drivers of Fire Under Climate Change", Reviews of Geophysics **60**, e2020RG000726 (2022) (p. 109).

[252] Vizzuality, *Forest Monitoring, Land Use & Deforestation Trends | Global Forest Watch*, https://www.globalforestwatch.org/ (visited on 02/06/2023) (p. 109).

[253] B. Zheng, P. Ciais, F. Chevallier, E. Chuvieco, Y. Chen, and H. Yang, "Increasing forest fire emissions despite the decline in global burned area", Science Advances **7**, eabh2646 (2021) (p. 109).

[254] J. T. Randerson, G. R. Van Der Werf, L. Giglio, G. J. Collatz, and P. S. Kasibhatla, "Global Fire Emissions Database, Version 4.1 (GFEDv4)", ORNL DAAC, 10.3334/ORNLDAAC/1293 (2015) (p. 109).

[255] G. R. van der Werf, J. T. Randerson, L. Giglio, G. J. Collatz, M. Mu, P. S. Kasibhatla, D. C. Morton, R. S. DeFries, Y. Jin, and T. T. van Leeuwen, "Global fire emissions and the contribution of deforestation, savanna, forest, agricultural, and peat fires (1997-2009)", Atmospheric Chemistry and Physics **10**, 11707–11735 (2010) (p. 109).

[256] A. M. Sayer, N. C. Hsu, C. Bettenhausen, and M.-J. Jeong, "Validation and uncertainty estimates for MODIS Collection 6 "Deep Blue" aerosol data", Journal of Geophysical Research: Atmospheres **118**, 7864–7872 (2013) (p. 110).

[257] M. S. Team, *MYD04_l2 MODIS/Aqua Aerosol 5-Min L2 Swath 10km*, (2014) http://modaps.nascom.nasa.gov/services/about/products/c6/MYD04_L2.html (visited on 02/06/2023) (p. 110).

[258] M. A. S. Team, *MOD04_l2 MODIS/Terra Aerosol 5-Min L2 Swath 10km*, (2015) http://modaps.nascom.nasa.gov/services/about/products/c6/MOD04_L2.html (visited on 02/06/2023) (p. 110).

[259] J. A. Limbacher, R. A. Kahn, and J. Lee, "The new MISR research aerosol retrieval algorithm: a multi-angle, multi-spectral, bounded-variable least squares retrieval of aerosol particle properties over both land and water", Atmospheric Measurement Techniques **15**, 6865–6887 (2022) (p. 110).

[260] S. K. Gulev, P. W. Thorne, J. Ahn, F. J. Dentener, C. M. Domingues, S. Gerland, D. Gong, D. S. Kaufmann, H. C. Nnamchi, J. Quaas, J. A. Rivera, S. Sathyendranath, S. L. Smith, B. Trewin, K. von Schuckmann, and R. S. Vose, "Changing State of the Climate System. In Climate Change 2021: The Physical Science Basis. Contribution of Working Group I to the Sixth Assessment Report of the Intergovernmental Panel on Climate Change.", 287–422 (2021) (p. 110).

[261] NASA, *Aerosol Robotic Network (AERONET) Homepage*, (2023) https://aeronet.gsfc.nasa.gov/ (visited on 02/06/2023) (p. 110).

[262] T. D. Toth, J. Zhang, J. R. Campbell, J. S. Reid, Y. Shi, R. S. Johnson, A. Smirnov, M. A. Vaughan, and D. M. Winker, "Investigating enhanced Aqua MODIS aerosol optical depth retrievals over the mid-to-high latitude Southern Oceans through intercomparison with co-located CALIOP, MAN, and AERONET data sets", Journal of Geophysical Research: Atmospheres **118**, 4700–4714 (2013) (p. 112).

[263] V. Schenzinger and A. Kreuter, "Reducing cloud contamination in aerosol optical depth (AOD) measurements", Atmospheric Measurement Techniques **14**, 2787–2798 (2021) (p. 112).

[264] C. R. Terai, S. A. Klein, and M. D. Zelinka, "Constraining the low-cloud optical depth feedback at middle and high latitudes using satellite observations", Journal of Geophysical Research: Atmospheres **121**, 9696–9716 (2016) (p. 113).

[265] M. Wild, "Global dimming and brightening: A review", Journal of Geophysical Research: Atmospheres **114**, 10.1029/2008JD011470 (2009) (pp. 115, 128).

[266] G. L. Stephens, D. O'Brien, P. J. Webster, P. Pilewski, S. Kato, and J.-l. Li, "The albedo of Earth", Reviews of Geophysics **53**, 141–163 (2015) (pp. 115, 117, 119, 120).

[267] M. Wild, "Enlightening Global Dimming and Brightening", Bulletin of the American Meteorological Society **93**, 27–37 (2011) (p. 115).

[268] M. Yuan, T. Leirvik, and M. Wild, "Global Trends in Downward Surface Solar Radiation from Spatial Interpolated Ground Observations during 1961–2019", Journal of Climate **34**, 9501–9521 (2021) (p. 115).

[269] H. Douville, S. Qasmi, A. Ribes, and O. Bock, "Global warming at near-constant tropospheric relative humidity is supported by observations", Communications Earth & Environment **3**, 1–7 (2022) (p. 117).

[270] M. S. Diamond, J. J. Gristey, J. E. Kay, and G. Feingold, "Anthropogenic aerosol and cryosphere changes drive Earth's strong but transient clear-sky hemispheric albedo asymmetry", Communications Earth & Environment **3**, 1–10 (2022) (pp. 117, 119).

[271] N. G. Loeb, W. Su, N. Bellouin, and Y. Ming, "Changes in Clear-Sky Shortwave Aerosol Direct Radiative Effects Since 2002", Journal of Geophysical Research: Atmospheres **126**, e2020JD034090 (2021) (pp. 119, 122).

[272] H. Bai, M. Wang, Z. Zhang, and Y. Liu, "Synergetic Satellite Trend Analysis of Aerosol and Warm Cloud Properties ver Ocean and Its Implication for Aerosol-Cloud Interactions", Journal of Geophysical Research: Atmospheres **125**, e2019JD031598 (2020) (p. 124).

[273] Y. Cao, Y. Zhu, M. Wang, D. Rosenfeld, Y. Liang, J. Liu, Z. Liu, and H. Bai, "Emission Reductions Significantly Reduce the Hemispheric Contrast in Cloud Droplet Number Concentration in Recent Two Decades", Journal of Geophysical Research: Atmospheres **128**, e2022JD037417 (2023) (p. 125).

[274] E. Gryspeerdt, J. Quaas, S. Ferrachat, A. Gettelman, S. Ghan, U. Lohmann, H. Morrison, D. Neubauer, D. G. Partridge, P. Stier, T. Takemura, H. Wang, M. Wang, and K. Zhang, "Constraining the instantaneous aerosol influence on cloud albedo", Proceedings of the National Academy of Sciences **114**, 4899–4904 (2017) (p. 125).

[275] M. Rantanen, A. Y. Karpechko, A. Lipponen, K. Nordling, O. Hyvärinen, K. Ruosteenoja, T. Vihma, and A. Laaksonen, "The Arctic has warmed nearly four times faster than the globe since 1979", Communications Earth & Environment **3**, 1–10 (2022) (p. 127).

[276] P. Keil, T. Mauritsen, J. Jungclaus, C. Hedemann, D. Olonscheck, and R. Ghosh, "Multiple drivers of the North Atlantic warming hole", Nature Climate Change **10**, 667–671 (2020) (p. 127).

[277] R. J. Millar, A. Otto, P. M. Forster, J. A. Lowe, W. J. Ingram, and M. R. Allen, "Model structure in observational constraints on transient climate response", Climatic Change **131**, 199–211 (2015) (p. 136).

[278] S. Jenkins, M. Cain, P. Friedlingstein, N. Gillett, T. Walsh, and M. R. Allen, "Quantifying non-CO2 contributions to remaining carbon budgets", npj Climate and Atmospheric Science **4**, 1–10 (2021) (pp. 140, 170).

[279] C. L. Quere, R. M. Andrew, P. Friedlingstein, S. Sitch, J. Hauck, J. Pongratz, P. A. Pickers, J. I. Korsbakken, G. P. Peters, J. G. Canadell, A. Arneth, V. K. Arora, L. Barbero, A. Bastos, L. Bopp, F. Chevallier, L. P. Chini, P. Ciais, S. C. Doney, T. Gkritzalis, D. S. Goll, I. Harris, V. Haverd, F. M. Hoffman, M. Hoppema, R. A. Houghton, G. Hurtt, T. Ilyina, A. K. Jain, T. Johannessen, C. D. Jones, E. Kato, R. F. Keeling, K. K. Goldewijk, P. Landschützer, N. Lefèvre, S. Lienert, Z. Liu, D. Lombardozzi, N. Metzl, D. R. Munro, J. E. M. S. Nabel, S.-i. Nakaoka, C. Neill, A. Olsen, T. Ono, P. Patra, A. Peregon, W. Peters, P. Peylin, B. Pfeil, D. Pierrot, B. Poulter, G. Rehder, L. Resplandy, E. Robertson, M. Rocher, C. Rödenbeck, U. Schuster, J. Schwinger, R. Séférian, I. Skjelvan, T. Steinhoff, A. Sutton, P. P. Tans, H. Tian, B. Tilbrook, F. N. Tubiello, I. T. v. d. Laan-Luijkx, G. R. v. d. Werf, N. Viovy, A. P. Walker, A. J. Wiltshire, R. Wright, S. Zaehle, and B. Zheng, "Global Carbon Budget 2018", Earth System Science Data **10**, 2141–2194 (2018) (p. 141).

[280] D. Huppmann, E. Kriegler, V. Krey, K. Riahi, J. Rogelj, S. K. Rose, J. Weyant, N. Bauer, C. Bertram, V. Bosetti, K. Calvin, J. Doelman, L. Drouet, J. Emmerling, S. Frank, S. Fujimori, D. Gernaat, A. Grubler, C. Guivarch, M. Haigh, C. Holz, G. Iyer, E. Kato, K. Keramidas, A. Kitous, F. Leblanc, J.-Y. Liu, K. Löffler, G. Luderer, A. Marcucci, D. McCollum, S. Mima, A. Popp, R. D. Sands, F. Sano, J. Strefler, J. Tsutsui, D. Van Vuuren, Z. Vrontisi, M. Wise, and R. Zhang, *IAMC 1.5°C Scenario Explorer and Data hosted by IIASA* (Integrated Assessment Modeling Consortium & International Institute for Applied Systems Analysis, 2018) (pp. 141, 143, 166).

[281] D. Ehlert and K. Zickfeld, "What determines the warming commitment after cessation of CO 2 emissions?", Environmental Research Letters **12**, 015002 (2017) (p. 141).

[282] H. D. Matthews, K. Zickfeld, R. Knutti, and M. R. Allen, "Focus on cumulative emissions, global carbon budgets and the implications for climate mitigation targets", Environmental Research Letters **13**, 010201 (2018) (p. 141).

[283] K. B. Tokarska, C.-F. Schleussner, J. Rogelj, M. B. Stolpe, H. D. Matthews, P. Pfleiderer, and N. P. Gillett, "Recommended temperature metrics for carbon budget estimates, model evaluation and climate policy", Nature Geoscience **12**, 964–971 (2019) (pp. 141, 142).

[284] UNFCCC, *Report on the Structured Expert Dialogue on the 2013-2015 review*, tech. rep. (2015) (pp. 142, 157, 158).

[285] N. Mengis, A.-I. Partanen, J. Jalbert, and H. D. Matthews, "1.5 °C carbon budget dependent on carbon cycle uncertainty and future non-CO 2 forcing", Scientific Reports **8**, 1–7 (2018) (p. 143).

[286] N. J. Leach, R. J. Millar, K. Haustein, S. Jenkins, E. Graham, and M. R. Allen, "Current level and rate of warming determine emissions budgets under ambitious mitigation", Nature Geoscience **11**, 574 (2018) (pp. 146, 161).

[287] N. Mengis and H. D. Matthews, "Non-CO 2 forcing changes will likely decrease the remaining carbon budget for 1.5 °C", npj Climate and Atmospheric Science **3**, 1–7 (2020) (pp. 146, 153).

[288] M. Allen, S. Jenkins, F. Sha, and A. Macey, "Defining Carbon Neutrality, Climate Neutrality and Net Zero Emissions", (2021) (p. 147).

[289] P. Friedlingstein, M. W. Jones, M. O'Sullivan, R. M. Andrew, J. Hauck, G. P. Peters, W. Peters, J. Pongratz, S. Sitch, C. L. Quéré, D. C. E. Bakker, J. G. Canadell, P. Ciais, R. B. Jackson, P. Anthoni, L. Barbero, A. Bastos, V. Bastrikov, M. Becker, L. Bopp, E. Buitenhuis, N. Chandra, F. Chevallier, L. P. Chini, K. I. Currie, R. A. Feely, M. Gehlen, D. Gilfillan, T. Gkritzalis, D. S. Goll, N. Gruber, S. Gutekunst, I. Harris, V. Haverd, R. A. Houghton, G. Hurtt, T. Ilyina, A. K. Jain, E. Joetzjer, J. O. Kaplan, E. Kato, K. Klein Goldewijk, J. I. Korsbakken, P. Landschützer, S. K. Lauvset, N. Lefèvre, A. Lenton, S. Lienert, D. Lombardozzi, G. Marland, P. C. McGuire, J. R. Melton, N. Metzl, D. R. Munro, J. E. M. S. Nabel, S.-I. Nakaoka, C. Neill, A. M. Omar, T. Ono, A. Peregon, D. Pierrot, B. Poulter, G. Rehder, L. Resplandy, E. Robertson, C. Rödenbeck, R. Séférian, J. Schwinger, N. Smith, P. P. Tans, H. Tian, B. Tilbrook, F. N. Tubiello, G. R. v. d. Werf, A. J. Wiltshire, and S. Zaehle, "Global Carbon Budget 2019", Earth System Science Data **11**, 1783–1838 (2019) (p. 150).

[290] R. G. Williams, P. Ceppi, and A. Katavouta, "Controls of the transient climate response to emissions by physical feedbacks, heat uptake and carbon cycling", Environmental Research Letters **15**, 0940c1 (2020) (p. 153).

[291] H. Matthews, K. B. Tokarska, J. Rogelj, C. J. Smith, A. H. MacDougall, K. Haustein, N. Mengis, S. Sippel, P. M. Forster, and R. Knutti, "An integrated approach to quantifying uncertainties in the remaining carbon budget", Communications Earth & Environment **2**, 1–11 (2021) (pp. 153, 158, 166).

[292] M. J. Mace, "Mitigation Commitments Under the Paris Agreement and the Way Forward", Climate Law **6**, 21–39 (2016) (p. 158).

[293] United Nations Environment Programme, *The emissions gap report 2019* (2019) (p. 158).

[294] A. L. Ganesan, S. Schwietzke, B. Poulter, T. Arnold, X. Lan, M. Rigby, F. R. Vogel, G. R. v. d. Werf, G. Janssens-Maenhout, H. Boesch, S. Pandey, A. J. Manning, R. B. Jackson, E. G. Nisbet, and M. R. Manning, "Advancing Scientific Understanding of the Global Methane Budget in Support of the Paris Agreement", Global Biogeochemical Cycles **33**, 1475–1512 (2019) (p. 162).

[295] T. e. a. Stocker, *Summary for Policymakers. In: Climate Change 2013: The Physical Science Basis. Contribution of Working Group I to the Fifth Assessment Report of the Intergovernmental Panel on Climate Change*, tech. rep. (IPCC, 2013) (p. 165).

[296] UK Govt., *UK becomes first major economy to pass net zero emissions law*, (June 2019) https://www.gov.uk/government/news/uk-becomes-first-major-economy-to-pass-net-zero-emissions-law (visited on 07/09/2020) (p. 165).

[297] F. Joos, M. Bruno, R. Fink, U. Siegenthaler, T. F. Stocker, C. Le Quéré, and J. L. Sarmiento, "An efficient and accurate representation of complex oceanic and biospheric models of anthropogenic carbon uptake", Tellus B: Chemical and Physical Meteorology **48**, 394–417 (1996) (p. 167).

[298] N. Tarshish, N. Jeevanjee, and I. Fung, "Constraining the post-emissions temperature change", https://doi.org/10.21203/rs.3.rs-1519965/v1 (2022) (pp. 168, 189).

[299] P. Friedlingstein, M. O'Sullivan, M. W. Jones, R. M. Andrew, J. Hauck, A. Olsen, G. P. Peters, W. Peters, J. Pongratz, S. Sitch, C. Le Quéré, J. G. Canadell, P. Ciais, R. B. Jackson, S. Alin, L. E. O. C. Aragão, A. Arneth, V. Arora, N. R. Bates, M. Becker, A. Benoit-Cattin, H. C. Bittig, L. Bopp, S. Bultan, N. Chandra, F. Chevallier, L. P. Chini, W. Evans, L. Florentie, P. M. Forster, T. Gasser, M. Gehlen, D. Gilfillan, T. Gkritzalis, L. Gregor, N. Gruber, I. Harris, K. Hartung, V. Haverd, R. A. Houghton, T. Ilyina, A. K. Jain, E. Joetzjer, K. Kadono, E. Kato, V. Kitidis, J. I. Korsbakken, P. Landschützer, N. Lefèvre, A. Lenton, S. Lienert, Z. Liu, D. Lombardozzi, G. Marland, N. Metzl, D. R. Munro, J. E. M. S. Nabel, S.-I. Nakaoka, Y. Niwa, K. O'Brien, T. Ono, P. I. Palmer, D. Pierrot, B. Poulter, L. Resplandy, E. Robertson, C. Rödenbeck, J. Schwinger, R. Séférian, I. Skjelvan, A. J. P. Smith, A. J. Sutton, T. Tanhua, P. P. Tans, H. Tian, B. Tilbrook, G. van der Werf, N. Vuichard, A. P. Walker, R. Wanninkhof, A. J. Watson, D. Willis, A. J. Wiltshire, W. Yuan, X. Yue, and S. Zaehle, "Global Carbon Budget 2020", Earth System Science Data **12**, 3269–3340 (2020) (pp. 169, 177).

[300] Z. R. J. Nicholls, M. Meinshausen, J. Lewis, R. Gieseke, D. Dommenget, K. Dorheim, C.-S. Fan, J. S. Fuglestvedt, T. Gasser, U. Golüke, P. Goodwin, C. Hartin, A. P. Hope, E. Kriegler, N. J. Leach, D. Marchegiani, L. A. McBride, Y. Quilcaille, J. Rogelj, R. J. Salawitch, B. H. Samset, M. Sandstad, A. N. Shiklomanov, R. B. Skeie, C. J. Smith, S. Smith, K. Tanaka, J. Tsutsui, and Z. Xie, "Reduced Complexity Model Intercomparison Project Phase 1: introduction and evaluation of global-mean temperature response", Geoscientific Model Development **13**, 5175–5190 (2020) (p. 170).

[301] P. Forster et al., "Supplementary Material of Chapter 2, IPCC Special Report on the Global Warming of 1.5C", (2018) (p. 171).

[302] T. L. Frölicher and D. J. Paynter, "Extending the relationship between global warming and cumulative carbon emissions to multi-millennial timescales", Environmental Research Letters **10**, 075002 (2015) (pp. 172, 175).

[303] D. Archer, H. Kheshgi, and E. Maier-Reimer, "Dynamics of fossil fuel CO2 neutralization by marine CaCO3", Global Biogeochemical Cycles **12**, 259–276 (1998) (p. 173).

[304] E. S. Egleston, C. L. Sabine, and F. M. M. Morel, "Revelle revisited: Buffer factors that quantify the response of ocean chemistry to changes in DIC and alkalinity", Global Biogeochemical Cycles **24**, 10.1029/2008GB003407 (2010) (p. 173).

[305] K. L. Ricke and K. Caldeira, "Maximum warming occurs about one decade after a carbon dioxide emission", Environmental Research Letters **9**, 124002 (2014) (p. 175).

[306] C. D. Koven, B. M. Sanderson, and A. L. S. Swann, "Much of zero emissions commitment occurs before reaching net zero emissions", Environmental Research Letters **18**, 014017 (2023) (p. 189).

[307] *A new satellite to understand how Earth is losing its cool*, https://www.esa.int/Applications/Observing_the_Earth/FutureEO/A_new_satellite_to_understand_how_Earth_is_losing_its_cool (visited on 02/24/2023) (p. 189).

[308] S. Bauer, G. A. Schmidt, N. G. Loeb, T. Andrews, P. J. Durack, and V. Ramaswamy, "CERESMIP: An updated protocol for understanding the changes in the Earth Energy Imbalance", in (Dec. 2022) (p. 190).

[309] A. Bodas-Salcedo, M. J. Webb, S. Bony, H. Chepfer, J.-L. Dufresne, S. A. Klein, Y. Zhang, R. Marchand, J. M. Haynes, R. Pincus, and V. O. John, "COSP: Satellite simulation software for model assessment", Bulletin of the American Meteorological Society **92**, 1023–1043 (2011) (p. 190).

[310] B. Stevens, S. C. Sherwood, S. Bony, and M. J. Webb, "Prospects for narrowing bounds on Earth's equilibrium climate sensitivity", Earth's Future **4**, 512–522 (2016) (p. 191).

[311] J. Terhaar, T. L. Frölicher, M. T. Aschwanden, P. Friedlingstein, and F. Joos, "Adaptive emission reduction approach to reach any global warming target", Nature Climate Change **12**, 1136–1142 (2022) (p. 191).